Modeling Dose-Function Response and Toxicity Pathways in Non-Small Cell Lung Cancer Patients Undergoing Radiation Treatment

by

Daniel Rockwell Owen

A dissertation submitted in partial fulfillment
of the requirements for the degree of
Doctor of Philosophy
(Nuclear Engineering and Radiological Sciences)
in The University of Michigan
2021

Doctoral Committee:

Associate Professor Martha Matuszak, Chair
Professor Alex Bielajew
Associate Professor Phil Boonstra
Assistant Professor Benjamin Viglianti

We forsee cancer research developing into a logical science, where the complexities of the disease, described in the laboratory and clinic, will become understandable in terms of a small number of underlying principles

– Hanahan and Weinberg

The Hallmarks of Cancer

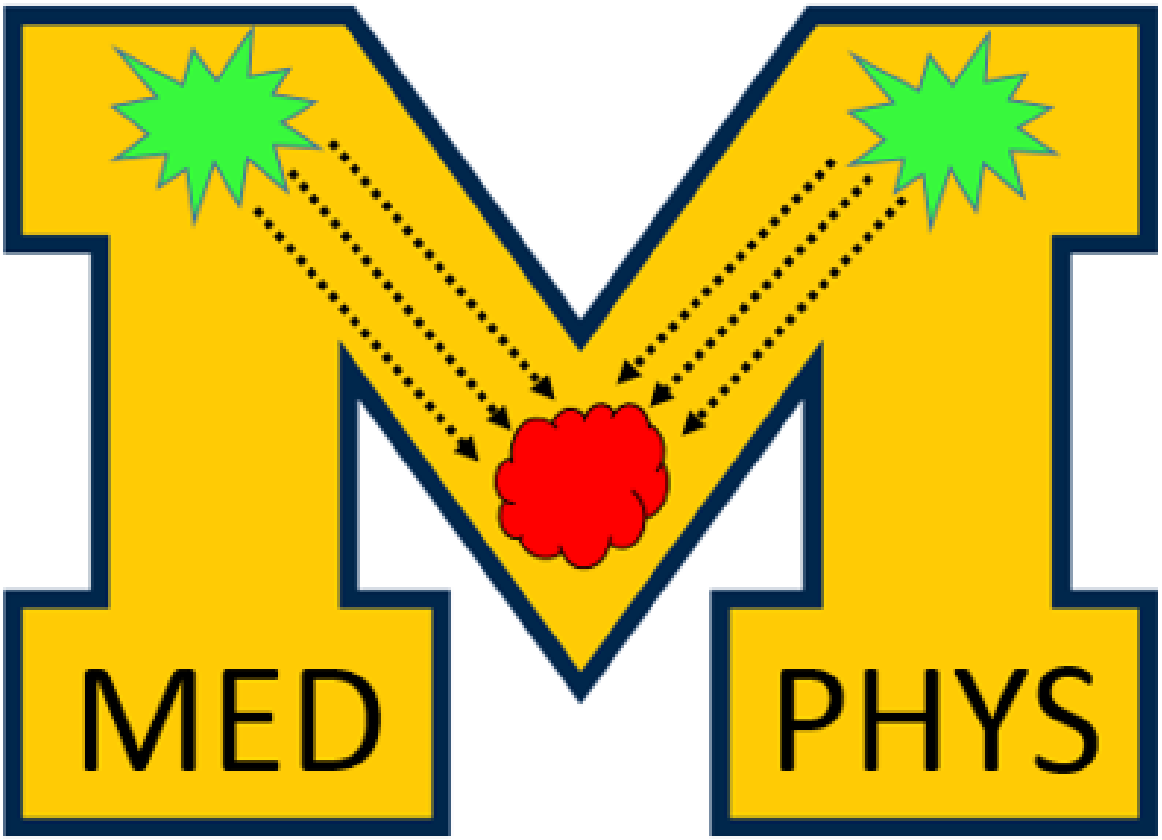

D. Rocky Owen

ORCID ID: 0000-0003-1106-3616

rockyo@umich.edu

This dissertation was conducted with the hopes to specifically help improve the treatment of cancer patients undergoing radiation therapy and to broadly guide the integration of technical quantification with clinical understanding across the medical field.

ACKNOWLEDGEMENTS

First and foremost, my family has been instrumental in providing me the love, support, and values that have made me the man I am today. From day one, my mom, Deborah, and my dad, Daniel, have instilled in me an appreciation for education and hard work, and these ideals have been profoundly influential in driving me to pursue and complete a doctorate degree. As my big sister, Daphne is my role model and has provided me an incredible example in how to succeed in life and witnessing her passion for medicine has subsequently guided my interest to the field. My younger brother, Jayme, has been my best friend and has motivated me to become the role model Daphne has been to me. Finally, I met my girlfriend, Cait, the night of my doctorate qualification exam, and she has been the most amazing partner throughout the roller-coaster of this work, and her genuine love and care for me has been invaluable and has helped me to further push myself as a person and professional.

From a technical standpoint, I feel extremely fortunate to have a dissertation committee in which each of the members have directly impacted my work. Dr. Martha Matuszak, the dissertation chair and my Ph.D. advisor, initially realized my potential and desire to work in personalized medicine, and she has continually provided me the mentorship, funding, and opportunities to succeed with this dissertation. As a transfer student from the University of Oregon physics department, Dr. Alex Bielajew first introduced me to the possibilities for nuclear engineers in medical physics, and the breadth of his understanding and finesse with how he taught the material were instrumental in helping me become a true student focused on learning as opposed to simply completing. Through his vast clinical experience, Dr. Ben Viglianti provided me with an in-depth understanding of nuclear medicine imaging, and his guidance greatly expanded my research vision. Lastly, I

am very thankful for all the effort contributed by Dr. Phil Boonstra, who worked closely with me through numerous iterations of statistical analysis, and ultimately, was the primary inventor of the patient-specific dose-function response models that are presented in chapter V.

I would also like to thank Dr. Yilun Sun for his statistical analysis of the dose-function metrics presented in chapter VI, and Dr. Craig Galban for his collaboration regarding the implementation of parametric response mapping for therapeutic purposes, which is presented in chapter VII. Dr. James Balter was a constant mentor throughout my Ph.D. and continuously taught me and challenged me to better understand medical imaging principles. Dr. Randy Ten Haken was also a great mentor in guiding my work, and Dr. Ted Lawrence has been a constant source of knowledge at research meetings and has been an inspiring leader of the Radiation Oncology department.

I am extremely grateful to the University of Michigan Department of Radiation Oncology for providing the funding and data that facilitated my research and to the University of Michigan Department of Nuclear Engineering for providing a comprehensive education and extensive research opportunities.

TABLE OF CONTENTS

LIST OF FIGURES

Figure

LIST OF TABLES

Table

LIST OF ABBREVIATIONS

4DCT four-dimensional computed tomography

ADL average dose to lower region of lung structure

API application programming interface

AUC area under the curve

Ci curie

cm centimeters

CMF cyclophosphamide, methotrexate and 5-fluorouracil

COPD chronic obstructive pulmonary disease

cpm counts per minute

CT computed tomography

CTCAE common terminology criteria for adverse events

DFH dose-function histogram

DICOM digital imaging and communications in medicine

DIR deformable image registration

DLCO diffusing capacity of the lungs for carbon monoxide

DSC dice similarity coefficient

DTPA diethylenetriaminepentaacetic acid

DVH dose-volume histogram

EQD2 equivalent dose per 2 Gy fraction

F normal-function lung

F20 ventilation or perfusion normal-function volume receiving $\geq$20 Gy, as a percent of total lung structure volume

FDG fluorodeoxyglucose

fDVH functional dose-volume histogram

FEV1 forced expiratory volume during the first second

fMLD functional-weighted mean lung dose

fV5 functional intensity receiving $\geq$ 5 Gy

fV20 functional intensity receiving $\geq$ 20 Gy

fV30 functional intensity receiving $\geq$ 30 Gy

FVC forced vital capacity

GLSZM gray level size zone matrix

GTV gross tumor volume

Gy gray

HAA high attenuation area

HF high-function lung

HF20 ventilation or perfusion high-function volume receiving $\geq$20 Gy, as a percent of total lung structure volume

highVQ20 intersection volume between high-function ventilation and high-function perfusion receiving $\geq$20 Gy, as a percentage of total lung structure volume

HU Hounsfield units

IL interleukin

ILD interstitial lung disease

IMRT intensity-modulated radiation treatment

in inches

IPF idiopathic pulmonary fibrosis

IRB institutional review board

ITV internal tumor volume

iV5 average functional intensity receiving $\geq$5 Gy

iV20 average functional intensity receiving $\geq$20 Gy

keV kiloelectron volt

KPS Karnofsky Performance Status

LF low-function lung

LF20 ventilation or perfusion low-function volume receiving $\geq$20 Gy, as a percent of total lung structure volume

lowVQ20 intersection volume between low-function ventilation and low-function perfusion receiving $\geq$20 Gy, as a percentage of total lung structure volume

LPS lung perfusion score

MAA macroaggregated albumin

MBq megabecquerel

midVQ20 intersection volume between normal-function ventilation and normal-function perfusion receiving $\geq$20 Gy, as a percentage of total lung structure volume

MLD mean lung dose

mm millimeters

Mo molybdenum

MOPP/ABV mechlorethamine, oncovin (vincristine), procarbazine, prednisone/adriamycin, bleomycin and vinblastine

MpLD mean perfusion-weighted lung dose

MRI magnetic resonance imaging

mRNA messanger ribonucleic acid

NaI sodium iodide

NKI Netherlands Cancer Institute

NSCLC non-small cell lung cancer

NTCP normal tissue complication probability

OR odds ratio

PD parenchymal disease

PET positron emitted tomography

PMT photomultiplier tube

PFT pulmonary function test

PRM parametric response mapping

PTV planning treatment volume

Q perfusion

RILI radiation-induced lung injury

RILT radiation-induced lung toxicity

ROC receiver operating curve

RP radiation pneumonitis

RT radiation treatment

SAD small airways disease

SBRT stereotactic body radiation therapy

SPECT single-photon emission computed tomography

SZLGE short-zone low gray-level emphasis

Tc technetium

TD5 total dose producing 5% probability of complication within five years following treatment

TD50 total dose producing 50% probability of complication within five years following treatment

TGF transforming growth factor

Tl thallium

TLCO transfer factor of the lungs for carbon monoxide

TPS treatment planning system

UI user interface

V ventilation

V5 volume of lung receiving $\geq$ 5 Gy

V20 volume of lung receiving $\geq$ 20 Gy

V30 volume of lung receiving $\geq$ 30 Gy

VMAT volumetric modulated arc therapy

WHO World Health Organization

ABSTRACT

Radiotherapy is currently the standard of care for treating non-small cell lung cancer (NSCLC) patients, and while technological advancements in the field continue to improve our ability to successfully treat these patients, serious side-effects, i.e. toxicities, may occur in response to the delivered radiation. In fact, Grade 2 radiation pneumonitis (RP) {i.e. symptomatic, requiring medical intervention} has been reported to occur in 20-30% of NSCLC patients that receive radiation treatment (RT), whereas Grade 5 RP {i.e. death directly related to radiation treatment} is estimated to occur in $\sim$5% of NSCLC patients that undergo RT.

In an effort to better understand functional lung response to radiation, our group developed a novel method to model the patient-specific dose-function response using perfusion and ventilation SPECT intensity as a surrogate measure of lung function. Because a patient's signature, i.e. patient-, treatment-, and disease-related factors, influences the dose-function response across all dose bins, there is an inherent correlation amongst data points contributed by each patient. To account for these interdependencies, a mixed-effects nonlinear regression model was implemented to allow for patient-specific parameters to be assigned to each patient's dose-function response curve individually. Once each patient's dose-function response was modeled, a population-level model was derived by averaging the patient-specific parameters to more accurately represent the expected dose-function response for a future arbitrarily selected patient. As such, we believe this patient-specific modeling approach can facilitate an enhanced characterization of personalized functional changes from a population-based estimate.

Furthermore, by measuring the dose delivered to functional lung categorizations in NSCLC patients undergoing RT, this thesis explicitly analyzed specific dose-function vulnerabilities that may lead to increased rates of toxicities and found that high dose to low-functioning lung was

strongly associated with radiation-induced lung toxicity (RILT) incidence. Although surprising and contrary to the prevailing mantra, this result suggests that low-functioning regions of the lung, which are indicative of pulmonary dysfunction and possibly underlying disease, are susceptible to high dose and should not be disregarded in treatment planning. While it is generally accepted that the primary driving force of toxicity is dose to the normal lung, it is also known that pulmonary comorbidities can become exacerbated in response to radiation and have the potential to influence the incidence of severe forms of RILT. Consequently, by better understanding the mechanisms that cause functional damage and the various toxicity pathways, there is great potential to further mitigate RILT rates in NSCLC patients undergoing RT.

Based on these findings, a preliminary investigation regarding the utility of identifying and quantifying specific phenotypes of pulmonary disease prior to RT was performed. By utilizing parametric response mapping (PRM) of high-resolution inspiration/expiration computed tomography (CT) scans, pre-treatment voxelwise classifications that characterized lung parenchyma as normal, emphysema, small airways disease, or parenchymal disease were analyzed in a cohort of lung cancer patients to determine the expected distribution of each PRM category and to assess their correlation with RILT incidence. As a CT-based imaging technique, PRM offers significant upside due to its wide-availability and its capability to provide spatially-resolved estimates for various forms of pulmonary disease.

In summary, the aims of this thesis were to better understand the dose-function response in lung cancer patients during and after RT, identify functional lung targets that may be useful in mitigating toxicity incidence, and propose solutions to enhance personalized radiation treatment of NSCLC patients in an effort to optimize patient outcomes.

CHAPTER I

Introduction

1.1 Motivation

Lung cancer is a widespread, severe disease that can lead to pulmonary complications, and in many cases, results in death. In fact, it is estimated that 235,760 adults will be diagnosed with lung cancer and 131,880 will die as a direct result from lung cancer in 2021 alone [2]. Overall, lung cancer accounts for about 25% of all cancer deaths, and specifically, non-small cell lung cancer (NSCLC) encompasses a group of lung cancer subtypes, including adenocarcinoma, squamous cell carcinoma, and large cell carcinoma, that all have similar prognoses and treatments and make up $\sim$80-85% of all lung cancer diagnoses [2]. Based on numerous clinical trials, radiation therapy has proven to be the most effective treatment for NSCLC, and it is often prescribed concurrently with systemic therapies, such as chemotherapy or immunotherapy [3]. While the targeted radiation is efficient in killing cancer cells, normal tissue cells and organs surrounding the tumor are also damaged in the radiation delivery process, which can lead to negative side-effects. In the lung, the possible side-effects, i.e. toxicities, are primarily pneumonitis, which is an acute inflammation of the alveolar, or fibrosis, which is long-term scarring of the parenchyma. Because pneumonitis and fibrosis are the main detriments affecting a patient's quality of life following radiation treatment, these toxicities are encompassed by the term radiation-induced lung toxicity (RILT).

Current radiation treatment plans are designed to limit dose to a large volume of the lung in an effort to minimize the incidence of RILT. However, because these plans are developed

using only CT imaging, which does not provide good resolution within the lung given its low density, all regions of the lung are considered to be functionally-equivalent, and thus, are assumed to respond equally to radiation. And yet, this assumption is often inaccurate due to tumor burden or underlying disease that can causes regions of decreased functional capability, i.e. reduced ability to exchange oxygen and carbon monoxide, which can consequently affect the tissue's response to radiation. In an effort to account for and understand the effect of radiation on these varying regions of underlying functional lung, there has been a concerted effort to incorporate functional lung imaging in radiation treatment planning, which has become known as functional-guided radiation therapy.

Functional-guided radiation therapies have long been hypothesized to improve patient outcomes [4–11]. By quantifying perfusion and/or ventilation in normal lung tissue, a patient's three-dimensional functional lung distribution can be spatially-aligned with the anatomical CT scan and incorporated into treatment planning to personalize radiation delivery [12–15]. This is especially important in NSCLC patients who are known to have comorbidities and functional lung defects that change during the course of fractionated radiation therapy [16–19]. Recent clinical studies have shown significant differences between anatomical- and functional-guided radiation treatment plans using a variety of functional imaging modalities, such as single-photon emission computed tomography SPECT [20–23], four-dimensional computed tomography (4DCT) [24–27], and hyperpolarized magnetic resonance imaging (MRI) [28, 29]. While preliminary studies have predicted toxicity reduction using functional-guided radiotherapy [30–32], further work is still required to explicitly understand normal tissue dose-function response and its effect on RILT incidence.

Ventilation and perfusion SPECT/CT imaging provides a quantitative measure of pulmonary function such that normalized intensities within each lung voxel are representative of local concentrations of oxygen and blood, respectively [33]. In 1994, Boersma et al. first proposed using a logistic model to describe dose-function response [34]. Due to the observed high variation in patient-to-patient dose-response, Marks et al. used a voxel-weighted average to determine composite perfusion loss [1]. These studies provided the foundation to longitudinally quantify functional

lung using SPECT/CT imaging [4, 5] and the basis of these methodologies has been extensively applied to characterize dose-function response for various treatments, timepoints, and regions of the lung [35–40]. And yet, most normal tissue complication probability (NTCP) models currently used to assess risk of RILT rely on volumetric dose metrics that do not account for the heterogeneous distribution of functional lung [41–45]. While dose-volume metrics are important determinants of RILT incidence, recent evidence suggests functional information can provide additional benefit in assessing and predicting treatment response [46, 47].

Ideally, a patient's risk for developing toxicity could be predicted by quantifying the expected cumulative functional lung damage for a given radiation treatment plan and by identifying patient-, disease-, and treatment-related characteristics that may predispose a given patient to increased toxicity risk. However, enhanced modeling methods are still needed to accurately characterize lung function response, and patient-specific risk-factors need to be better understood such that functional lung imaging can be appropriately applied to facilitate clinical implementation of personalized radiation therapy, and ultimately, optimize patient outcome.

1.2 Thesis Overview

The goals of this dissertation were to quantify the longitudinal dose-function response in NSCLC patients treated with radiation therapy, identify patient-specific risk-factors that correlate with RILT incidence, and introduce potential mechanisms to reduce negative reactions following RT.

A historical background, including the previous works regarding the dose-function response in lung cancer patients receiving RT and the risk factors associated with RILT incidence, is presented in chapter II. Details on the methods and patient population used in this dissertation are then described in chapter III. To facilitate the necessary analyses needed to accomplish the aims of this dissertation, a novel software was developed in C# through the Varian Eclipse treatment planning system (TPS) application programming interface (API) and the main applications and functionality of this code are shown in chapter IV.

The dose-function response, as characterized by ventilation (V)/perfusion (Q) SPECT imaging, in a cohort of 81 NSCLC patients (60 treated with conventional RT; 21 treated with stereotactic body radiation therapy (SBRT)) was described in chapter V. A patient-specific modeling approach was applied to retrospectively characterize functional reduction using perfusion SPECT/CT during and after RT such that a population-level model could be established to better represent the expected dose-function response in a presenting patient (section 5.7). The model was applied in well-perfused voxels (section 5.8) and segmented by functional categorization at baseline (section 5.9) to enhance the prediction of functional lung damage based on an individual's pre-treatment condition.

Subsequently, pre-treatment dose-function metrics were quantified using perfusion, ventilation, and combined VQ functional categorizations to analyze the sensitivity to radiation in each of these functional lung regions (chapter VI). These novel dose-function metrics were implemented into logistic regression models and receiver operator characteristic curves were used to compare predictability of the various models. Through this analysis, it was determined that high dose to a large portion of the lung, and specifically, dose to the lower lung region and dose to low-functioning lung were most correlated with RILT incidence (section 6.4).

Based on the findings of this work, a collaborative imaging solution, known as PRM of high-resolution inspiration/expiration CT scans, was proposed and analyzed in chapter VII as a means to circumvent the availability and interpretability issues that are associated with current functional imaging modalities. Finally, the broad lessons learned through this dissertation and suggestions for future research in this area are described in chapter VIII.

CHAPTER II

Historical Context

2.1 SPECT Imaging

The mechanistic basis of SPECT imaging, the Anger gamma camera, was invented in 1958 by Hal Anger [48]. This invention, as shown in Figure 2.1, facilitated the measurement and imaging of emitted gamma radiation through the use of a collimator, scintillating crystal, and photomultiplier tubes (PMTs).

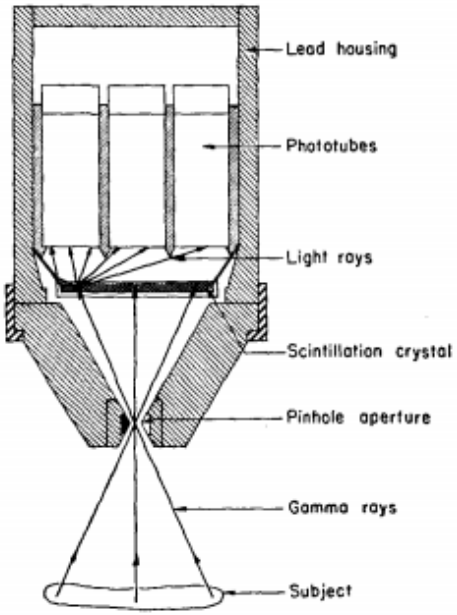

Figure 2.1: A sectional drawing of the original gamma camera invented by Hal Anger in 1958. **Note:** Image from "Scintillation Camera" by Hal O. Anger, 1958, *Review of Scientific Instruments*, 29, pp. 27-33.

In summary, the scintillator crystal was used to absorb energy from the incident photons and re-emit that deposited energy in the form of light. A collimator, in this case a pinhole aperture, was applied in front of the scintillating crystal such that the incident radiation can only be detected from a given area. Because the generated luminescence is produced isotropically within the scintillator, the origin of the gamma radiation can be further refined based on the amount of absorbed light in each of the PMTs. Once the light is detected within the PMTs, it is convert into an electrical current and that signal is then amplified such that it can be read out by an oscilloscope.

Year	Description
1958	Invention of the gamma camera
1963	First SPECT system described
1966	First transmission scan
1967–74	SPECT using a rotating chair
1968–72	Early focal plane emission tomography
1970–73	Clinical SPECT using translating detectors
1973–75	First clinical studies using CT leading to the first commercial CT system
1977–80	SPECT using a rotating gamma camera
1977–83	First description of Compton cameras
1978–79	Development of Cleon/Harvard brain scanner
1980–86	Various dedicated brain SPECT systems: SPRINT, Tomomatic, Headtome
1984–87	Transmission scanning using a flood source
1990–92	First SPECT/CT designs
1992–93	Early simultaneous emission/transmission: scanning line source
1999	First commercial SPECT/CT: Hawkeye
2009–10	Commercial CZT-based cardiac SPECT

Table 2.1: A timeline of notable developments in SPECT imaging. **Note:** Table from "The origins of SPECT and SPECT/CT" by Brian F. Hutton, 2014, *Journal of Nuclear Medicine and Molecular Imaging*, 41(Suppl 1), pp. S3-S16.

While Hal Anger was the pioneer of the SPECT imaging hardware, Kuhl and associates first proposed [49] and demonstrated [50] the use of sectional imaging with a gamma camera, which formed the basis for clinical SPECT imaging methodology. Their technique utilized linear motion of the scintillation camera at various projection angles such that an image could be reconstructed

to represent the distribution of the radioactive sources and served as the first work to employ single-slice images such that only the radiation within a given plane was viewed. These seminal works provided the foundation for SPECT imaging, and while many of these concepts still form the basis for current SPECT imaging, there have been numerous innovations primarily focused on improving spatial resolution, scatter correction, and anatomical localization. A timeline of the technological developments related to SPECT imaging are listed in Table 2.1.

A schematic diagram for a typical SPECT detector system currently used in the clinic is shown in Figure 2.2 [51].

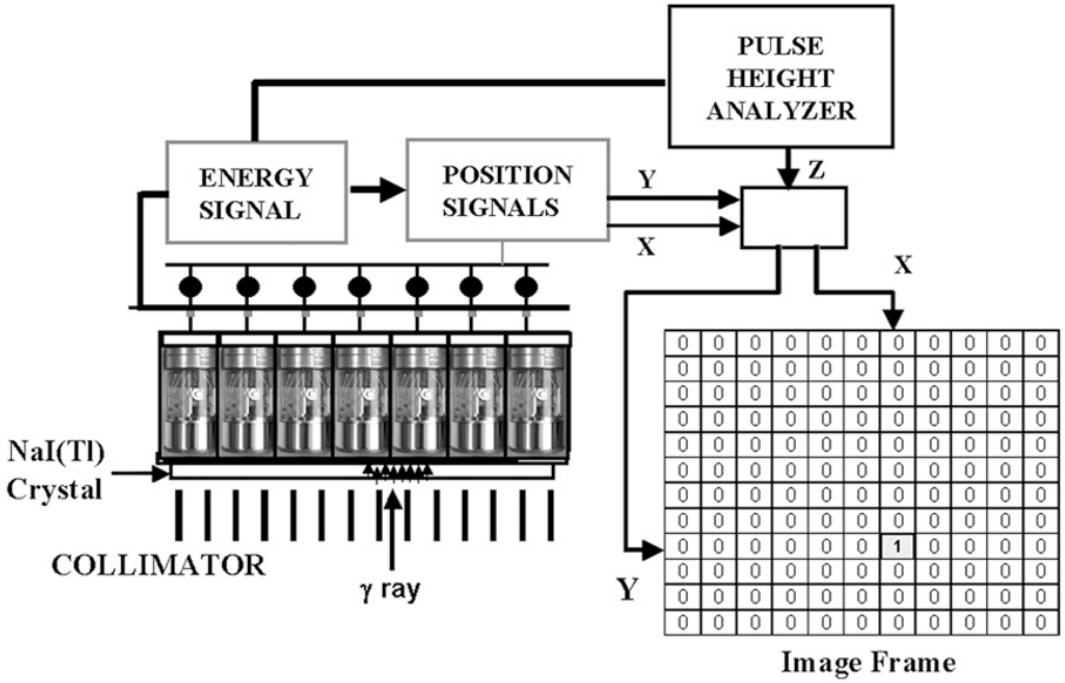

Figure 2.2: SPECT detector system schematic. **Note:** Image from "Recent Advances in SPECT Imaging" by M. Madsen, 2007, *Journal of Nuclear Medicine*, 48, pp. 661-673.

As observed, photons incident on the SPECT system pass through a collimator, which in this case is a parallel hole collimator. Assuming the gamma ray enters at such an angle that it is not filtered out, it deposits energy within the sodium iodide (NaI) scintillating crystal that is doped with thallium (Tl) to enhance sensitivity and light output. The generated light is then sampled by the array of photomultiplier tubes that generate an electrical signal and subsequently locational coordinates based on where the light is collected within the array. If the signal falls within the

set pulse height analyzer window, the event is counted and tallied in the appropriate image frame. This process continues for a given time until the detector is translated to a new projection angle to gather more counts. This is known as the step and shoot mode. The three-dimensional SPECT image can then be reconstructed using either a filtered back projection or iterative method.

Nowadays, most SPECT devices are combined with a CT scanner (SPECT/CT) to enhance the CT-based attenuation map and provide improved anatomical localization. Shown in figure Figure 2.3 is a Siemens Symbia T6 SPECT/CT imaging system that was used to acquire the SPECT images used in this thesis [52]. As observed, the large doughnut-shaped CT gantry is connected to a dual-headed SPECT detector with a mobile patient couch that is utilized to position the patient.

Figure 2.3: Siemens Symbia T6 SPECT/CT imaging system. **Note:** Image from *Siemens Healthineers*, 11-19-2020, https://www.siemens-healthineers.com/en-us/molecular-imaging/spect-and-spect-ct/symbia-t

For this particular imaging system, the NaI crystal has a size of 23.25 inches (in) x 17.5 in and thickness of 5/8 in. A total of 59 photomultiplier tubes (with 53 having diameter of 3 in and 6 having a diameter of 2 in) are arranged in a hexagonal pattern that is used in each detector head. The collimator used in this particular imaging system is a variation on the parallel hole collimator, which is known as the BiCore collimator shown in figure Figure 2.4 [53]. For the low energy-high resolution mode used in this study, the collimator is equipped with 148,000 holes that have a length of 24.05 millimeters (mm), a septal thickness of 0.16 mm, and hole diameter of 1.11 mm. As such, the collimator is quoted to have a sensitivity at 10 centimeters (cm) of 202 cpm/μCi, a system resolution at 10 cm of 7.5 mm, and a septal penetration of 1.5%.

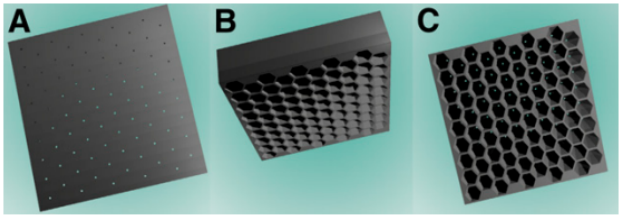

Figure 2.4: BiCore collimator used in the Siemens Symbia T6 SPECT system shown from the A) face, B) side, and C) back of the collimator. **Note:** Image from "A Parallel-Cone Collimator for High-Energy SPECT" by C. Beijst et al., 2015, *Journal of Nuclear Medicine*, 56(3), pp. 476-482.

SPECT imaging facilitates the diagnosis and characterization of various metabolic processes. By selecting targeted molecules that are tagged with gamma-emitting radionuclides and injected into a patient's body, internal radiation is imaged to display the distribution of the radiopharmaceutical molecule, which consequently provides insight into the physiology of an organ or pathophysiology of a disease. In this thesis, SPECT imaging has been utilized to quantify local lung function, and specifically, the distribution of pulmonary perfusion and ventilation within the lungs. To accomplish this, the metastable state of technetium (Tc)-99, i.e. Tc-99m, is utilized as a gamma emitting radionuclide. The decay scheme of molybdenum (Mo)-99, the parent nuclide of Tc-99, is shown in Figure 2.5 [54]. Because the Mo-99 has a relatively stable half-life (66 h), it can be housed at a medical institution and the produced Tc-99m daughter nuclide can be extracted for use when needed. Tc-99m decays through a 141 kiloelectron volt (keV) gamma ray, which is in the optimal energy range for detection by the NaI scintillating crystal.

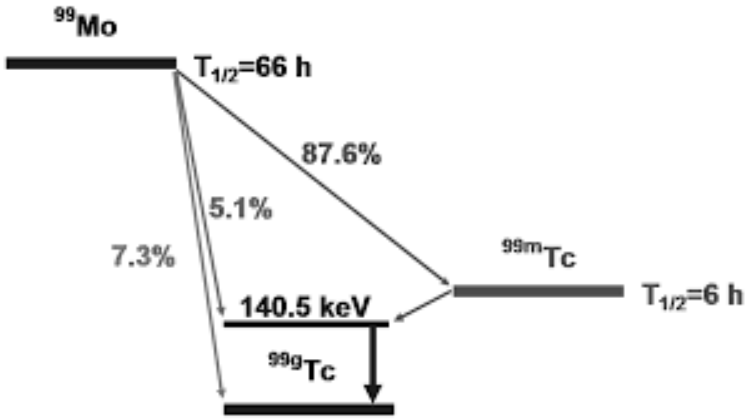

Figure 2.5: Molybdenum-99 decay scheme demonstrating the production of Technetium-99m and emission of the 141 keV gamma ray used in pulmonary SPECT imaging. **Note:** Image from "Cyclotron Based Production of Technetium-99m" from IAEA Radioisotopes and Radiopharmaceuticals Reports No. 2, *International Atomic Energy Agency*, 2017.

To specifically target pulmonary ventilation and perfusion, the Tc-99m radionuclide is attached to molecules that mimic oxygen and blood, respectively. In the case of ventilation imaging, a diethylenetriaminepentaacetic acid (DTPA) aerosol is utilized as the carrier molecule. As such, the patient is instructed to breathe at tidal volume for around 5 minutes from an oxygen mask that delivers the DTPA-labeled aerosol. Through this inhalation, the aerosol is deposited into the bronhoalveolar spaces, where it can be imaged to represent pulmonary ventilation. Generally, the half-time clearance from the lungs is 45-60 minutes but is often shorter in smokers ($\sim$20 minutes). In patients with chronic obstructive pulmonary disease (COPD), an increased turbulent flow compared to healthy patients can cause saturation within the central bronchial tree [55]. Because the radiopharmaceutical is inhaled, the distribution of imaged ventilation depends on the breathing condition of the patient, which can cause instability in the quantification. The DTPA aerosol will eventually cross the alveolar-capillary membrane, enter pulmonary circulation, and finally, be biologically-cleared through the kidneys. Therefore, while the physical half-life of Tc-99m is 6 hours, the biological half-life of the DTPA aerosol is typically only around one hour.

Alternatively, to assess pulmonary perfusion, Tc-99m is tagged to macroaggregated albumin (MAA) particles, which are essentially blood plasma proteins. The prepared Tc-99m MAA particles are injected into the patient's peripheral vein, then travel through the heart and into the lungs

[56]. These particles are then localized due to the mechanism of capillary blockade. It is estimated that 95% of the MAA particles will be filtered out of circulation after the first pass through the capillary bed. The biological half-life for these particles is generally 2-3 hours, and they are removed by the liver and spleen [55]. In the administration of both the ventilation and perfusion imaging agents, the patient is laying supine in the treatment position to maintain constant circulation that is minimally affected by patient motion.

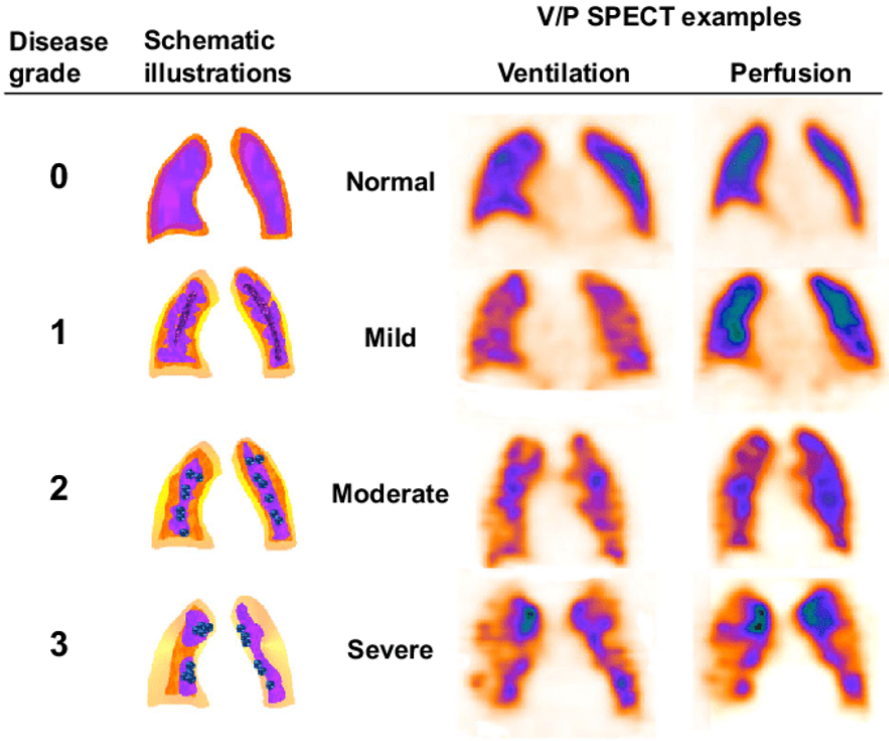

Figure 2.6: Example SPECT images demonstrating normal and various degrees of abnormal perfusion and ventilation distributions. **Note:** Image from "Grading obstructive lung disease using tomographic pulmonary scintigraphy in patients with chronic obstructive pulmonary disease (COPD) and long-term smokers" by M. Bajc et al., *Annals of Nuclear Medicine*, 2015, 29(1), pp. 91-99.

Example SPECT images demonstrating the perfusion and ventilation distribution in normal and various degrees of abnormal are shown in Figure 2.6 [57]. Because the imaging is based on the distribution of the DTPA and MAA particles, it is theorized that a normal healthy patient should have a completely homogeneous distribution of imaged intensity throughout the lungs. On the contrary, pulmonary abnormalities or diseases, such as a pulmonary embolism, COPD, or

interstitial lung disease (ILD), may cause vessels or airways to be blocked such that a given region does not receive a full influx of perfusion or ventilation [58, 59]. As such, patients with a more heterogeneous distribution of lung function are generally considered to have a worse pulmonary condition. While much of the analysis regarding the interpretation of a patient's SPECT scan has historically been qualitative, numerous works have been conducted to implement quantitative assessment of pulmonary perfusion and ventilation intensity such that these scans can be used in a broader clinical context.

2.2 Quantifying Functional Lung Dose-Response

In 1993, studies out of Duke University [4] and the Netherlands Cancer Institute (NKI) [5] first investigated the application of functional lung imaging in RT planning. By utilizing SPECT imaging, both Boersma [34] and Marks [1] demonstrated the ability to quantify longitudinal functional changes in lung cancer patients following RT. This development was significant because it created the potential to model functional lung damage such that, in theory, RT plans could be prospectively tailored, based on a patient's baseline distribution of lung function, to minimize the expected damage, and ultimately, optimize patient outcome.

Preceding these studies, radiation treatment plans for lung cancer patients were designed solely based on anatomical localization through CT scans. However, because of the limited resolution within the lung on CT, this method essentially assumes each patient has a homogeneous distribution of lung function. Furthermore, before the use of SPECT in RT assessment and planning, the only method implemented to determine a patient's pulmonary condition prior to treatment was the use of pulmonary function tests (PFTs). Effectively, spirometric PFTs are a noninvasive method to measure the capacity and capability of a patient's lungs by performing various breathing tests that are quantified through an external electronic device. The primary metrics determined from the PFTs are forced vital capacity (FVC), forced expiratory volume during the first second (FEV1), and diffusing capacity of the lungs for carbon monoxide (DLCO), which respectively measure the volume of air that can be retained within the lung, the initial flow rate upon expiration, and the

ability for inspired gas to be transferred into the bloodstream. Based on these PFT metrics, three diagnoses of pulmonary function are possible: 1) normal, 2) restrictive, or 3) obstructive. While these clinical indications can be informative, PFTs do not provide any spatial or regional information and have limited sensitivity to chronic diseases [60]. For these reasons, SPECT imaging was proposed as an alternative modality to provide a higher resolution regarding a patient's pulmonary condition before and after RT [4].

An example SPECT image from the seminal work of Marks et al. is shown in Figure 2.7 and demonstrates one of the first ever prospective functional-guided RT plans to limit dose to functional lung [4].

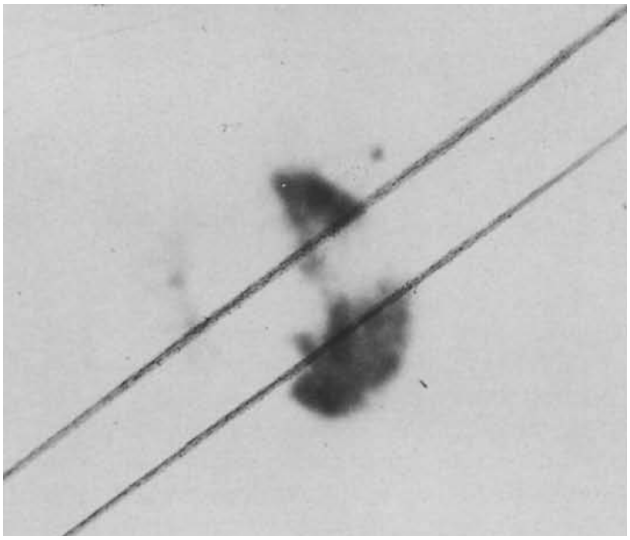

Figure 2.7: Example perfusion SPECT image with an oblique opposed pair of treatment fields. This is one of the first functional-guided RT plans applied to limit dose to functional lung. **Note:** Image from "The utility of SPECT lung perfusion scans in minimizing and assessing the physiologic consequences of thoracic irradiation" by L.B. Marks et al., *International Journal of Radiation Oncology Biology Physics*, 1993, 26(4), pp. 659-668.

As noted in their work, this patient was diagnosed with a 3 cm NSCLC tumor in the left lung and had a history of smoking and COPD with markedly abnormal pulmonary function tests. From the transverse SPECT scan, it is apparent that there is a functional defect surrounding the tumor in the left lung. It can also be observed that nearly the entire portion of the contralateral lung in this slice is poorly perfused with minimal intensity accumulation. Without the SPECT image in this

particular case, the authors state that the treatment plan would have been designed using opposing anterior-posterior (AP/PA) treatment fields. However, based on the supplemental functional lung information, an alternative treatment plan was developed using opposing left anterior oblique and right posterior oblique (LAO/RPO) treatment fields such that the functioning anterior and posterior regions of the ipsilateral lung could be spared from the high dose fields. Although the authors state that the "use of SPECT in the design of therapy clearly resulted in a superior treatment strategy" and that because the region "is very dysfunctional prior to radiotherapy, the physiological consequences of irradiating this area are probably small", there is no direct evidence presented or cited to support these statements [4].

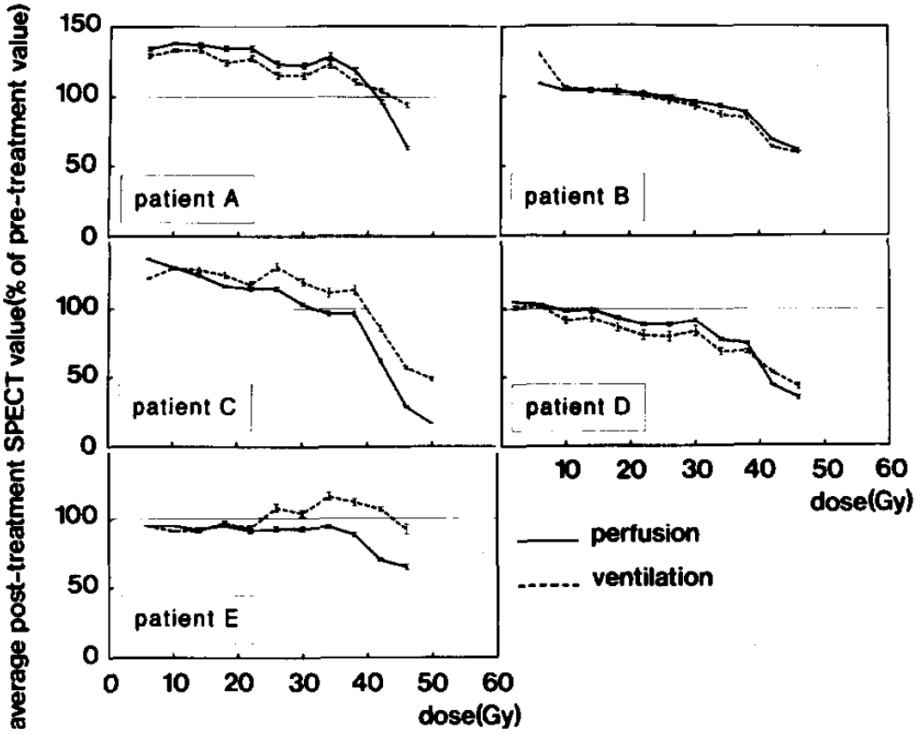

Figure 2.8: Inidividual perfusion and ventilation dose-function response curves from the seminal work of Boersma et al. in 1993. **Note:** Image from "A new method to determine dose-effect relations for local lung-function changes using correlated SPECT and CT data" by L.J. Boersma et al., *Radiotherapy and Oncology*, 1993, 29(2), pp. 110-116.

In the other seminal work regarding the use of functional lung in RT planning, Boersma et al. produced some of the first dose-function response curves using three-dimensional SPECT

imaging as shown in Figure 2.8 [5]. These dose-response curves represent the percentage change in perfusion and ventilation relative to the pre-treatment scan in five individual patients, and intensity values were normalized to the total counts. As noted by the authors in their work, each of these five patients exhibited perfusion reductions in relation to the delivered dose, while four of the five patients demonstrate dose-dependent reductions in ventilation (patient E apparently does not have a decrease in ventilation in the high dose bins). While most of the functional reduction is observed to occur in the dose bins >40 gray (Gy), the authors note that there is a high dose gradient (>5 Gy/cm) in the 12-40 Gy dose bins, which caused less voxels to contribute in these bins and increased the probability of registration errors in these regions [5].

Both of these studies [4, 5] were critically important to the development of SPECT imaging in RT planning because they provided much of the methodology, and many of the subsequent studies, that guided the direction of dose-function response modeling in the lung. Specifically, these studies outlined the blueprint for SPECT normalization, SPECT-CT registration, joint perfusion and ventilation response assessment, and quantifying functional changes as as percentage of baseline intensity.

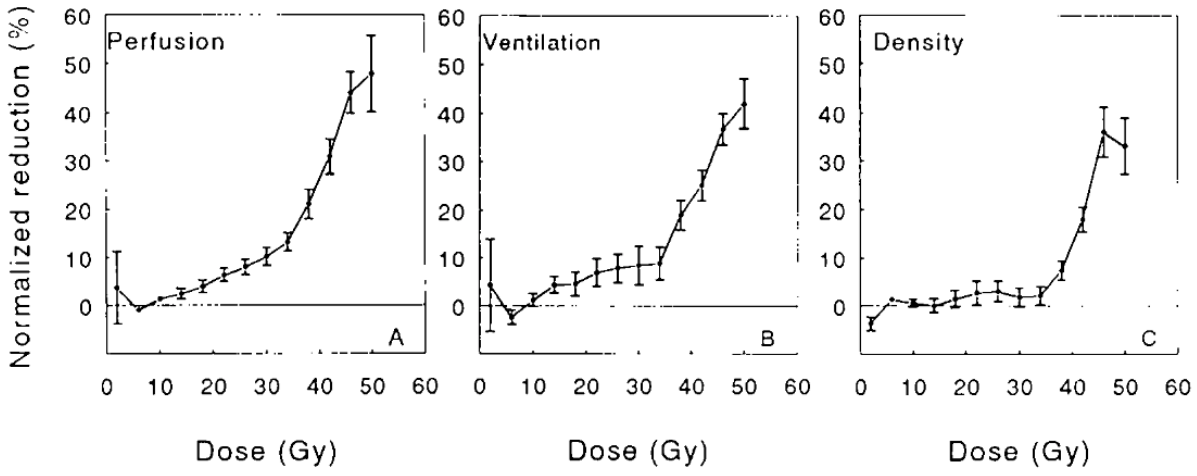

Figure 2.9: Population-averaged perfusion (left), ventilation (middle), and density (right) dose-response curves, normalized to the response in the 0-12 Gy dose bins, for 25 lymphoma patients treated with RT from Boersma et al. in 1994. **Note:** Image from "Dose-effect relations for local functional and structural changes of the lung after irradiation for malignant lymphoma" by L.J. Boersma et al., *Radiotherapy and Oncology*, 1994, 32(3), pp. 201-209.

In 1994, the NKI group produced their follow-up work regarding the dose-function response in 25 patients that received RT for malignant lymphomas, and these results were used to correlate the lung function response to CT-based structural, i.e. density, estimates. As such, this study analyzed local changes in both perfusion, ventilation, and density at 3-4 months following irradiation, as a percentage of the pre-treatment value, within 4 Gy dose bins for each patient. These individual patient data were then averaged across the entire cohort to produce the plots shown in Figure 2.9 [34].

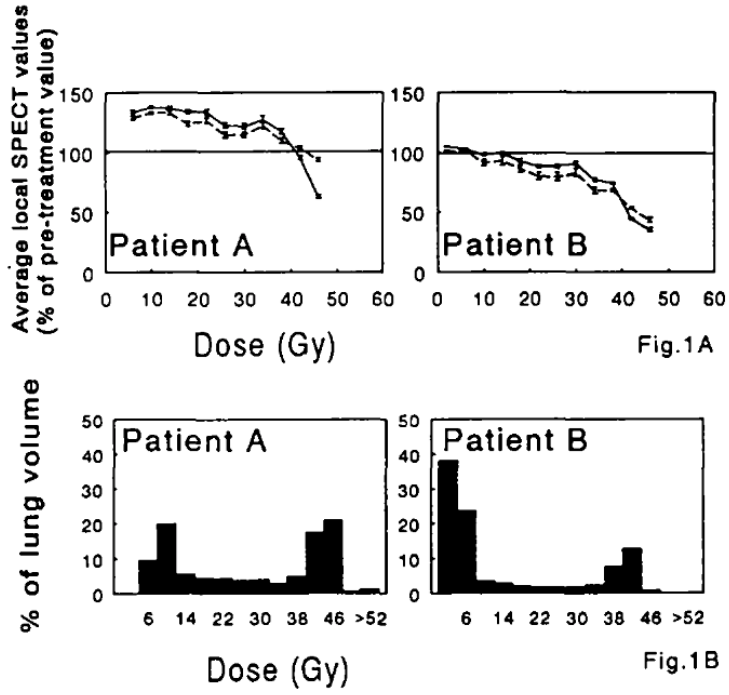

Figure 2.10: Perfusion (solid lines) and ventilation (dashed lines) dose-function response curves and associated lung volume histograms for two example patients, in which a functional improvement following RT is demonstrated in Patient A from Boersma et al. in 1994. **Note:** Image from "Dose-effect relations for local functional and structural changes of the lung after irradiation for malignant lymphoma" by L.J. Boersma et al., *Radiotherapy and Oncology*, 1994, 32(3), pp. 201-209.

It should be noted that perfusion and ventilation intensities were normalized to the average intensity in the 0-12 Gy region for each patient. This low-dose region was used for normalization because it was believed that no significant functional changes would occur longitudinally in these areas. However, this study noted that most patients exhibited a functional increase in this region

following RT, which was theorized to be due to redistribution of lung function caused by changes in other areas of the lung. While compensation may occur in limited cases, an offset in some of the dose-response curves (shown in Figure 2.10) from the same Boersma et al. study suggests that this may due to a relatively small number of initially low-functioning voxels that have higher intensity counts at the post-RT timepoint [34]. Essentially, this may be an artifact of the limited number of voxels in this region and can be further exacerbated by the use of a relative percentage change to measure the functional response and errors in the registration process. These effects will be discussed in greater detail in chapter V.

Table 1
Values of D_{50} and the steepness parameter, k, resulting from the fit of the dose–effect data (see Fig. 2) to a logistic dose–effect relation

	D_{50}(± SE) (Gy)	k (± SE)
Perfusion	50.5 (±0.9)	4.2 (±0.3)
Ventilation	54.3 (±1.7)	4.0 (±0.5)

Table 2
Values of the D_{50} and the steepness parameter, k, resulting from the fit of the dose–incidence data for the fraction of patients with changes larger than 20% (see Fig. 3), to a logistic dose-response relation

	D_{50}(± SE) (Gy)	k (± SE)
Perfusion	38.3 (±0.6)	10.3 (±1.6)
Ventilation	37.2 (±0.8)	7.8 (±1.2)
Density	44.2 (±0.8)	9.4 (±1.8)
Density[a]	33.7	5.2

[a]Data of Van Dyk et al. [23].

Table 2.2: Dose-response logistic model parameters for the entire cohort (left) and for patients with an average functional reduction larger than 20% (right) from Boersma et al. in 1994. **Note:** Image from "Dose-effect relations for local functional and structural changes of the lung after irradiation for malignant lymphoma" by L.J. Boersma et al., *Radiotherapy and Oncology*, 1994, 32(3), pp. 201-209.

Using the population-averaged data points, a logistic function of the form $1/(1+(D_{50}/D)^k)$ was fitted to determine the population-averaged dose-effect, where D_{50} is the dose causing 50% of the maximum functional reduction and k is the steepness parameter. Because the changes in function were believed to represent changes in alveolar/vascular subunits, the logistic model was selected as it is what is generally used to describe dose-effect relations for cell survival. As such, this was the first study to apply a logistic model to quantify functional lung damage following RT, and the model parameter values for D_{50} and k for the entire cohort and the patients with an average functional reduction larger than 20% are shown in Table 2.2 [34]. While the perfusion and ventilation reductions were generally similar, the authors noted that the ventilation scans for

7 patients were excluded due to excessive saturation and that there was a large variation in the individual patient dose-response for both imaging modalities.

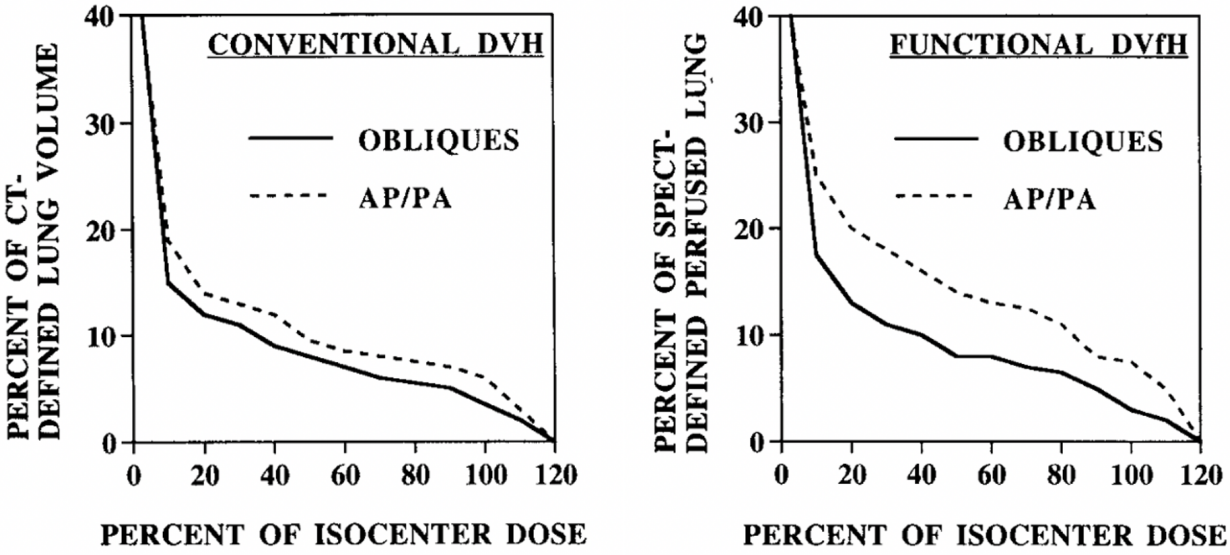

Figure 2.11: Conventional dose-volume histogram (left) versus enhanced dose-function histogram (right) from Marks et al. in 1995. **Note:** Image from "The role of three dimensional functional lung imaging in radiation treatment planning: The functional dose-volume histogram" by L.B. Marks et al., *International Journal of Radiation Oncology Biology Physics*, 1995, 33(1), pp. 65-75.

In their follow-up work in 1995, Marks et al. studied SPECT scans from 56 patient lung cancer patients and 30 patients with cancers originating in adjacent areas to the lung (14 breast, 12 lymphoma, and 4 others). Through this work, perfusion defects were identified, their location in relation to the tumor was tallied, and ultimately, treatment fields were chosen based on the potential to reduce radiation dose to functional lung. As such, it was determined that in the 50 lung cancer patients without prior resection, perfusion defects at the tumor, adjacent to the tumor, and separate from the tumor were found in 47 patients (94%), 37 patients (74%), and 21 patients (42%), respectively. While sustained hypoperfusion at the tumor site was expected, this was one of the first study to demonstrate the potential for reperfusion following RT in defects adjacent to the tumor, which was attributed to a reduction in pulmonary arterial compression following tumor shrinkage. Alternatively, the frequency of hypoperfusion separate from the tumor was found to be highest in patients with the poorest pulmonary function, as determined by DLCO, and these regions were not

found to reperfuse following RT, which the authors suggested represented regions of permanent dysfunction caused by ”severe emphysema or scarring”. As such, the authors noted that ultimately it is imperative to differentiate between permanent and reversible functional defects. Furthermore, while it is noted that some of the perfusion defects were identified as severe bullous disease on corresponding CT scans, this was not always the case, which supports the idea that functional-guided RT plans and dose-function histograms may provide superior value compared to CT-based RT plans and dose-volume histograms. To demonstrate this benefit, a dose-function histogram was plotted, as shown in Figure 2.11, for an example patient in which functional avoidance was implemented through oblique beams as opposed to the conventional AP/PA paired beams [6].

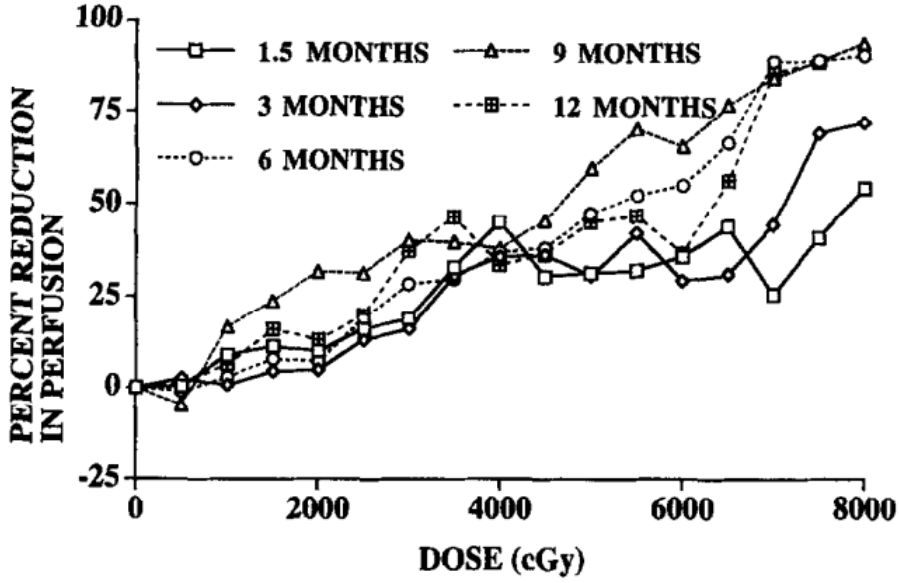

Figure 2.12: Longitudinal perfusion dose-response curves for 20 cancer patients that received RT. **Note:** Image from “Quantification of radiation-induced regional lung injury with perfusion imaging” by L.B. Marks et al., *International Journal of Radiation Oncology Biology Physics*, 1997, 38(2), pp. 399-409.

The modeling methods established by these preliminary studies were then implemented in larger cohorts of patients at both Duke and NKI. In 1997, Marks et al. demonstrated the perfusion dose-response for 20 cancer patients (7 breast cancer, 5 lymphoma, 1 esophagus, 1 sarcoma, and 6 lung) at multiple post-RT timepoints as shown in Figure 2.12, which suggested a time-dependent functional reduction in the high dose regions [1].

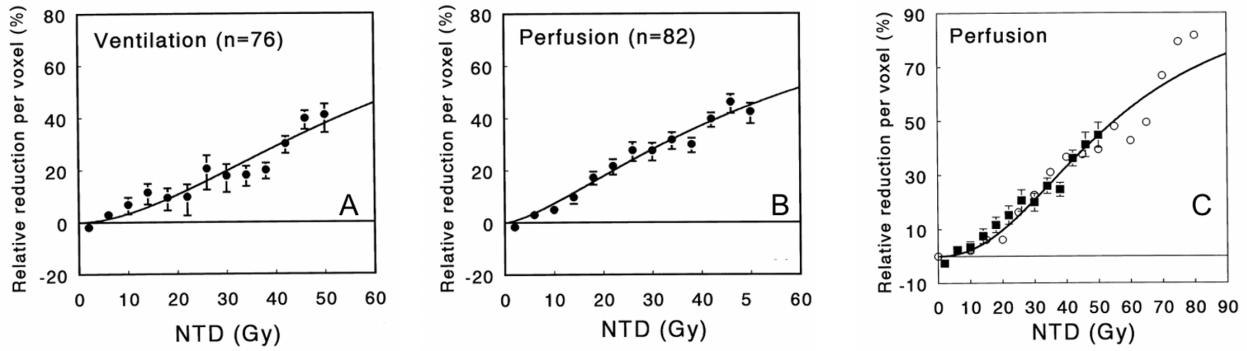

Figure 2.13: Ventilation (panel A) and Perfusion (panel B) dose-response curves for 82 cancer patients that received RT. A comparison between perfusion dose-response curves from Theuws et al. (squares) and Marks et al. (circles) [1] is also provided (panel C). **Note:** Images from "Dose–effect relations for early local pulmonary injury after irradiation for malignant lymphoma and breast cancer" by J.C.M. Theuws et al., *Radiotherapy and Oncology*, 1998, 48(1), pp. 33-43.

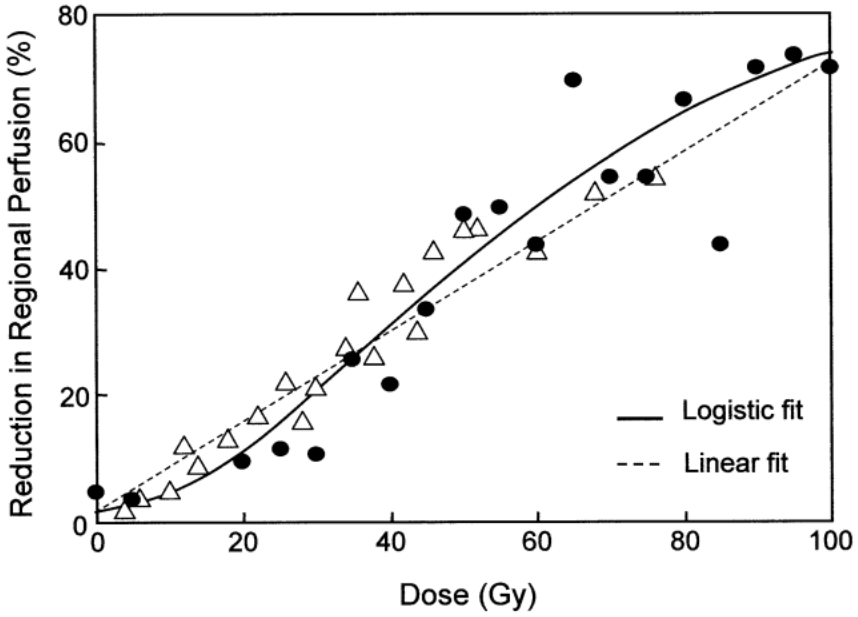

Figure 2.14: Perfusion dose-response data from NKI (circles) and Duke University (triangles) fit with both linear and logistic models. **Note:** Image from "Pulmonary function following high-dose radiotherapy of non–small-cell lung cancer" by Katrien De Jaeger et al., *International Journal of Radiation Oncology Biology Physics*, 2003, 55(5), pp. 1331-1340.

In 1998, the NKI group published a comprehensive analysis of the perfusion and ventilation dose-response in 82 patients (42 malignant lymphoma and 40 breast cancer). Using the previously described logistic model [34], the perfusion (ventilation) paramerters were found to be $D_{50} = 57 \pm 3 (66 \pm 7)$ and $k = 1.5 \pm 0.1 (1.8 \pm 0.3)$. The fitted population-level data are shown in Figure 2.13

alongside a comparison to the previously discussed Marks et al. perfusion dose-response study [1, 61]. Although a logistic model was fitted to these data, the dose-response curves show a fairly linear response. Furthermore, there is clearly a strong agreement between the data from Duke and NKI as shown on panel C, but this surprisingly shows an increasing functional reduction past 90 Gy, which is an exceedingly high dose for conventional fractionation RT. The difference in the linear and logistic modeling methods is explicitly shown in Figure 2.14, which utilized the patient data from NKI and Duke University to directly compare the perfusion dose-response [62].

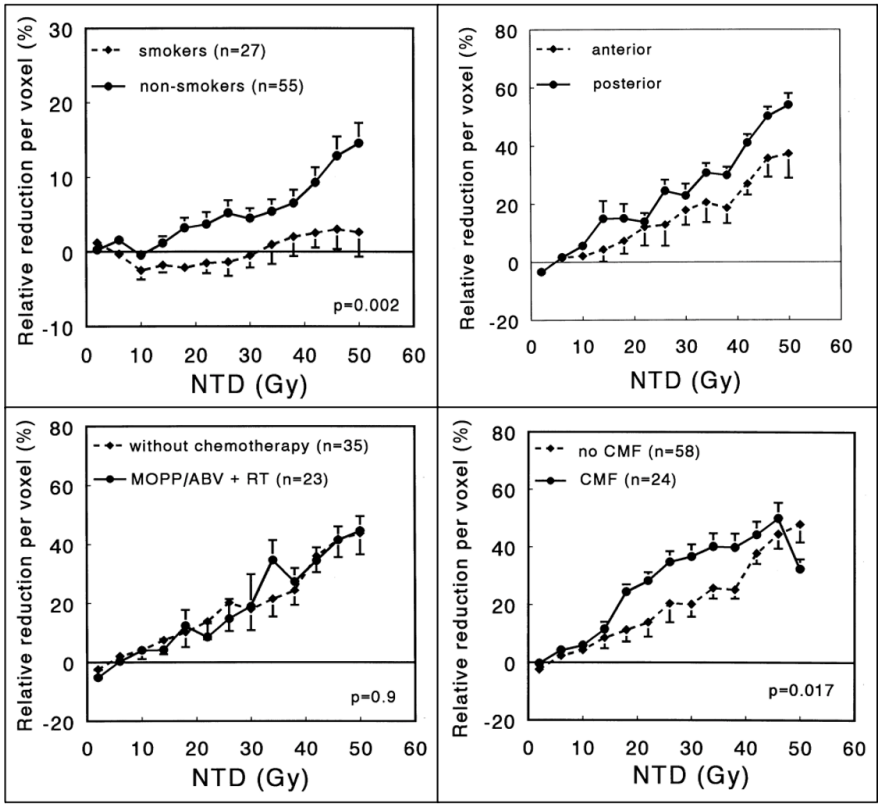

Figure 2.15: Perfusion dose-response curves for various patient subgroups including smokers vs. non-smokers (top-left), anterior vs. posterior regions of the lung (top-right), patients receiving concurrent chemotherapy (MOPP/ABV) vs. those without (bottom-left), and patients receiving post-RT chemotherapy (CMF) vs. those without. **Note:** Images from "Dose–effect relations for early local pulmonary injury after irradiation for malignant lymphoma and breast cancer" by J.C.M. Theuws et al., *Radiotherapy and Oncology*, 1998, 48(1), pp. 33-43.

The Theuws et al. study also quantified the perfusion dose-response in various subgroups and regions, as shown in Figure 2.15, including: smokers versus non-smokers, anterior versus posterior, patients treated with concurrent chemotherapy (MOPP/ABV), prior to RT versus no chemother-

apy, and patients treated with post-RT chemotherapy (CMF) versus no post-RT chemotherapy [61]. From these plots, it appears that the perfusion reduction is increased in non-smokers (due to generally healthier lungs), the posterior lung (due to gravitational accumulation), and patients the received post-treatment chemotherapy (due to increased cytotoxicity).

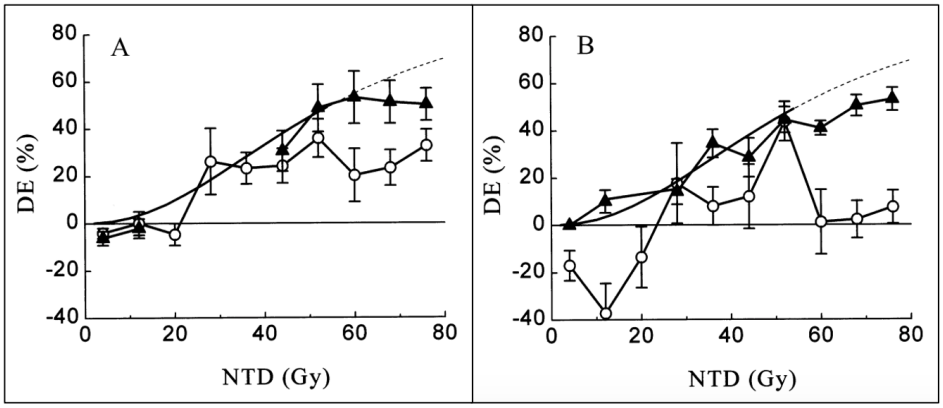

Figure 2.16: Dose-response curves for patients (panel A) and regions (panel B) considered to be well-perfused (triangles) versus hypoperfused (circles) prior to RT. **Note:** Images from "Radiation dose-effect relations and local recovery in perfusion for patients with non–small-cell lung cancer" by Y. Seppenwoolde et al., *International Journal of Radiation Oncology Biology Physics*, 2000, 47(3), pp. 681-690.

In 2000, the work by Seppenwoolde et al. further expanded on this type of segregated dose-effect analysis by separately quantifying the functional response in well-perfused patients (n=6) and well-perfused regions versus in patients with perfusion defects (n=19) and hypoperfused regions [36]. The study included 25 NSCLC patients and the dose-response was compared to 81 patients, from the Theuws et al. study [61], that were considered to have healthy lungs as shown in Figure 2.16.

As observed from these plots, the dose-response in patients with homogeneous perfusion prior to RT generally matches the dose-response in the reference healthy patients, whereas patients with hypoperfusion exhibit less reduction in the high dose bins. This is especially pronounced in the regional plots in panel B of Figure 2.16 that demonstrate an increase in perfusion, i.e. reperfusion, in the low dose regions and minimal damage in the high dose regions. To further analyze the effect of reperfusion, the work of Seppenwoolde et al. examined the amount of observed reperfusion in relation to the initial perfusion deficiency in both the NSCLC patients and the lymphoma/breast cancer

patient reference group as shown in Figure 2.17 [36]. It is not surprising to see that the NSCLC group generally exhibited a larger area of perfusion defects due to tumor burden and propensity for smoking, but clearly, more reperfusion occurs in patients with increased hypoperfusion prior to RT.

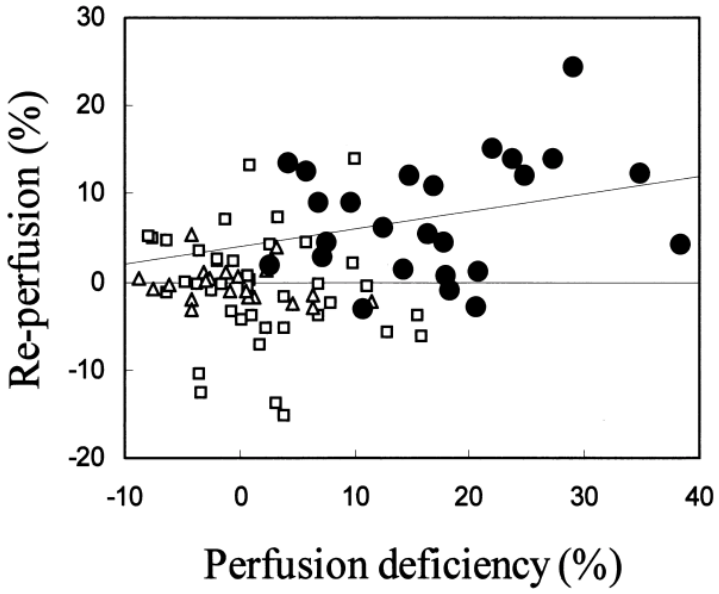

Figure 2.17: The observed reperfusion effect in relation to the initial pre-RT perfusion defect for malignant lymphoma (open squares), breast cancer (open triangles), and NSCLC patients (solid circles). **Note:** Images from "Radiation dose-effect relations and local recovery in perfusion for patients with non–small-cell lung cancer" by Y. Seppenwoolde et al., *International Journal of Radiation Oncology Biology Physics*, 2000, 47(3), pp. 681-690.

Based on these results, Seppenwoolde et al. stated [36]:

> "Because the overall effect of reperfusion is 7% at most (if membrane function is retained), optimization of treatment plans by sparing the well-perfused regions will probably result in the best possible lung function after treatment. Placing beams through bullous lung regions can also be considered as advantageous because bullous regions will never regain their original lung function."

It should also be noted that this study did not find an association between reperfusion and recovery in tissue density. Therefore, while the recommendation to place beams though bullous lung

may be useful in preserving the most lung function, it was based on the limited ability for defected lung to reperfuse following RT and was not based on the study of its direct impact to patient outcome. Despite this subtle distinction, this recommendation formed the basis for functional-avoidance radiotherapy, and subsequent studies by Seppenwoolde et al. (2002) [8], Christian et al. (2005) [63], and Maguire et al. (2006) [64] all demonstrated methodologies to incorporate functional-sparing in RT planning. However, as stated by Lavrenkov et al. in 2007 [20]:

> "The assumption that the radiation dose to [functional lung (FL)] is a determinant of radiation lung damage is a limitation of this study as the functional consequences of replacing [whole lung (WL)] volumes by FL volumes in [RT planning] are not known. Seppenwoolde et al. reported that radiation pneumonitis incidence increased with mean perfusion-weighted lung dose (MpLD). However, validated predictive values of MpLD for pneumonitis or reliable parameters for NTCP-like models which explicitly include functional data are not available to date, due to a lack of data correlating functional imaging to clinical outcomes in radiotherapy."

Despite the evidence being circumstantial that universal functional-avoidance can reduce toxicity, the overwhelming belief regarding the best application of functional-guided radiation treatments for lung cancer patients is to avoid high-functioning regions of the lung, by allocating more dose to low-functioning regions, to improve outcomes. Although functional-avoidance may play a vital role in the treatment of some patients, further investigation of functional targets is needed to better understand the specific pathways that lead to RILT and ensure optimal patient-specific dose delivery. As such, a growing number of research studies and clinical trials have sought to study functional-based metrics that could be utilized in treatment planning to mitigate pulmonary toxicity in lung cancer patients undergoing RT, which will be discussed further in section 2.3.

In 2010, a study out of Duke University by Zhang et al. analyzed the longitudinal dose-function response up to 9 years post-RT. Through this analysis, both individual patient and population-averaged dose-response curves were generated as shown in Figure 2.18 [38]. However, while the patient-specific response was shown to exhibit a logistic shape in the study by Zhang et al., the

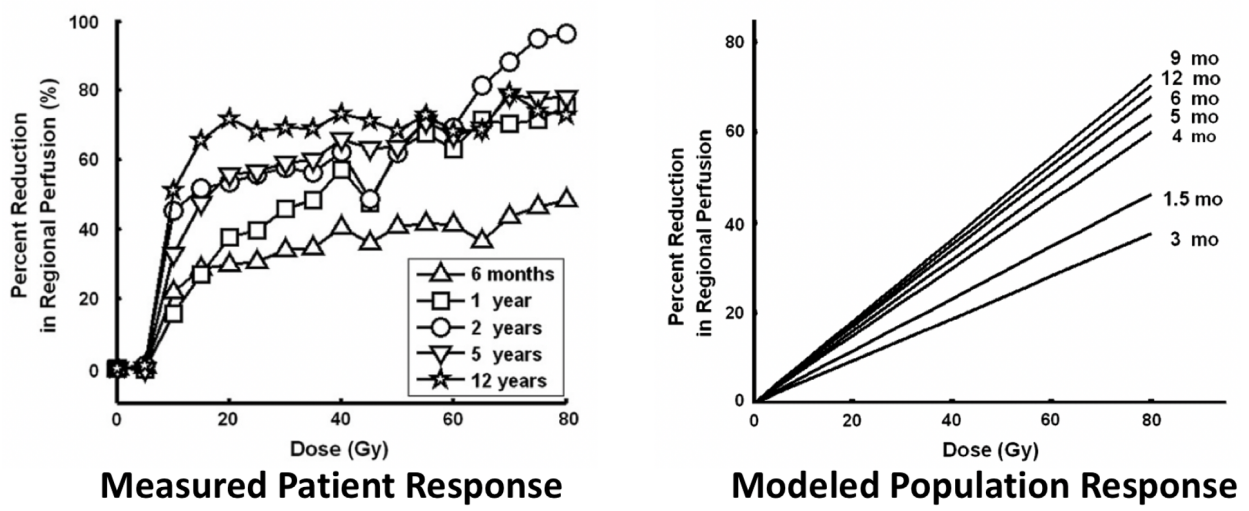

Figure 2.18: Longitudinal dose-response curves for individual patient data (left) versus the population-averaged data. **Note:** Images from "Radiation-Induced Reductions in Regional Lung Perfusion: 0.1–12 Year Data From a Prospective Clinical Study" by J. Zhang et al., *International Journal of Radiation Oncology Biology Physics*, 2010, 76(2), pp. 425-432.

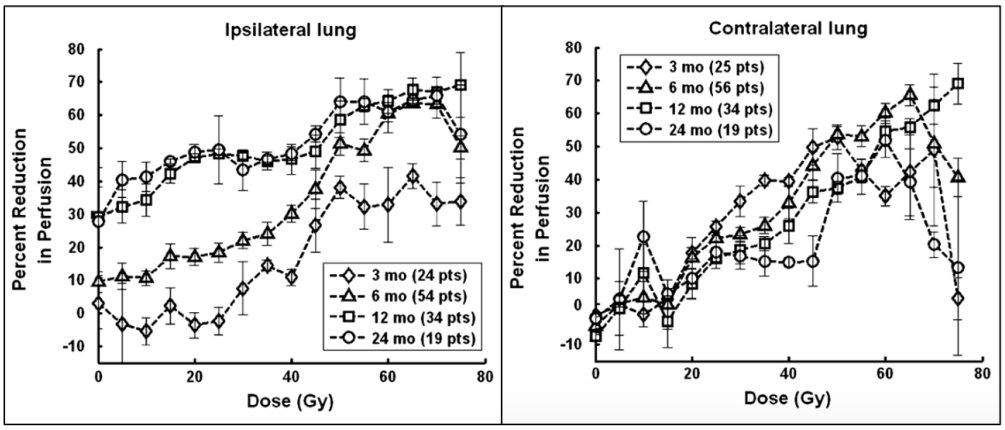

Figure 2.19: Dose-response curves in the ipsilateral lung (left) and contralateral lung (right). **Note:** Images from "Radiation-Induced Reductions in Regional Lung Perfusion: 0.1–12 Year Data From a Prospective Clinical Study" by J. Zhang et al., *International Journal of Radiation Oncology Biology Physics*, 2010, 76(2), pp. 425-432.

population-averaged data was modeled using a linear fit. The dose-response in the ipsilateral lung versus the contralateral lung was also studied, as shown in Figure 2.19, which demonstrated a more erratic response in the ipsilateral lung due to an increased tumor burden and presence of functional defects [38].

Although the majority of research had previously analyzed the dose-response in conventionally

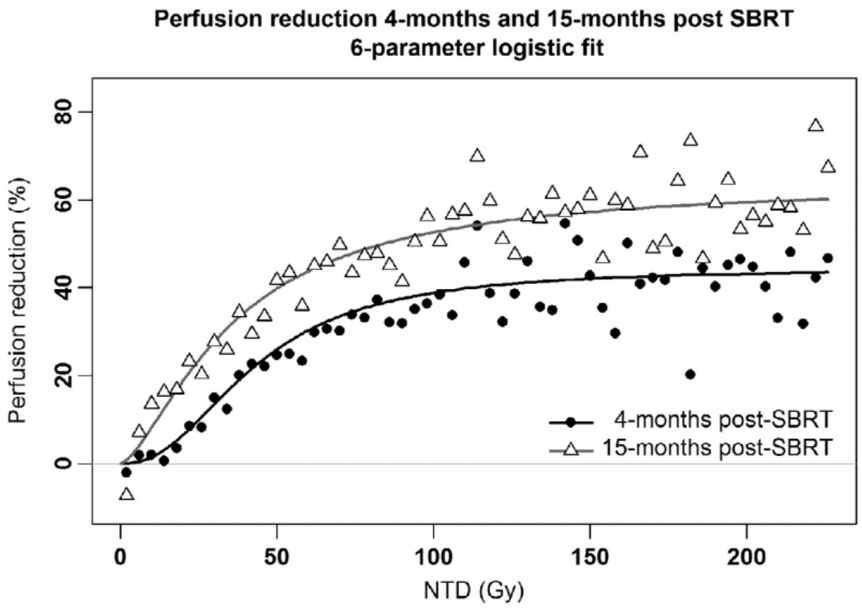

Figure 2.20: Perfusion dose-response curves in lung cancer patients that received SBRT. **Note:** Image from "Local dose–effect relations for lung perfusion post stereotactic body radiotherapy" by J. Scheenstra et al., *Radiotherapy and Oncology*, 2013, 107(3), pp. 398-402.

fractionated RT, Scheenstra et al. published a work in 2013 regarding the perfusion reduction in 42 lung cancer patients that received SBRT [39]. As shown in Figure 2.20, a logistic model was used to characterize the functional reduction, which demonstrates a good agreement.

While numerous other studies have since analyzed the dose-function response within various patient populations, the studies highlighted in this section provided much of the data that has been used to understand functional lung changes following radiation therapy. Furthermore, as shown in Figure 2.21, there is a good agreement amongst the five perfusion dose-response models accumulated in the meta-analysis by Bucknell et al. [65].

In summary, there are a couple of main points to note regarding the methodologies and results of these previous dose-function response studies:

1. All of these previous studies have utilized relative dose-response curves in which the change in functional intensity for patient j within dose bin d is calculated as:

$$R_{j,d} = \frac{f_{j,d,t} - f_{j,d,t=0}}{f_{j,d,t=0}} \times 100 \tag{2.1}$$

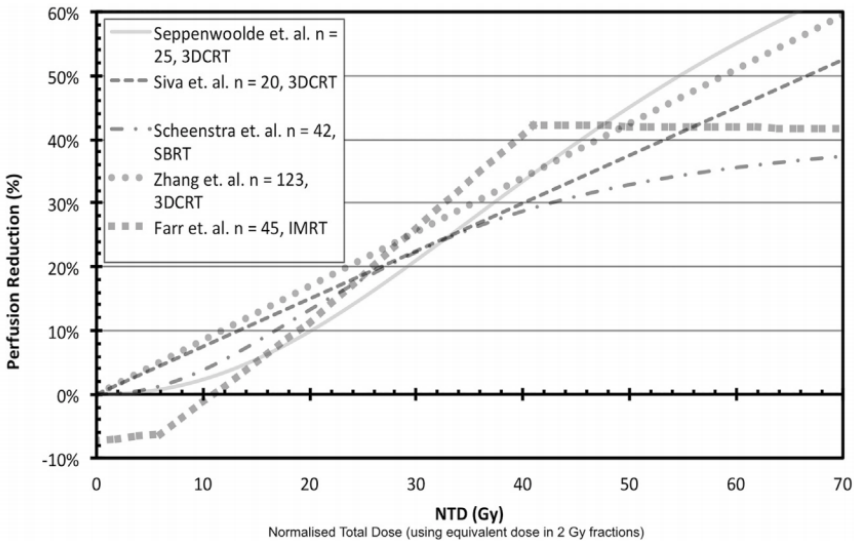

Figure 2.21: A historical comparison of the dose-response models characterizing perfusion SPECT changes following RT. **Note:** Image from "Functional lung imaging in radiation therapy for lung cancer: A systematic review and meta-analysis" by N.W. Bucknell et al., *Radiotherapy and Oncology*, 2018, 129(2), pp. 196-208.

where $f_{j,d,t}$ is the average functional intensity at timepoint t and $f_{j,d,t=0}$ is the average functional intensity prior to RT.

2. Population-level dose-function curves are generated by averaging the response in each dose bin across the cohort and then applying a linear or logistic model to the population-averaged data points.

3. While good agreement amongst the historical perfusion dose-response models was demonstrated in Figure 2.21, there was uncertainty regarding the response in low-dose bins and the magnitude of reperfusion and compensation effects.

4. A normalization factor, which standardizes the intensity value for normal lung, is necessary to relate the functional intensities between patients and timepoints.

5. Perfusion SPECT is the gold standard of functional lung dose-response modeling, and ventilation SPECT is widely considered too unstable to quantify longitudinally.

6. There is a clear time- and dose-dependent reduction in functional lung after RT.

7. The ipsilateral lung, which receives the majority of the radiation dose, tends to have a more erratic functional dose-response than the contralateral lung, primarily due to tumor burden and the presence of functional defects.

2.3 Risk Factors for RILT

Similar to the previous section that detailed the historical works that contributed to the quantification of functional lung response to RT, the timeline of studies that have investigated risk factors associated with RILT incidence is important to understanding how radiation-induced lung toxicities are currently mitigated in the radiation oncology clinic. In an attempt to thoroughly discuss and organize the myriad of research regarding the various factors that may be associated with RILT, this section was divided into the subsections listed below, which represent the broad categories of influence that are believed to affect patient outcome.

1. Radiation Dosimetrics and Pulmonary Function
2. Patient Characteristics and Pre-Existing Disease
3. Geometric Characteristics
4. Biological Characteristics

2.3.1 Radiation Dosimetrics and Pulmonary Function

The use of radiation for cancer treatments is a double-edged sword. Although radiotherapy is an effective mechanism for targeted treatment of cancerous nodules, dose to normal tissues can cause extraneous complications. While this conundrum has been understood by radiation oncologists for decades, Emami et al. produced the seminal work that provided concerted, literature-driven estimates for the tolerance radiation doses in various organs at risk [41]. Based on this work, it was estimated that the total dose producing 5% probability of complication within five years following treatment (TD5) and the total dose producing 50% probability of complication within

five years following treatment (TD50) for the whole lung volume, in terms of radiation pneumonitis as the complication, was 17.5 Gy and 24.5 Gy, respectively. While these dose limits were useful starting points, it was quickly recognized that a patient's dosimetric tolerance varied based on a variety of factors. Specifically, these estimates did not account for the underlying lung function of the patient, and thus, it was hypothesized that utilizing SPECT imaging, which at this time was becoming more available and more developed (see Table 2.1), may provide an enhanced resolution regarding a patient's tolerance to radiation.

Mean perfusion in ipsi-lateral lung zones (as %) followed by the range in 18 patients.

Tumours	MZ + UZ	MZ + UZ + LZ
Hilar	22 (0–32)	32[a] (5–53)
Suprahilar	28[a] (19–36)	46 (27–51)

[a] The zones regarded as at risk (see text) from irradiation.
LZ = lower zone; MZ = mid zone; UZ = upper zone.

The proportion of patients who manifest a decreased TLCO at follow up is statistically significantly higher if the lung perfusion was more than 35% in the zones at risk from radiation at presentation.

	Yes	No
Perfusion >35%	5	2
Perfusion <35%	1	8

$p = 0.024$ Fisher's exact test.

Table 2.3: The cohort averaged perfusion distribution in various lung regions (left) and the relation between the perfusion distribution in the irradiated regions with a >10% loss of TLCO after RT (right). **Note:** Tables from "Lung cancer in patients with borderline lung functions - zonal lung perfusion scans at presentation and lung function after high dose irradiation" by Raymond P. Abratt, 1990, *Radiothearpy and Oncology*, 19(4), pp. 317-322.

The use of functional-avoidance RT fields was initially justified based on the logical theory that avoiding healthy lung would decrease the physiological impact to the patient. Furthermore, a 1990 study by Abratt et al. correlated reductions in carbon monoxide transfer factor with the irradiation of regions that had reduced perfusion accumulation prior to treatment. As shown in Table 2.3, the average perfusion intensity in the ipsilateral lung appears to be lower than 35% in most patients, and yet, the patients that incurred a decreased diffusion capacity of carbon monoxide, i.e. DLCO or transfer factor of the lungs for carbon monoxide (TLCO), tended to have >35% prior to RT. However, as noted by Abratt et al. the reductions in DLCO were not correlated to negative patient outcomes and the perfusion intensity was based on planar scans not three-dimensional SPECT [66]. Therefore, it is possible that the patients with large declines in TLCO were generally healthy

prior to treatment, whereas the patients with perfusion defects were at a lower initial TLCO, and thus, appear to have less decline following RT. Either way, this was not a direct study of patient outcome with regard to irradiating SPECT regions.

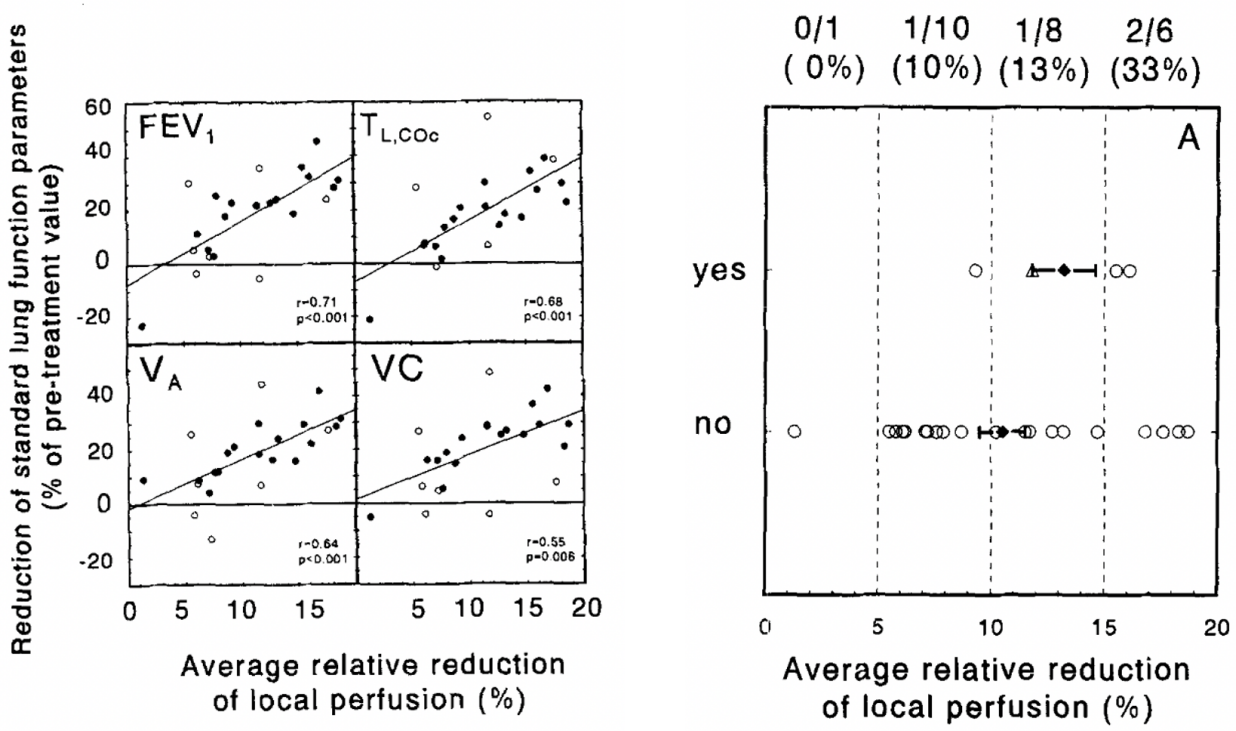

Figure 2.22: The relationship between the overall perfusion response parameter, i.e. the total reduction in perfusion from pre-RT to 3-4 months post-RT, and reductions in PFTs (left) and the incidence of radiation pneumonitis (right) in 25 malignant lymphoma patients. **Note:** Image from "Estimation of overall pulmonary function after irradiation using dose-effect relations for local functional injury" by L.J. Boersma et al., *Radiotherapy and Oncology*, 1995, 36(1), pp. 15-23.

In 1995, Boersma et al. produced a corollary to their previous work [34], using the same cohort of patients studied to determine local dose-function changes, in an effort to understand and estimate which patients would be subjected to the largest loss of perfusion and ventilation based on pre-treatment PFTs and post-treatment changes in PFTs. As such, this was one of the first studies to analyze patient factors that might correlate with functional lung changes and incidence of RILT after radiotherapy. In contrast to the study by Abratt et al. [66], this study found that values of DLCO were not significantly different in patients that incurred RP [7]. However, a fairly strong relationship between the decrease in PFTs and the reduction in perfusion following

RT was established as shown in Figure 2.22. This study also found that the integral perfusion reduction was higher on average in patients that incurred RP incidence, also shown in Figure 2.22. Alternatively, ventilation response was found to be too unstable to be properly correlated with PFTs or RP incidence.

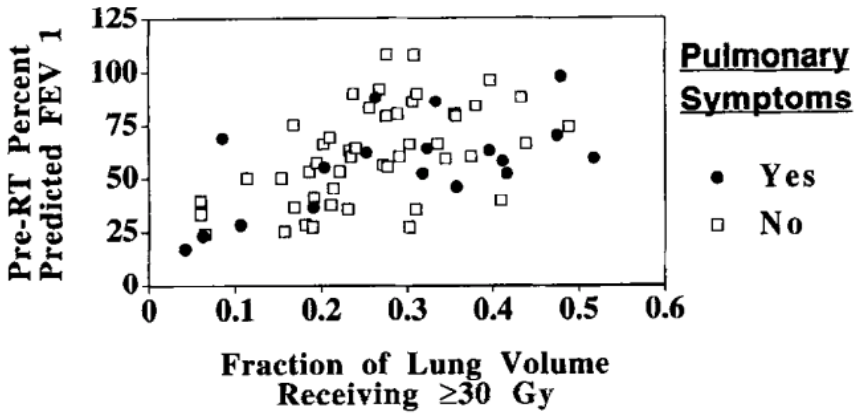

Figure 2.23: The fraction of lung volume receiving $\geq$ 30 Gy versus the pre-treatment predicted FEV1 in patients with (filled circles) and without (open squares) RT-induced pulmonary symptoms from Marks et al. in 1997. **Note:** Image from "Physical and biological predictors of changes in whole-lung function following thoracic irradiation" by L.B. Marks et al., *International Journal of Radiation Oncology Biology Physics*, 1997, 39(3), pp. 563-570.

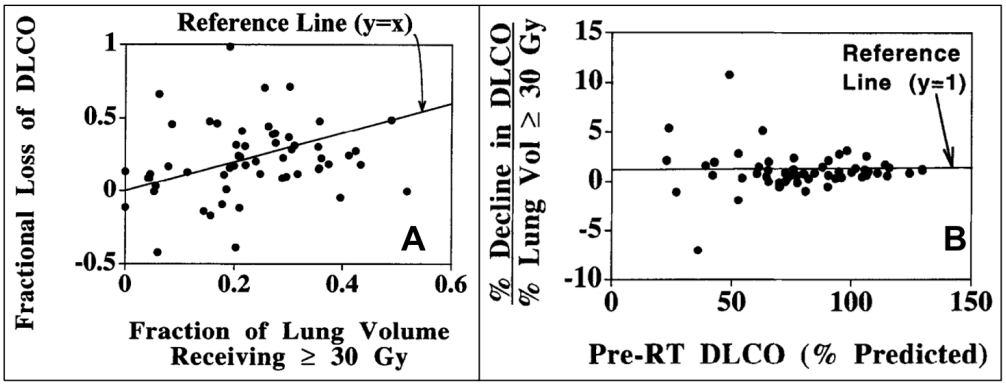

Figure 2.24: The relationship between fractional reduction in the percent predicted DLCO and V30 (left). The ratio between the x and y axes from panel A (left) is then plotted against the pre-RT DLCO value (right). **Note:** Image from "Physical and biological predictors of changes in whole-lung function following thoracic irradiation" by L.B. Marks et al., *International Journal of Radiation Oncology Biology Physics*, 1997, 39(3), pp. 563-570.

In 1997, Marks et al. produced a similar analysis regarding the physical and biological factors that correlated with reductions in pulmonary function and incidence of RT-induced pulmonary

symptoms. In 100 patients (50 of whom had SPECT scans available) that received partial-lung irradiation, 21 were scored to have incurred RT-induced pulmonary symptoms. As noted in their work and observed in Figure 2.23, the patients with RT-induced pulmonary symptoms tended to either receive a high volume of lung receiving ≥ 30 Gy (V30) or exhibit poor FEV1 prior to treatment [67]. As such, high dose and pre-RT PFTs were noted to be significant predictors of RT-induced pulmonary symptoms and decline of DLCO. As shown in Figure 2.24A, patients receiving a higher V30 exhibited a larger fractional loss of DLCO, however, it can also be observed in the left side of Figure 2.24B that in patients with poor DLCO prior to RT, the correlation breaks down. When patients with poor pre-RT PFTs were excluded, the association between dose-volume parameters and symptomatic outcome was markedly stronger. Overall, the CT-based NTCP was found to be the best predictor of RT-induced pulmonary symptoms, while the SPECT-derived perfusion V30 and SPECT-based NTCP were found to not add any predictive value, which was contrary to the previous hypothesis that dose to the functional regions of the lung would be most predictive of patient outcome. The authors noted this result could be due to a limited amount of SPECT scans available compared to dose-volume data, and furthermore, that perfusion defects in the distal regions of the lung can occur due to occlusion of blood vessels, which subsequently causes variations in the perfusion-based metrics [67]. However, these results were an early indications that dose to functional lung, as defined by high perfusion intensity, was not a straightforward predictor of poor patient outcomes.

This work by Marks et al. clearly delineates a difference in the responses between patients with poor pre-RT PFTs and those with more normal pre-RT PFTs, which was further reinforced by a study in 2002 from their group at Duke University. Through an assessment of various receiver operating curves (ROCs) to predict RT-induced symptomatic pulmonary injury conducted by Lind et al., mean perfusion-weighted lung dose (MpLD) produced an area under the curve (AUC) of 0.5, signifying that this metric was completely unable to predict toxicity in these 100 patients. Overall, single metrics did not perform well in predicting toxicity as mean lung dose (MLD), V30, and pre-RT FEV1 were all found to have an AUC of 0.56. Alternatively, the best models of prediction

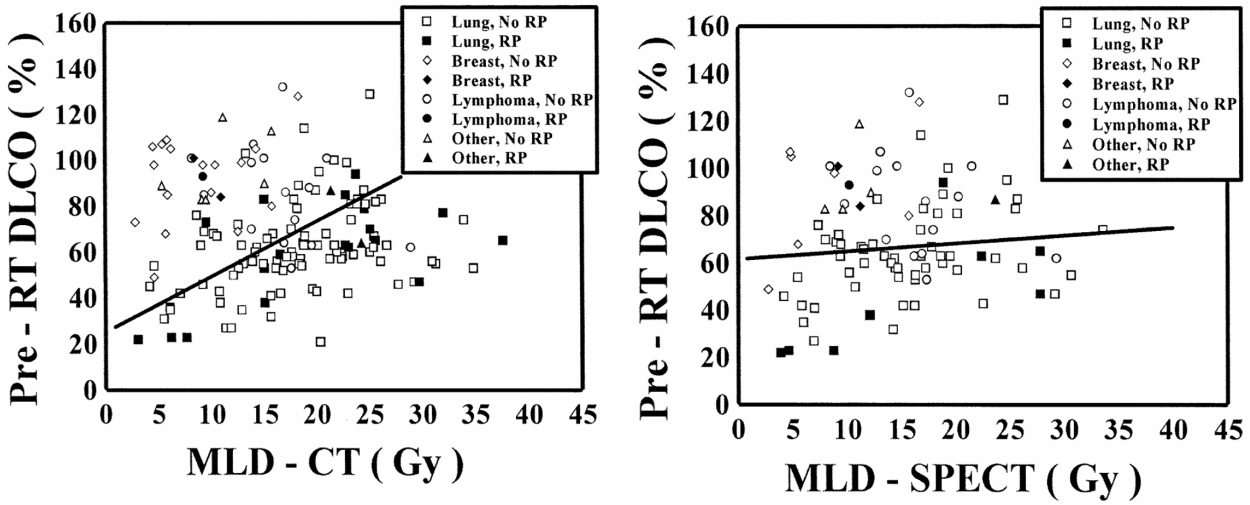

Figure 2.25: Scatterplot of patients that incurred RP (filled) and did not incur RP (open) with respect to MLD (left) and perfusion-weighted MLD (right) versus pre-RT DLCO. **Note:** Image from "Receiver operating characteristic curves to assess predictors of radiation-induced symptomatic lung injury" by Pehr A. Lind et al., *International Journal of Radiation Oncology Biology Physics*, 2002, 54(2), pp. 340-347.

used the MLD-ratio, i.e. MpLD/MLD, or the MLD-diff,i.e. the difference between MLD and MpLD, in conjunction with pre-RT DLCO (AUCs of 0.71 and 0.72), which seems to indicate that multiple factors are at play in the onset of toxicity making a single metric unable to accurately predict RP. A scatter plot showing each patient's MLD or perfusion-weighted MLD versus their pre-RT DLCO value is shown in Figure 2.25. When removing patients with pre-RT DLCO $<40\%$, the AUC for MpLD increased to 0.83, which demonstrates that in patients with good pulmonary condition prior to RT there is a predictable reduction in pulmonary function. However, this result also further enforces the inability for MpLD to predict toxicity in patients with poor PFTs prior to RT [68].

Shortly after, in a study by De Jaeger et al., MpLD was found to be the best predictor of PFTs, specifically reductions in FEV1 and DLCO, following RT as shown in Figure 2.26 [62]. While this result is similar to the findings of Marks et al. [67], this particular analysis utilized MpLD instead of MLD. Based on this result, De Jaeger et al. stated [62]:

> "The consistent and statistically significant (albeit weak) association of the reduction of PFTs with the MpLD supports the hypothesis that for patients with unequal perfu-

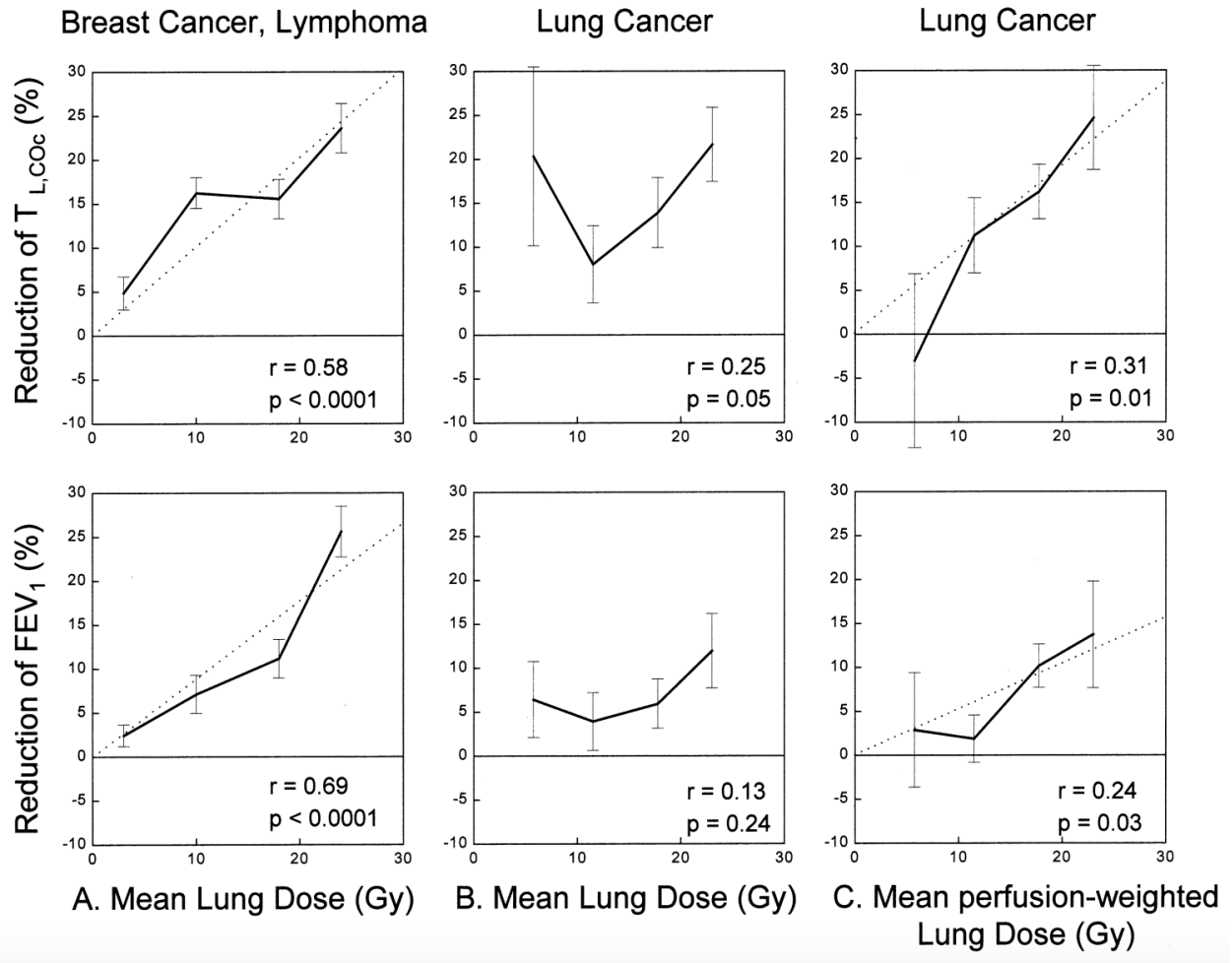

Figure 2.26: The measured reduction in TLCO (top) and FEV1 with respect to mean lung dose or mean perfusion-weighted lung dose in breast cancer and lung cancer patients. **Note:** Image from "Pulmonary function following high-dose radiotherapy of non–small-cell lung cancer" by Katrien De Jaeger et al., *International Journal of Radiation Oncology Biology Physics*, 2003, 55(5), pp. 1331-1340.

> sion the radiation dose delivered to nonperfused lung regions contributes less to functional lung damage. By directing radiation beams preferentially through hypoperfused lung regions, the MpLD can be minimized resulting in less functional lung damage."

However, the MLD and MpLD metrics are known to have a high correlation (shown in Figure 2.27), and furthermore, the relationship between delivered dose and change in PFTs has been shown to break down in patients with low PFTs at baseline (shown in Figure 2.24). Therefore, because the change in PFTs are not a direct indicator of patient outcome and because there is

evidence that patients with compromised PFTs at baseline still incur toxicity with relatively low delivered dose (exhibited by the 4 patients that incurred RP in the bottom left of Figure 2.25), it should not be presumed that all patients will benefit from dose funneled through hypoperfused lung regions. This is a subtle, but important, point: despite a correlation between increased reduction in PFTs given increased MLD/MpLD, this association does not directly translate to a guaranteed improvement in patient outcome given a decreased MLD/MpLD.

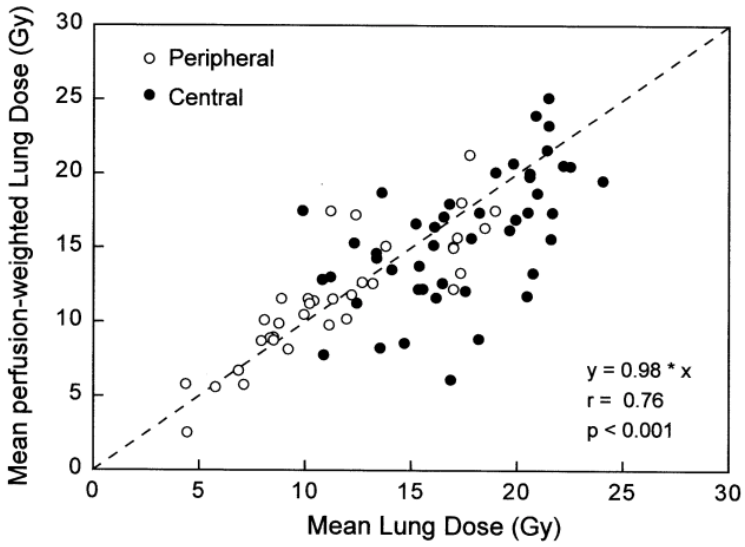

Figure 2.27: Scatterplot of the mean lung dose versus the mean perfusion-weighted lung dose in patients with peripheral (open circles) and central (filled circles) tumors. **Note:** Image from "Pulmonary function following high-dose radiotherapy of non–small-cell lung cancer" by Katrien De Jaeger et al., *International Journal of Radiation Oncology Biology Physics*, 2003, 55(5), pp. 1331-1340.

And yet, despite the poor predictability of MpLD in patients with compromised pulmonary function, subsequent works investigating the use of functional-avoidance RT fields determined that patients with small perfusion defects prior to treatment would receive a minimal benefit, and thus, recommended that functional-avoidance should primarily be applied in patients with large defects [8, 21]. As stated by Seppenwoolde et al. in 2002 [8]:

> "Only for patients with a large pre-treatment perfusion defect, perfusion-weighted optimization resulted in clinically well applicable treatment plans, which may have caused less radiation damage to functioning lung, compared to treatment plans that

were optimized on the mean lung dose and a homogeneous target dose alone. For patients with small perfusion defects, perfusion-weighted optimization yielded a treatment plan equal to the non-perfusion weighted optimized plan."

However, these perfusion-weighted RT plans were optimized and theorized to cause less radiation damage based on a reduction in the MpLD, which is calculated as shown:

$$MpLD = \frac{1}{N}\sum_{n=1}^{N} C_n \cdot D_n \tag{2.2}$$

where N is the number of voxels, D_n is the dose in voxel n, and C_n is the number of perfusion counts, normalized to the average perfusion counts for that patient, prior to RT in voxel n. Therefore, by definition, the MpLD is only reduced when less dose is delivered or when dose is delivered to below-average perfusion voxels.

Table 2. p values and logistic regression model coefficients for correlations with ≥ Grade 3 pneumonitis

Variable	Total lung	Ipsilateral	Contralateral	Lower	Upper
Mean dose	**0.04** (−5.4, 0.22)	**0.03** (−5.6, 0.14)	0.30 (−2.2, 0.093)	**0.05** (−2.6, 0.10)	0.52 (−2.3, 0.036)
d_{eff}	**0.05** (−5.9, 0.23)	**0.03** (−5.9, 0.15)	0.28 (−2.3, 0.091)	**0.05** (−2.7, 0.10)	0.53 (−2.4, 0.034)
NTCP	**0.06** (−2.3, 4.7)	0.16 (−3.1, 0.022)	0.78 (−1.4, −5.7)	**0.04** (−1.9, 4.0)	0.80 (−1.6, 0.25)
F_{dam}	**0.05** (−4.3, 11.4)	**0.02** (−5.3, 9.0)	0.48 (−1.8, 3.7)	**0.06** (−2.4, 6.1)	0.46 (−2.4, 2.5)
V20	0.10 (−3.4, 0.064)	**0.02** (−4.9, 0.068)	0.14 (−2.1, 0.040)	0.10 (−2.3, 0.043)	0.51 (−2.2, 0.017)

Notes: The coefficients *b0*, *b1* are in parentheses below the p values. For mean dose and d_{eff}, *b1* has dimensions of Gy^{-1}, and *b0* is dimensionless. The other coefficients are dimensionless, but in the logistic regression, *NTCP* and f_{dam} were entered as fractions and *V20* as percent.

Table 2.4: Dosimetric correlations, based on a fitted logistic regression, for mean dose, d_{eff}, NTCP, f_{dam} and V20 in the total lung, ipsilateral lung, contralateral lung, upper lung, and lower lung. The study included 49 NSCLC patients of which 9 incurred Grade 3+ RP. **Note:** Table from "Dose-volume factors contributing to the incidence of radiation pneumonitis in non-small-cell lung cancer patients treated with three-dimensional conformal radiation therapy" by Ellen D. Yorke, 2002, *International Journal of Radiation Oncology Biology Physics*, 54(2), pp. 329-339.

Also in 2002, Yorke et al. published an analysis quantifying radiosensitivity in various regions of the lung. Through this study, it was determined that dose to the ipsilateral lung and dose to the lower lung were most significantly correlated with grade 3+ pneumonitis, whereas dose to the

contralateral lung and upper lung were found to not be associated as shown in Table 2.4 [69]. It was reported that the ipsilateral lung had the highest mean dose (median=26.3 Gy; range=6.1-51.6 Gy), the whole lung dose was intermediate (median=17.1 Gy; range=4.1-29.3 Gy), and the contralateral lung dose was low (median=6.6 Gy; range=0.08-18.0 Gy). Alternatively, only 8/49 patients exhibited greater than 50% of the PTV volume in the lower lung, and the lower lung structure (inferior, geometric half of both lungs) had a median dose of 8.0 Gy (range=0.15-27.2 Gy) while the upper lung structure (superior, geometric half of both lungs) had a median dose of 24.0 Gy (range=2.3-35.07 Gy). As such, the ipsilateral lung appears to be susceptible to radiation based on increased delivered dose, whereas the lower lung susceptibility appears to be more of a locational, or anatomical, vulnerability.

Table 3. Mean perfusion in different lung regions averaged over all patients

Region	Mean regional perfusion	*p*
Anterior	0.85 (0.12)	<0.001
Posterior	1.10 (0.08)	
Cranial	0.98 (0.19)	0.15
Caudal	1.03 (0.18)	
Ipsilateral	0.88 (0.20)	<0.001
Contralateral	1.11 (0.26)	
Central	0.96 (0.10)	<0.001
Peripheral	1.04 (0.08)	

Data presented as average value, with SD in parentheses.

Table 2.5: Mean perfusion values in various regions of the lung averaged over all patients. P-values were calculated using a two-tailed *t* test. **Note:** Table from "Regional differences in lung radiosensitivity after radiotherapy for non–small-cell lung cancer" by Yvette Seppenwoolde, 2004, *International Journal of Radiation Oncology Biology Physics*, 60(3), pp. 748-758.

This lower lung radiosensitivity was further confirmed in a study by Seppenwoolde et al. in 2004 [70]. Specifically, a statistically significant difference was found in the incidence of RP in patients with cranial versus caudal tumors (11% vs. 40%, respectively). This study also quantified the average perfusion, with all SPECT counts normalized to the average number of perfusion counts, i.e. global lung perfusion average is 1.0, in various regions of the lung as shown in Table 2.5. Based on this table, there are clear differences in the perfusion distributions between the

ipsilateral and contralateral lung (tumor burden), the peripheral and central regions (vessel delivery), and the anterior and posterior regions (gravitational accumulation in supine position). This study also found that the MpLD was typically lower than the MLD because the perfusion defects were generally localized near the tumor and received a high dose, and it was reported that the TD50 was 30 Gy for MLD and 27 Gy for MpLD. This result is slightly confounding because if functional lung was more susceptible to radiation than non-functional lung, the TD50 for MpLD should be higher than the TD50 for MLD.

As previously noted in section 2.2, despite much work to investigate the use of functional-avoidance RT, a study by Lavrenkov et al. in 2007 clearly notes the need for more evidence to support a tangible benefit through the avoidance of functional lung:

> "If the dose to [functional lung] is shown to be the primary determinant of lung toxicity, IMRT would allow for effective dose escalation by specific avoidance of [functional lung]." [20]

TABLE 1. Lung Perfusion Score System as a Mean of Evaluating Lung Function

Largest localized perfusion Defect Score (DS) in each lung as seen on SPECT
0 = No defect
1 = Defect <25% of one lung
2 = Defect 25–49% of one lung
3 = Defect 50–74% of one lung
4 = Defect 75–100% of one lung
Remaining Lung Perfusion Score (RLPS) as seen on planar and SPECT images
1 = Homogeneous
2 = Mild heterogeneity
3 = Moderate heterogeneity
4 = Marked heterogeneity
Total Lung Perfusion Score (LPS) = right lung DS + left lung DS + RLPS = 1–12

SPECT, single photon emission computed tomography.

Table 2.6: The lung perfusion score grading scale based on visual assessment of SPECT scans. **Note:** Image from "Lung Perfusion Imaging Can Risk Stratify Lung Cancer Patients for the Development of Pulmonary Complications after Chemoradiation" by Isis W. Gayed et al., *Journal of Thoracic Oncology*, 2008, 3(8), pp. 858-864.

In 2008, a study by Gayed et al. of 50 patients that received RT (18 of whom incurred Grade 2+ pulmonary complications within 8 months following treatment) found that there were no significant differences in the pulmonary function tests, mean dose delivered, volume of lung irradiation, or volume of lung receiving $\geq$20 Gy between the patients with and without complications. However, they did report that there was a significant difference in the lung perfusion score (LPS), which was a grading system developed to guide the visual assessment of SPECT perfusion scans by 5 manual reviewers. As shown by the scale in Table 2.6, a higher value of the LPS equates to a lower quality of lung function. In the 18 patient that incurred pulmonary complications, the mean LPS was found to be 4.9 versus 3.5 in the patients that did not incur complications. Furthermore, as the patients' LPS increased, the odds of the patient having complications also increased, and the association remained significant through multivariate analysis that adjusted for age, sex, history of COPD, stage of tumor, RT technique, total RT dose, mean lung dose, and volume of lung receiving $\geq$ 20 Gy (V20). Overall, an AUC of 0.7 was determined for the ability of LPS to predict the onset of pulmonary complications. As such, this work demonstrates that patients with perfusion defects prior to RT are at-risk for adverse reactions to radiation [71].

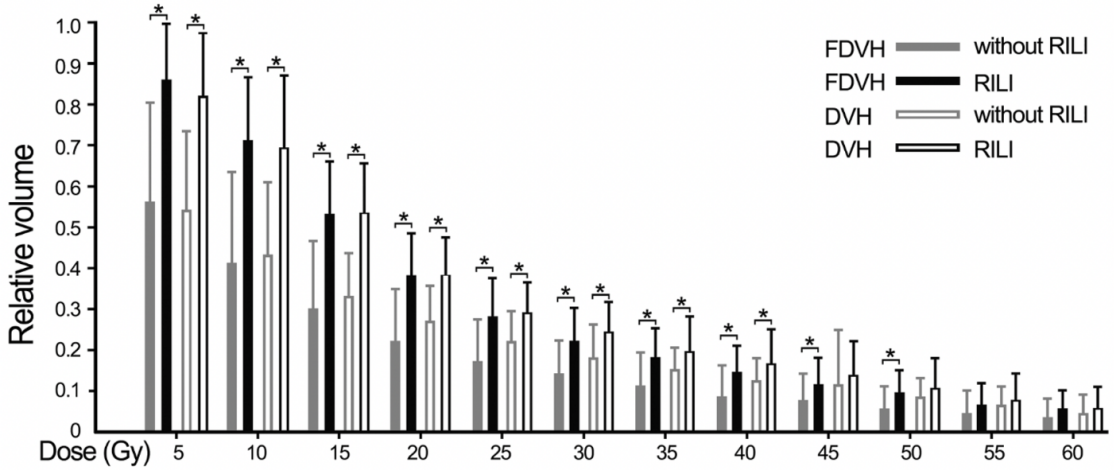

Figure 2.28: A comparison of the distribution of relative volumes between standard and functional dosimetrics, further broken down by patients that incurred radiation-induced lung injury (RILI) and without RILI. **Note:** Image from "Functional dosimetric metrics for predicting radiation-induced lung injury in non-small cell lung cancer patients treated with chemoradiotherapy" by Dongqing Wang, 2012, *Radiation Oncology*, 7(69).

Table 2 Univariate analysis of functional and standard dosimetric parameters association with radiation-induced lung injury (RILI)

Parameters	[a]Cut-off value	RILI rate (%)	p value
FV5 / V5	**0.80** / 0.70	[b]**5.3: [c]47.4** / [b]5.4: [c]45.0	**0.001** / 0.001
FV10 / V10	**0.45** / 0.56	**5.4: 45.0** / 5.1: 50.0	**0.001** / 0.001
FV15 / V15	**0.40** / 0.40	**2.9: 43.5** / 0.0: 39.3	**0.001** / 0.001
FV20 / V20	**0.30** / 0.32	**5.6: 42.9** / 3.2: 38.5	**0.001** / 0.001
FV25 / V25	**0.28** / 0.26	**9.1: 53.8** / 5.9: 39.1	**0.001** / 0.004
FV30 / V30	**0.21** / 0.21	**7.7: 44.4** / 8.6: 36.4	**0.002** / 0.015
FV35 / V35	**0.15** / 0.17	**7.3: 50.0** / 7.9: 42.1	**0.001** / 0.004
FV40 / V40	**0.14** / 0.17	**7.1: 53.3** / 7.1: 31.0	**0.001** / 0.041
FV45 / V45	**0.11** / 0.13	**7.1: 53.3** / 9.7: 30.8	**0.001** / 0.089
FV50 / V50	**0.07** / 0.11	**7.1: 53.3** / 12.8: 37.5	**0.001** / 0.061
FV55 / V55	**0.06** / 0.08	**9.5: 50.0** / 15.8: 31.3	**0.003** / 0.270
FV60 / V60	**0.04** / 0.03	**10.0: 43.8** / 15.0:22.6	**0.008** / 0.721

Note: functional dosimetric parameters associated with RILI were typed with bold.
a Cut-off value was optimized by receiver operating characteristic curve.
b RILI rate calculated when Vx < cut-off value.
c RILI rate calculated when Vx ≥ cut-off value.

Table 2.7: Chi-suare univariate analysis for the association between functional and volumetric dosimetric parameters with radiation induced lung injury. Cut-off values for each metric, based on optimizing the ROC analysis, and the RILI rate above and below that cut-off value are also listed. **Note:** Table from "Functional dosimetric metrics for predicting radiation-induced lung injury in non-small cell lung cancer patients treated with chemoradiotherapy" by Dongqing Wang, 2012, *Radiation Oncology*, 7(69).

Following the initial studies that demonstrated minimal benefit of functional-weighted metrics to predict negative outcomes, recent works have reported more promising results regarding the use of dose-function metrics for determining patients at risk for radiation-induced lung injury. By analyzing 57 stage III NSCLC patients that received chemoradiotherapy, Wang et al. concluded that although dose-volume and dose-function metrics had strong correlations with each other, functional metrics seemed to have increased predictive power in the high dose ranges. However, the Pearson correlation coefficients were calculated between the volumetric and functional dosimetric values in 5 Gy increments, i.e. V5/FV5-V60/FV60, and all but one of the pairs (V45/FV45) had a coefficient greater than $r>0.6$, which indicates a significant correlation between the metrics. Due to this colinearity between the dose-volume histogram (DVH) and functional dose-volume histogram (fDVH) metrics, a multivariable analysis was not implemented, and instead, univariate Chi-square and ROC analyses were performed. The results of the univariate Chi-square analysis

are shown in Table 2.7 [72].

As demonstrated by the relative volume distribution for each of these volumetric and functional dosimetrics shown in Figure 2.28, there is clearly less volume and functional intensity receiving higher doses than lower doses, which also means there is a higher uncertainty in the high dose metrics. It is also interesting to note a consistent trend, shown in both Table 2.7 and Figure 2.28, where the functional metric, in terms of relative volume and cut-off value, appears to be greater than the volumetric dosimetric in the low-dose bins, but in the high-dose bins, the functional dosimetric appears to be less than the volumetric dosimetric in patients with RILI.

ROC analysis for standard volumetric dosimetrics as predictors of radiation-induced lung injury

Variable	Area	p value	95% Confidence Interval	
			Lower	Upper
V5	0.871	0.001	0.753	0.988
V10	0.893	0.001	0.792	0.994
V15	0.902	0.001	0.813	0.992
V20	0.885	0.001	0.785	0.986
V25	0.817	0.002	0.687	0.947
V30	0.737	0.021	0.578	0.895
V35	0.729	0.026	0.541	0.918
V40	0.695	0.058	0.488	0.902
V45	0.656	0.129	0.443	0.869
V50	0.590	0.380	0.368	0.812
V55	0.559	0.569	0.348	0.769
V60	0.511	0.915	0.309	0.713

ROC analysis for functional dosimetrics as predictors of radiation-induced lung injury

Variable	Area	p value	95% Confidence Interval	
			Lower	Upper
FV5	0.851	0.001	0.738	0.963
FV10	0.861	0.001	0.758	0.964
FV15	0.869	0.001	0.764	0.973
FV20	0.851	0.001	0.738	0.963
FV25	0.814	0.001	0.679	0.950
FV30	0.802	0.002	0.645	0.959
FV35	0.784	0.004	0.629	0.938
FV40	0.788	0.003	0.627	0.948
FV45	0.780	0.004	0.619	0.941
FV50	0.766	0.007	0.602	0.929
FV55	0.700	0.041	0.510	0.890
FV60	0.693	0.049	0.503	0.883

Table 2.8: ROC analyses for volumetric (left) and functional (right) dosimetrics as predictors for RILI incidence from Wang et al. in 2012. **Note:** Tables from "Functional dosimetric metrics for predicting radiation-induced lung injury in non-small cell lung cancer patients treated with chemoradiotherapy" by Dongqing Wang, 2012, *Radiation Oncology*, 7(69).

When the functional dosimetric is higher than the volumetric dosimetric, it tends to suggest that a higher portion of functional intensity is being irradiated, and alternatively, when the functional dosimetric is relatively less than the volumetric dosimetric, it suggests that more low-functioning tissue is receiving that dose. Therefore, this observed trend seems to suggest that irradiating a large portion of functional intensity with a low dose ($<$20 Gy) makes patients more susceptible to

RILI, whereas more high-dose to lower-functioning tissue makes patients more susceptible to RILI. While the Wang et al. study concluded that functional metrics may provide improved predictive outcome in the high dose region based on the ROC analyses shown in Table 2.8, there was no discussion regarding this potential that patients with a lower fDVH value, relative to the DVH value, are at a higher risk, which is contradictory to the idea that limiting dose to functional tissue can reduce toxicity incidence [72].

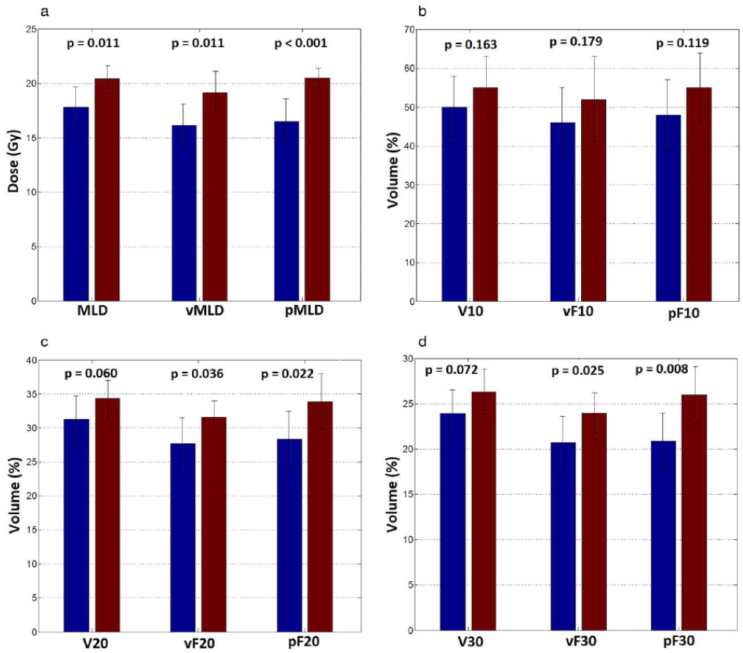

Figure 2.29: A comparison of the distribution of relative volumes between standard and functional dosimetrics, further broken down by patients that incurred RILI and without RILI. **Note:** Image from "SPECT-based functional lung imaging for the prediction of radiation pneumonitis: A clinical and dosimetric correlation" by Douglas A. Hoover, 2014, *Journal of Medical Imaging and Radiation Oncology*, 58, pp. 214-222

In a subsequent study by Hoover et al., it was similarly found that functional dosimetrics, including both perfusion and ventilation dosimetrics, performed better in predicting toxicity than volumetric dosimetrics. However, in this study, the functional and volumetric dosimteric values were very similar in patients that incurred RP, while the patients that did not incur RP clearly had lower functional dosimetric values than the corresponding volumetric dosimetric as shown in Figure 2.29. As such, this study appears to demonstrate evidence to support the use of functional-avoidance RT, although the sample size was quite limited with only 26 patients enrolled, and of

those patients, only 7 incurred grade 2+ RP [73].

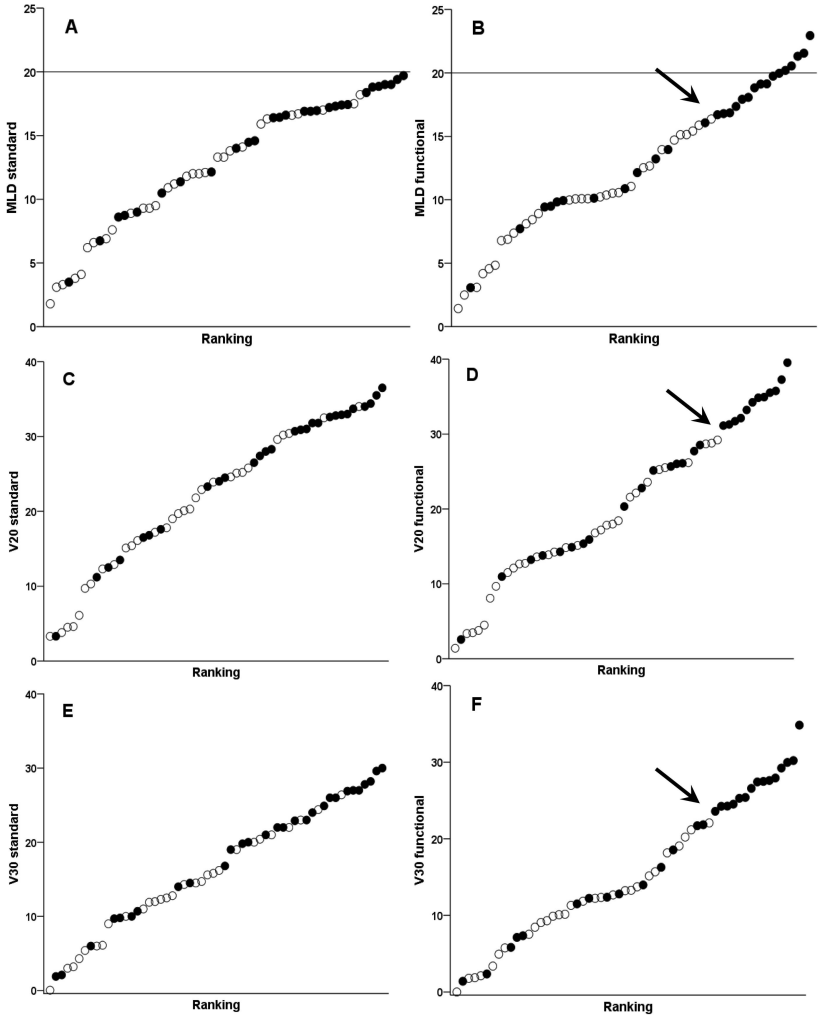

Figure 2.30: A ranking plot for standard (A:MLD, C:V20, E:V30) and functional (B:fMLD, D:fV20, F:fV30) dosimetrics in patients that incurred grade 2-5 RP (solid circles) and those with grade 0-1 RP (open circles). **Note:** Image from "Inclusion of functional information from perfusion SPECT improves predictive value of dose–volume parameters in lung toxicity outcome after radiotherapy for non-small cell lung cancer: A prospective study" by Katherina P. Farr, 2015, *International Journal of Radiation Oncology Biology Physics*, 117(1), pp. 9-16

Ultimately, the study that best supports the theory that decreasing radiation to functional lung can reduce the incidence of RILT was performed by Farr et al. in 2015 [46]. In this study of 58 NSCLC patients (primarily 58% Stage III), a strong correlation between perfusion SPECT dosimetrics, specifically functional-weighted mean lung dose (fMLD) and functional intensity receiving $\geq$ 20 Gy (fV20), and RP incidence was found. As shown in the ranking plot in Figure 2.30,

it appears that all patients who received an fV20 >30% incurred RP. Similarly, threshold cutoffs for fMLD and functional intensity receiving $\geq$ 30 Gy (fV30) also demonstrate a clear stratification in which functional dosimetrics above these bounds relate to near imminent toxicity incidence. While the horizontal line, shown in Figure 2.30A, relating to an MLD=20 Gy represents the clinical constraint used in the RT planning of these cases, it is often suggested that V20 should also be limited to less than 30% to maintain rates of RP below 20% incidence [45]. Because this bound was exceeded in many of the cases that incurred RP, it is believed that the excessive amount of high dose delivered to a large area (a global lung V20>30% often relates to an exceedingly high V20 in the ipsilateral lung) is the cause of the high incidence (43%) of RP in this study. Furthermore, the high Spearman correlation coefficients (all metrics had r$\geq$0.85) demonstrate a close association between these standard and functional dosimetrics suggesting they represent similar information. Therefore, although the functional dosimetrics appear to better delineate the cutoff for imminent toxicity incidence in the cases of RP, it is possible these particular cases of toxicity are caused due to an excessively high dose delivered across a large portion of the normal lung tissue. As such, this data suggests that V20 and fV20 should both be kept below 30% to ensure toxicity rates below 20%, but it is also clear that there are other cases of toxicity that are not captured strictly by the amount of dose delivered [46].

Despite this long history of promising research regarding the use of functional lung imaging for use in RT planning and outcome assessment, RT plans are currently developed solely to limit volumetric dosimetrics, such as MLD and V20. Clearly, normal lung doses should be kept to a minimum, however, these metrics do not account for patients with a heterogeneous distribution of lung function, which creates regions of varying functional capability that respond differently to radiation [74]. And yet, functional-guided RT has not yet been clinically adopted due to three primary factors: 1) inaccessibility of functional imaging in radiation oncology clinics, 2) uncertainty in clinical efficacy of functional-avoidance RT to reduce RILT, and 3) technological barriers to incorporate functional images in commercial treatment planning systems. As such, more research is needed to successfully integrate functional imaging in RT planning to improve patient outcomes.

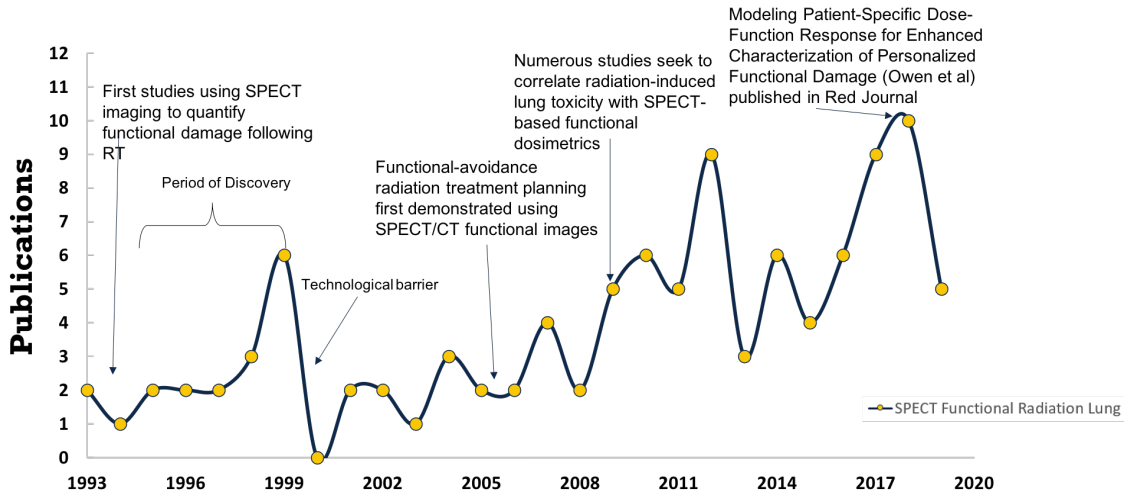

(a) SPECT Functional Radiation Lung Publications

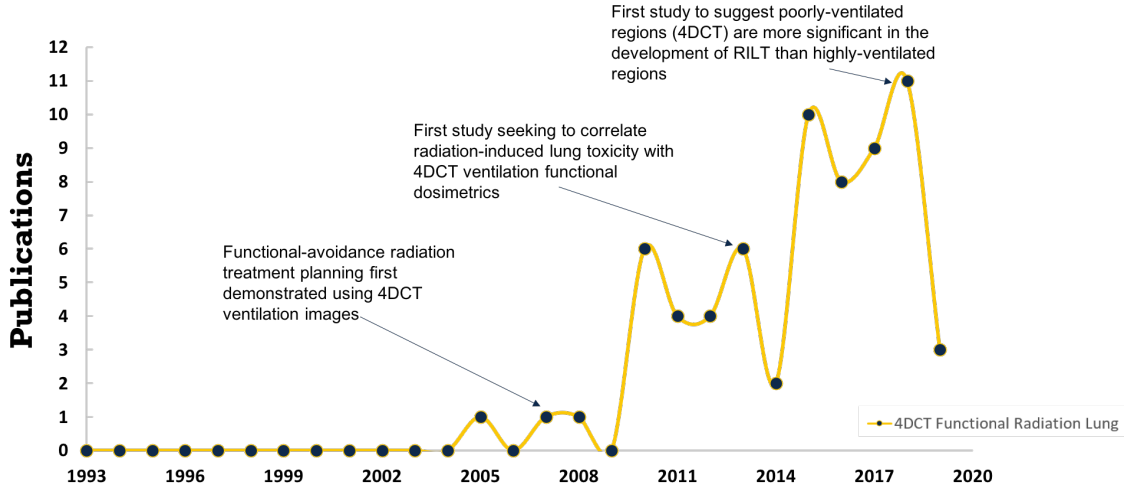

(b) 4DCT Functional Radiation Lung Publications

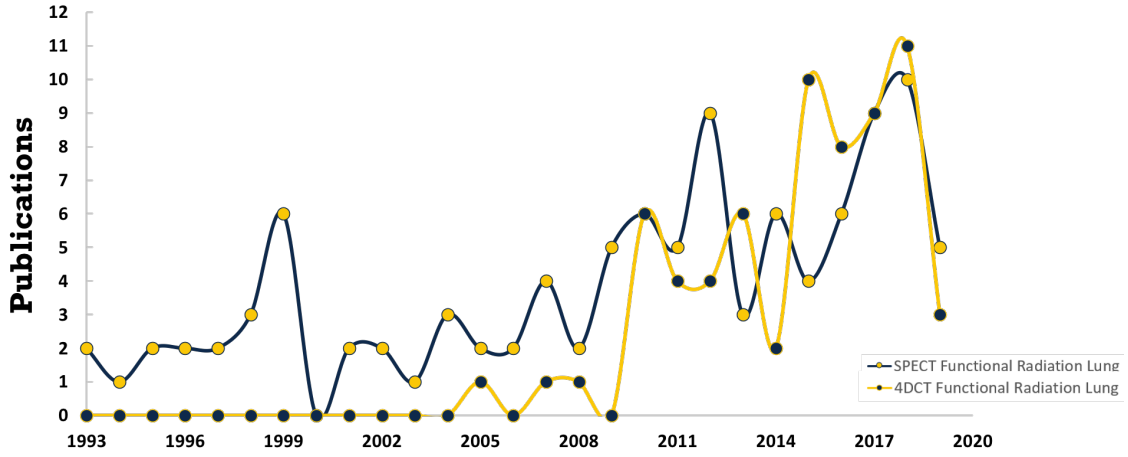

(c) SPECT/4DCT Functional Radiation Lung Publications

Figure 2.31: Annual PubMed publications containing keywords SPECT/4DCT Functional Radiation Lung.

While the majority of functional lung studies have been performed using V/Q SPECT imaging, its limited accessibility has constrained the widespread use of SPECT imaging in clinical radiation oncology applications. As shown by the number of annual publications containing the keywords "SPECT Functional Radiation Lung" in Figure 2.31(a), the seminal functional imaging studies in the early 1990s generated a short period of discovery, but the lack of technological capability at the time hindered any significant advancements regarding the use of functional information in RT planning. As this technological gap closed, more studies began to investigate the use of SPECT/CT for functional-avoidance RT [63, 64].

More recently, 4DCT has become of interest as a functional imaging modality due to its ability to quantify ventilation-based metrics and its wide-availability in the clinic. The number of publications containing the keywords "4DCT Functional Radiation Lung" are shown in 2.31(b), which portrays the sharp increase in research in this area in the past decade, and 2.31(c) demonstrates a similar recent trajectory with SPECT functional imaging in CT.

As mentioned, the major advantage of CT-based ventilation imaging is its accessibility in the radiation oncology clinic since nearly all RT patients are already required to receive a CT scan for anatomical localization and RT beam arrangement. As such, if this CT information could also be utilized for functional lung quantification, it is essentially free data that does not require any extra appointments or scans. However, the primary drawback for CT-based ventilation imaging is the uncertainty in whether its estimates are physiologically accurate in quantifying true lung function. Whereas V/Q SPECT imaging is a direct measure of oxygen and blood flow, CT-based ventilation is based on quantifying mechanical deformation and/or density changes within lung parenchyma [75], which provides an indirect indication regarding the presence of local functional gas exchange.

The use of phase-resolved CT images was first proposed in 2005 by Rietzel et al. [76] and this technique was extended to quantify ventilation by Guerrero et al. [77] shortly after. Many of the subsequent studies in this area focused on the 4DCT ventilation quantification technique and its potential implications [15]. In 2013, Vinogradskiy et al. produced the first study seeking to correlate radiation-induced lung toxicity incidence with 4DCT ventilation metrics [78]. Shown in

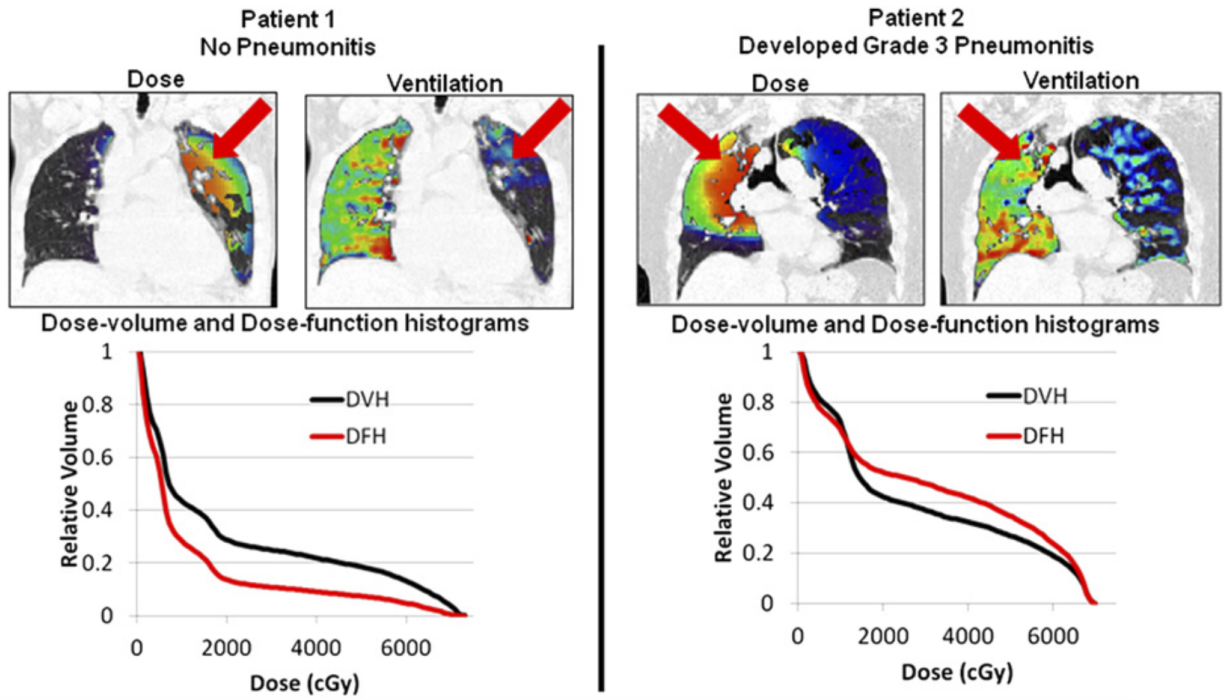

Figure 2.32: 4DCT ventilation slice images and the corresponding dose-volume and dose-function histograms for two example patients. **Note:** Image from "Use of 4-Dimensional Computed Tomography-Based Ventilation Imaging to Correlate Lung Dose and Function With Clinical Outcomes" by Yevgeniy Y. Vinogradskiy, 2013, *International Journal of Radiation Oncology Biology Physics*, 86(2), pp. 366-371

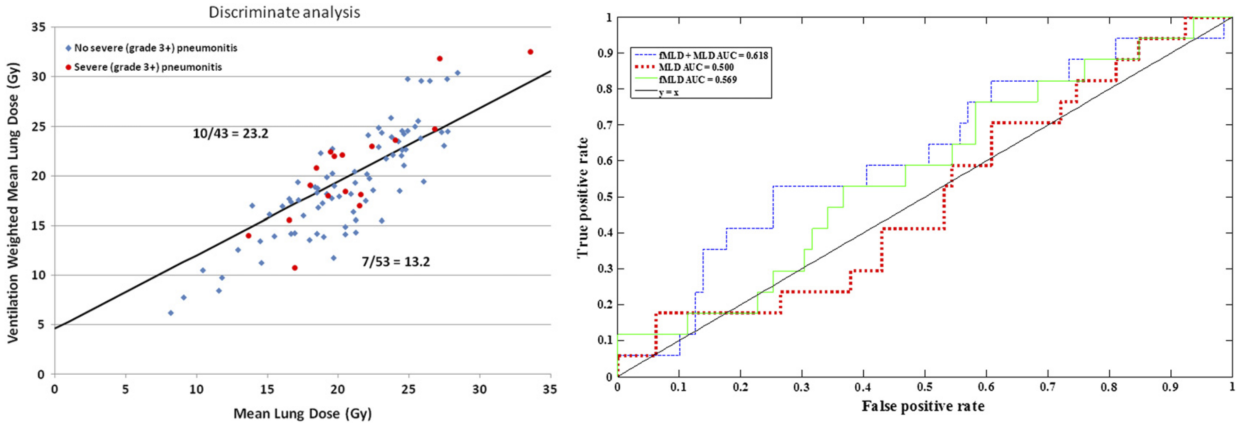

Figure 2.33: Scatter plot of mean lung dose versus ventilation-weighted mean lung dose (left) and ROC analysis of volumetric and functional dosimetrics as predictors for RP incidence (right). **Note:** Image from "Use of 4-Dimensional Computed Tomography-Based Ventilation Imaging to Correlate Lung Dose and Function With Clinical Outcomes" by Yevgeniy Y. Vinogradskiy, 2013, *International Journal of Radiation Oncology Biology Physics*, 86(2), pp. 366-371

Figure 2.32 are the distributions of 4DCT-derived ventilation and dose, along with the corresponding DVH and dose-function histograms (DFHs), for two example patients included in the study. As demonstrated by these example patients, there is a stark difference between the ventilation distributions within each individual lung, with each patient exhibiting a near complete ventilation defect in one lung. However, in these particular cases, the patient that received a large dose to the ventilated lung (signified by the DFH curve greater than the DFH curve in patient 2) was the patient that incurred grade 3 RP, whereas patient 1 did not incur RP and received the majority of dose in the lung with the ventilation defect (represented by the relatively lower DFH curve). As such, these two cases are suggestive of the potential benefit for using 4DCT ventilation to reduce radiation to functional lung in an attempt to decrease toxicity rates. While this patient appeared to derive a benefit from the inadvertent functional-avoidance, this study did not find a significant correlation between functional dosimetrics and RP across the cohort. However, it was suggested that the CT-based ventilation dosimetrics had better predictive power than the standard dosimetrics, despite both showing a limited association with toxicity incidence, as shown in Figure 2.33 [78].

In a subsequent analysis by Vinogradskiy et al., 4DCT ventilation estimates were compared to SPECT ventilation estimates in a cohort of 15 lung cancer patients [79]. Through this study, a moderate correlation was found between the two functional imaging modalities in regards to the functional balance between the right/left lung as shown in Figure 2.34. In certain cases though, there appears to be a strong agreement as shown in Figure 2.35. However, the comparative analysis between these modalities is difficult because it relies on a relative analysis regarding the amount of functional intensity within each lung or region. More recent studies comparing 4DCT ventilation with SPECT ventilation have also reported only marginal correlations with large inter-patient and inter-method variability between the two functional lung imaging modalities [80, 81].

In addition, Vinogradskiy et al. has reported on the extensive functional defects in Grade III NSCLC patients [19] and has also demonstrated functional-avoidance techniques using 4DCT ventilation images [27]. In 2017, two studies by Faught et al. reported on the 4DCT-based ven-

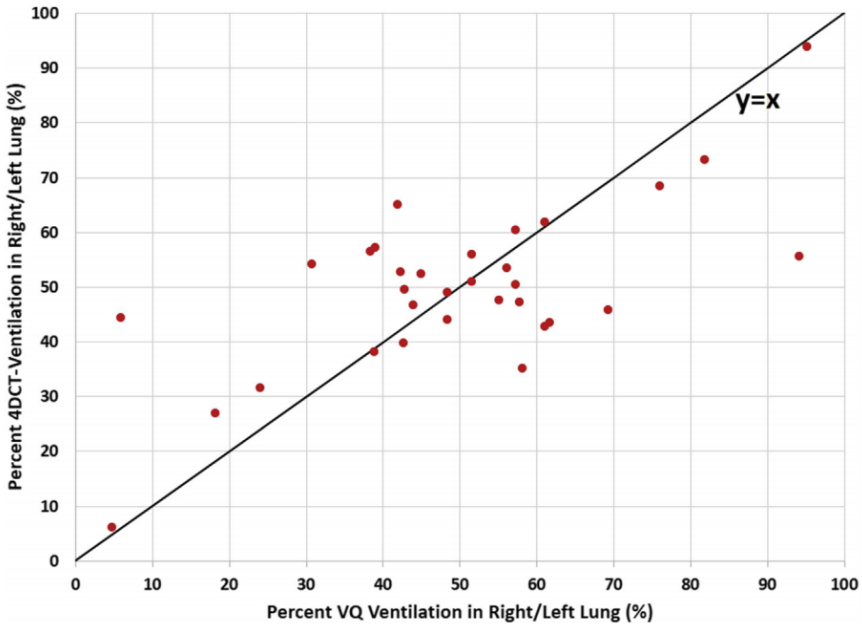

Figure 2.34: Fraction of 4DCT ventilation versus SPECT ventilation in the right/left lung in a cohort of 15 lung cancer patients. **Note:** Image from "Comparison of 4-Dimensional Computed Tomography Ventilation With Nuclear Medicine Ventilation-Perfusion Imaging: A Clinical Validation Study" by Yevgeniy Y. Vinogradskiy, 2014, *International Journal of Radiation Oncology Biology Physics*, 89(1), pp. 199-205

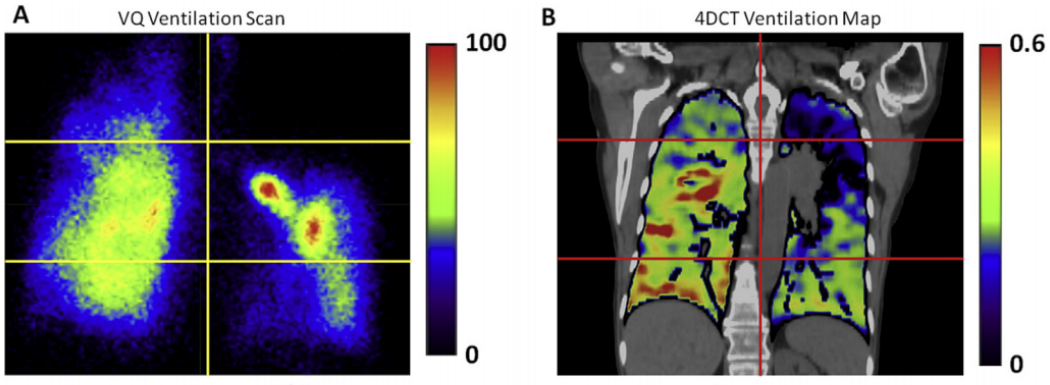

C

	VQ Ventilation		4DCT Ventilation	
	Right (%)	Left (%)	Right (%)	Left (%)
Top	9.5	2.7	16.8	8.1
Middle	30.2	21.1	21.9	12.4
Lower	21.4	15.1	23.2	17.7
Total	61.1	38.9	61.8	38.2

Figure 2.35: SPECT ventilation (A), 4DCT ventilation (B), and quantitative assessment for each of the relative distributions. **Note:** Image from "Comparison of 4-Dimensional Computed Tomography Ventilation With Nuclear Medicine Ventilation-Perfusion Imaging: A Clinical Validation Study" by Yevgeniy Y. Vinogradskiy, 2014, *International Journal of Radiation Oncology Biology Physics*, 89(1), pp. 199-205

tilation dose-function metrics that were most associated with RP incidence and the potential reduction in toxicity rates if functional-avoidance methods were implemented using 4DCT-based ventilation images [26, 31]. Both of these analyses have been used as evidence that 4DCT-based functional-avoidance should be implemented for all patients, however, a number of questions regarding functional-avoidance RT techniques remain: 1) if the correlations between 4DCT and SPECT ventilation estimates are only marginal, how do we ensure that the CT-based ventilation estimates are properly quantifying functional lung? 2) While functional-guided radiation treatments offer the potential to limit radiation damage in certain cases, the implications of shifting dose from high-functioning regions into low-functioning regions, which are indicative of pulmonary dysfunction, have not yet been directly studied, so are we confident that functional-avoidance is the optimal strategy for all lung cancer patients?

In an attempt to answer these questions, functional-guided RT clinical trials are underway at the institutions listed in Table 2.9.

While most of these clinical trials are still active (and the contents of this thesis will describe the results from the completed University of Michigan clinical trial), an interim analysis has been published by the University of Colorado group, which demonstrates feasibility and acceptability regarding the 4DCT-based ventilation functional-avoidance RT technique [82]. In the first 17 patients treated on this trial, toxicity rates for grade $\geq$2 and $\geq$3 radiation pneumonitis were found to be 17.6% and 5.9%, respectively. These results are promising, as they demonstrate a reduction from the historical RP rate of 25%. However, the functional-avoidance technique was reported to have only reduced the mean dose to functional lung by 1.4 Gy and decreased V20 by 3.2%, which demonstrates the limited ability to drastically redistribute dose to functional lung due to the numerous other strict clinical constraints and lack of functional heterogeneity in other cases.

Ultimately, the extensive studies conducted as a part of these clinical trials will help to clarify the utility of functional imaging in radiation treatment planning and motivate the development of technology to better incorporate these imaging modalities into the radiation oncology clinic. As such, this thesis will describe the knowledge gained and technology developed as a part of three

Functional-Guided Radiotherapy Clinical Trials

Institution	Study Title	Study Summary	Start Date	Status (on 1/2021)
University of Colorado	Feasibility Study Incorporating Lung Function Imaging Into Radiation Therapy for Lung Cancer Patients	The proposed study is in the field of thoracic radiation oncology where radiation therapy is used to treat lung cancer. The primary objective of the early phase clinical trial will be to evaluate the safety of performing functional avoidance radiation therapy for lung cancer patients using 4D computed tomography (4DCT) ventilation imaging.	4/22/16	Active, not recruiting
University of Wisconsin	Improving Pulmonary Function Following Radiation Therapy	The purpose of this study is to develop radiation plans that will help preserve lung function in healthy tissue surrounding the tumor. We believe that 4DCT scans can be useful in designing radiation treatment plans that help us avoid healthy normal functioning lung tissue close to lung tumors. Currently 4DCT scans are used to help us determine exactly where the tumor is and how it moves when you breathe. In this study we will also use the 4DCT scans to try to identify high functioning normal lung tissue.	8/17/16	Active, recruiting
University of Washington	FLARE RT for Patients With Stage IIB-IIIB Non-small Cell Lung Cancer: Personalizing Radiation Therapy Using PET/CT and SPECT/CT Imaging	This phase II trial studies how well positron emission tomography (PET)/computed tomography (CT) and single positron emission computed tomography (SPECT)/CT imaging works in improving radiation therapy treatment in patients with stage IIB-IIIB non-small cell lung cancer. PET/CT imaging mid-way through treatment may be able to accurately show how well radiation therapy and chemotherapy are working. SPECT/CT imaging may be able to tell which parts of the lung tissue are healthier than others. Based on the result of the imaging, treatment adjustments may be made to the radiation therapy to improve survival and decrease toxicity.	5/20/16	Active, recruiting
University of Michigan	Using Imaging and Molecular Markers to Predict Tumor Response and Lung Toxicity in Lung Cancer	Successful treatment of non-small cell lung cancer with radiation therapy requires that the physicians determine exactly where the tumor is in your body and protect your normal tissue. This study is designed to apply functional imaging, Fluorodeoxyglucose-Positron Emission Tomography (FDG-PET) and Ventilation/Perfusion Single Photon Emission Computerized Tomography (V/Q SPECT), before treatment and then again during treatment to see if it helps predict how well the treatment works for your cancer and how well your lung functions during treatment. A Computerized Tomography (CT) will also be performed along with both of these procedures to help the researchers see clearly where your cancer or your healthy lung is located.	5/1/07	Completed

Table 2.9: Fraction of 4DCT ventilation versus SPECT ventilation in the right/left lung in a cohort of 15 lung cancer patients. **Note:** Image from "Comparison of 4-Dimensional Computed Tomography Ventilation With Nuclear Medicine Ventilation-Perfusion Imaging: A Clinical Validation Study" by Yevgeniy Y. Vinogradskiy, 2014, *International Journal of Radiation Oncology Biology Physics*, 89(1), pp. 199-205

functional imaging clinical trials conducted at the University of Michigan.

2.3.2 Patient Characteristics and Pre-Existing Disease

In 2010, a group of experts in radiation oncology convened to update the tolerance doses originally established by Emami et al. in 1991. This work resulted in the recommendation that V20 should be kept below 30%, and that MLD was recommended to remain below 20 Gy in order to maintain symptomatic pneumonitis rates below 20% [45]. Despite these updated guidelines, numerous studies reported that MLD and V20 alone were insufficient to effectively stratify toxicity incidence because these suggested ranges are often adhered to within the clinic. In a study by Dehnig-Oberije et al., Grade 2+ dyspnea was best predicted by combining MLD with age, World Health Organization (WHO) performance scale, smoking status, and FEV1. While age, performance scale and FEV1 are all factors that point to patients in worse condition having a higher risk for toxicity, the smoking status is interesting because it actually showed that patients who were current smokers at the time of treatment were protected from toxicity. While there has been conflicting data regarding this result, the theory is that smokers have poorer oxygenation in their lung parenchyma, which leads to less production of cytotoxic free radicals, and consequently, less radiation damage [83].

Alternatively, numerous studies have reported a strong connection between pulmonary comorbidities and radiation-induced lung toxicity [84, 85]. Despite this known risk factor, functional-avoidance therapies have assumed funneling dose to low functioning regions will not cause a negative reaction. However, these low functioning regions are perfusion and/or ventilation defects that are often indicative of diseased tissue [86]. Recent studies have suggested patients with pre-existing ILD [87, 88] or idiopathic pulmonary fibrosis [89, 90] prior to RT are disproportionately prone to developing severe toxicity. In fact, grade 4-5 RP was reported in 57% of patients with pre-existing interstitial pneumonitis (versus 2% in those without interstitial pneumonitis) prior to SBRT [91]. Furthermore, not only have symptomatic and severe RP have been reported at much higher rates in NSCLC patients with pre-existing ILD [92], but the rate of out-of-field RP has also been shown to be significantly higher in patients with subclinical ILD, which demonstrates the potential for the acute exacerbation of pre-existing lung disease following RT [93, 94]. There are

also indications that underlying COPD is associated with an increased risk of RILT [95, 47], but there have also been conflicting studies regarding this association [96, 97]. Specifically, because emphysema is indicative of air trapping in the lung parenchyma, there may be less pulmonary tissue exposed to radiation in these areas. Alternatively, given that COPD can significantly decrease a patient's pulmonary function, any further loss of functional lung may have a more severe impact.

Although many of these studies have suggested that lung cancer patients should be screened for pre-existing pulmonary comorbidities, such as ILD or idiopathic pulmonary fibrosis (IPF), there is currently no standard method or process to ensure these comorbidities are understood prior to irradiation. A study by Castillo et al. in 2014 reported that elevated levels of fluorodeoxyglucose (FDG)-positron emitted tomography (PET), a marker of pulmonary inflammation, prior to RT were a risk factor for RILT [98]. Another analysis Kimura et al. sought to utilized combined SPECT perfusion and CT-based ventilation metrics to identify patients with COPD and demonstrated an association between toxicity incidence and a reduction in functional lung [47]. In 2018, Otsuka et al published one of the first studies to conclude that high dose to poorly functioning regions, as determined by 4DCT ventilation, was associated with the highest risk of toxicity [99]. And still, more work is necessary to fully understand the impact of pre-existing pulmonary comorobidities on patient condition following RT.

2.3.3 Geometric Characteristics

As previously described, lower lobe tumors have been shown to be more associated to the risk of RILT, compared to upper lobe tumors [69, 70, 100]. Possible explanations include a greater density of target cells in this region and a connected physiological reaction that has the potential to cause more out-of-field damage. There is some evidence that tumor stage and tumor volume may be associated with toxicity incidence, but it has also been suggested that these tumor characteristics are confounded by other clinical risk factors. Previous radiation, previous chemotherapy, and concurrent chemotherapy are also suggested to have an impact on the risk for toxicity [85].

2.3.4 Biological Characteristics

While the complete pathophysiology of early- and late-stage radiation-induced lung toxicity is still not fully understood, radiation pneumonitis is generally believed to result from alveolar cell depletion and severe inflammation, whereas pulmonary fibrosis is thought to be the manifestation of fibroblast production, collagen accumulation, and destruction of normal lung architecture, which ultimately leads to permanent parenchymal scarring [101]. This complex process is triggered by radiation damage to parenchymal cells and is mediated by the cascade of cytokines that infiltrate normal lung tissue following RT [102, 103]. While this influx of inflammatory infiltrates is expected, there are a number of specific cytokines that have been identified as possible drivers of RILT.

2.3.4.1 IL-1

Two interleukin (IL) variants, IL-1α and IL-1β, are known to be involved in acute and chronic inflammation through the accumulation of myofibroblasts and extracellular matrix deposition. The over-expression of IL-1β in the epithelial cells of mouse lungs has been linked with inflammation and tissue destruction, leading to long-term production of transforming growth factor (TGF)-β and interstitial fibrosis [104]. IL-1β has specifically been observed at elevated levels in alveolar macrophages within the lungs of patients with IPF [105, 106], suggesting a direct link between acute lung injury, initiated by pro-inflammatory cytokines, and the development of progressive fibrosis. Furthermore, in vitro studies have demonstrated that irradiated alveolar macrophages exhibit dose-dependent increases in IL-1 expression and subsequently recruit other inflammation-related molecules [107, 108]. Specifically, elevated levels of IL-1α messanger ribonucleic acid (mRNA) expression have been associated with radiation-induced lung toxicity [109].

2.3.4.2 IL-6

Previous studies have suggested IL-6 as the mechanism causing nearly 80% of patients with pulmonary comorbidities to incur toxicity [87, 88, 107, 108]. While a cytokine release during and

after radiotherapy is common in NSCLC patients receiving RT [103, 102], mechanistic studies of IL-6 have demonstrated both anti- and pro-inflammatory properties [110, 111]. Specifically, Moodley et al reported that signaling of IL-6 can become reversed in patients with IPF prior to RT such that fibrotic cells resist apoptosis, and alternatively, cause a profibrotic effect [112]. This reverse signaling has the potential to promote a global pro-fibrotic effect that can cause severe out-of-field lung tissue damage following radiation treatment, which has been linked with severe, systemic toxicities within the lungs [113, 114]. Furthermore, numerous studies have reported a correlation between elevated levels of pre- and post-treatment IL-6 with radiation-induced lung toxicity [115, 107], which may also be due to the initiation of lymphocyte alveolitis [116].

2.3.4.3 TGF-β1

Another cytokine, transforming growth factor (TGF)-β1, plays a vital role in normal lung repair after irradiation, specifically by stimulating collagen production and facilitating fibrotic tissue remodeling [117]. Dose-dependent changes in TGF-β1 have been reported in animal and human studies, further suggesting TGF-β1 signaling can contribute to the overproduction of collagen and fibroblasts in the lung following RT [118, 119]. Elevated expression of TGF-β1 during or after RT has frequently been associated with the incidence of radiation-induced lung toxicity [120, 121]. Recent studies have investigated anti-TGF-β1 antibody as a potential concurrent therapeutic option to inhibit fibrosis in patients receiving RT and have reported that patients with lower levels of TGF-β1 tend to have more favorable outcomes [122, 123].

2.3.4.4 TNF-α

Another possible mechanism causing radiosensitivity in patients with pulmonary defects could be an increased accumulation of tumor necrosis factor alpha (TNF-α). Production of (TNF-α) can be caused by inflammatory tissue response and may be present in reperfused areas at mid-treatment [124]. Rübe et al. demonstrated elevated levels of (TNF-α) mRNA expression in the lung tissue of mice starting 2-4 weeks after irradiation, which is similar to the duration between the start of

RT and the mid-treatment timepoint [109]. Radiation-induced production of (TNF-α) is known to be related to early cell apoptosis and could be causing increased latent functional damage [125].

CHAPTER III

Patient Characteristics and Experimental Design

3.1 Patient Population

The patients included in this study were prospectively accrued from three separate IRB-approved clinical trials (ClinicalTrials.gov Identifiers: NCT00603057 & NCT02492867 & NCT03121287) performed at the University of Michigan. Written informed consent for participation in the trial was obtained from all patients. The details of patient accrual from these two trials is shown in Figure 3.1.

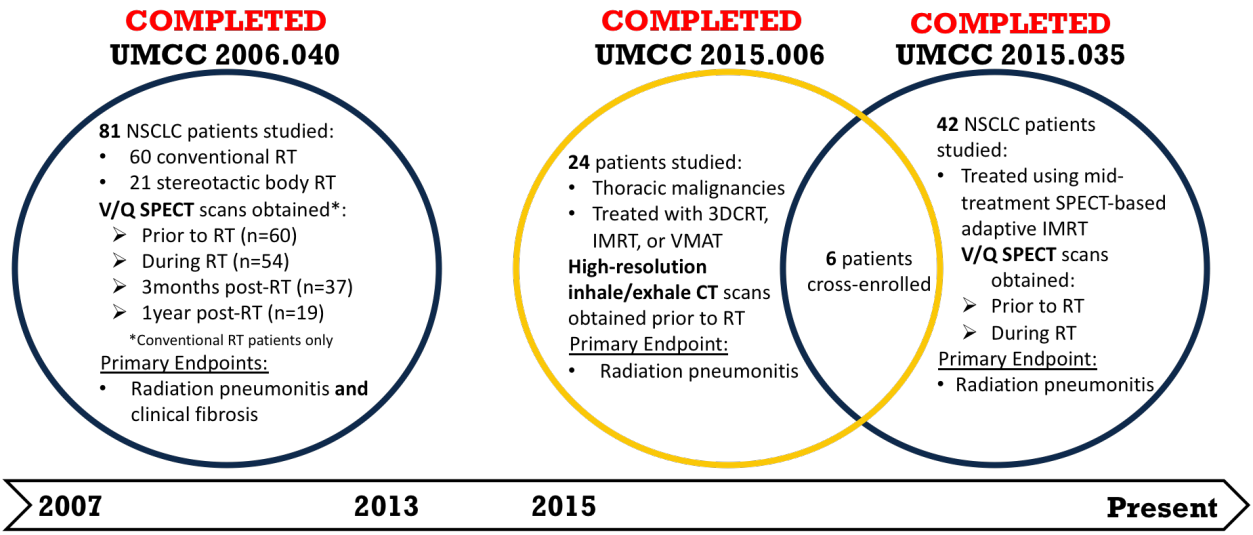

Figure 3.1: Patient data accrued from three IRB-approved clinical trials between 2007-2020.

Because this dissertation work began in 2016, the first project, i.e. longitudinal dose-response

modeling, was performed using only the 2006.040 cohort of patients. However, as this work progressed and new SPECT scans were accrued, the population was updated to include patients from both the 2006.040 and 2015.035 trials because the SPECT imaging, patient characteristics, and treatment regimens were considered to be similar. The validity of combining these cohorts is discussed further in chapter VI.

All patients were diagnosed and staged for the presence of lung cancer and the patients involved in the SPECT analyses, both the dose-function longitudinal (n=81 patients) modeling and toxicity risk assessment (n=88 patients),were histologically-verified to have NSCLC. A summary of patient characteristics for each of the cohorts with SPECT scans available is presented in Table 3.1.

3.2 SPECT Imaging

The 2006.040 patient cohort, used for the modeling of longitudinal dose-function response, included V/Q SPECT images acquired at four separate imaging time points: (1) pre-treatment; (2) mid-treatment; (3) three months post-treatment; and (4) one year post-treatment. The amount of available scans at each of these four timepoints is shown in Table 3.1. Conversely, the 2015.035 cohort only included V/Q SPECT images from the pre- and mid-treatment timepoints.

SPECT imaging was performed using a dual-head SPECT/CT system (Symbia T6, Siemens Medical Solutions, Malvern, PA) with the patient immobilized in the supine treatment position using a standard thorax support device for reproducibility. Each patient was first scanned for pulmonary ventilation by inhaling aerosolized 99^mTc-diethylenetriaminepentaacetic acid from a 1850 megabecquerel (MBq) reservoir. Pulmonary perfusion was subsequently scanned after intravenous injection of 185 MBq of 99^mTc-labeled macroaggregated albumin particles.

SPECT scans were obtained over a non-circular orbit with a 360° arc in 60 projections and 128 frames (19 s/frame, 3° increments, 128 pixels × 128 pixels, ∼3.5 mm × ∼3.5 mm × ∼2 mm) using the stop-and-shoot mode. SPECT images were reconstructed by initially applying attenuation and scatter corrections and subsequently implementing a 3-dimensional ordered subset expectation-maximization iterative reconstruction with resolution, scatter, and attenuation corrections.

Table 3.1: Longitudinal Image Acquisition and Baseline Patient Characteristics

	2006.040 Conventional RT Cohort (n = 60)	2006.040 SBRT Cohort (n = 21)	2015.035 Conventional RT Cohort (n=30)
V/Q SPECT Scans Available			
Baseline	60	21	30
Mid-Tx	54	20	28
3Month Post-Tx	37	14	0
1Year Post-Tx	19	7	0
Age [years]			
Mean	68	71	65
Range	39 – 85	53 – 83	49 – 82
Gender			
Male	47 (78%)	13 (62%)	18 (60%)
Female	13 (22%)	8 (38%)	12 (40%)
Race			
Caucasian	55 (92%)	17 (81%)	28 (93%)
African American	4 (7%)	4 (19%)	1 (3%)
Asian	1 (1%)	0	0
Unknown	0	0	1 (3%)
Smoking Status			
Never	2 (3%)	3 (14%)	1 (3%)
Former	31 (52%)	10 (48%)	18 (60%)
Current	24 (40%)	8 (38%)	11 (37%)
Unknown	3 (5%)	0	0
Simple Stage			
Stage I	8 (13%)	16 ((76%)	0
Stage II	5 (8%)	4 (19%)	1 (3%)
Stage III	47 (78%)	1 (5%)	28 (93%)
Stage IV	0	0	1 (3%)
Karnofsky Performance Score			
50	1 (2%)	1 (5%)	0
60	2 (3%)	2 (10%)	0
70	13 (22%)	3 (14%)	1 (3%)
80	20 (33%)	5 (24%)	9 (30%)
90	20 (33%)	8 (38%)	13 (43%)
100	4 (7%)	2 (10%)	7 (23%)
Concurrent Chemotherapy			
No	13 (22%)	21 (100%)	0
Yes	47 (78%)	0	30 (100%)
RILT Grade			
Grade 0	25 (42%)	10 (48%)	20 (67%)
Grade 1	26 (43%)	9 (43%)	4 (13%)
Grade 2	6 (10%)	1 (5%)	5 (17%)
Grade 3	1 (2%)	1 (5%)	1 (3%)
Grade 5	2 (3%)	0	0

*Percentages rounded to nearest whole number

Table 3.1: Summary of patient information in the cohorts with SPECT images available.

3.3 SPECT Registration

Each SPECT scan was rigidly registered to the treatment planning CT through an alignment tool embedded in the clinical, commercial treatment planning system (Eclipse, Varian Medical Systems, Palo Alto, CA). Rigid registrations were manually reviewed for accuracy. After registration, each voxel within the normal lung tissue contained both a dose value and function value (ie, normalized perfusion SPECT intensity). Rigid registration was performed instead of deformable registration to avoid uncharacterized errors that may be caused by low spatial resolution and unmatched breathing states between the SPECT/CT and planning CT images.

3.4 SPECT Normalization

To account for varying absolute intensity in SPECT scans taken across different time points and patients, the raw intensity value in each voxel was normalized. Shown in Equation 3.1, raw SPECT intensities (f_i) were converted to normalized SPECT intensities ($f_i^{\mathbb{N}}$) using the average intensity in the low-dose ($\leq$5 Gy), functional region of the contralateral lung as the normalization constant ($\mathbb{N}$). This region was assumed to be stable against radiation-induced longitudinal functional changes, thus facilitating intra- and inter-patient comparisons such that normalized functional intensity of 1.0 equates to the average intensity of normal-functioning lung for all patients and timepoints. Although compensation effects have been hypothesized to occur following initial radiation delivery, where healthy tissue essentially performs more functional gas exchange than normal, there is little direct evidence to support this theory [126]. Reasons for why compensation effects may have been detected erroneously are also discussed in chapter V.

$$\forall \textit{ voxels in the lungs: } f_i^{\mathbb{N}} = \frac{f_i}{\mathbb{N}} \textit{ where } \mathbb{N} = \sum_{i=1}^{N_{norm}} \frac{f_i}{N_{norm}} \tag{3.1}$$

where N_{norm} is the number of voxels in the contralateral lung that had functional intensity greater than 15%, i.e. functional, and received $\leq$5 Gy, i.e. low-dose. Normalized perfusion and ventilation

SPECT intensities were used as a direct surrogate for lung function, and therefore, normalized intensity signal in any voxel can be considered a relative measure of local lung function compared with the average functional value in unaffected tissue.

3.5 SPECT Artifact Cleaning

To reduce the well-documented effect of 99^mTc aerosol-trapping artifacts in patients with obstructive airway disease [127, 128], an automated artifact cleansing strategy was developed. Initially, any voxel with an intensity value greater than 3 standard deviations above the mean intensity in each individual lung was excluded. To more aggressively eliminate these artifacts, the strategy was subsequently refined to exclude any voxel greater than 2 standard deviations above the mean intensity in each individual lung. However, because the mean intensity may be skewed by the presence of artifacts and defects, an upper and lower intensity limit was implemented such that only voxels representing the expected intensity in normal-functioning lung were included in the mean intensity calculation. The artifact cleansing strategy is described in full detail in chapter IV.

On average, 0.3% of perfusion voxels and 2.0% of ventilation voxels were excluded from the normal lung volume.

3.6 SPECT Functional Categorizations

$$\left\{\begin{array}{c} \textbf{\textit{Low Function}}\ (\textbf{\textit{LF}})\ if\ f_i^{\mathbb{N}} < \mathbf{15}\%\ of\ f_{maximum}^{\mathbb{N}} \\ \textbf{\textit{Normal Function}}\ (\textbf{\textit{F}})\ if\ \mathbf{15}\%\ of\ f_{maximum}^{\mathbb{N}} \leq f_i^{\mathbb{N}} < \mathbf{70}\%\ of\ f_{maximum}^{\mathbb{N}} \\ \textbf{\textit{High Function}}\ (\textbf{\textit{HF}})\ if\ f_i^{\mathbb{N}} \geq \mathbf{70}\%\ of\ f_{maximum}^{\mathbb{N}} \end{array}\right\}$$

Table 3.2: Voxelwise functional categorization scheme.

In the dose-function response analysis, the well-perfused and well-ventilated regions were defined as any voxel >50% of the maximum intensity, but in the latter dose-function toxicity analysis, the high-functioning region was defined as >70% of the maximum intensity. Three functional

categorizations were created to represent low-function lung (LF), normal-function lung (F), and high-function lung (HF) lung. Each voxel with normalized functional intensity ($f_i^{\mathbb{N}}$) was assigned a functional categorization based on the schema shown in Table 3.2, where $f_{maximum}^{\mathbb{N}}$ is the maximum normalized intensity in the global lung structure.

3.7 CT-Based Simulation and Treatment Planning

Simulation CT scans were acquired from each patient, in the supine position, prior to treatment. Early in the study period, patients were assessed for motion through analysis of inhale and exhale CT scans. As the study progressed, 4DCT was incorporated for motion assessment. Patients with extensive motion were prescribed breath-hold treatments, and all free-breathing patients were treated with an internal target volume approach. The Eclipse Analytical Anisotropic Algorithm (AAA) (Varian Medical Systems, Palo Alto, CA) photon dose model was used to retrospectively calculate the delivered dose to each voxel in the CT matrix (512 pixels $\times$ 512 pixels, 0.98 mm $\times$ 0.98 mm $\times$ 3 mm). Essentially, the AAA model employs a three-dimensional convolution of Monte Carlo scatter kernels that are modified by the CT-based electron density matrix [129]. For each patient, the calculated dose in each normal lung voxel was then corrected to the nominal equivalent dose per 2 Gy fraction (EQD2) using the linear quadratic model with an α/β ratio of 2.5 Gy [130].

3.8 Lung and Tumor Contouring

All global lung and tumor structures were clinically contoured during treatment planning and edited according to a thoracic atlas [131]. Normal lung tissue was defined as all voxels within the normal lungs structures, excluding the gross tumor volume (GTV) or internal tumor volume (ITV) if treated while free-breathing. The individual lung and regional lung structures were contoured using the boolean operator process in the Eclipse treatment planning system. Regional lung structures were defined as follows: upper lung above the carina, lower lung below the inferior pul-

monary vein, and middle lung between the upper and lower segments. In the toxicity analysis, a 4mm inner margin was applied to the global lung structure, and all subsequent structures, to reduce the partial volume effect, which has the potential to create erroneous low-functioning regions on the periphery of the lung structures.

3.9 Radiation Therapy

Table 3.2: Volume and Global Lung Dose Statistics Across the Various Patient Cohorts

	2006.040 Conventional RT Cohort (n = 60)	2006.040 SBRT Cohort (n = 21)	2015.035 Conventional RT Cohort (n=30)
Tumor Volume [cm^3]			
Mean	158	15	192
SD	130	12	239
Range	7 – 533	2 – 50	10 – 1286
Normal Lung Volume [cm^3]			
Mean	3983	3994	3553
SD	1323	1422	1085
Range	1838 – 9540	1809 – 6489	2023 – 6919
Max Dose [Gy]			
Mean	68.9	68.8	71.9
SD	8.6	4.6	5.2
Range	47.7 – 97.5	64.0 – 80.2	63.6 – 86.6
Mean Dose [Gy]			
Mean	15.4	4.6	16.1
SD	4.1	1.6	4.2
Range	3.9 – 22.5	2.2 – 7.8	5.7 – 23.9
V5 [%]			
Mean	52.6	22.6	65.7
SD	15.2	8.6	15.9
Range	16.1 – 88.6	7.5 – 45.7	26.6 – 94.8
V20 [%]			
Mean	26.1	6.0	27.3
SD	8.2	2.7	8.3
Range	5.7 – 42.8	2.8 – 13.2	8.6 – 41.3

*No margin applied to lung contours
* No EQD2 correction applied

Table 3.3: Normal lung volume, tumor volume, and global lung dose statistics across the various patient cohorts.

While more patients and images are beneficial to building stable models, patients treated with

conventionally-fractionated RT and SBRT were analyzed separately due to the distinct patient-specific factors, such as age, tumor size, and patient condition, that are used for the prescription of SBRT [132]. While patient age and condition did not appear to be significantly different in the patients that received SBRT versus conventionally-fractionated RT, the SBRT patients clearly had smaller tumors (158 cm^3 v. 15 cm^3) that were typically at an early stage (78% Stage III v. 76% Stage I), which subsequently, led to delivery of a lower mean lung dose (4.6 Gy v. 15.4 Gy) and no concurrent chemotherapy as shown in Table 3.3.

Because the patient population was accrued from 2007 through 2019, there were some notable shifts in the radiation treatment prescription and delivery techniques that occurred over the course of this study. For patients treated with conventionally-fractionated RT, the RT course was generally administered over 30 fractions with 2-2.2 Gy delivered per faction, and the prescription dose was typically either 60-66 Gy or 70-74 Gy for cases where dose escalation was thought to be advantageous, primarily based on tumor size and location. Patients enrolled in the 2006.040 study were treated with three-dimensional conformal RT, whereas patients in the 2015.035 and 2015.006 trials were treated with intensity-modulated radiation treatment (IMRT). All dose values were converted to EQD2 to biologically equate the various treatment regimens. The EQD2 conversion is based on the linear-quadratic model, which accounts for the biological effect of various fractionation regimens, however, the EQD2 conversion is known to become less accurate at high dose per fractions [133] so conventional fractionation RT and SBRT were not directly compared in most cases.

3.10 Radiation-Induced Lung Toxicity Grading

RILT was defined as grade 2+ RP and/or grade 2+ clinical pulmonary fibrosis. RP and pulmonary fibrosis were diagnosed and graded prospectively according to a pre-specified system [134], as shown in Figure 3.2, Using this grading scheme, which is consistent with the common terminology criteria for adverse events (CTCAE) v4.0 [135]. The maximal RP or fibrosis grade was reported as the RILT grade [135]. While the RP and fibrosis pathologies are often considered distinct clinical processes, RILT was used because it encompasses the primary dose-limiting pul-

monary complications that impact patient survival and quality of life [101]. Furthermore, there is some evidence that suggests these toxicities may be linked [103, 101].

	Radiation induced Pneumonitis	**Clinical Fibrosis**
Grade 1	Minimal or mild symptoms of **dry cough** and/or **dyspnea** on exertion, without evidence of tumor progression or other etiology, with **radiographic evidence of acute pneumonitis**	**Radiographic evidence of radiation fibrosis** without or with minimal dyspnea
Grade 2	**Persistent dry cough** requiring narcotic antitussive agents or steroid, and/or dyspnea with minimal effort but not at rest, without evidence of tumor progression or other etiology, with **radiographic evidence of acute pneumonitis, and requiring steroid for treatment**	**Radiographic evidence of radiation fibrosis** causing **dyspnea** with minimal effort but not at rest, not interfering with activities of daily living
Grade 3	**Severe cough**, unresponsive to narcotic antitussive agent and /or dyspnea at rest, with **radiographic evidence of acute pneumonitis**, and **requiring oxygen** (intermittent or continuous) for treatment	**Radiographic evidence of radiation fibrosis** causing **dyspnea** at rest, interfering with activities of daily living, and home oxygen indicated
Grade 4	**Radiation pneumonitis** causes respiratory insufficiency, requiring assisted ventilation	**Radiation fibrosis** causes respiratory insufficiency, requiring assisted ventilation
Grade 5	**Radiation pneumonitis** directly contributes to the cause of the death	**Radiation fibrosis** directly contributes to the cause of the death

Figure 3.2: Radiation-induced lung toxicity grading scheme encompassing radiation pneumonitis and clinical fibrosis.

CHAPTER IV

Development of the Dose Function Analysis Infrastructure

Functional image information is being increasingly used in treatment planning as well as outcomes modeling. However, the ability to compute image-based metrics and directly incorporate them into treatment planning is limited, especially in commercial software. Our work integrates functional image analysis directly into the treatment planning system via scripting, which allows computation of custom metrics and the use of those metrics in other areas of treatment planning, such as plan optimization. These capabilities bring us a step further to direct use of functional image evaluation, targeting, and avoidance, within a commercial clinical system while still allowing the flexibility of a research system.

Using the API within the Eclipse treatment planning system, a novel software program, written in C# and named Dose-Function Analysis, was developed and implemented to process and analyze the spatially aligned dose-function data. Because the Eclipse system does not support analysis of functional lung images, the V/Q SPECT images had to be converted to pseudo-CT DICOM files using an in-house command-line program written by Guillaume Cazolat. Once the converted SPECT images were uploaded to Eclipse, a consistent naming convention was instilled to ensure the code could recognize the data properly. Two applications, a plugin user interface (UI) and standalone batch program, were developed to view/analyze the dose-function data for a single patient or for an entire patient cohort. The underlying methods and code structure were analogous for both applications, but the presentation of the data differed. In the following sections, each application's

functionality, and the shared methods used by each application, will be briefly described to provide an understanding for the code that produced the data that was used within this dissertation.

4.1 Plugin User Interface Analysis

As part of the initial development and validation of the Dose-Function Analysis code, a plugin script was created to visualize individual patient functional lung metrics and graphs. An overview of the UI code structure and basic operations are shown in the diagram in Figure 4.1, where a box=C# dialog box, rounded box=C# method, and ellipse=C# button.

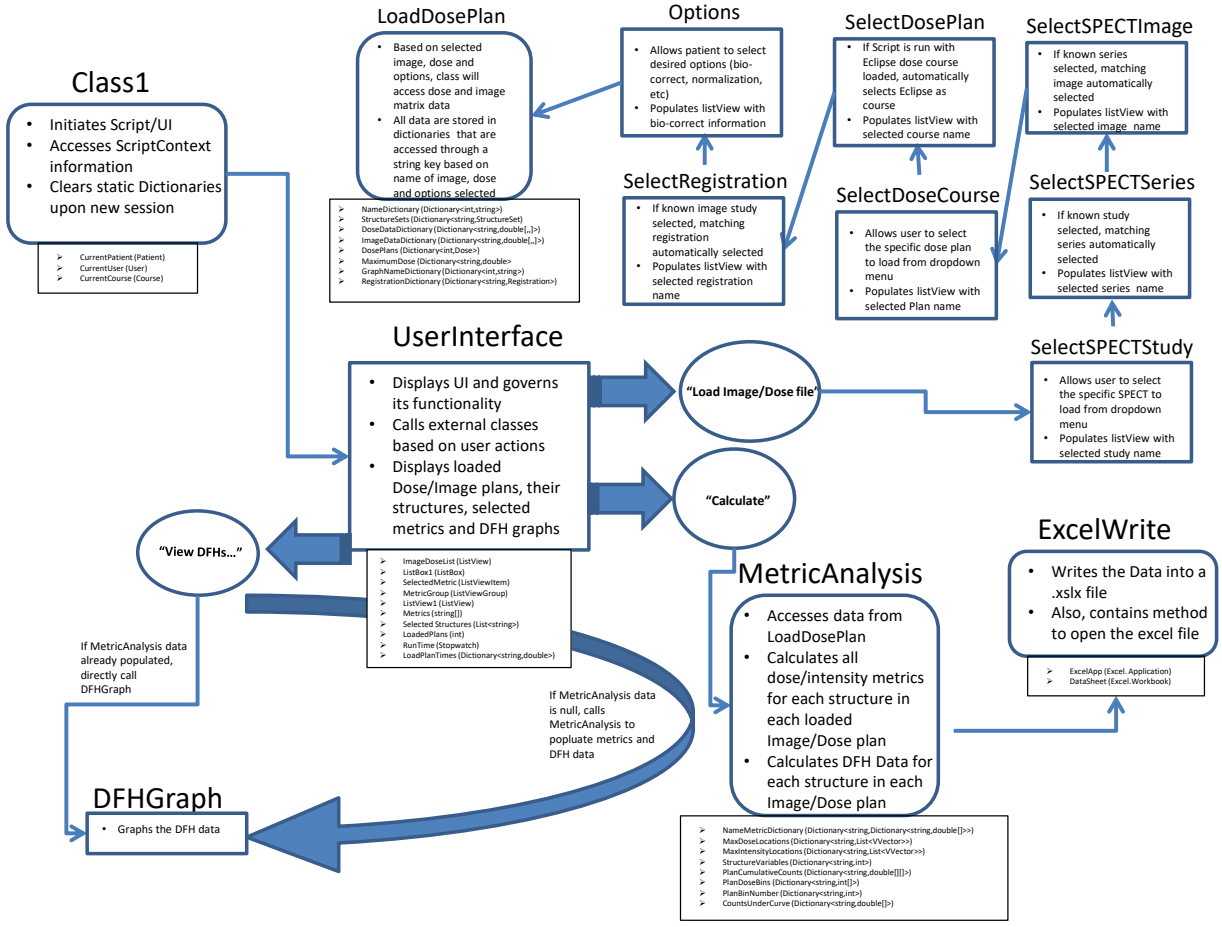

Figure 4.1: Plugin UI Code Structure.

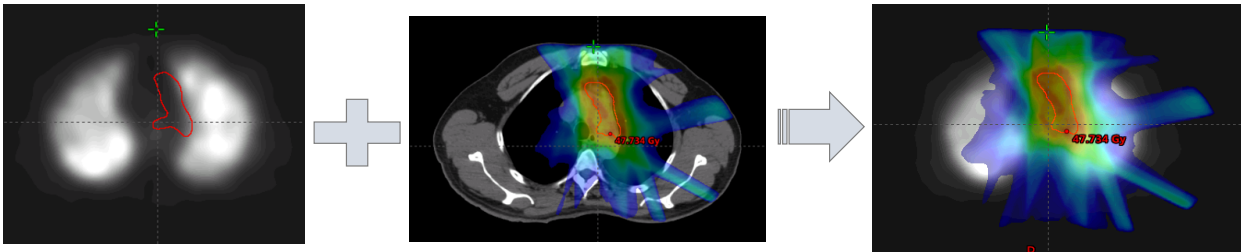

Functional SPECT Imaging

Anatomical Dose Profile

Functional Dose Profile

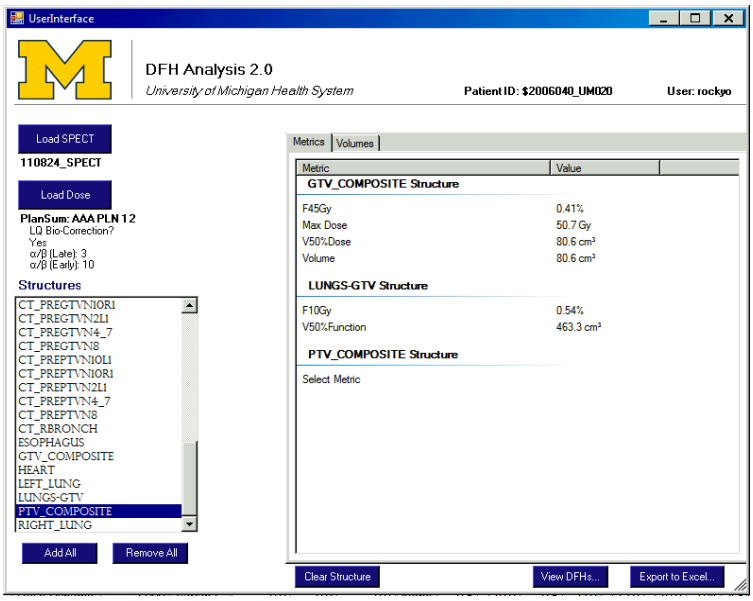

User Interface

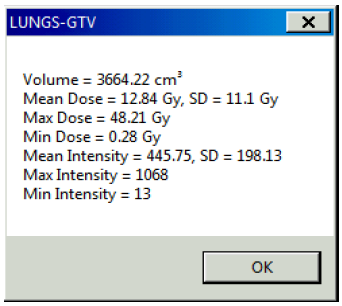

Structural Dose-Function Metrics

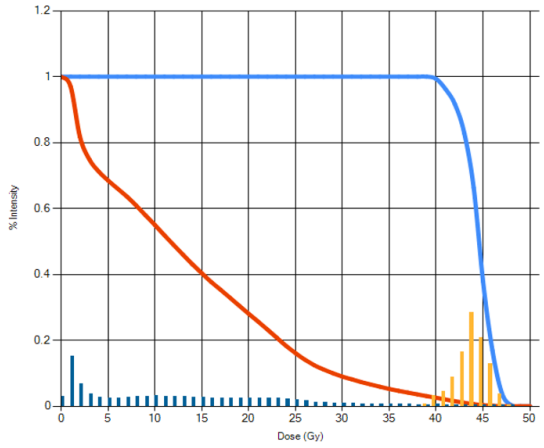

Structural Dose-Function Histogram

Functional imaging data is registered to a treatment planning CT and dose plan. The resulting functional dose profile is analyzed to produce image-based metrics and histograms that are displayed through a user interface, which allows customized parameter inputs and user control of graphical properties.

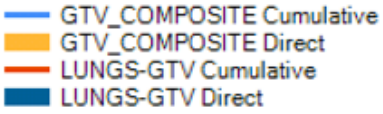

Figure 4.2: Preliminary version of the Dose Function Analysis UI.

4.1.1 Code Initialization

The code is initialized through the VMS.TPS namespace, and the .Net environment (class1.cs) is populated with the various class libraries shown at the top of the code. Below these installed libraries, accessible properties are declared, meaning the public static variables that can be called by other classes within the domain and their values remain stored unless otherwise changed or erased.

Specifically, the properties - CurrentUser, CurrentPatient, and CurrentCourse - are instantiated to hold the values of the Eclipse user, patient ID, and dose course associated with the current Eclipse workspace. The ScriptContext class, available through the VMS.TPS.Common.Model.API library, is then utilized within the Execute void to actively grab the Eclipse workspace values. Once these values are acquired, a new instance of the UserInterface windows form class, i.e. userForm, is created at line 62. Once the method userForm.ShowDialog() is called, the code enters the UserInterface class and a modal dialog box, i.e. the user interface, is opened, meaning the user must interact with the modal window before returning to the shell code.

At the end of this UI initialization class, the static variables and options are cleared to preserve the integrity of the script once the code is recalled.

4.1.2 UserInterface

Upon entering the UserInterface.cs windows form class, a user interface dialog box is displayed to the user as shown in Figure 4.3. An early version of the Dose-Function Analysis UI is shown in Figure 4.2, and the difference between cumulative and direct DFH is specifically shown in the graph on the bottom-left. Many of the UI properties, i.e. listView, and variables, i.e. LoadPlanTimes, are made to be public static structures such that they can be accessed and modified by other classes within the code domain. The inherent UI properties developed through the window forms designer and the initial assignments declared in the UserInterface_Load method are populated at initiation. By accessing the VMS.TPS.Script class, the sciptContext is used to access the current Eclipse workspace. If no patient is loaded in Eclipse, an exception will be thrown. Ideally, this

could be protected from an unhandled exception with a try/catch block.

Once the UserInterface is displayed, the code is stable, and the user is expected to load a functional image through either button1, ”Load Image/Dose” or button 14, “Load All...”.

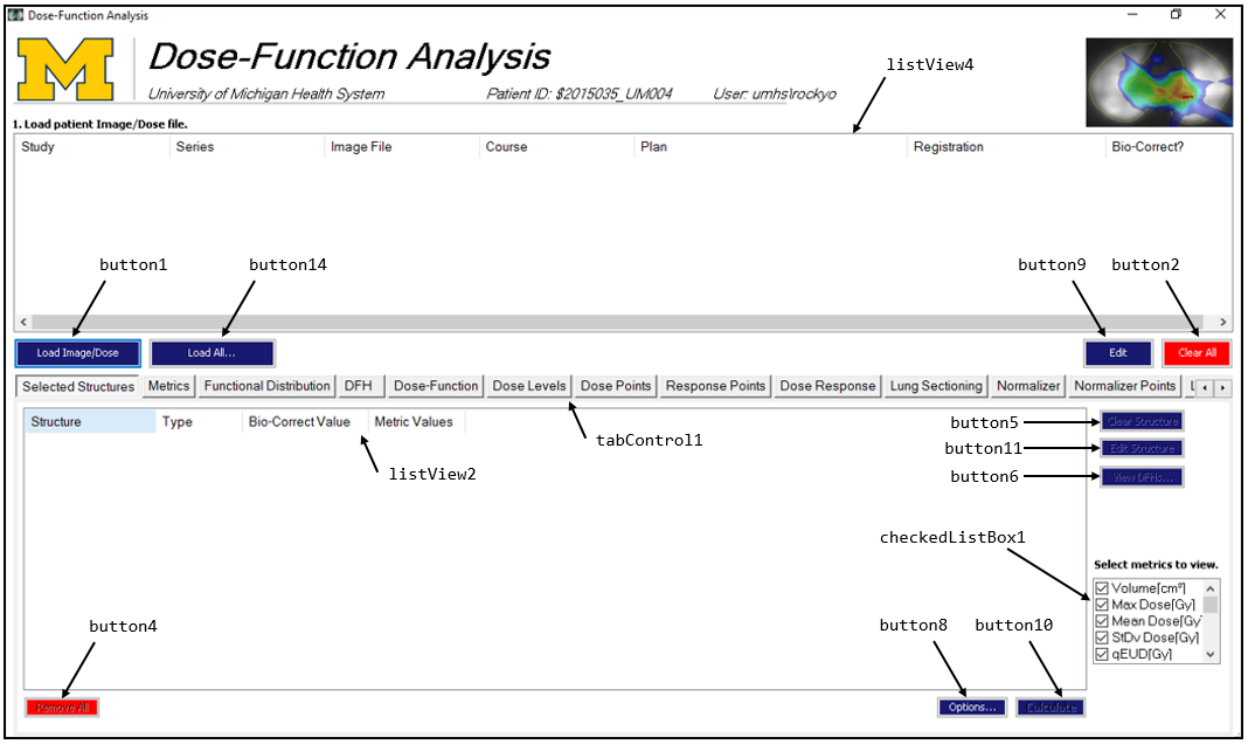

Figure 4.3: UserInterface window shown to user upon initiation of the code.

Essentially, these two options allow the ability to load a single functional image/dose plan pair or utilize a load all solution that automatically loads every available functional image along with a selected dose plan and options.

4.1.2.1 Load Individual Image/Dose Pair

As shown in the upper-right section of Figure 4.1, once button1 “Load Image/Dose File” is selected, a series of dialog boxes are initiated to help the user select: 1) a study, series, and image file that represents the functional image, 2) an Eclipse dose course, plan, and registration that represents the dose matrix, and 3) options such as dose bio-correction.

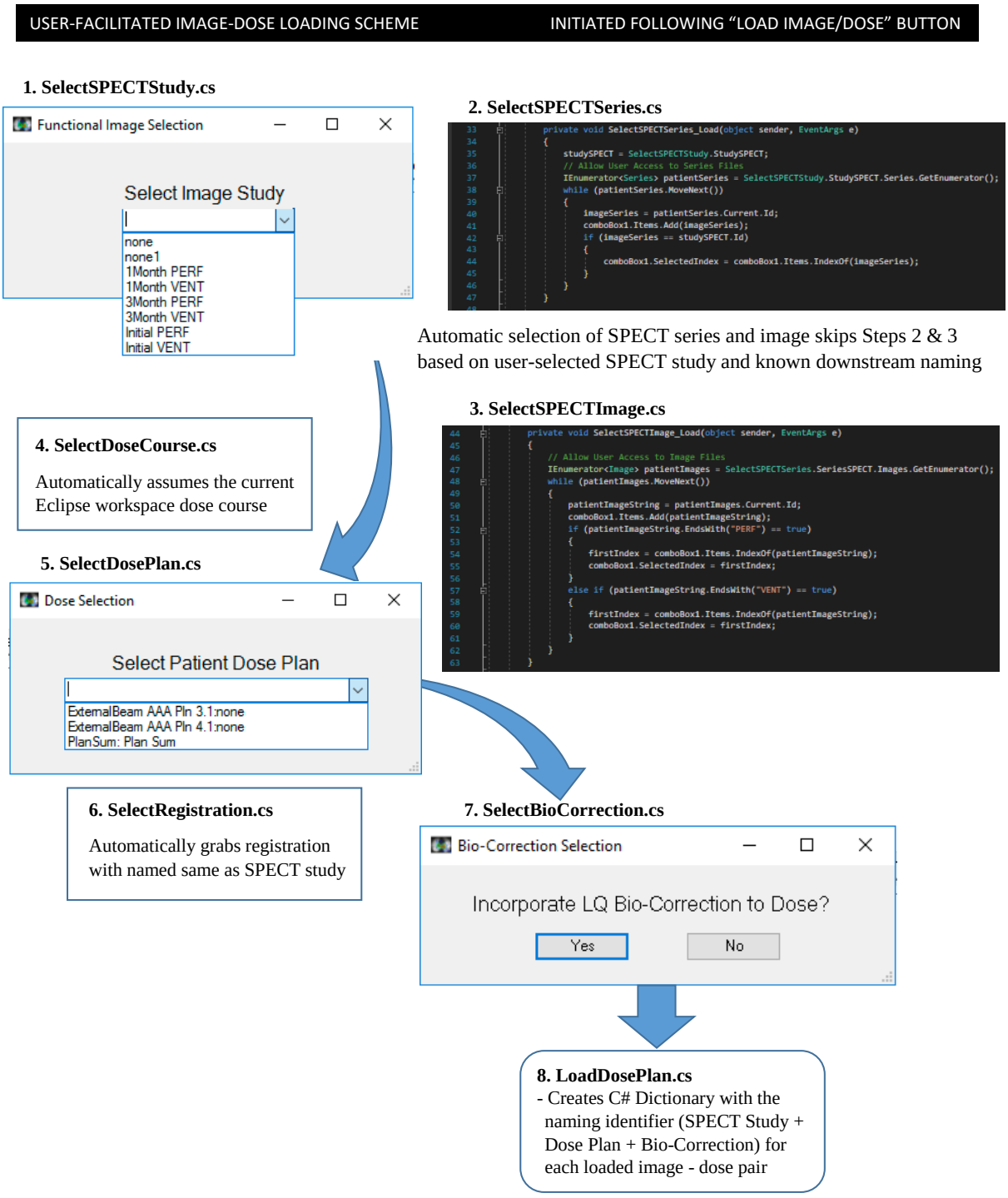

Figure 4.4: User-Facilitated Individual Image/Dose Loading Scheme.

Because this UserInterface code was used frequently to quantify dose-function metrics and to visualize the data, an update was performed to automatically skip user-demanded selection of the SPECT series, SPECT image , dose course, and registration by anticipating the expected downstream naming as shown in Figure 4.4. As such, this update reduced the number of user-demanded dialog boxes from 7 down to 3 (SPECT study, dose plan, bio-correction). Throughout this selection process, a public ListViewItem is being modified, such that the loaded parameters can be viewed in listView4 at the head of the UI following the return to the main code.

4.1.2.2 Load All Solution

Based on the need to quickly analyze and compare functional images at multiple timepoints, a time-saving solution was developed to facilitate the automatic loading of all available SPECT image files for a given dose plan and options as shown in Figure 4.5.

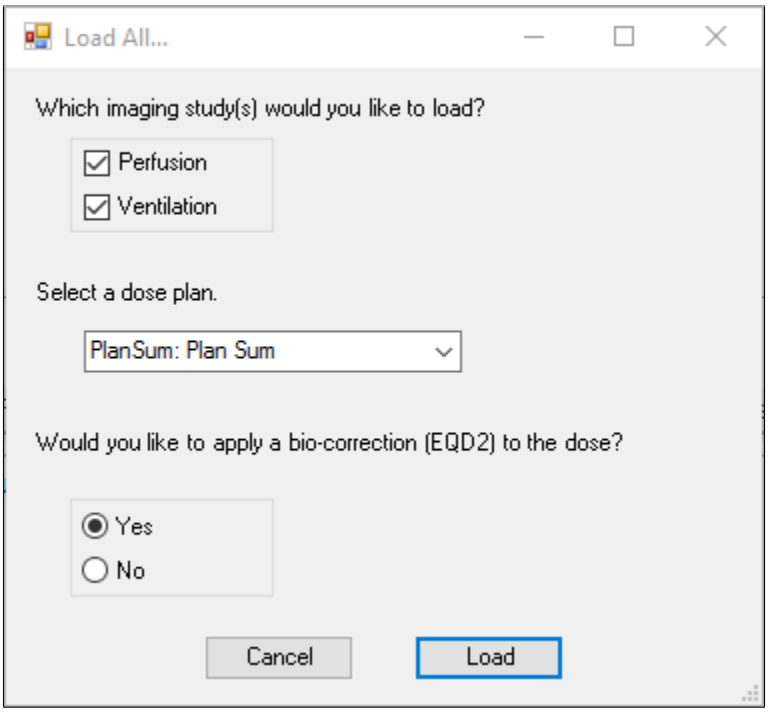

Figure 4.5: Load All interface window for selection of dose plan and load options.

Both the perfusion and ventilation check boxes are checked as a default. Furthermore, if there is only one dose plan or if a plan contains ”PlanSum”, it will automatically be selected. And

lastly, “Yes” is inherently chosen for the bio-correction option. Once button1 ”Load” is pushed, the LoadPlan method iterates through eight functional imaging options, including four imaging timepoints (Initial, 1Month, 3Month, and 1Year) and two functional modalities (PERF and VENT). If an imaging study with a name matching any of these eight options is found, that SPECT study name is combined with the dose plan name and bio-correction option in the LoadDosePlan.cs NameDictionary, which tracks the functional image-dose plan pairs that will be analyzed. The loaded image-dose pairs are reflected by the listView items shown at the top of Figure 4.6. In this particular example, the load all solution was executed and six perfusion and ventilation scans were found for the given patient ($2006040_VA004).

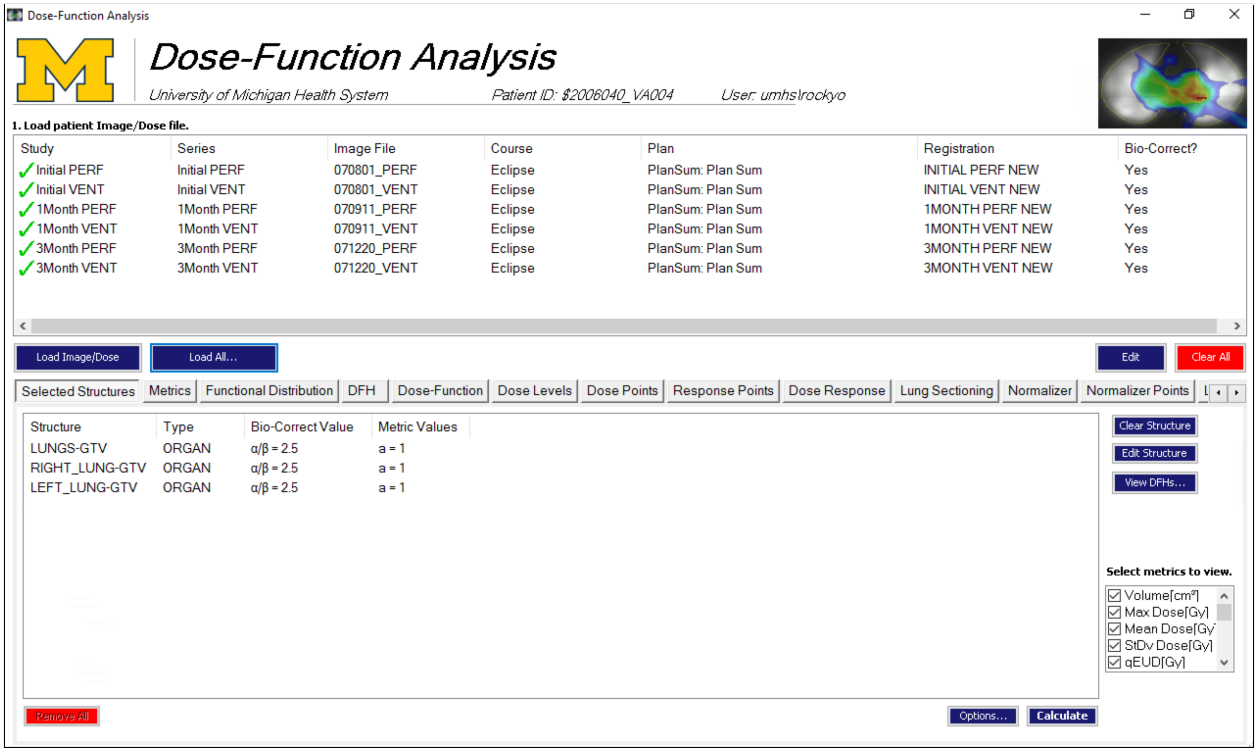

Figure 4.6: UserInterface window after using the Load All solution.

While the upper listView shows each loaded image/dose pair, the lower listView displays the analytics. A C# tabControl element is used to add the numerous analysis windows that are available. In the first panel ”Selected Structures”, three lung structures - Lungs-GTV, Right_Lung-GTV, and Left_Lung-GTV - are automatically loaded in preparation for analysis. Initially, more flexibility in structure selection was allowed, however, this analysis primarily focused on SPECT

distributions within the global lungs and each individual lung, so the three lung structures shown are automatically assumed to be the selection. A structure can still be cleared using the “Clear Structure” button. The α/β or a-value of each structure can also be edited using the ”Edit Structure” button as shown in Figure 4.7. Default values are set to $\alpha/\beta = 2.5$ and a=1.

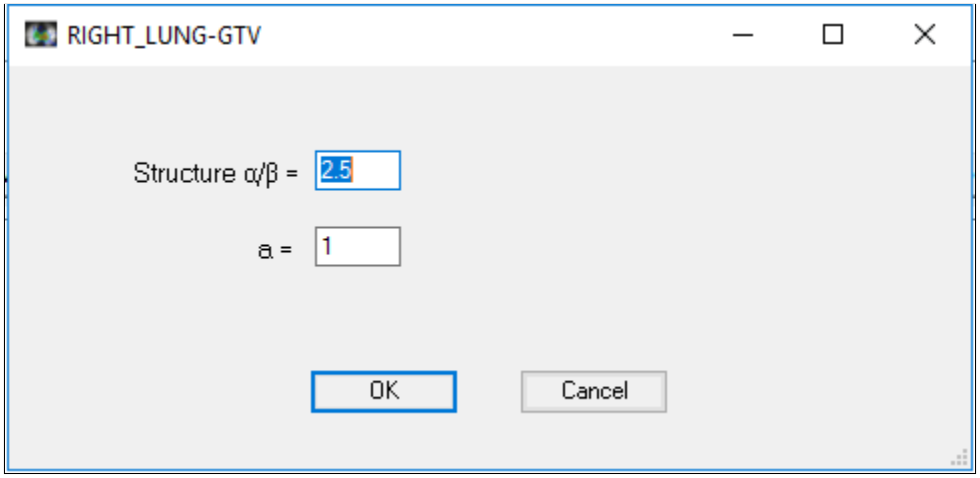

Figure 4.7: Interface window used to edit structure properties.

At this point, the rest of the analysis tabs are empty and the code is waiting for a user selection. The “Options...” button can be used to edit the normalization strategy of the analysis as shown in Figure 4.8.

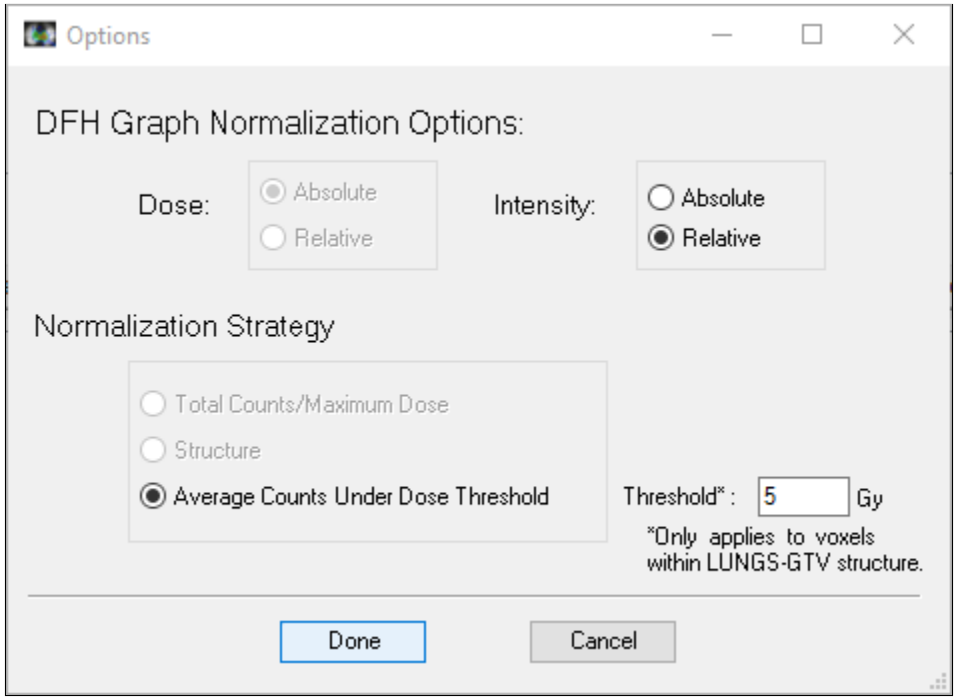

Figure 4.8: Interface window used to select normalization options.

Although normalization using total intensity counts or using a set structure are written in the code, these options are unavailable to selection for simplicity. Ultimately, the user is expected to select ”Calculate” or “View DFHs...”, either of which will initiate the DataProcess.cs method followed by the MetricAnalysis.cs method. These two classes perform the necessary processing and quantitative analysis required to analyze the combined dose-function data. Once the DataProcess and MetricAnalysis methods are complete. The user is prompted with a display box showing the total run time and is now free to explore the generated data.

4.2 Standalone Batch Analysis

Upon initiating the Dose-Function Analysis Batch code, the user is prompted with an interface, as shown in Figure 4.9, which establishes the data, metrics, and options that will be used in the analysis. The user is guided through a number of simple selections and can select the “Metric Options” button to edit the properties of the gEUD/gEUfD and the Vd/fVd variables (Figure 4.9B). As shown in Figure 4.9A, the “Run” button is disabled because a patient data file has not been

selected. Therefore, the user is required to load an input file through the "Select data file" button, which opens a dialog box to navigate the computer's various drives (Figure 4.9C). The specific input file used in this study to access the batch patient data can be found in Appendix A. Through this file, the patient's dose course/plan, CT study/image, and SPECT study name are provided to ensure the proper data is analyzed.

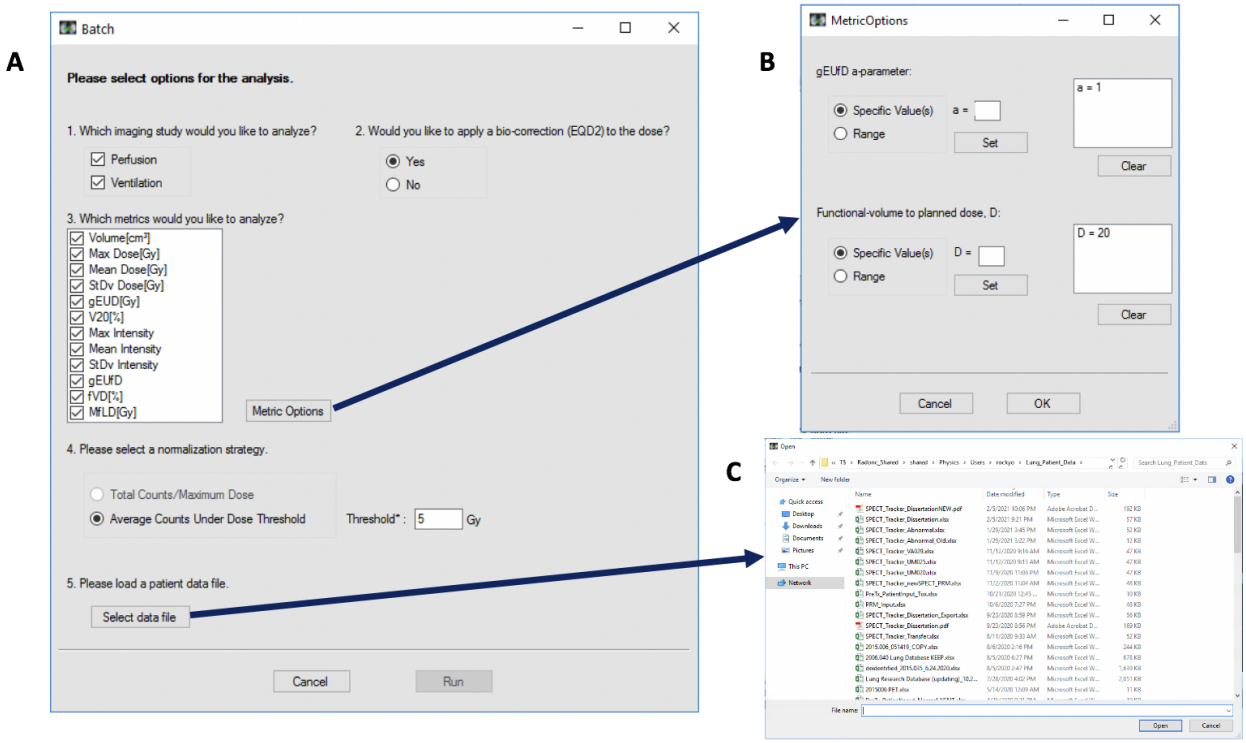

Figure 4.9: A) The interface prompting the user upon initiating the Dose-Function Analysis Batch code, B) the interface to customize the analyzed metrics, and C) the dialog box to select the desired patient input file.

The main output for the batch code includes files for the following data: 1) lookup.csv contains the generated dose-function metrics; 2) dataVQ.csv contains the combined VQ dose-function metrics; 3) [lungStructure]_Intensity.csv contains the average intensity within dose bins for each of the lung structures; 4) [lungStructure]_Function.csv contains the functional change and contributing voxels within each dose bin for each of the three lung structures; 5) dose, perfusion, ventilation, and CT values within each voxel for each patient. Files 3) and 4) also have a associated error file that quantifies the uncertainty in each dose bin estimate. As mentioned above, the three lung struc-

tures used in these analyses are the Lungs-GTV, Right_Lung-GTV, and the Left_Lung-GT clinical contours, either with or without an applied 4mm inner margin. It should be noted that if any of the files listed above are existing and open, an error will be thrown because these files are deleted and a new file is initiated immediately upon initiation of the batch code.

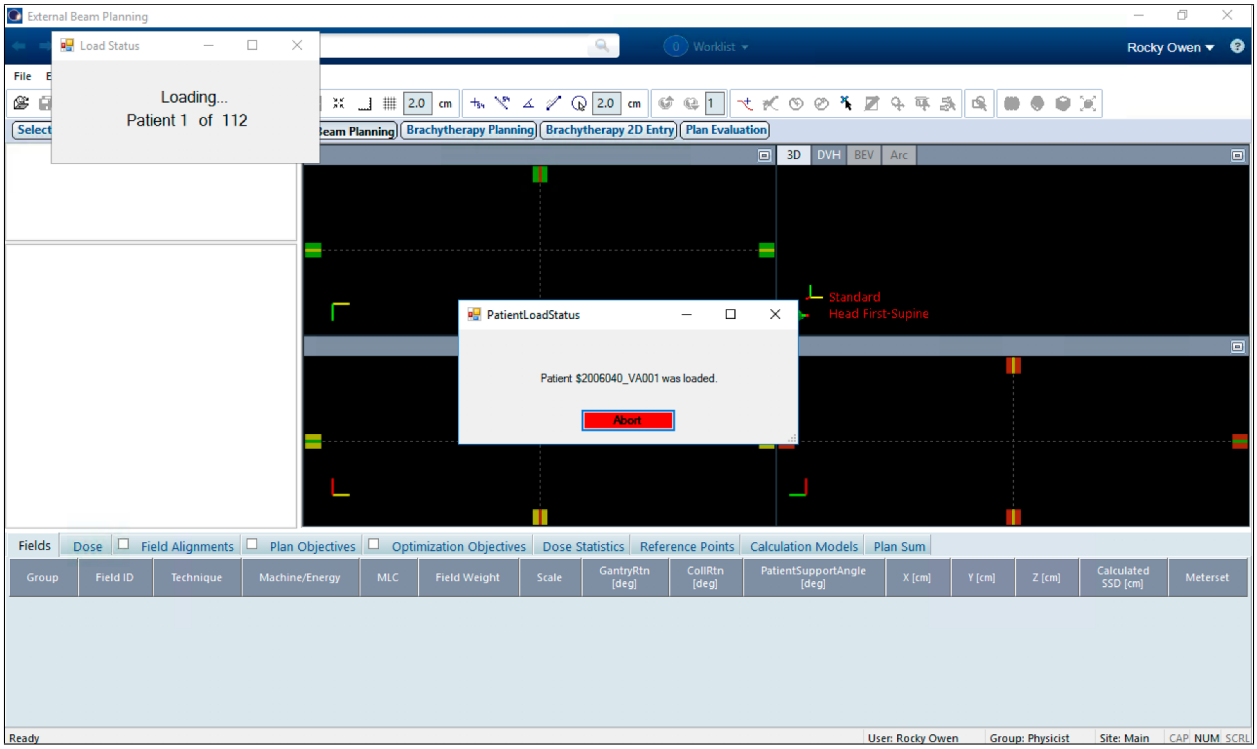

Figure 4.10: Example of the running batch code demonstrating the loaded patient and the current status of the analysis.

Once all the options are selected, an input file is loaded, and the "Run" button is executed, the batch code is initiated and the provided information is passed to the Program.cs shell, which manages the execution and memory for the iterations through each patient's data. The patient being currently analyzed is displayed by the "PatientLoadStatus" interface shown in Figure 4.10, which signifies the creation of a new VMS.TPS workspace with that loaded patient's data (similar to the initialization process described for a single patient in subsection 4.1.1). This "PatientLoadStatus" window stays active for 3 seconds prior to beginning analysis on the loaded patient in order to provide the opportunity to abort the code. A window in the top left corner is provided to track the overall progress of the batch analysis.

At this point, the underlying process that will used for accessing, processing, and quantifying of each patient's dose-function data are instantiated and these methods will be described briefly below.

4.3 Underlying Dose-Function Analysis Code Methodology

As previously mentioned, these methods are analogous for the plugin UI and standalone batch scripts. If the following process are performed under the plugin UI, the methods are only performed for the patient open in the Eclipse workspace, whereas when performed under the standalone batch script, these methods are iterated through for each patient provided in the input file, assuming the data can be properly accessed.

4.3.1 Accessing the Dose/Image Data

To begin, the Program.cs shell provides the patient's dose course, dose name, and selected bio-correction option to a class called LoadDosePlan.cs, with separate methods depending on whether the plan type is a single course or a plan sum. The LoadDosePlan class is essentially a method used to access the dose matrix, the maximum dose value, the number of fractions, and the associated structure set. Each of these objects are stored in public variables, and the code is returned to the Program.cs shell.

Next, a similar process is performed to access the functional imaging data through a class called LoadAllImages.cs. A new instance of this class is created for each of the four imaging timepoints, and within each timepoint, a string variable with the timepoint identifier (Initial, 1Month, 3Month, and 1Year) is combined with the functional modality identifier (PERF or VENT) to search whether a imaging study exists that matches the provided identifier. The imaging data is stored within Eclipse with the following hierarchy: Study / Series / Images. Thus, when a matching imaging study is found, the subsequent imaging series, image file, and associated registration are obtained based on the known downstream naming convention, i.e. "Initial PERF" would be the name for each of those downstream files, similar to that shown in Figure 4.4. The CT study, series, and

image variables are also accessed based on the data provided in the input file.

Subsequently, within each unique instance of the LoadAllImages class, the dose file, image file, dose-image registration, and the CT file are all passed to the DataProcess.cs method.

4.3.2 Dose/Image Data Processing

Although the dose and image files previously accessed are three-dimensional meshes, these files are in their current form are not spatially aligned and each has a different voxel resolution. In summary, the DataProcess class uses the manual rigid registration created in Eclipse and applies it to transform the image data to the coordinates of the dose data, such that the SPECT intensities and dose data are spatially-aligned. Both the dose data and SPECT intensities are then sampled at the center of each dose voxel, resulting in a dose-function martix with the same resolution as the dose data. The bio-correction, if selected, is also applied to the dose value at sampling.

UM020, AAA PLNSUM 12 - Perfusion Percent Error							
Structure	**Volume**	**Max Dose**	**Mean Dose**	**StDev Dose**	**Max Intensity**	**Mean Intensity**	**StDv Intensity**
LUNGS-GTV	0.000%	0.003%	0.091%	0.102%	0.747%	0.031%	0.789%
GTV_COMPOSITE	0.000%	0.003%	0.115%	4.537%	3.526%	1.336%	1.814%
RIGHT_LUNG	0.000%	0.127%	0.138%	0.162%	0.747%	0.189%	0.610%
LEFT_LUNG	0.002%	0.003%	0.192%	0.034%	0.789%	0.162%	0.949%
PTV_COMPOSITE	0.000%	0.003%	0.099%	1.710%	0.353%	0.196%	0.442%
HEART	0.000%	0.007%	0.797%	1.548%	7.648%	0.526%	0.143%
ESOPHAGUS	0.000%	0.007%	1.747%	0.381%	3.285%	0.886%	0.810%
CORD	0.000%	1.472%	0.768%	0.769%	1.000%	0.397%	2.505%

Figure 4.11: The relative difference between the sampled perfusion SPECT and dose data compared to the analogous values quoted in Eclipse.

UM020, AAA PLNSUM 12 - Ventilation Percent Error							
Structure	**Volume**	**Max Dose**	**Mean Dose**	**StDev Dose**	**Max Intensity**	**Mean Intensity**	**StDv Intensity**
LUNGS-GTV	0.000%	0.003%	0.091%	0.102%	3.903%	0.051%	1.049%
GTV_COMPOSIT	0.000%	0.003%	0.115%	4.537%	0.903%	2.538%	3.574%
RIGHT_LUNG	0.000%	0.127%	0.138%	0.162%	6.267%	0.122%	1.157%
LEFT_LUNG	0.002%	0.003%	0.192%	0.034%	3.086%	0.131%	0.867%
PTV_COMPOSIT	0.000%	0.003%	0.099%	1.710%	4.828%	0.178%	1.960%
HEART	0.000%	0.007%	0.797%	1.548%	4.828%	0.373%	3.566%
ESOPHAGUS	0.000%	0.007%	1.747%	0.381%	3.847%	2.775%	4.249%
CORD	0.000%	1.472%	0.768%	0.769%	1.111%	1.536%	3.028%

Figure 4.12: The relative difference between the sampled ventilation SPECT and dose data compared to the analogous values quoted in Eclipse.

The relative accuracy of the dose-function sampling method compared to the value given in Eclipse for an example patient is shown in Figure 4.11. The volume value is directly obtained

from the Eclipse API so the only difference are based on rounding the float. The sampled maximum and mean doses are shown to have $<1\%$ difference compared to the quoted Eclipse value in the primary structures of interest. These difference arise because Eclipse performs an 8-point sampling (one sample at each of the voxels vertices) of the calculated dose mesh, whereas the Dose Function Analysis code only samples the value at the center of the voxel. This also causes a slight difference at the edge of the structures where voxels may be partial within and partially outside of the contour. In Eclipse, the vertices within the structure are included, but in this code, only voxels with the center of the voxel within the contour are included in the calculation. For these reasons, the standard deviation of the dose and intensity values, which are also upsampled at a finer resolution than the original image file, present with slightly higher differences. These difference are clearly exacerbated in structures with smaller volumes as well. Similar agreements were observed for the sampled ventilation intensities shown in Figure 4.12, however, due to the presence of saturation artifacts that cause a high intensity gradient, the max intensity and standard deviation in the ventilation samples are increased, which is the same reason the error in the dose standard deviation is increased in the GTV. This same high gradient causes a downstream increase in the mean intensity error in the smaller volume strucutures, i.e. GTV, esophagus, and cord. Overall, the agreement was deemed acceptable, especially in the lung structures.

To reduce the runtime, a box around the contour is created prior to sampling. Therefore, because the voxels are sampled based on the resolution of the dose mesh, which in turn is based on the resolution of the treatment planning CT mesh, the sample dose-function matrices have a size equal to the size of the box divided by the dose resolution. Furthermore, the data matrices, including one for dose, SPECT, and CT values, are generated, within each lung contour such that a maximum, mean, and standard deviation can be calculated within the right lung, the left lung, and the global lung (which is a union of the right and left lung data). The voxels containing saturation artifacts were then cleansed from these data matrices.

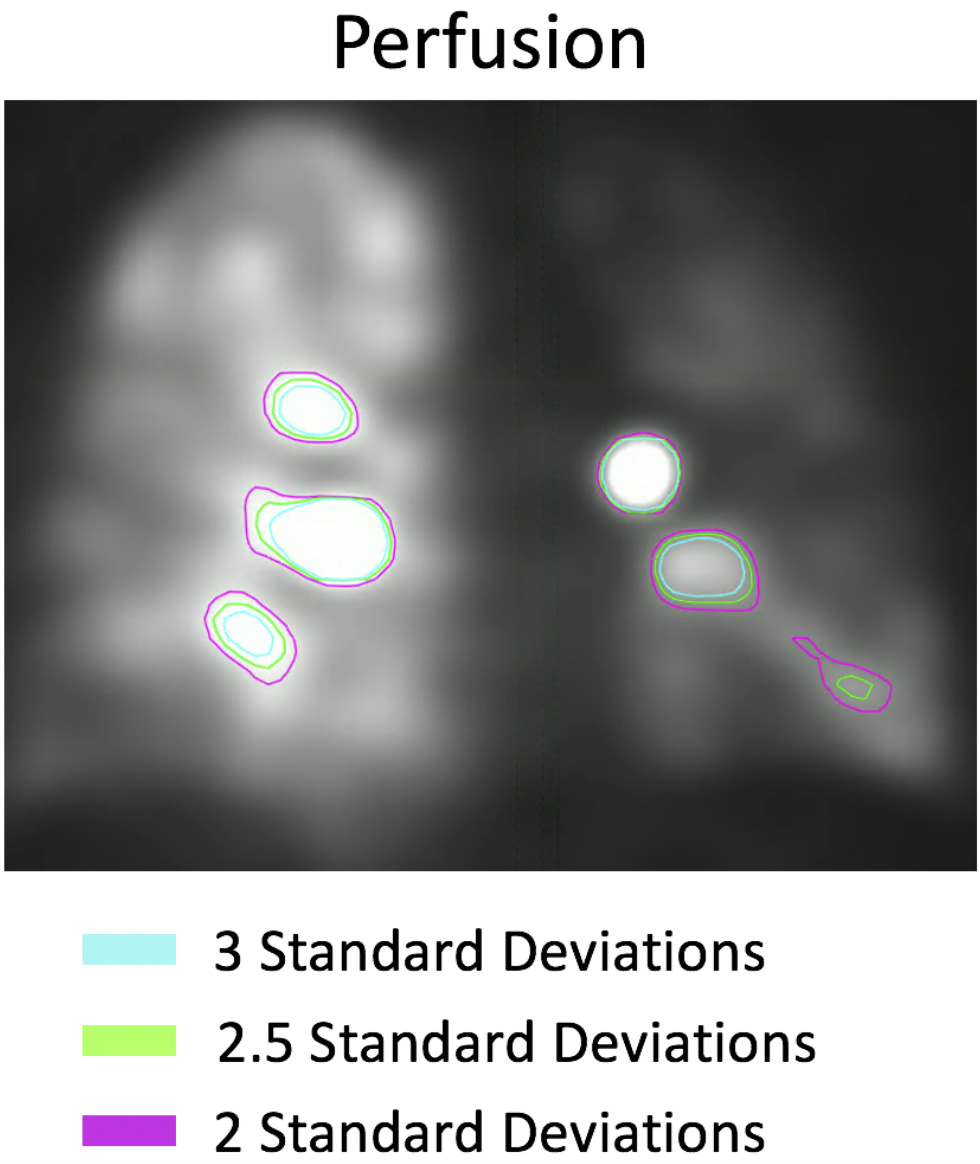

Figure 4.13: Perfusion artifacts in an example patient using 2 (cyan), 2.5 (green), and 3 (magenta) standard deviations above the mean intensity as the saturation cleansing cutoff.

4.3.2.1 Artifact Cleansing Code

Patients with abnormally high absolute intensities, due to large saturation artifacts, can cause a problem for the high-functioning categorization given that the artifacts have not yet been removed. Therefore, using the maximum, mean and standard deviation values that were just calculated, voxels were cleansed based on their deviation from the expected distribution.

To begin this process, a preliminary upper bound was selected based on whichever value was

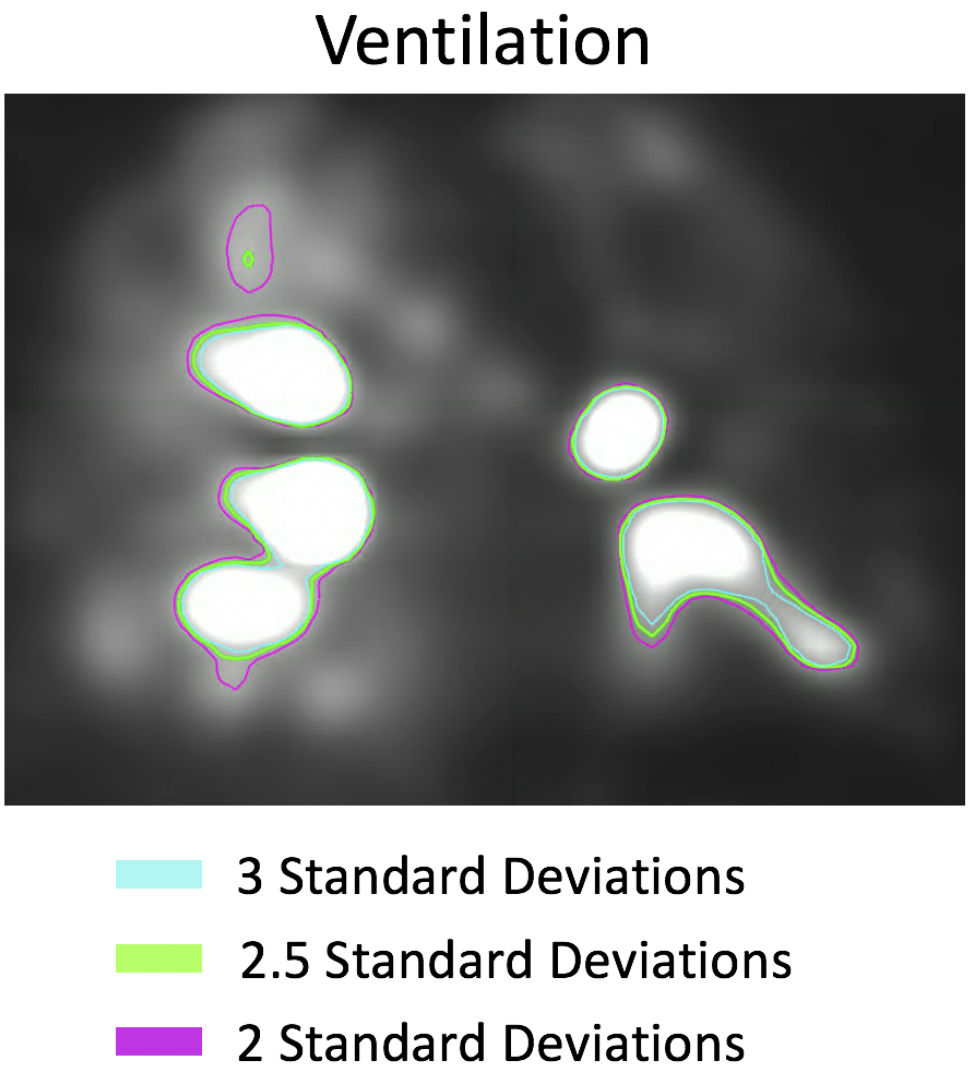

Figure 4.14: Ventilation artifacts in an example patient using 2 (cyan), 2.5 (green), and 3 (magenta) standard deviations above the mean intensity as the saturation cleansing cutoff.

lower: the intensity value equal to 70% of the maximum intensity or hard cutoffs of 1500 for perfusion or 750 for ventilation. Furthermore, a preliminary lower bound of 100 was also selected. Using these initial cutoffs, a new mean intensity and standard deviation were calculated in each lung structure. The final saturation cutoff value was determined by excluding any voxel with an intensity $>$3 standard deviations above the new calculated mean intensity. However, a minimum bound of 350 was implemented for cases in which the ventilation cutoff intensity was calculated to be less than this value.

While this strategy was implemented to reduce subjectiveness, it is not perfect and may create issues in the high intensity regions if portions of the artifact are not removed. As such, it is possible to increase the aggressiveness of the cleansing strategy by reducing the number of standard deviations used to determine the saturation cutoff. By more aggressively cleansing the image, the edge of the saturation artifacts can better be caught, but it may come at the cost of removing other voxels that are not clear artifacts, which presents the question of what is truly a saturation artifact and what is not. This trade-off is explicitly demonstrated by Figure 4.13 and Figure 4.14, which shows the contoured artifacts using various standard deviations for perfusion and ventilation cleansing, respectively. Previous studies have typically employed a manual removal of these saturation artifacts, which may introduce a subjective bias. However, it is suggested that machine learning techniques may be able to help implement a more consistent approach based on clinical guidance. Either way, a robust strategy to remove saturation artifacts is a necessary and clear way to improve the true quantification of SPECT images.

Following this process to determine the saturation cutoff, any voxels with intensity values above the set threshold are removed from the analysis.

4.3.2.2 Intensity Normalization

Using the new cleansed data, the individual lung structure with the higher mean dose is identified as the contralateral lung. Based on the need to normalize longitudinal and interpatient intensity values, a normalization value was calculated to represent the average intensity value of normal lung. And given that the contralateral lung has less tumor burden and receives less dose, these intensity values were considered relatively stable. As such, the normalization value in this study was determined as the average intensity in the contralateral lung for voxels with normal lung function, i.e. $>15\%$ of the maximum intensity, that received <5 Gy. While this value was generally used to represent normal-functioning lung, this may be a limitation of functional lung quantification that could be further improved through test-retest studies.

The longitudinal voxelwise distribution of the intensity values in this normalizer region for an

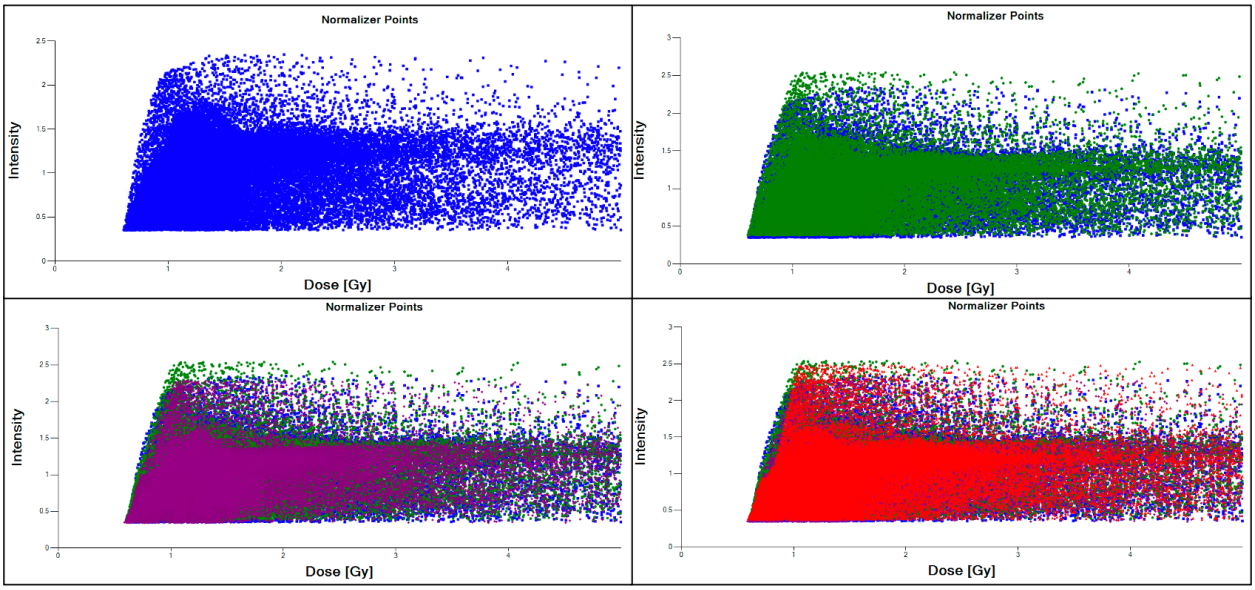

Figure 4.15: Voxelwise perfusion intensity values within the normalizer region for an example patient at baseline (blue), mid-treatment (green), 3-month post-treatment (purple), and 1-year post-treatment (red).

example patient are shown Figure 4.15, which demonstrates a consistent distribution of intensity values for this given patient. The accumulated intensity histogram and average distribution binned by dose for the same patient are shown in Figure 4.16. These figures shown good agreement and suggest a stable longitudinal distribution, which serves as a reference point of dose-dependent changes and interpatient comparisons. To reiterate, the average intensity value in this region is used as the normalization value for all other intensity points within the given image, and thus, this normalization value is equal to a normalized intensity of 1.0.

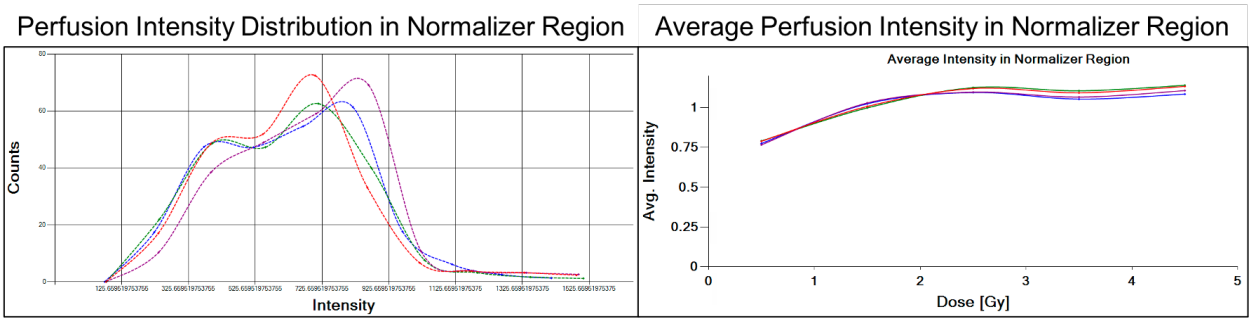

Figure 4.16: Perfusion intensity histogram and average values binned by dose within the normalizer region for an example patient at baseline (blue), mid-treatment (green), 3-month post-treatment (purple), and 1-year post-treatment (red).

After each voxel intensity is normalized, the rest of the DataProcess class is used to bin, store, and export the voxelwise values. Upon completion, the data is passed to the MetricAnalysis.cs method.

4.3.3 Metric Analysis

The MetricAnalysis class then performs the calculations to produce the dose-function metrics. These voxelwise calculations are performed for each of the three main lung structures, as well as in the regional (upper, middle, and lower) lung sections. The CsvWrite.cs method then exports these metrics to the lookup.csv file for external analysis.

A separate class FunctionalChange also calculates the longitudinal average intensity and voxelwise change, binned by dose, and accumulates a tally of the total functional reduction. The FunctionalWrite.cs method then exports this data to the appropriate .csv files. ErrorPropogation.cs and ErrorWrite.cs are used to calculate and export the uncertainty in the functional change and average intensity estimates. PerfVentAnalysis.cs and PerfVentWrite.csv calculate and export the combined perfusion and ventilation data.

Once these processes are completed for a given functional image, the rest of the available SPECT scans are iterated through using the same methods, and ultimately, all imaging files and all patients are analyzed.

4.4 Conclusion

A script was written that interfaces with a commercial TPS via an API. The script executes a program that performs dose-functional volume analyses. Written in C#, the script reads the dose grid and correlates it with image data on a voxel-by-voxel basis through API extensions that can access registration transforms. A user interface was designed through WinForms to input parameters and display results. To test the performance of this program, image- and dose-based metrics computed from perfusion SPECT images aligned to the treatment planning CT were generated, validated, and compared.

The integration of image analysis information was successfully implemented as a plug-in to a commercial TPS. Perfusion SPECT images were used to validate the calculation and display of image-based metrics as well as dose-intensity metrics and histograms for defined structures on the treatment planning CT. Various biological dose correction models, custom image-based metrics, dose-intensity computations, and dose-intensity histograms were applied to analyze the image-dose profile.

It is possible to add image analysis features to commercial TPSs through custom scripting applications. A tool was developed to enable the evaluation of image-intensity-based metrics in the context of functional targeting and avoidance. In addition to providing dose-intensity metrics and histograms that can be easily extracted from a plan database and correlated with outcomes, the system can also be extended to a plug-in optimization system, which can directly use the computed metrics for optimization of post-treatment tumor or normal tissue response models.

The full C# code for both the plugin UI (https://github.com/rockyowen5/DoseFunctionAnalysis_UI.git) and the standalone batch (https://github.com/rockyowen5/DoseFunctionAnalysis_Batch) applications are available on GitHub.

CHAPTER V

Modeling Patient-Specific Dose-Function Response

5.1 Purpose

Functional-guided RT has the potential to limit damage to normal tissue and reduce toxicity. And yet, while functional imaging modalities have continued to improve, a limited understanding of the functional response to radiation and its application to personalized RT has hindered clinical implementation. The purpose of this chapter was to retrospectively model the longitudinal dose-function response in non-small cell lung cancer patients treated with RT in order to better characterize the expected functional damage in future, unknown patients.

5.2 Introduction

Logistic models have classically been used to describe dose-effect relations for cell survival. In 1994, Boersma et al first proposed using a logistic model to describe changes in vascular subunits within the lung [34]. Due to the observed high variation in patient-to-patient dose-response, Marks et al. used a voxel-weighted average to determine composite perfusion loss [1]. These seminal works provided the foundation to longitudinally quantify functional lung using V/Q SPECT/CT images [4, 5], and the basis of these methodologies has been extensively applied to characterize the dose-function response for various timepoints, treatments, and regions of the lung [35–40] (as discussed in section 2.2). While the exact modeling methodologies vary amongst these studies,

the most common approach to quantify the dose-function response has been to average functional reduction across the population within numerous dose bins and subsequently apply a linear or logistic fit depending on the shape of the perceived data. However, this approach has the potential to induce inconsistencies in the reported dose-function response models.

While this work quantified the population-average dose-function response to compare to previous models and gain preliminary insights, ultimately, a patient-specific mixed-effects logistic model was applied to each individual patient's dose-function response. These generated patient-specific model parameters were then averaged to create a population-level logistic dose-response model. Using these methods a significant longitudinal decrease in lung function was observed after RT by analyzing the voxelwise change in normalized perfusion intensity. Differential treatment responses based on the functional status of the voxel at baseline suggest that initially higher-functioning voxels are damaged at a higher rate than lower-functioning voxels. As such, the generated population-level dose-function response models were derived from individual patient assessment to better represent the expected voxelwise reduction in function, and the associated uncertainty, for an unknown patient receiving conventionally fractionated RT or stereotactic body RT. This type of patient-specific modeling approach can be applied broadly to other functional response analyses to better capture intrapatient dependencies and characterize personalized functional damage.

5.3 Study Population

A total of 81 patients with histologically verified NSCLC were enrolled in an institutional review board-approved study and retrospectively analyzed. Written informed consent was obtained from all patients. Patients were treated with conventionally fractionated 3-dimensional conformal RT, with (n = 47) or without (n = 13) concurrent chemotherapy, or with SBRT (n = 21). A summary of the patient, disease, and treatment characteristics of the cohort is presented in Table 5.1.

Patient Characteristics

	Conventional RT Cohort (n = 60)	SBRT Cohort (n = 21)
V/Q SPECT Scans Available		
Baseline	60	21
Mid-Tx	54	20
3Month Post-Tx	37	14
1Year Post-Tx	19	7
Age [years]		
Median	65	72
Range	39 - 85	53 - 83
Gender		
Male	47	13
Female	13	8
Volume (Lungs-GTV) [cc]		
Median	3842	3901
Range	1837 - 9540	1808 - 6489
Mean Dose (Lungs-GTV)		
Median	13.1	7.4
Range	3.0 – 21.2	3.7 – 16.2

Abbreviations: 1Year Post-Tx = 1 year post-treatment; 3Month Post-Tx = 3 months post-treatment; GTV = gross tumor volume; Mid-Tx = midcourse treatment; SBRT = stereotactic body radiation therapy; SPECT = single-photon emission computed tomography.

Table 5.1: Patient characteristics for the 2006.040 cohort that was used in the dose-function response modeling study.

5.4 SPECT Imaging

V/Q SPECT scans were acquired and analyzed as described in chapter III. In summary, SPECT images were rigidly registered to the treatment planning CT and intensity values were normalized using the average intensity in the low-dose, normal-functioning region of the contralateral lung as shown in Equation 5.1.

$$f_i^{\mathbb{N}} = \frac{f_i}{\mathbb{N}} \tag{5.1}$$

where $f_i^{\mathbb{N}}$ is the normalized V/Q intensity in the ith voxel and $\mathbb{N}$ is the normalization factor (calculated in Equation 3.1). Saturation artifacts were cleansed by excluding any voxel with intensity greater than three standard deviations above the mean intensity of normal-functioning lung as de-

scribed in chapter III.

5.5 Quantifying Lung Function and Dose-Response in Individual Patients

In this study, either normalized perfusion or ventilation intensity was applied directly as a surrogate for local lung function. As such, perfusion and ventilation were analyzed separately, with a primary focus on using perfusion intensity due to its enhanced stability over ventilation intensity. To illustrate this process, an example patient (UM020) was chosen to represent the expected functional distribution and resulting dose-function response in a "normal" patient that did not incur Grade 2+ RILT. Alternatively, the two grade 5 RILT patients (UM025 & VA029) will also be examined individually to demonstrate the functional distribution and dose-response in patients with the worst outcomes, i.e. death directly related to RT. Subsequently, the results from analyzing the total cohort functional intensities and dose-function responses will be presented.

5.5.1 Example "Normal" Patient UM020

As mentioned, example patient UM020 was chosen to represent a patient with a mostly homogeneous distribution of lung function, who ultimately did not incur Grade 2+ RILT following treatment. For context, patient UM020 was a 56 year old Caucasian male who was a current smoker at the time of RT. This patient was diagnosed with stage III (T stage=3; N stage=3) NSCLC with a tumor size of 80.6 cubic centimeters and was determined to have a Karnofsky Performance Status (KPS) of 90 prior to treatment. According to the PFT results, example patient UM020 exhibited normal spirometry but with mild hyperinflation and a mildly decreased DLCO. This patient was treated with conventionally-fractionated RT to a prescribed dose of 55 Gy and was also treated with concurrent chemotherapy. The delivered dose metrics for this patient are listed in Table 5.2, which demonstrate a relatively low global mean lung dose (10.8 Gy) and V20 (18.03%) with hot spots in the upper left lung. Ultimately, this patient was determined to have Grade 1 clinical fibrosis at the end of the RT course and was known to still be living 5 years after the completion of RT.

5.5.1.1 Quantifying Perfusion for Example Patient UM020

Dosimetric Parameters for Example Patient UM020

Patient	Structure	Volume	Max Dose [Gy]	Mean Dose [Gy]	Std. Dev. Dose [Gy]	V20 [%]	fV20 [%]	iV20 [%]	Upper Avg. Dose† [Gy]	Middle Avg. Dose† [Gy]	Lower Avg. Dose† [Gy]
UM020	LUNGS-GTV	3593.52	56.04	10.80	10.98	18.03	19.26	1.06	16.29	12.15	0.89
	RIGHT_LUNG-GTV	1986.16	49.50	8.80	8.52	10.45	11.37	1.05	9.03	12.09	0.95
	LEFT_LUNG-GTV	1607.05	56.04	13.27	12.99	27.40	28.56	1.06	24.37	12.22	0.80

†Regional lung segments defined as: Upper above the carina; Lower below inferior pulmonary vein; Middle between the two
V20 = Volume of lung structure receiving ≥20 Gy, as a percent of total lung structure volume
fV20 = functional intensity receiving ≥20 Gy, as a percent of total functional intensity
iV20 = average functional intensity receiving ≥20 Gy in arbitrary units

Table 5.2: Delivered dose metrics for example patient UM020.

Figure 5.1: A qualitative example of patient UM020 demonstrating the dose-function response during and after radiation treatment. Planned dose >30 Gy is overlaid on the pre-treatment perfusion scan and the red contours are included to show areas of observed perfusion reduction both in-field and out-of-field.

The perfusion scans in the global lung at the first three imaging timepoints for patient UM020 are shown in Figure 5.1. Although these single-slice images are of limited value to understand the true functional distribution in this patient, it can be qualitatively observed that there is a fairly homogeneous distribution of perfusion at the pre- and mid-treatment timepoints. Whereas at the 3-months post-treatment timepoint, there are noticeable functional changes that can be observed both in and out of the high dose field (signified by the red outlines).

To assess the distribution of functional intensity at each imaging timepoint, histograms were plotted by binning the relative intensity, i.e. functional intensity divided by the maximum intensity,

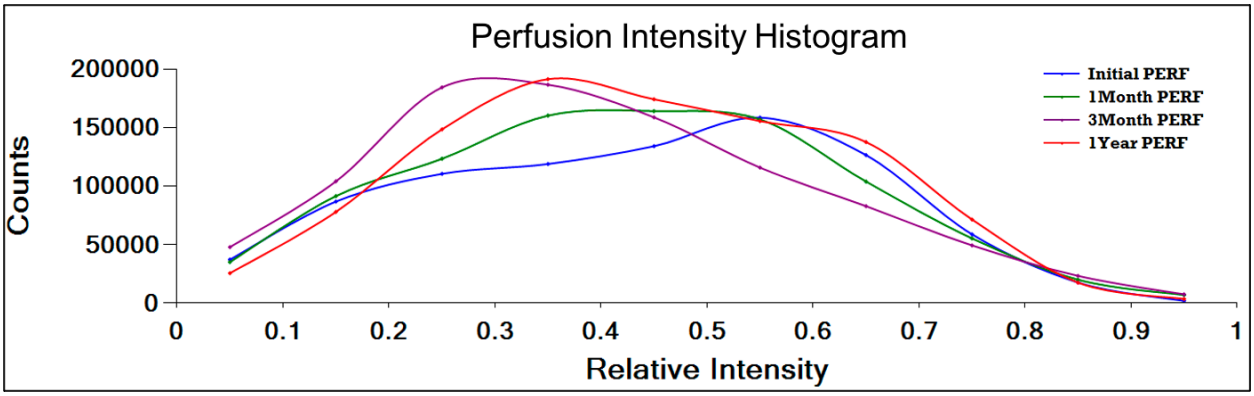

Figure 5.2: Perfusion intensity histograms in the global lungs at pre-treatment (blue), mid-treatment (green), 3-months post-treatment (purple), and 1-year post-treatment (red).

using a bin width of 0.1 arbitrary intensity units. Although the resolution in these histograms is limited, it appears that the initial perfusion scan demonstrates a fairly normal distribution with a slight skew towards the higher-intensity values. As the RT course progresses, a shift toward the lower-intensity values becomes evident, albeit with a slight increase in intensity value from the 3-month to 1-year timepoint, possibly suggesting a slight recovery.

Perfusion Parameters for Example Patient UM020

Structure	Timepoint	Max Intensity	Mean Intensity	Std. Dev. Intensity	Total Intensity	LF [%]	F [%]	HF [%]	Upper Avg. Intensity†	Middle Avg. Intensity†	Lower Avg. Intensity†
LUNGS-GTV	Initial PERF	2.25	0.99	0.45	189749.19	8.92	81.85	9.21	0.94	1.01	1.01
	1Month PERF	2.08	0.90	0.41	171273.79	8.30	82.49	8.98	0.83	0.89	0.99
	3Month PERF	1.99	0.79	0.39	151144.10	9.28	82.08	8.36	0.78	0.75	0.92
	1Year PERF	1.91	0.84	0.36	160960.42	5.90	84.81	9.23	0.81	0.78	1.05
RIGHT_LUNG-GTV	Initial PERF	2.25	0.97	0.44	102621.83	9.04	83.41	7.53	0.96	0.97	0.98
	1Month PERF	2.08	0.86	0.41	90865.21	9.65	81.73	8.21	0.77	0.84	1.01
	3Month PERF	1.99	0.80	0.42	84595.01	10.15	79.58	9.99	0.85	0.73	0.92
	1Year PERF	1.91	0.85	0.36	89511.73	5.70	84.44	9.79	0.92	0.74	1.02
LEFT_LUNG-GTV	Initial PERF	2.25	1.02	0.46	87127.36	8.78	79.92	11.30	0.91	1.06	1.05
	1Month PERF	2.08	0.94	0.39	80408.59	6.63	83.43	9.93	0.89	0.95	0.96
	3Month PERF	1.99	0.78	0.36	66549.09	8.20	85.17	6.35	0.70	0.77	0.91
	1Year PERF	1.91	0.83	0.35	71448.69	6.13	85.27	8.55	0.69	0.82	1.09

†Regional lung segments defined as: Upper above the carina; Lower below inferior pulmonary vein; Middle between the two
LF = low-function volume, as a percent of total lung structure volume
F = normal-function volume, as a percent of total lung structure volume
HF = high-function volume, as a percent of total lung structure volume

Table 5.3: Quantified perfusion SPECT metrics for example patient UM020.

Quantitatively, these trends of a homogeneous distribution of lung function prior to RT and longitudinally decreasing lung function following RT are also observed in the perfusion SPECT metrics shown in Table 5.3. The pre-RT mean intensity for this patient in both lungs is near 1.0,

which is the average value of normal-functioning lung, and steadily decreases during treatment and 3-months following RT but appears to slightly improve at the 1-year post-RT timepoint. The functional lung categorizations metrics also appear to follow this same progression. It can also be observed that although the upper lung initially did appear to be slightly lower in intensity, the regional average intensities at baseline across both lungs are quite consistent.

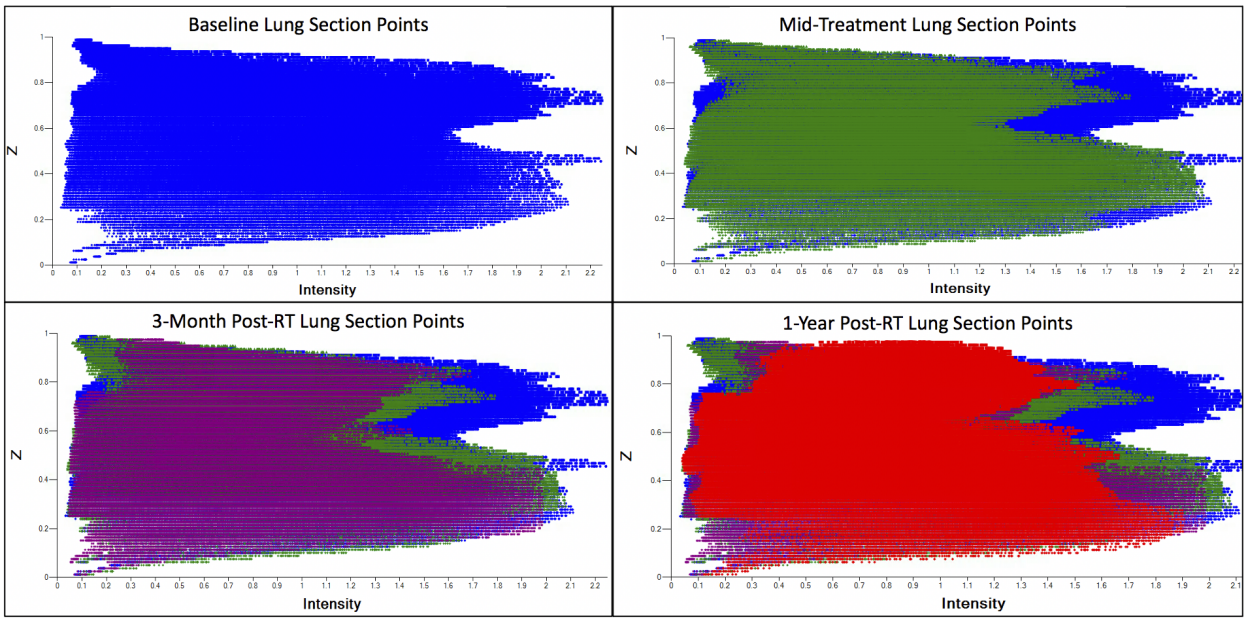

Figure 5.3: Global lungs voxelwise, absolute perfusion intensity plotted versus the voxel's relative location on the z-axis for pre-treatment (blue), mid-treatment (green), 3-months post-treatment (purple), and 1-year post-treatment (red). The z-axis represents the axial axis such that larger values of z indicate superior portions of the lung and lower values of z indicate inferior portions of the lung.

While the spatial component of the functional distributions can be difficult to incorporate quantitatively in metrics and plots, an attempt was made to visually demonstrate this dynamic in regards to the functional intensity distribution within the upper, middle, and lower lung by plotting the each voxel's absolute intensity versus the voxel's relative location on the z-axis. This plot, at each imaging timepoint, for patient UM020 is shown in Figure 5.3. In these plots, the most inferior part (lowest point on the z-axis) of the lung contour is given the value of 0, while the most superior part (highest point on the z-axis) of the lung contour is given a value of 1. Each voxel's location on the z-axis is then calculated by dividing the length to the given voxel from the bottom of the lung con-

tour by the total height of the lung contour. Although these values do not directly correlate to the regional lung segments, which were contoured based on anatomical markers, the plots are capable of providing some locational information. As such, it can be inferred that most of the functional damage in this patient occurred in the upper half of the lung until the 1-year post-RT timepoint, when a reduction in the highest intensities is observed in the inferior portion of the lungs.

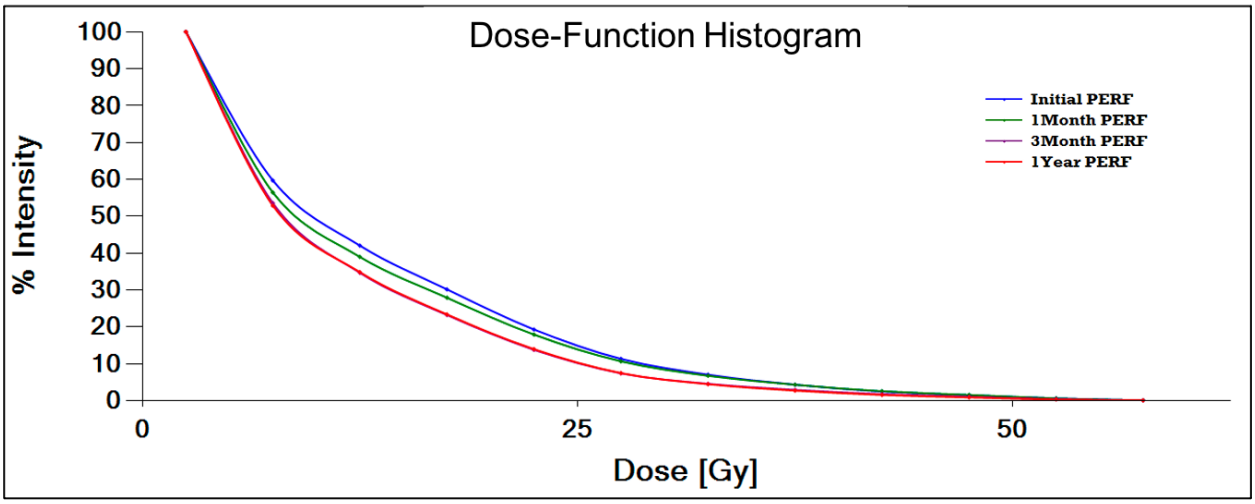

Figure 5.4: Perfusion dose-function histograms in the global lungs at pre-treatment (blue), mid-treatment (green), 3-months post-treatment (purple), and 1-year post-treatment (red).

In most previous studies analyzing the dose-function effect in the lung, a DFH has been employed to measure the interaction between functional lung and delivered dose. The basis for the DFH plots is to demonstrate the cumulative percent of functional intensity that is receiving a given dose value because the more functional intensity receiving a higher dose is theoretically worse for the patient. The DFH plot is also the basis for the fV20 metric, which is equal to the y-axis value where x-axis(Dose)=20 Gy on the DFH curve. However, because the cumulative percent of functional lung is plotted, there is a very limited resolution regarding the interaction between functional intensity and the delivered dose, especially when analyzing the global lung in patients with a homogeneous distribution of intensity. The longitudinal DFHs for patient UM020 is shown in Figure 5.4, which demonstrates only a slight change in the histograms despite a clear reduction in lung function in the high dose area in Figure 5.1. Again, this lack of resolution is due to the fact that the majority of functional volume received no dose or a relatively low dose, such that only a

slight change in the overall cumulative intensity is observed in the higher dose bins.

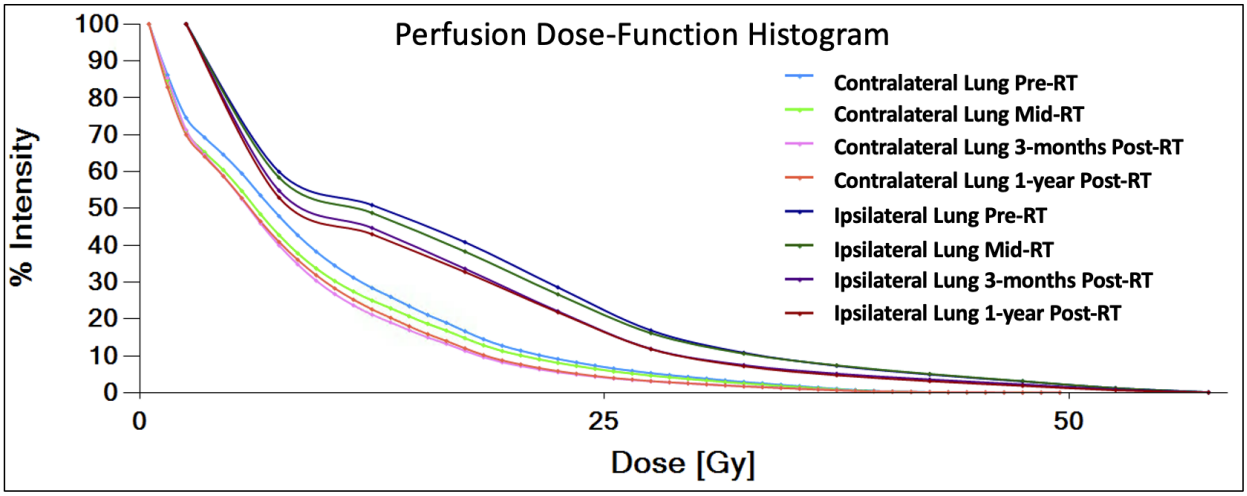

Figure 5.5: Perfusion dose-function histograms in the ipsilateral and contralateral lungs at pre-treatment, mid-treatment, 3-months post-treatment, and 1-year post-treatment.

However, if the DFH is separated into the ipsilateral and contralateral lung curves, a higher resolution is available as shown in Figure 5.5. Based on these curves, it is clear the left lung (the ipsilateral lung) received more dose to a larger fraction of the functional intensity than the right lung (the contralateral lung). Hence, the larger fV20 as shown in Table 5.2.

An alternative approach to quantify the interaction between functional lung and delivered dose is to plot the average normalized perfusion intensity as a function of delivered dose. To accomplish this, a simple average of the functional intensity within each dose bin is calculated as shown in Equation 5.2.

$$\overline{f^{\mathbb{N}}_{t,j,d}} = \frac{\sum_{i=1}^{n_{j,d}} f^{\mathbb{N}}_{t,j,i}}{n_{j,d}} \tag{5.2}$$

where $f^{\mathbb{N}}_{t,j,i}$ is the normalized intensity at timepoint t for patient j in dose bin d and $n_{i,d}$ is the number of voxels in dose bin d.

As such, the perfusion intensity at each imaging timepoint, i.e. the perfusion progression, was quantified for example patient UM020 and is shown in Figure 5.6. For reference, a normalized functional intensity of 1.0 represents the average functional intensity within the normal lung and

is equal to the normalization factor.

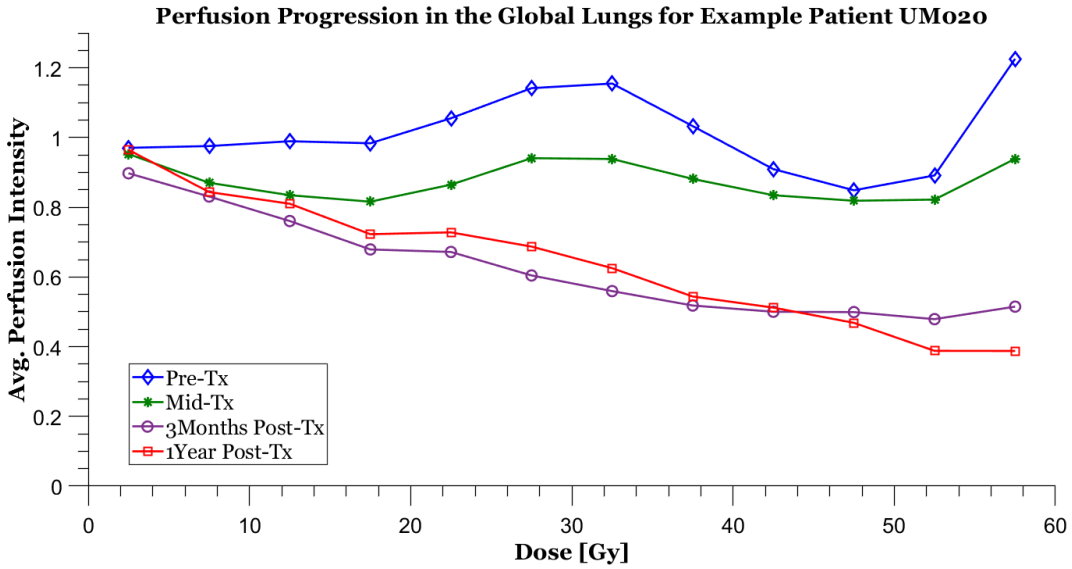

Figure 5.6: Quantitative assessment of the average perfusion intensity in the global lungs binned by dose at each imaging timepoint: prior to RT (blue diamonds), midway through the RT course (green asterisks), 3-months after RT completion (purple circles), and 1-year after RT completion (red squares).

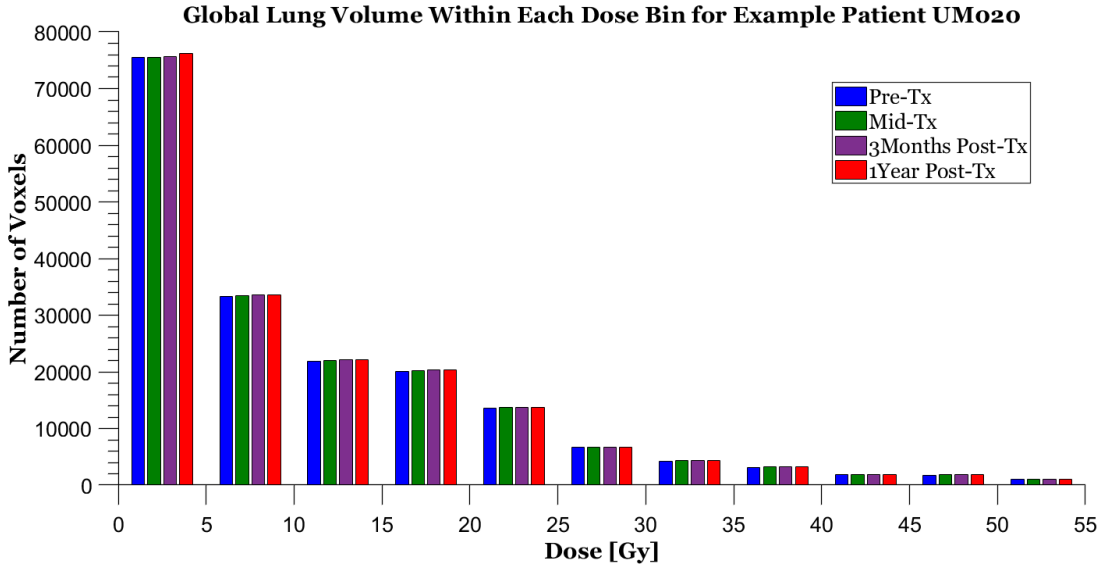

Figure 5.7: Number of voxels in the global lungs contributing within each dose bin for example patient UM020.

A couple points to note in Figure 5.6: 1) 5 Gy dose bins were used to average the functional intensity and the data points were plotted at the center of each dose bin; 2) The uncertainties were

not plotted in these curves, but there are less voxels in the higher dose bins, which contributes to the higher uncertainty and more fluctuation in those regions (the distribution of global lung voxels within these dose bins is shown in Figure 5.7, where the slight, longitudinal variation in the number of voxels in each dose bin is caused by either the removal of saturation artifacts that changes at each timepoint or differences in the rigid registration that translates voxels between the 5 Gy dose thresholds); 3) While the average functional intensity in the 0-5 Gy dose appears quite consistent, there is a slight offset that is observed at the 3-months post-RT timepoint. As shown in Figure 5.8B, the dose-perfusion intensity distribution exhibits good agreement in the normalizer region, which may suggest a good normalization and registration in this region. However, it is difficult to truly decipher whether this deviation is a true functional difference or an artifact of the normalization and registration processes.

From this example "normal" patient, it is observed that at pre-treatment in the 0-20 Gy dose bins there is a fairly stable functional intensity in the global lungs that approaches 1.0. However, there is clearly more undulation in the higher dose bins, which represents a splotchy pattern of intensity deposition. Specifically, the hot spots observed in the upper lung regions in Figure 5.1 are likely responsible for the increased average intensity in the pre-treatment curve that is centered around the 30 Gy dose bin, especially given the increased density in the high dose intensity ($\sim$1.5) shown by the red square in Figure 5.9. At mid-treatment, a slight but distinct reduction in perfusion is observed in the quantitative assessment that is not particularly noticeable through qualitative evaluation. Finally, at both post-RT timepoints, a significant reduction in lung function is observed across nearly all dose bins.

In order to provide a higher resolution regarding the distribution of functional intensity in relation to the delivered dose, each individual lung, i.e. the ipsilateral and contralateral lungs, were plotted separately as shown in Figure 5.10. Because NSCLC tumors are often primarily located in one lung, the dose in these cases is also mainly confined to the ipsilateral lung. Due to this potential large inequity in dose between the individual lungs, the contralateral lung plots are plotted using dose bins of 1 Gy instead of 5 Gy that are used in the global lungs and ipsilateral lung.

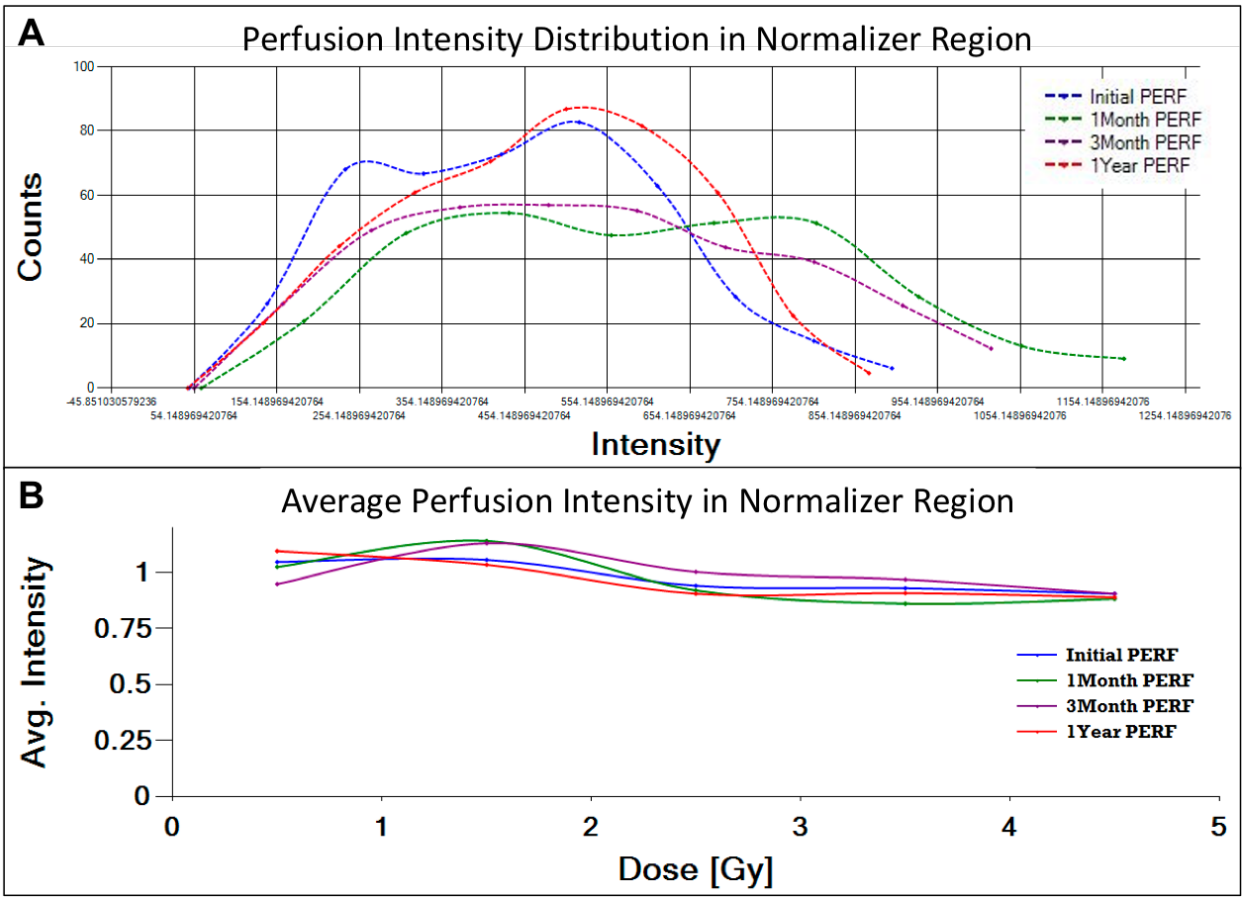

Figure 5.8: Perfusion intensity in the normalizer region for example patient UM020 including: A) the perfusion intensity histogram and B) dose-function intensity distribution for all four imaging timepoints.

However, there can be tumor involvement in both lungs or in the mediastinum so the difference in delivered dose may not always be significantly different. In either case, the ipsilateral lung was defined as the individual lung with the higher mean dose. For example patient UM020, the primary tumor involvement was in the mediastinum, which equated to a maximum dose of 56.0 Gy vs. 49.5 Gy and mean dose of 13.3 Gy vs. 8.8 Gy in the ipsilateral lung versus contralateral lung, respectively, as shown in Table 5.2. While the maximum dose is similar, the number of voxels receiving between 40-50 Gy was 3250 versus 426 in the ipsilateral and contralateral lung, respectively, which demonstrates that a much larger area received a high dose in the ipsilateral lung.

Another method to visualize the interaction between dose and functional lung is to plot the

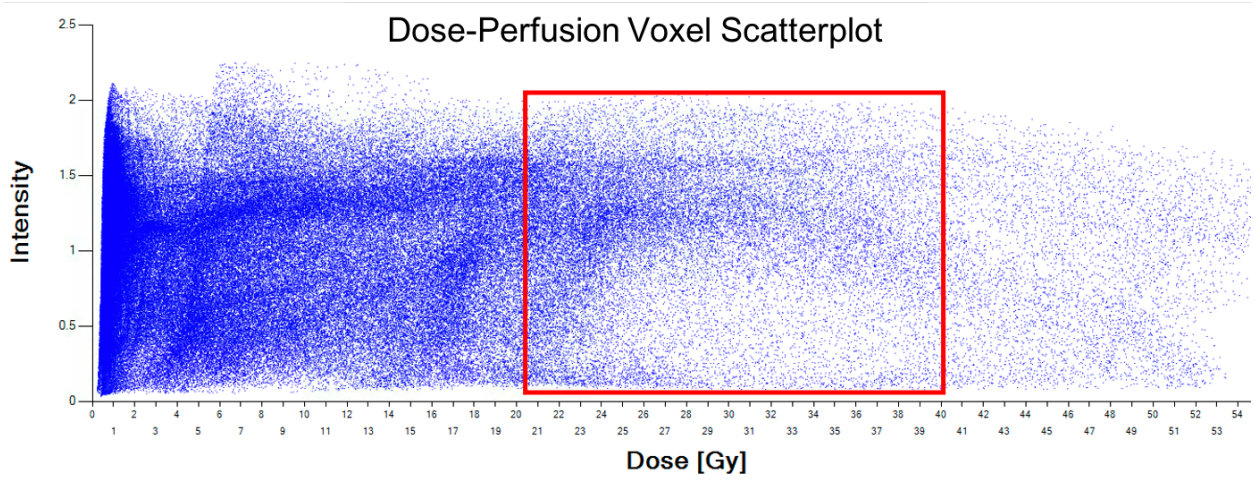

Figure 5.9: Pre-treatment perfusion intensity in each voxel plotted within 1 Gy dose bins for example patient UM020.

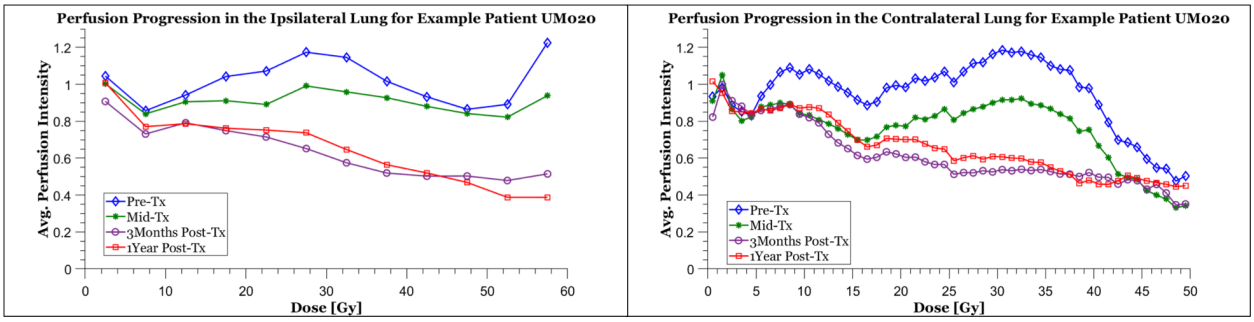

Figure 5.10: Average perfusion intensity binned by dose in the ipsilateral lung (left) versus the contralateral lung (right). Dose bins of 5 Gy were used in the ipsilateral lung whereas dose bins of 1 Gy were used in the contralateral lung.

average dose within functional intensity bins, as shown in Figure 5.11 for example patient UM020. While it is a bit more difficult to discern specific information regarding the dose-function interaction from this plot on its own, based the knowledge that this patient had a homogeneous distribution of perfusion prior to RT, it seems clear that the nearly horizontal blue line represents a dose plan that is distributed fairly evenly across the complete range of functional intensities. However, at the post-RT timepoints, it becomes clear that the high dose is more concentrated in relatively lower-functioning lung based on the larger peaks in these areas. This again is an indication of the reduction in lung function following RT in the high dose regions.

While the plots of average functional intensity are informative to understand the distribution

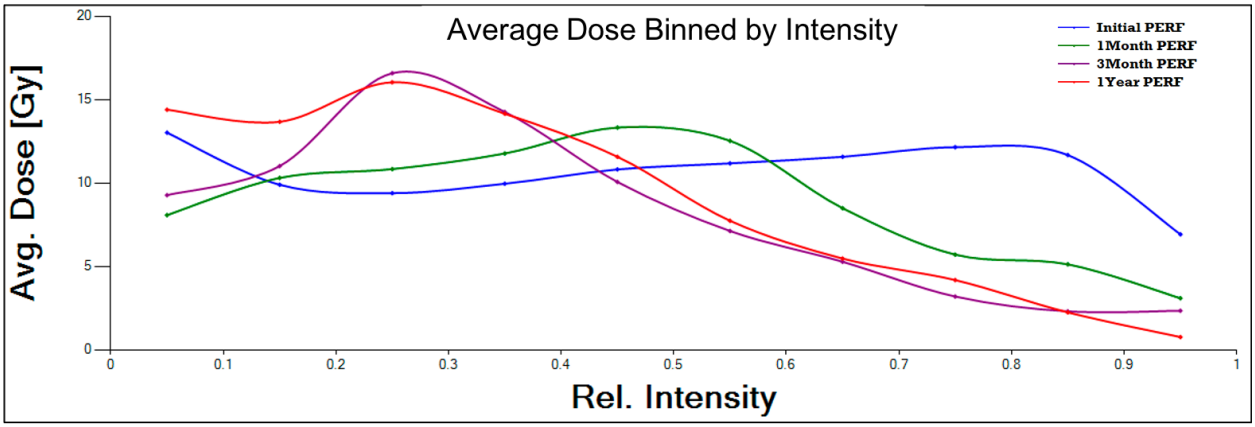

Figure 5.11: Average dose delivered in the global lungs within perfusion intensity bins (quantified relative to the maximum intensity) using a bin size 0.1 for example patient UM020.

of lung function relative to delivered dose, quantifying the longitudinal change in lung function is imperative to improve our ability to optimize radiation delivery. To characterize each patient's dose-function response over time, the normalized intensity in each voxel at the mid-treatment, 3-month post-treatment, and 1-year post-treatment timepoints was compared directly to the normalized intensity in the same voxel at baseline. Historically, this functional change has typically been quantified as a percentage relative to the pre-treatment function in the given voxel as shown in Equation 5.3.

$$\delta_{f,t,j,i}^{relative} = \frac{f_{i,t}^{\mathbb{N}} - f_{i,t=0}^{\mathbb{N}}}{f_{i,t=0}^{\mathbb{N}}} \times 100 \tag{5.3}$$

where $f_{i,t=0}^{\mathbb{N}}$ is the normalized functional intensity signal in the *i*th voxel at time point t = {0 = *baseline*; 1 = *Mid-Tx*; 2 = *3Month Post-Tx*; 3 = *1Year Post-Tx*}.

However, the relative functional difference is inflated in patients with reduced lung function at baseline (because the denominator is inherently reduced in these cases and will be discussed in further detail later in this section), so the absolute difference in lung function was primarily calculated in this study as shown in Equation 5.4. Furthermore, because the lowest functional intensities are not expected to longitudinally decrease and to reduce the effect of erroneous increases in functional intensity, any voxel below 10% of the maximum intensity at baseline was excluded from the

dose-function response analysis.

$$\delta_{f,t,j,i}^{absolute} = f_{i,t}^{\mathbb{N}} - f_{i,t=0}^{\mathbb{N}} \tag{5.4}$$

For either methodology, the voxelwise functional change relative to baseline was then tallied within dose bins as shown in Equation 5.5.

$$\Delta_{f,t,j,d} = \frac{\sum_{i=1}^{n_{j,d}} \delta_{f,t,j,i}}{n_{j,d}} \tag{5.5}$$

where $n_{j,d}$ is the number of voxels in dose bin d for patient j.

Using these techniques, the absolute and relative dose-function response in the global lungs for example patient UM020 are shown in Figure 5.12. While the general shape of these dose-response curves is very similar, there is a pronounced increase in the estimated response at mid-treatment using the relative quantification, which is theorized to be due to initially low-functioning voxels that have seen an increase in function during the course of RT. However, this increase in functional intensity could be true reperfusion or could be an artifact of poor registration such that the inferior or lateral portion of the lung receives functional intensity at one timepoint that was simply absent on the baseline scan. While the absolute dose-function response curves quantified for all voxels and for voxels $>10\%$ of the maximum intensity show a slight increase in the high dose regions, these curves are clearly more robust to the effect of a small number of voxels seeing drastic percentage increases. Furthermore, the absolute dose-response curves suggest that there is not a true reperfusion effect in the high region, whereas the relative response is suggestive that the voxels receiving a high dose actually increased in functional intensity at mid-treatment. As an example of this flaw in the relative response quantification, if a voxel had a normalized intensity of 0.1 prior to treatment and increased to a normalized intensity of 0.5 at mid-treatment, the absolute functional change is only 0.4, but the relative functional change is $\frac{(0.5-0.1)}{0.1} x100 = 400\%$! Alternatively, an increase of 0.4 for a voxel with baseline intensity of 0.8 is only an increase of 50%.

Of course, each individual patient has a unique functional response to radiation, however, ex-

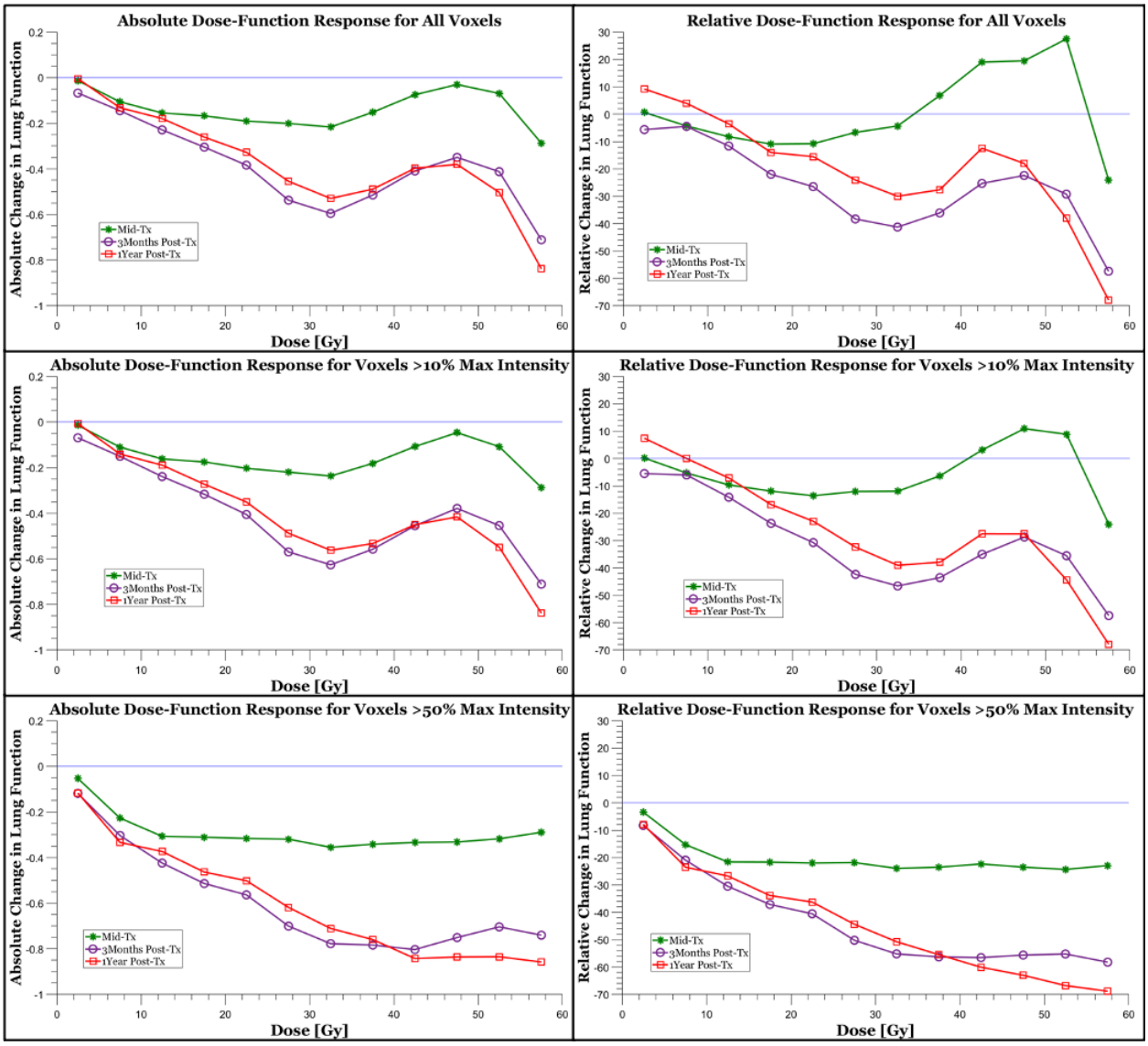

Figure 5.12: The perfusion dose-function response in the global lungs using the absolute (left) and relative (right) methods for quantification in various subsets of voxels stratified by the baseline maximum intensity for example patient UM020.

ample patient UM020 is representative of what is expected from a patient who presents for radiation with a generally normal distributed lung function at baseline: a limited response at mid-treatment, with a possible increase in functional lung in the high-dose, low-functioning voxels, followed by a significant decline in lung function at the post-treatment timepoints. While the curves in these plots are simply generated by connecting the data points with lines, the data points shown in the absolute dose-function response curves in Figure 5.12 are representative of the data

that will be used to generate the patient-specific dose-response models.

5.5.1.2 Quantifying Ventilation for Example Patient UM020

While all of these data previously exhibited for example patient UM020 were based on perfusion intensity, the average ventilation intensity and dose-ventilation response can also be analyzed using the images shown in Figure 5.13. The quantified ventilation SPECT metrics from these images are explicitly shown in Table 5.4. However, as depicted in the average intensity curves shown in Figure 5.14, the trends in the average ventilation intensity estimates are typically not as clear as those in the perfusion estimates. Part of this can be attributed to the increase in saturation artifacts shown in Figure 5.13, which can blur the dose-response trends that were previously observed for this patient.

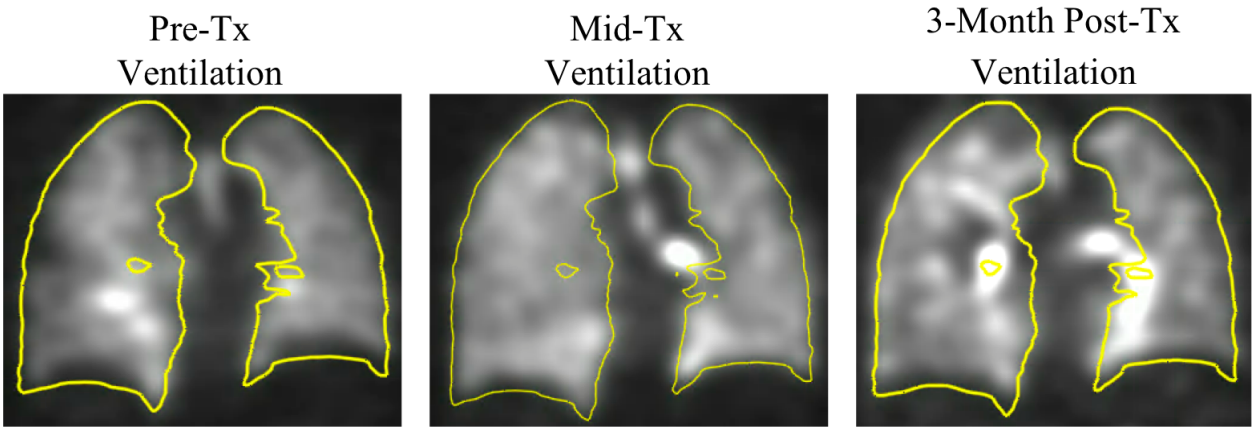

Figure 5.13: Qualitative example of the ventilation SPECT images for patient UM020 that demonstrates the dose-function response using ventilation intensity during and after radiation treatment.

The variation in functional change is especially pronounced in the dose-response curves shown in Figure 5.15 because of the instability in the average functional intensity at baseline. As such, although the absolute and relative dose-response curves exhibit similar shapes, the relative dose-response shows a larger increase in ventilation is estimated in the low-dose bins. And while the percentage change cannot be directly equated to the absolute intensity change, there is clearly a larger integral above baseline in the relative dose-function response curve, which appears to be an overestimation of the response due to initially low-ventilated voxels seeing a large increase in

Ventilation Parameters for Example Patient UM020

Structure	Timepoint	Max Intensity	Mean Intensity	Std. Dev. Intensity	Total Intensity	LF [%]	F [%]	HF [%]	Upper Avg. Intensity†	Middle Avg. Intensity†	Lower Avg. Intensity†
LUNGS-GTV	Initial VENT	2.52	0.89	0.49	168670.70	13.59	78.76	6.57	0.69	0.91	1.07
	1Month VENT	2.17	0.96	0.37	181547.34	3.05	88.15	7.68	0.96	0.96	0.96
	3Month VENT	3.05	0.84	0.41	160830.12	18.7	80.77	0.48	0.74	0.8	1.06
	1Year VENT	2.37	0.89	0.36	169714.41	5.31	92.49	2.19	0.77	0.87	1.07
RIGHT_LUNG-GTV	Initial VENT	2.52	0.88	0.54	91180.48	16.77	73.51	8.01	0.69	0.87	1.08
	1Month VENT	2.17	0.97	0.42	101830.32	3.01	84.03	11.77	1.01	0.95	0.98
	3Month VENT	3.05	0.81	0.4	85871.33	20.8	78.86	0.28	0.78	0.72	1.06
	1Year VENT	2.37	0.9	0.38	95644.61	3.87	92.93	3.2	0.88	0.83	1.09
LEFT_LUNG-GTV	Initial VENT	2.52	0.91	0.43	77490.23	9.66	85.25	4.81	0.69	0.96	1.04
	1Month VENT	2.17	0.94	0.30	79717.03	3.09	93.24	2.63	0.9	0.97	0.92
	3Month VENT	3.05	0.88	0.41	74958.79	16.11	83.12	0.72	0.71	0.89	1.06
	1Year VENT	2.37	0.86	0.33	74069.80	7.1	91.95	0.95	0.66	0.91	1.03

†Regional lung segments defined as: Upper above the carina; Lower below inferior pulmonary vein; Middle between the two
LF = low-function volume, as a percent of total lung structure volume
F = normal-function volume, as a percent of total lung structure volume
HF = high-function volume, as a percent of total lung structure volume

Table 5.4: Quantified ventilation SPECT metrics for example patient UM020.

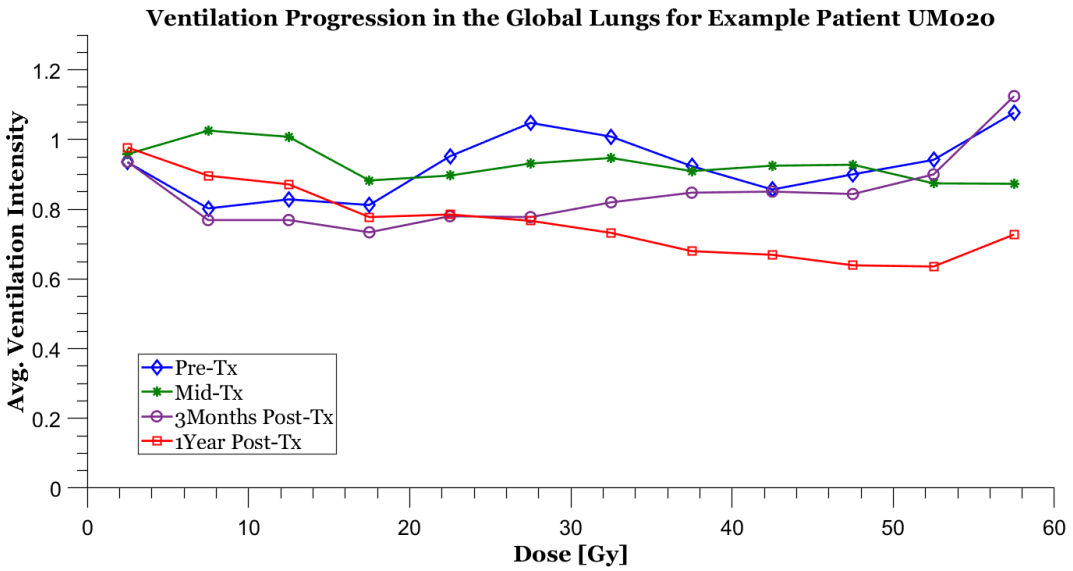

Figure 5.14: Quantitative assessment of the average ventilation intensity in the global lungs binned by dose at each imaging timepoint for example patient UM020.

ventilation at mid-treatment. This is partially an artifact of the poor rigid registration (especially in the diaphragm region), which was subsequently attempted to be resolved by applying an inner boundary to the Lungs-GTV contour, however, this correction was not applied in the dose-response analysis. Furthermore, although a decrease in ventilation at 1-year post-treatment is observed, the 3-month post-treatment curve appears to return to baseline in the high-dose bins, which is theorized to be due to ineffective removal of the saturation artifacts that are depicted in Figure 5.13.

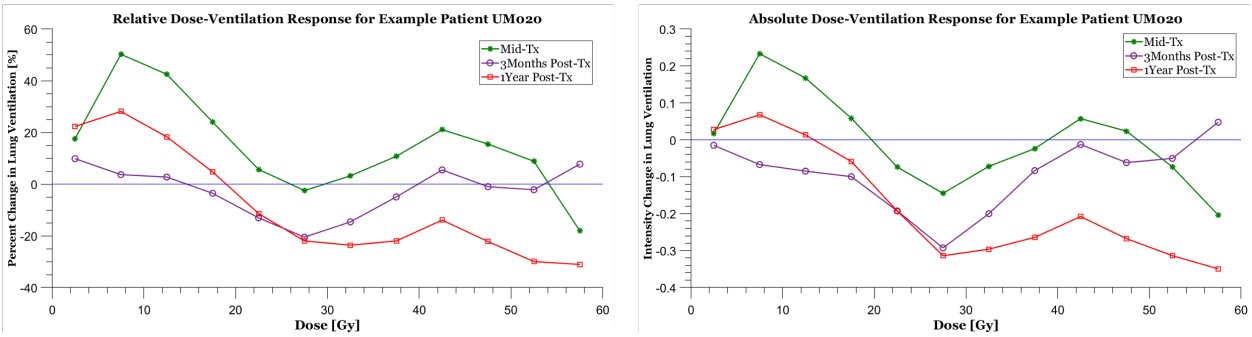

Figure 5.15: Relative (left) and absolute (right) dose-ventilation response in the global lungs for example patient UM020.

Therefore, while the ventilation SPECT data can be beneficial, especially in conjunction with the perfusion SPECT data, the processing and clinical interpretation required to properly quantify the functional intensities has proven to be challenging.

5.5.2 Grade 5 RILT Patients

As has been alluded to previously, both of these grade 5 RILT patients were judged to have died as a direct result of the radiation treatment they received. Because this is the worst outcome achievable, these patients will be extensively examined throughout this work in an effort to decipher any potential determinants that can be identified to help avoid these severe toxicities in future patients.

5.5.2.1 Quantifying Perfusion for Example Grade 5 RILT Patient UM025

Example grade 5 RILT patient UM025 was a 60 year-old Caucasian male, who was a former smoker and was determined to have a KPS of 75 prior to treatment. This patient was diagnosed with stage III (T stage=2; N stage=2) NSCLC that was located in the medial-inferior portion of the right lung with a tumor size of 378.3 cubic centimeters. In terms of PFT results, this patient was found to have a moderate restrictive defect and a severely decreased DLCO. Furthermore, the clinical report states that there was evidence based on CT imaging of pervasive interstitial pulmonary fibrosis that was also redemonstrated following RT. A planning treatment volume (PTV) dose of

60 Gy was prescribed and included treatment with concurrent chemotherapy. The patient endured a number of toxicities during and following RT including: grade 1 dysphagia (abnormal transit of liquids and/or solids while swallowing) on three occasions towards the end of the RT course; grade 2 odynophagia (painful swallowing) on one occasion towards the end of the RT course; grade 3 pneumonitis & acute respiratory failure with hypoxia on two occasions around 3-months post-RT completion; and ultimately, grade 5 RP/clinical fibrosis 3 months and 4 days after the completion of RT. The clinical note regarding the death of this patient was as follows: "possibly died of pneumonia related to IPF or possibly grade 5 radiation pneumonitis". Therefore, while it is unclear if it was specifically radiation pneumonitis or clinical fibrosis that ultimately killed this patient, it is clear that a severe negative reaction to the radiation treatment induced a series of toxicities that culminated with acute respiratory failure.

Dosimetric Parameters for Example Patient UM025

Patient	Structure	Volume	Max Dose [Gy]	Mean Dose [Gy]	Std. Dev. Dose [Gy]	V20 [%]	fV20* [%]	iV20* [%]	Upper Avg. Dose† [Gy]	Middle Avg. Dose† [Gy]	Lower Avg. Dose† [Gy]
UM020	LUNGS-GTV	2715.64	73.32	12.87	16.87	24.4	22.05	0.71	9.97	14.52	13.38
	RIGHT_LUNG-GTV	1379.19	73.32	22.68	18.86	47.85	50.54	0.71	16.96	24.37	29.16
	LEFT_LUNG-GTV	1335.86	23.78	2.74	3.04	0.18	0.03	0.14	1.79	3.05	3.28

†Regional lung segments defined as: Upper above the carina; Lower below inferior pulmonary vein; Middle between the two
V20 = Volume of lung structure receiving ≥20 Gy, as a percent of total lung structure volume
fV20 = functional intensity receiving ≥20 Gy, as a percent of total functional intensity
iV20 = average functional intensity receiving ≥20 Gy in arbitrary units
*Quantified using perfusion intensity

Table 5.5: Delivered dose metrics for example patient UM025.

From the dosimetric parameters listed in Table 5.5, it is apparent that this patient had less normal lung volume than the previous example patient UM020 (2716 cc vs. 3594 cc), which is partially due to the increased tumor size (378.3 cc vs. 80.6 cc). Furthermore, while the global lungs MLD and V20 for this patient are not drastically greater than in patient UM020, the right lung in this case received an excessively high amount of dose, with nearly 50% irradiated to a dose $>$20 Gy. Another difference is the large accumulation of dose in the middle and lower lung segments as opposed to the upper lung in patient UM020. Clearly, this larger dose distribution is due to the larger tumor size and higher prescription dose and is further exacerbated by a limited

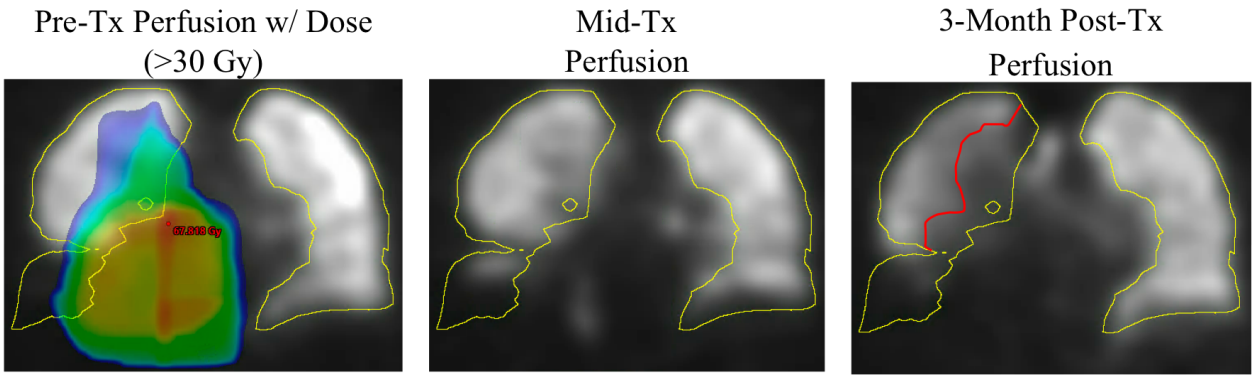

Figure 5.16: A qualitative example of the perfusion SPECT scans for patient UM025 demonstrating the dose-function response during and after radiation treatment. Planned dose >30 Gy is overlaid on the pre-treatment perfusion scan and the red contour is included to show areas of observed perfusion reduction.

ability to avoid normal tissue dose through the 3D conformal RT delivery technique.

Perfusion Parameters for Example Patient UM025

Structure	Timepoint	Max Intensity	Mean Intensity	Std. Dev. Intensity	Total Intensity	LF [%]	F [%]	HF [%]	Upper Avg. Intensity†	Middle Avg. Intensity†	Lower Avg. Intensity†
LUNGS-GTV	Initial PERF	2.14	0.78	0.42	113358.53	16.13	79.27	4.59	0.93	0.82	0.47
	1Month PERF	2.06	0.73	0.44	106466.00	21.57	72.45	5.97	0.88	0.78	0.41
	3Month PERF	2.02	0.67	0.41	97455.45	20.87	74.64	4.47	0.71	0.68	0.60
RIGHT_LUNG-GTV	Initial PERF	2.14	0.67	0.39	49428.54	23.76	76.24	0.00	0.86	0.73	0.08
	1Month PERF	2.06	0.64	0.39	46892.36	26.45	73.48	0.07	0.79	0.69	0.13
	3Month PERF	2.02	0.43	0.25	31725.34	34.32	65.67	0.00	0.49	0.48	0.14
LEFT_LUNG-GTV	Initial PERF	2.14	0.90	0.43	63929.99	8.26	82.39	9.34	1.00	0.93	0.72
	1Month PERF	2.06	0.83	0.48	59573.63	16.52	71.39	12.07	0.99	0.87	0.59
	3Month PERF	2.02	0.92	0.39	65730.11	6.99	83.89	9.08	0.96	0.91	0.90

†Regional lung segments defined as: Upper above the carina; Lower below inferior pulmonary vein; Middle between the two
LF = low-function volume, as a percent of total lung structure volume
F = normal-function volume, as a percent of total lung structure volume
HF = high-function volume, as a percent of total lung structure volume

Table 5.6: Perfusion SPECT metrics for example patient UM025.

Because this patient died shortly after 3-months following the completion of RT, only SPECT scans from the first three imaging timepoints were available for this patient, as shown in Figure 5.16. From these slice images, it is apparent that there is a fairly homogeneous distribution of pulmonary perfusion prior to treatment, with the exception of the complete defect in the inferior portion of the right lung that is directly adjacent to the tumor. The mostly homogeneous perfusion elsewhere is reflected by the nearly normal distribution of perfusion intensity shown in Figure 5.17. But an increase in low intensity counts (on the left side of the graph) signifies the apparent defect.

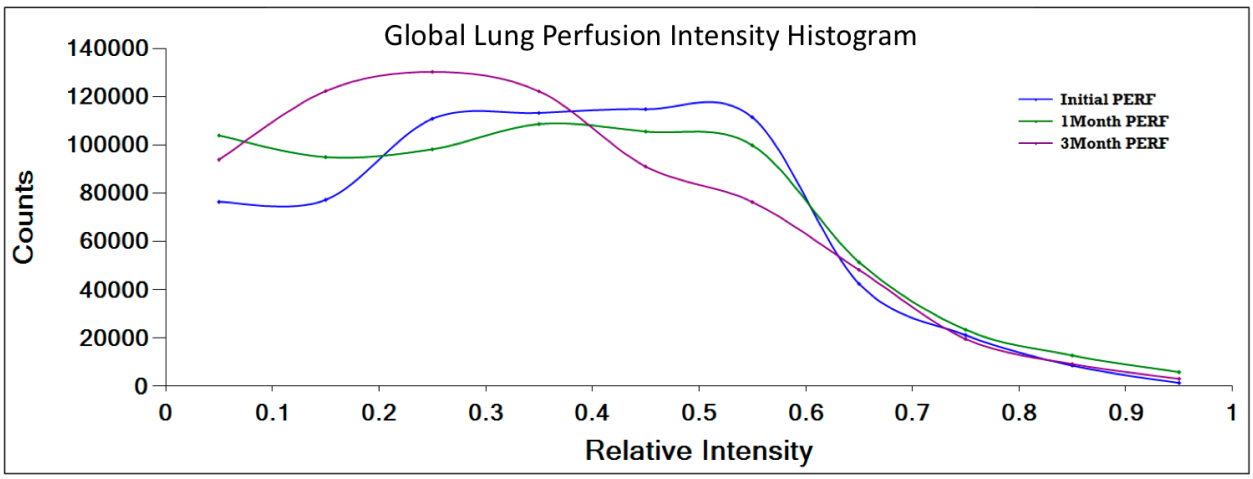

Figure 5.17: Perfusion intensity histograms in the global lungs at pre-treatment (blue), mid-treatment (green), and 3-months post-treatment (purple) for example patient UM025.

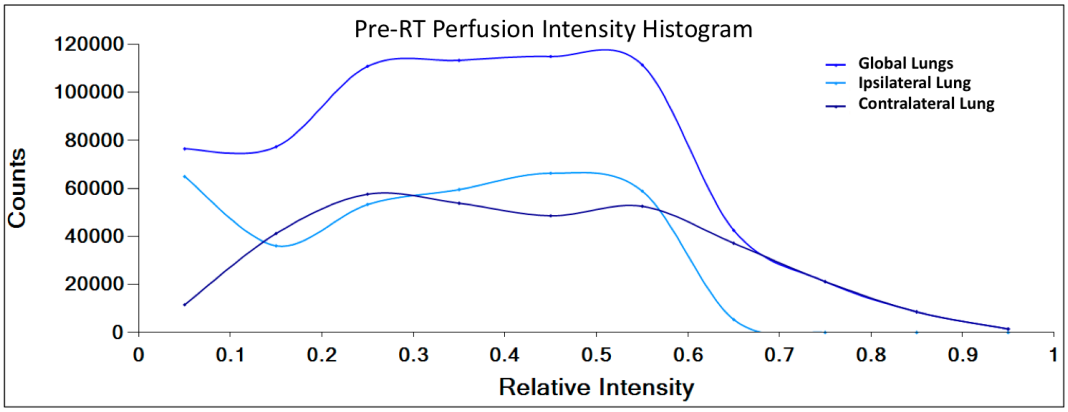

Figure 5.18: Pre-RT perfusion intensity histograms in the global lungs (blue), ipsilateral lung (light blue), and contralateral lung (dark blue) for example patient UM025.

This observation becomes even more clear when the perfusion histogram is plotted for each individual lung structure, as shown in Figure 5.18, which demonstrates a normal distribution in the contralateral lung (very similar in shape to the pre-RT distribution in the previous example patient UM020 shown in Figure 5.2). And yet, a clear uptick in the low intensities within the ipsilateral lung histogram is demonstrated. Because the ipsilateral and contralateral lung histograms intersect around 15% relative intensity, it suggests a delineation between what can be considered low-functioning lung in the contralateral lung and the severe defect in the ipsilateral lung. As such, this interpretation contributed to the selection of 15% as the cutoff for the low-function lung category.

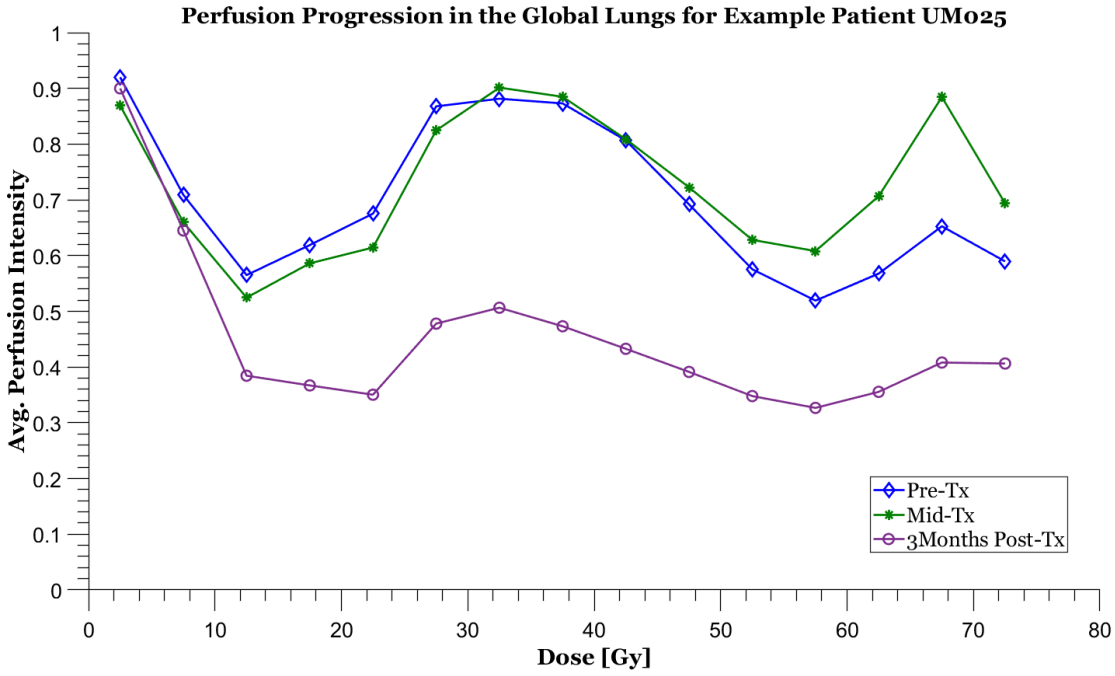

Figure 5.19: Average perfusion intensity in the global lungs quantified within 5 Gy dose bins at pre-treatment (blue), mid-treatment (green), and 3-months post-treatment for example patient UM025.

Only a slight decrease in perfusion is noticeable in the right upper lung on the mid-treatment scan, however, there is an indication of a slight reperfusion in the superior portion of the defected region, which is directly reflected by the average intensity curves binned by dose shown in Figure 5.19. From this chart, a slight increase in functional intensity in the high dose region is observed during RT, followed by a drastic loss of perfusion intensity at the 3-month post-RT. Furthermore, because this imaging timepoint was shortly before the patient's death and based on the qualitative observation that the ipsilateral lung function was severely decreased, it can be inferred that an absolute functional intensity below 0.5 may be non-functional lung. Note: although this plot is based on the global lung data, the contralateral lung received a maximum dose of 23.78 Gy so any intensity in dose bins $>$25 Gy is solely representative of the ipsilateral lung function.

While Figure 5.19 plots the average perfusion intensity within 5 Gy dose bins, this same type of plot can be generated on a voxelwise scale, such that the intensity in each voxel is plotted within 1 Gy dose bins as shown in Figure 5.20. The longitudinal trends are obviously the same, but these plots can help to impress the similarity in the pre- and mid-treatment functional distributions,

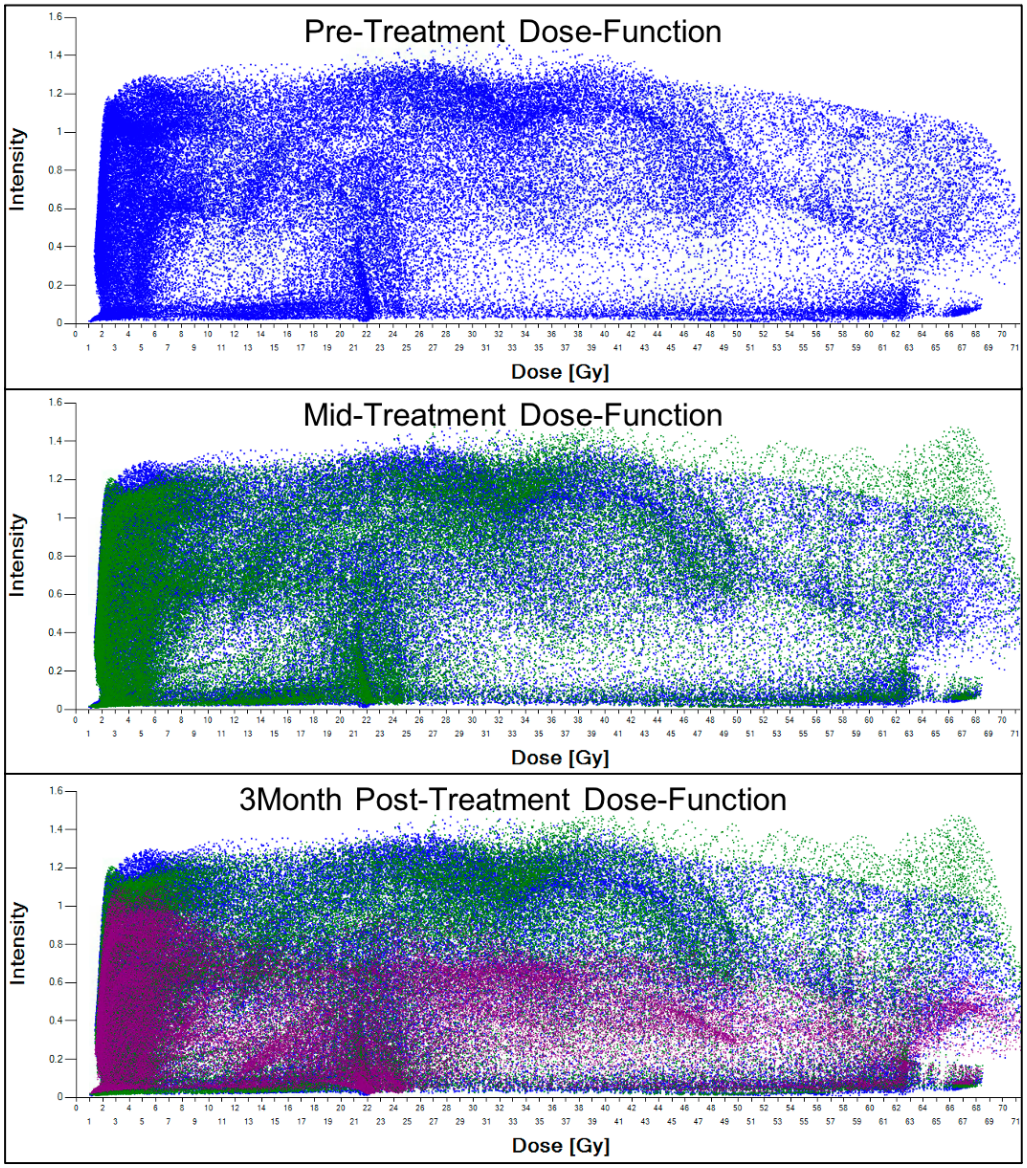

Figure 5.20: The voxelwise perfusion intensity distribution within 1 Gy dose bins in the global lungs at pre-treatment (blue), mid-treatment (green), and 3-months post-treatment (purple) for example patient UM025.

albeit with the apparent reperfusion in the high dose bins. It is also interesting to note the clear accumulation of low intensity voxels in the high dose bins throughout the three timepoints. Finally, the 3-month post-RT plot shows good agreement with the previous timepoints in the low-dose bins, but as was observed previously, there is an apparent dose-dependent reduction that occurs.

From Figure 5.21, which plots the average dose binned by relative intensity within each individual lung structure, it is clear that example grade 5 patient UM025 received a minimal amount

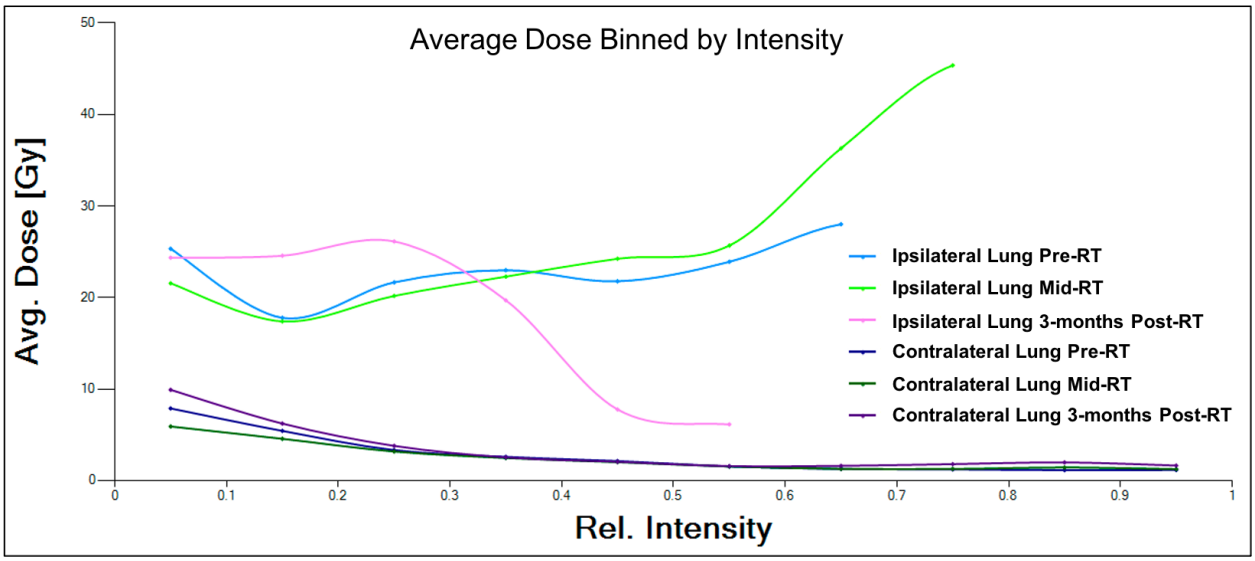

Figure 5.21: Average dose delivered to the global lungs with perfusion intensity bins (quantified relative to the maximum intensity) with bin size 0.1 for example patient UM025

of dose delivered to the contralateral lung, which was quantified to be a mean dose of 2.74 Gy. Alternatively, an average of >20 Gy was delivered fairly uniformly to the range of perfusion intensities present in the ipsilateral lung prior to RT. It can also be observed that the higher intensities received the largest dose at mid-treatment, suggesting a potential redistribution of functional intensity during treatment that was unknown to the radiation oncology treatment team. However, because the maximum intensity is slightly lower at the mid-treatment timepoint, it is possible the relative intensities in the 0.7-0.8 range are similar absolute intensities to the pre-treatment intensities in the 0.6-0.7 range, and thus, only a small portion of voxels receiving a high dose are skewing that portion of the curve. Finally, as evidenced by the 3-month post-treatment curve, the areas that received a significant portion of dose are now the relatively lowest intensity regions, again representing the significant reduction in perfusion intensity in the high dose areas.

This large reduction in perfusion intensity at the 3-month post-RT timepoint is explicitly shown in the dose-response curves in Figure 5.22. By directly quantifying the perfusion dose-response, in terms of both the absolute and relative intensity change (Equation 5.3 versus Equation 5.4) in various subsets of voxels, further information can be inferred regarding the specific dose-function changes that occurred. As such, the largest reduction in lung function is observed in voxels that

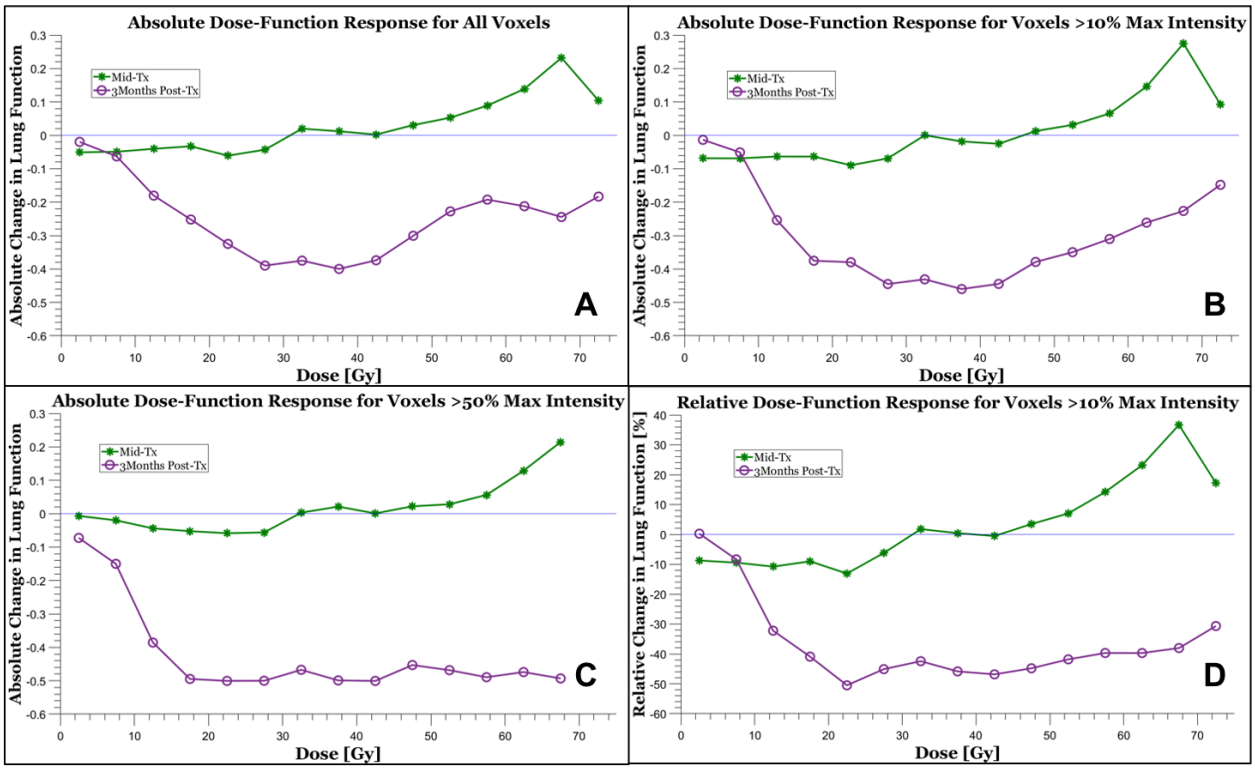

Figure 5.22: Perfusion dose-response at mid-treatment (green), and 3-months post-treatment (purple) relative to baseline intensity quantified for various voxel subsets.

are considered to be well-perfused, i.e. >50% of the maximum intensity. Furthermore, the dose-response in these well-perfused voxels exhibits a rather smooth logistic curve and suggests an undisturbed dose-effect, as was seen in example patient UM020. Alternatively, because this patient is known to have exhibited a large perfusion defect prior to RT, and hence presented with a relatively high percentage of low-functioning lung volume (nearly 24% in the ipsilateral lung), there are numerous voxels that initially were low-functioning but appear to improve slightly at the 3-month post-RT timepoint, which in effect reduces the measured reduction in lung function shown in Figure 5.22A and Figure 5.22B. There are two confounding factors that cause this effect: 1) because these voxels initially have less intensity, there is less room for a large reduction in intensity (which is the premise behind calculating the relative functional change) and 2) reperfusion can occur due to decreased tumor compression and vessel occlusion (however, reperfusion typically occurs either at mid-treatment or in areas that did not receive a high dose). Therefore, as will be discussed in the following sections, a decision was made to quantify the functional dose-response

in both well-perfused regions as well as in stratified functional categories with regard to baseline intensity.

5.5.2.2 Quantifying Ventilation for Example Grade 5 RILT Patient UM025

The ventilation SPECT scans at the first three imaging timepoints for patient UM025 are shown in Figure 5.23. From these images, a severe ventilation defect, which matches the perfusion defect, can be observed in the inferior portion of the right lung. It can also be observed that large saturation artifacts are present in each scan, which are indicative of airway restriction causing turbulent flow in the primary bronchus. In terms of the dose-response, a slight reventilation in the defected area is observed that appears to remain to some degree at the 3-month post-RT timepoint. While there is decreased ventilation intensity on this post-treatment scan, it is clearly not as diminished as the perfusion reduction that was observed.

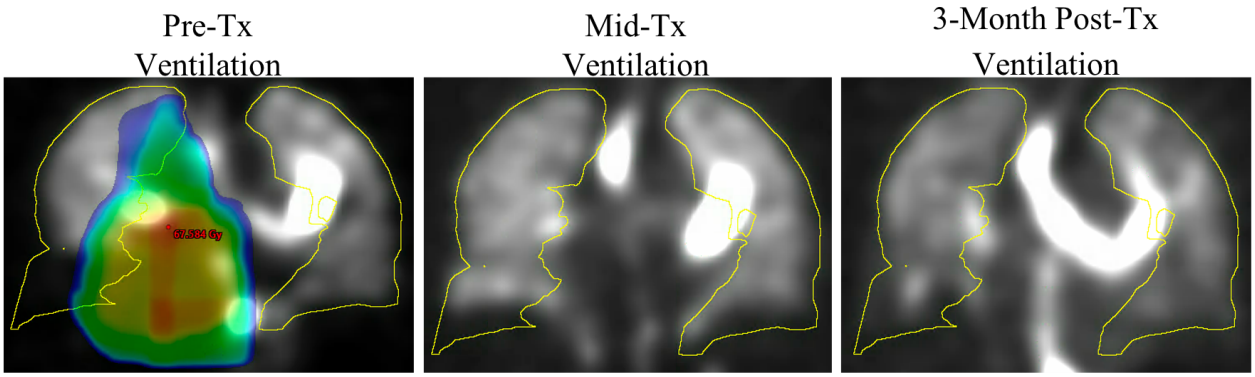

Figure 5.23: A qualitative example of the ventilation SPECT scans for patient UM025. Planned dose >30 Gy is overlaid on the pre-treatment ventilation scan.

The quantified ventilation dose-response curves are shown in Figure 5.24. Although the well-ventilated voxels exhibit a larger decrease in functional intensity at the 3-month post-RT timepoint, the large deviations suggest an imperfect removal of the saturation artifacts that were observed in Figure 5.23. A reventilation effect at the mid-treatment timepoint is also apparent in this patient suggesting that a similar reperfusion and reventilation occurred during treatment due to a reduction in tumor burden.

Ventilation Parameters for Example Patient UM025

Structure	Timepoint	Max Intensity	Mean Intensity	Std. Dev. Intensity	Total Intensity	LF [%]	F [%]	HF [%]	Upper Avg. Intensity†	Middle Avg. Intensity†	Lower Avg. Intensity†
LUNGS-GTV	Initial VENT	2.41	0.83	0.44	118394.27	16.30	79.37	3.10	0.92	0.88	0.56
	1Month VENT	2.37	0.78	0.42	112405.03	19.08	77.54	2.67	0.84	0.85	0.52
	3Month VENT	2.68	0.84	0.41	120346.06	14.62	82.94	1.60	0.87	0.86	0.72
RIGHT_LUNG-GTV	Initial VENT	2.41	0.75	0.41	54718.86	23.43	75.56	0.35	0.85	0.86	0.15
	1Month VENT	2.37	0.72	0.38	53247.45	20.71	78.37	0.78	0.73	0.81	0.40
	3Month VENT	2.68	0.76	0.39	55929.26	21.25	78.23	0.53	0.84	0.80	0.45
LEFT_LUNG-GTV	Initial VENT	2.41	0.91	0.45	63675.41	8.95	83.30	5.99	1.00	0.91	0.81
	1Month VENT	2.37	0.84	0.46	59157.58	17.39	76.68	4.65	0.97	0.89	0.60
	3Month VENT	2.68	0.92	0.41	64416.80	7.78	87.81	2.74	0.91	0.93	0.90

†Regional lung segments defined as: Upper above the carina; Lower below inferior pulmonary vein; Middle between the two
LF = low-function volume, as a percent of total lung structure volume
F = normal-function volume, as a percent of total lung structure volume
HF = high-function volume, as a percent of total lung structure volume

Table 5.7: Quantified ventilation SPECT metrics for example patient UM025.

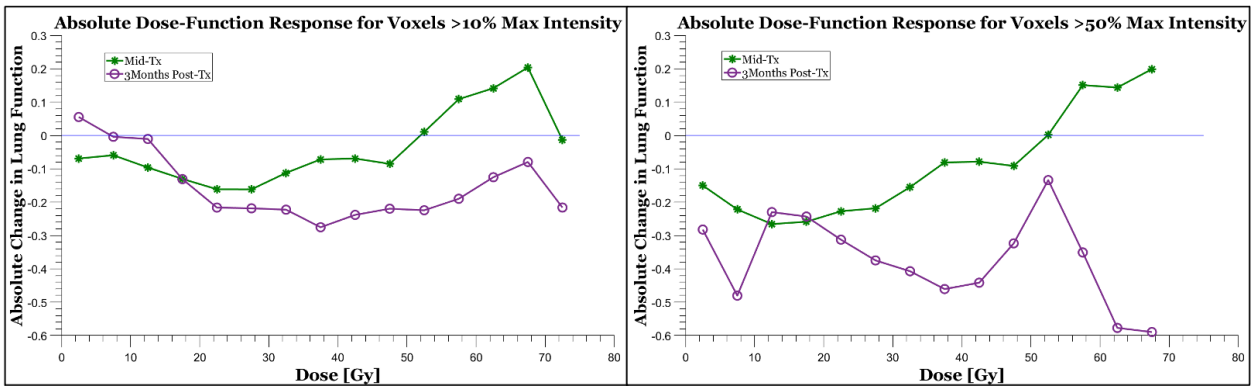

Figure 5.24: Ventilation dose-response at mid-treatment (green), and 3-months post-treatment (purple) relative to baseline intensity.

5.5.2.3 Quantifying Perfusion for Example Grade 5 RILT Patient VA029

Example grade 5 RILT patient VA029 was a 77 year-old Caucasian male with an unknown smoking status, who was determined to have a KPS of 90 prior to treatment. This patient was diagnosed with stage III (T stage=4; N stage=1) NSCLC that was located in the medial-inferior portion of the right lung extending up to the medial-middle lung region with a gross tumor volume of 445.3 cubic centimeters. In terms of PFT results, this patient was found to have a FEV1/FVC of 87%, which was one of the highest scores in the cohort, suggesting fairly good pulmonary function but no DLCO test was performed. However, a scheduled PFT at the mid-treatment timepoint was not performed because the patient could not take a deep breath without coughing, suggesting a severe decline in respiratory capability. While the clinical diagnostic reports for this patient were

not available, the treatment planning CT demonstrates evidence of ILD throughout the lungs as shown in Figure 5.25. A PTV dose of 64 Gy was prescribed and no concurrent chemotherapy was given. Ultimately, this patient died from hypoxic respiratory failure just over one month following the completion of the RT course, and it was determined retrospectively that the death was a direct result of the delivered radiation treatment. Due to the timing of the patient's death, SPECT scans were only available at the pre- and mid-treatment timepoints.

Dosimetric Parameters for Example Patient VA029

Patient	Structure	Volume	Max Dose [Gy]	Mean Dose [Gy]	Std. Dev. Dose [Gy]	V20 [%]	fV20* [%]	iV20* [%]	Upper Avg. Dose† [Gy]	Middle Avg. Dose† [Gy]	Lower Avg. Dose† [Gy]
	LUNGS-GTV	2321.55	74.39	17.52	22.09	30.56	23.04	0.61	14.59	21.44	11.97
UM020	RIGHT_LUNG-GTV	925.44	74.39	39.32	20.69	76.48	75.1	0.61	28.54	45.72	46.74
	LEFT_LUNG-GTV	1396.11	10.65	3.01	1.15	0	0	NaN	2.75	3.2	2.96

†Regional lung segments defined as: Upper above the carina; Lower below inferior pulmonary vein; Middle between the two
V20 = Volume of lung structure receiving ≥20 Gy, as a percent of total lung structure volume
fV20 = functional intensity receiving ≥20 Gy, as a percent of total functional intensity
iV20 = average functional intensity receiving ≥20 Gy in arbitrary units
*Quantified using perfusion intensity

Table 5.8: Delivered dose metrics for example patient VA029.

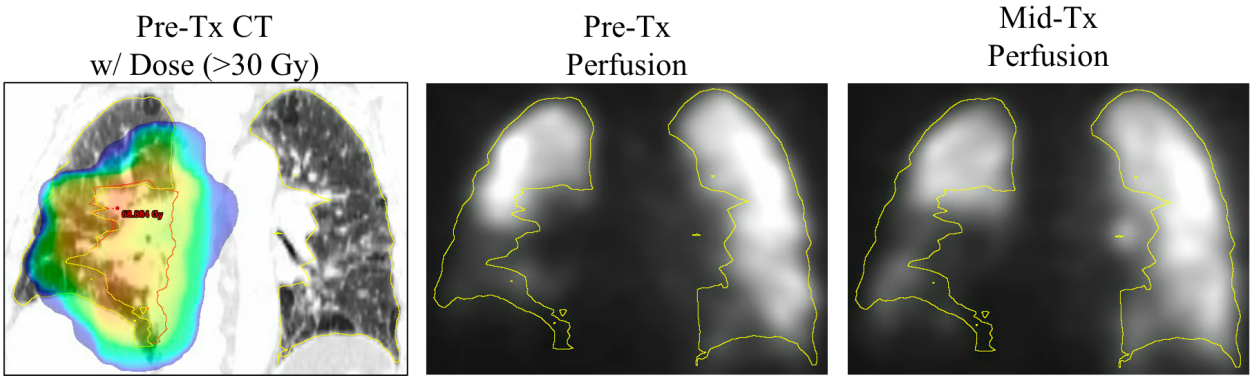

Figure 5.25: A qualitative example demonstrating the perfusion SPECT distribution prior to and during radiation treatment for example patient VA029. Planned dose >30 Gy is overlaid on the treatment planning CT scan.

Clearly, this patient presented with a relatively large tumor in a challenging location, however, the dosimetrics shown in Table 5.8 demonstrate an exorbitant amount of dose was delivered to the ipsilateral lung. While the global lung MLD and V20 were close to the clinical constraints of 20

Gy and 30%, respectively, the ipsilateral lung received a MLD of nearly 40 Gy and a V20 over 76%! Furthermore, while 75% of the functional intensity was irradiated to a dose >20 Gy, a large perfusion defect can be observed in the inferior portion of the ipsilateral lung, which incidentally received a significant amount of dose as well. And although the perfusion defect is still apparent on the mid-treatment scan, it appears as though there is slightly more perfusion that has reached the inferior region of the ipsilateral lung, possibly suggesting a slight reduction in tumor burden. No other noticeable changes are apparent in the perfusion image at mid-treatment. However, given that this mid-treatment scan was taken one day after the mid-treatment PFT was failed due to the patient's inability to take a deep breath without coughing, it can be inferred that the patient's pulmonary condition had significantly declined compared to baseline.

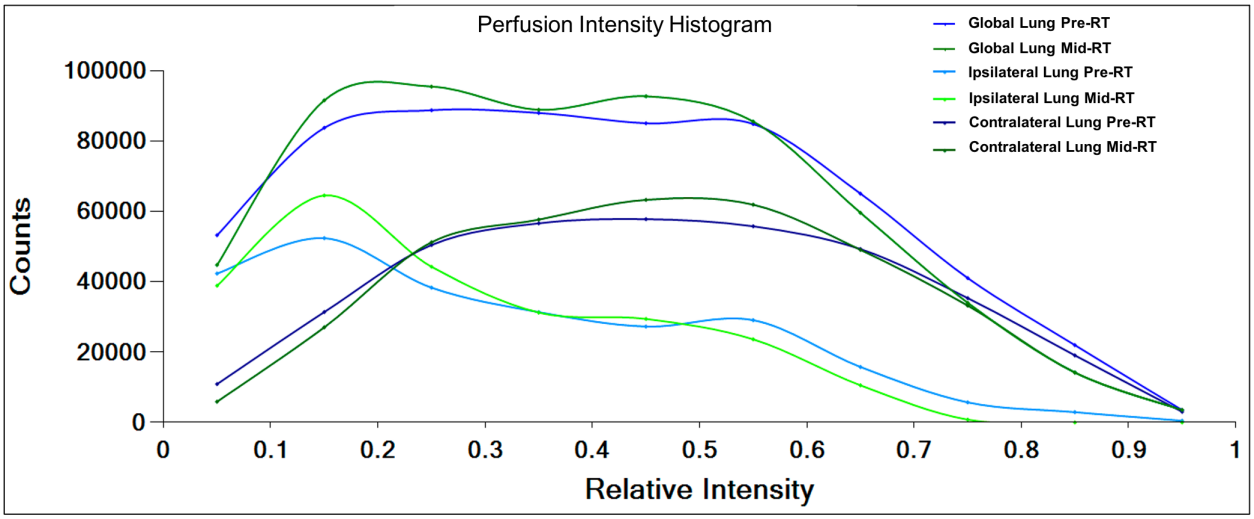

Figure 5.26: Perfusion intensity histograms in the global lungs, ipsilateral lung, and contralateral lung at pre-treatment and mid-treatment.

Quantitatively, the functional distribution for each lung structure is shown in Figure 5.26 and the perfusion SPECT metrics are listed in Table 5.9. While the contralateral lung exhibits a normal distribution graphically, the ipsilateral lung demonstrates a large number of counts in the low perfusion intensity values, which is associated with the defect observed in the inferior portion of the right lung in Figure 5.25. These distributions directly correlate with the mean intensities in each lung such that the left lung, the contralateral lung, is shown to have an average perfusion near 1.0 while the right lung, the ipsilateral lung, is demonstrated to have a mean intensity near 0.6.

Perfusion Parameters for Example Patient VA029

Structure	Timepoint	Max Intensity	Mean Intensity	Std. Dev. Intensity	Total Intensity	LF [%]	F [%]	HF [%]	Upper Avg. Intensity†	Middle Avg. Intensity†	Lower Avg. Intensity†
LUNGS-GTV	Initial PERF	2.01	0.81	0.45	100517.50	15.47	73.65	10.81	1.00	0.78	0.56
	1Month PERF	2.03	0.80	0.43	98344.19	14.32	77.00	8.48	0.96	0.78	0.53
RIGHT_LUNG-GTV	Initial PERF	2.01	0.62	0.41	30841.55	29.16	66.97	3.71	0.90	0.52	0.14
	1Month PERF	2.03	0.56	0.35	27697.87	29.08	70.13	0.33	0.81	0.45	0.17
LEFT_LUNG-GTV	Initial PERF	2.01	0.94	0.42	69675.95	6.36	78.10	15.54	1.09	0.98	0.67
	1Month PERF	2.03	0.95	0.40	70646.33	4.49	81.57	13.88	1.09	1.03	0.62

†Regional lung segments defined as: Upper above the carina; Lower below inferior pulmonary vein; Middle between the two
LF = low-function volume, as a percent of total lung structure volume
F = normal-function volume, as a percent of total lung structure volume
HF = high-function volume, as a percent of total lung structure volume

Table 5.9: Quantified perfusion SPECT metrics for example patient VA029.

Furthermore, the regional average intensities show a severely defected perfusion intensity ($\sim$0.15) in the inferior portion of the right lung. As observed, the two individual lung structures combine to generate the global lung perfusion distribution, which only appears slightly skewed toward the low-intensity region. This drastic difference in the ipsilateral and contralateral lung distributions and the minimal observed abnormality in the global lung distribution demonstrates the importance of quantifying functional metrics within the individual lung structures.

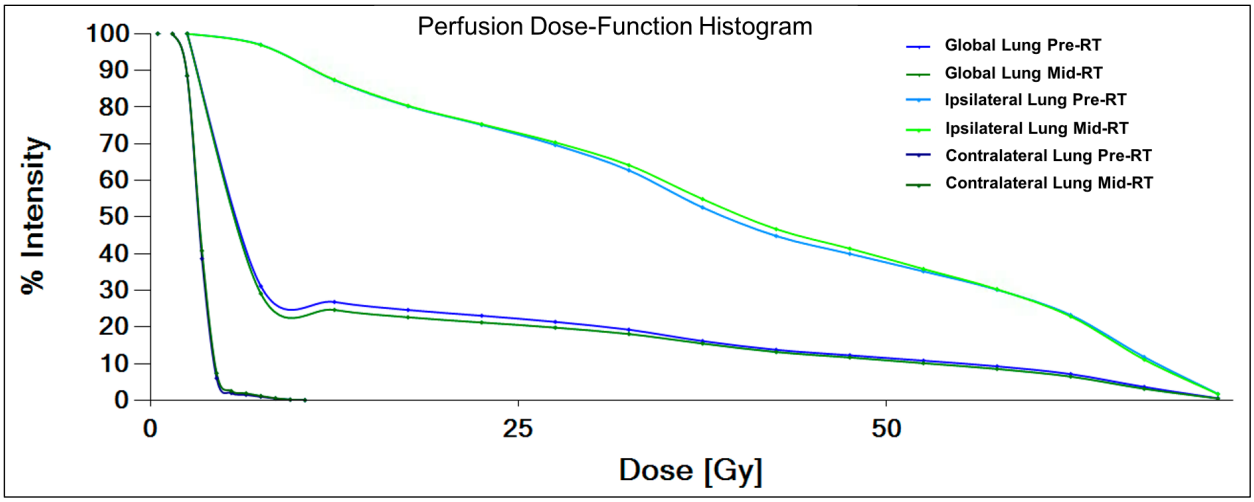

Figure 5.27: Perfusion dose-function histograms in the global lungs, ipsilateral lung, and contralateral lung at pre-treatment and mid-treatment.

This is also apparent in the dose-function histogram presented in Figure 5.27. Because of the drastic imbalance in dose delivered between the ipsilateral and contralateral lung, it is apparent that a large portion of the ipsilateral lung function was delivered a significantly high dose. However,

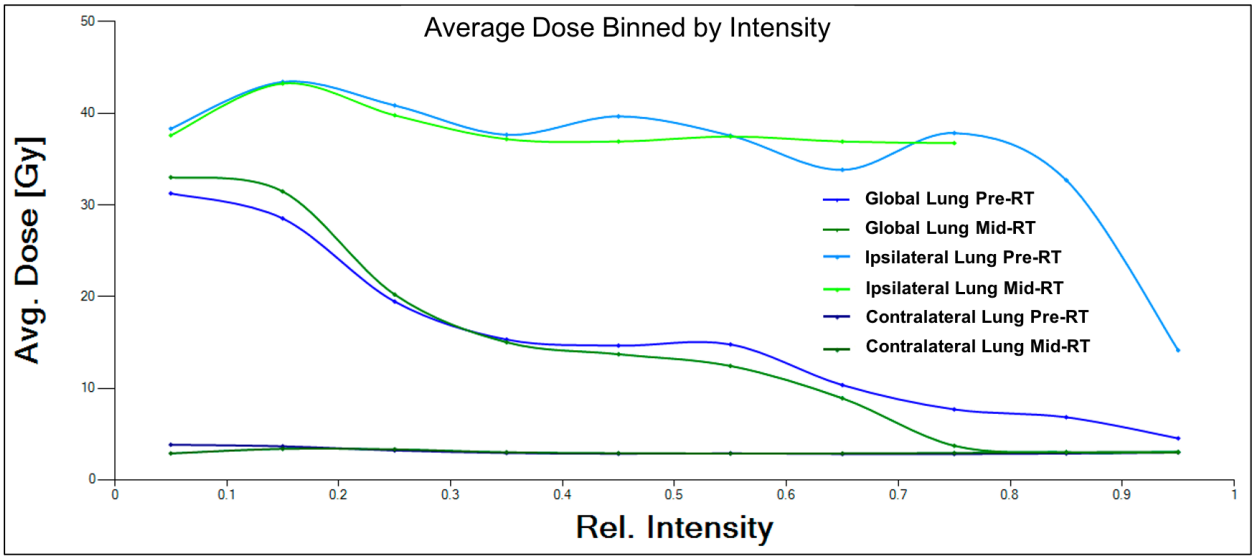

Figure 5.28: Average delivered dose binned by perfusion intensity (quantified relative to the maximum intensity) with bin size of 0.1 for the global lungs, ipsilateral lung, and contralateral lung at pre-treatment and mid-treatment.

this effect may not be overtly evident if only the global lungs DFH was presented. Furthermore, Figure 5.28 also demonstrates that the contralateral lung received relatively minimal amounts of dose while nearly the full range of functional intensities in the ipsilateral lung received an average dose of >30 Gy. This graph also shows that the lowest intensities in the global lung received the highest average dose.

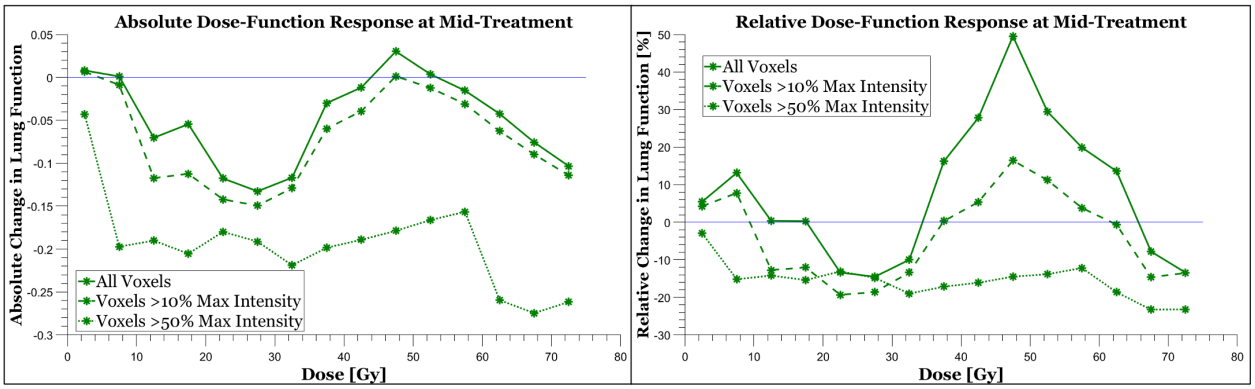

Figure 5.29: Perfusion dose-response at mid-treatment within various subsets of voxels delineated based on pre-treatment relative intensity.

Because this patient only has SPECT scans available at the pre- and mid-treatment timepoints, it is challenging to ascertain much in regard to their dose-function response. However, the ab-

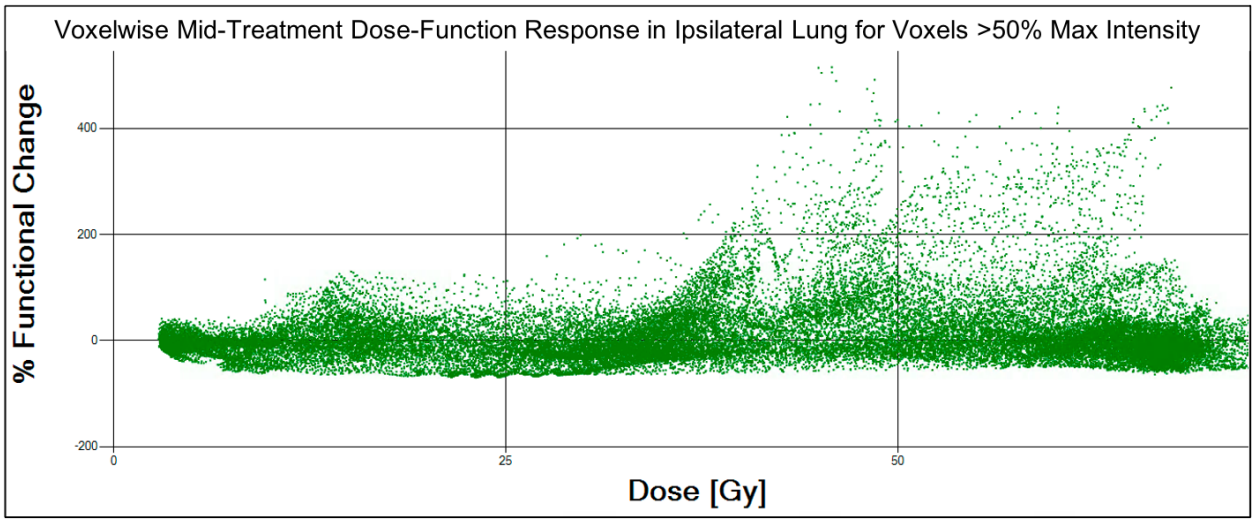

Figure 5.30: Voxelwise perfusion dose-response calculated as a percentage change relative to the baseline intensity for voxels that were initially categorized as well-perfused, i.e. >50% of the maximum intensity prior to RT.

solute and relative responses in various voxel subsets are shown in Figure 5.29, which demonstrates the similar trends observed in the previous example Grade 5 RILT patient UM025 at mid-treatment. Specifically, it is clear that the slight reperfusion effect is drastically overestimated using the relative quantification. This is further evidenced by the dose-response scatter plot shown in Figure 5.30. As such, it is clear that a relatively small number of voxels with abnormally large percentage increases are driving the average response estimates.

5.5.2.4 Quantifying Ventilation for Example Grade 5 RILT Patient VA029

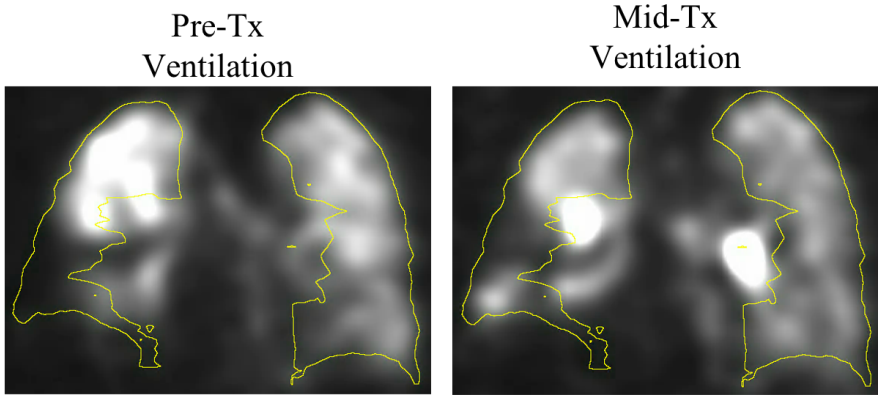

Figure 5.31: Example ventilation SPECT images at pre- and mid-treatment for patient VA029.

Ventilation Parameters for Example Patient VA029

Structure	Timepoint	Max Intensity	Mean Intensity	Std. Dev. Intensity	Total Intensity	LF [%]	F [%]	HF [%]	Upper Avg. Intensity†	Middle Avg. Intensity†	Lower Avg. Intensity†
LUNGS-GTV	Initial VENT	2.40	0.83	0.52	102456.17	19.29	71.71	8.28	1.01	0.76	0.73
	1Month VENT	2.87	0.81	0.47	100199.88	23.45	74.81	1.24	1.01	0.75	0.62
RIGHT_LUNG-GTV	Initial VENT	2.40	0.69	0.55	33735.63	34.20	56.74	7.43	1.04	0.54	0.19
	1Month VENT	2.87	0.67	0.50	32935.27	39.99	57.78	1.58	0.94	0.54	0.30
LEFT_LUNG-GTV	Initial VENT	2.40	0.92	0.47	68720.54	9.37	81.68	8.84	0.98	0.92	0.87
	1Month VENT	2.87	0.91	0.42	67264.62	12.44	86.14	1.01	1.06	0.91	0.70

†Regional lung segments defined as: Upper above the carina; Lower below inferior pulmonary vein; Middle between the two
LF = low-function volume, as a percent of total lung structure volume
F = normal-function volume, as a percent of total lung structure volume
HF = high-function volume, as a percent of total lung structure volume

Table 5.10: Quantified ventilation SPECT metrics for example patient VA029.

The ventilation SPECT scans from the first two imaging timepoints for example patient VA029 are shown in Figure 5.31. A matching defect in the inferior portion of the right lung is apparent, which coincides with excessive saturation of the aerosol in the superior portion of the ipsilateral lung. Consequently, 1.62% of the voxels in the lung contour were removed based on being classified as saturation artifacts. And while that may seem small given the artifacts shown in Figure 5.31, this slice is particularly saturated compared to the rest of the lung. However, it can be inferred that the ventilation is saturated due to the severe artifact that is caused by airway compression that seems to be reduced on the mid-treatment scan.

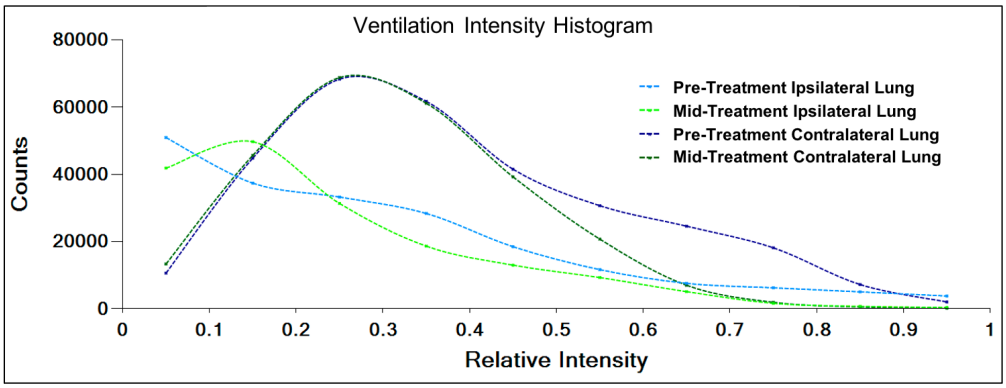

Figure 5.32: Ventilation SPECT intensity histograms in the ipsilateral and contralateral lungs at pre- and mid-treatment for patient VA029.

Similar to the perfusion metrics, the mean ventilation intensity was quantified to be near the expected normal of 1.0 in the contralateral lung, while the ipsilateral lung mean intensity was diminished, especially in the lower lung. The ventilation intensity histograms for both the ipsilateral

and contralateral lung are shown in Figure 5.32. The longer tails in the high intensity bins are suggestive that the saturation artifacts were not completely cleared. Notwithstanding that difference, the general shapes of the distributions in each individual lung are consistent with the perfusion distributions.

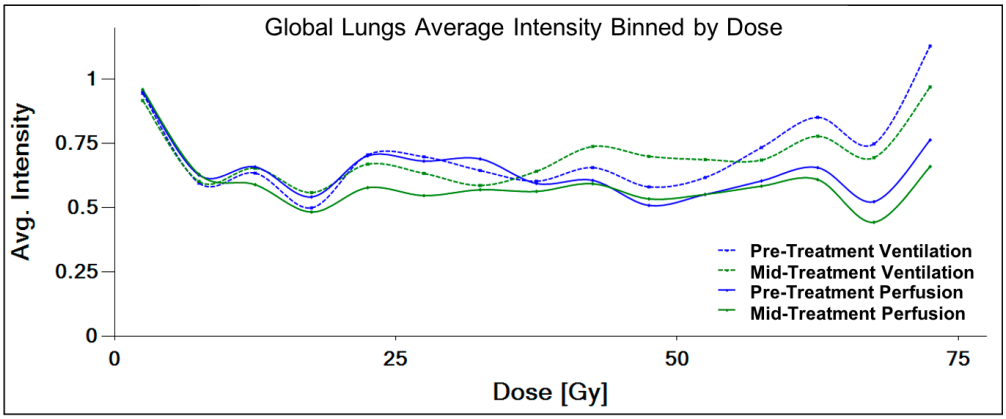

Figure 5.33: The average ventilation and perfusion at pre- and mid-treatment for example patient VA029.

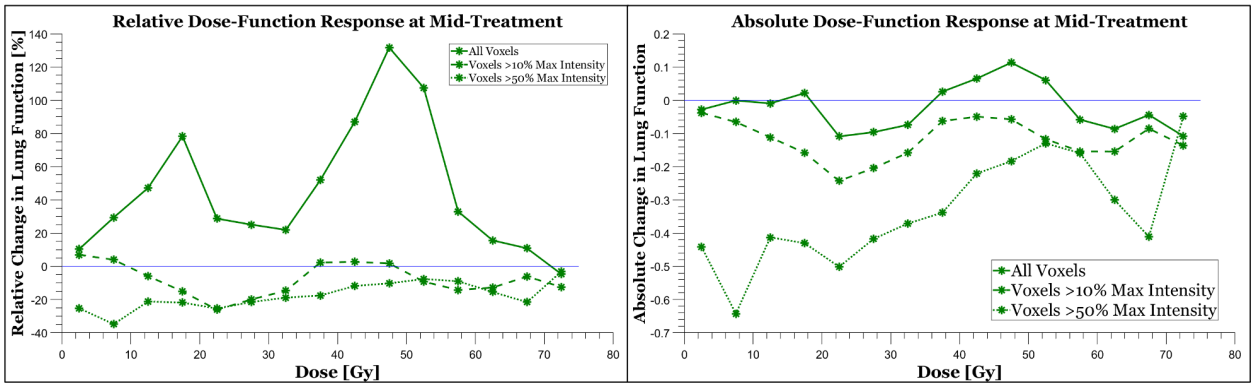

Figure 5.34: Ventilation dose-response at mid-treatment within various subsets of voxels delineated based on pre-treatment relative intensity.

Moreover, the ventilation and perfusion average intensity curves are plotted together in Figure 5.33, which demonstrate similar shapes using both modalities. As such, it can be inferred that this patient had matching perfusion and ventilation distributions, albeit with saturation slightly increasing the average intensity in the high dose bins. This effect is again exacerbated by the relative quantification of the dose-function response as shown in Figure 5.34.

A high uncertainty in the ventilation dose-response can also be observed due to the difficulty in removing the saturation artifacts.

5.6 Quantifying Lung Function and Dose-Response in the Patient Cohort

While the lung function and dose-function response in individual patients is important to characterize to demonstrate specific attributes of functional lung quantification, the ultimate goal of this thesis was to translate the knowledge gained regarding the underlying pulmonary condition of patients presenting for RT and their response to RT such that the treatment of new, unknown patients can be better managed to achieve superior outcomes. To accomplish this, it is imperative to employ these quantification and modeling methods across a broad range of patients with varying initial conditions, such that the full spectrum of potential outcomes can be understood. To this end, the various plots and metrics demonstrated in the previous sections, with a primary focus on the functional intensity prior to RT and its change during and after RT, will now be analyzed within the full patient cohort that includes 60 patient treated with conventionally-fractionated RT and 21 patients treated with SBRT.

As an initial characterization of this data, a cohort average of the mean intensity and percent functional change within each dose bin d at a given timepoint t were generated as shown in Figure 5.35. Standard error estimates are also plotted as error bars. The data points in the average functional intensity and percent change plots were calculated using Equation 5.6 and Equation 5.7, respectively.

$$\overline{F^{\mathbb{N}}_{t,d}} = \frac{\sum_{i=1}^{N_d} \overline{f^{\mathbb{N}}_{t,j,d}}}{N_d} \tag{5.6}$$

where $\overline{f^{\mathbb{N}}_{t,j,d}}$ is the average normalized intensity for patient j in dose bin d and N_d is the number of patients contributing to dose bin d. Because the prescription doses vary amongst the patients, there are less patients contributing in the higher dose bins, whereas all patients contribute to the

lower dose bins. There is also a decreasing number of patients contributing at the later imaging timepoints.

$$\overline{\Delta_{F,t,d}} = \frac{\sum_{i=1}^{N_d} \overline{\delta_{f,t,j,d}}}{N_d} \tag{5.7}$$

where $\overline{\delta_{f,t,j,d}}$ is the average functional change for patient j in dose bin $d$and N_d is the number of patients contributing to dose bin d. It should again be noted that all voxels with a baseline intensity $<$10% of the maximum intensity were excluded from the dose-function response analysis (not the average functional intensity quantification) because the focus was to quantify the functional reduction, and these voxels were demonstrated to have a propensity to increase in intensity as shown in the individual patient analyses.

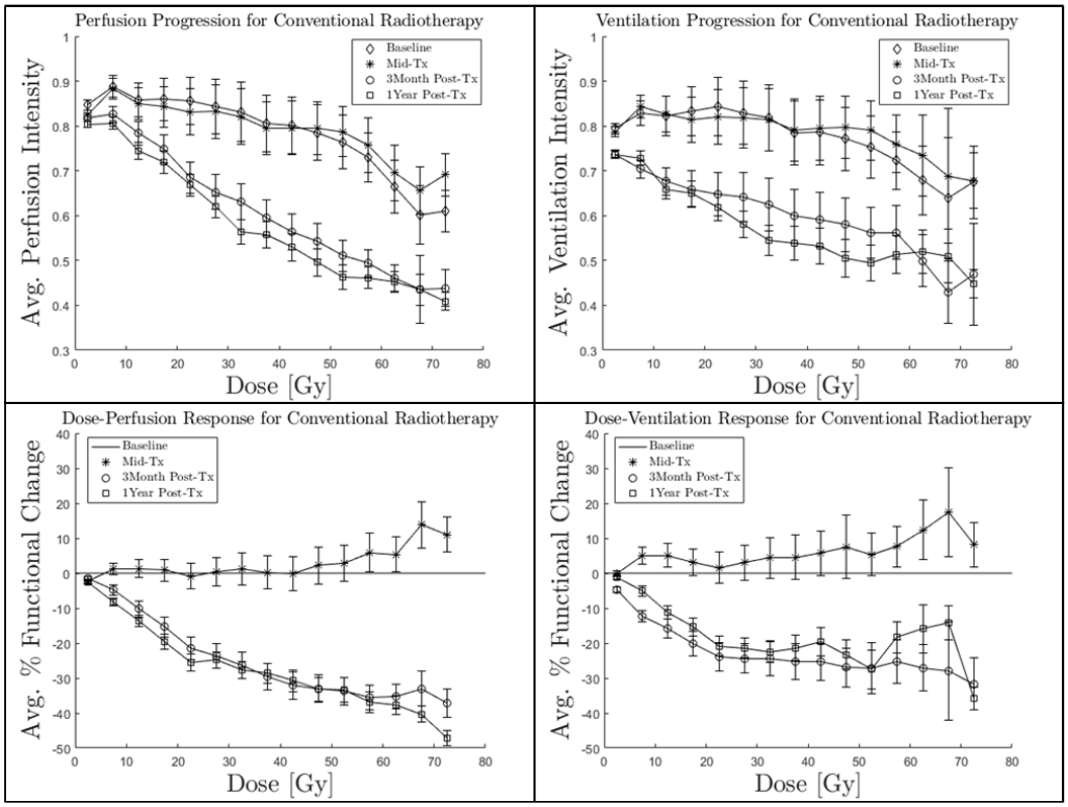

Figure 5.35: Perfusion (left) and ventilation (right) average functional intensity (top) and percent change (bottom) in the global lungs of 60 NSCLC patients treated with conventionally-fractionated RT. Standard error values based on the number of voxels contributing for each patient are presented as the uncertainty estimates.

Overall, as observed from these plots, there is a strong agreement between the perfusion and ventilation functional averages, albeit the ventilation plots are clearly presented with more variation and uncertainty. Specifically, in the dose bins between 0-30 Gy, an average functional intensity of $\sim$0.8 is observed followed by a decreasing intensity in the higher dose bins. This trend is not surprising given the findings of Marks et al. that showed functional defects were primarily located at or adjacent to the tumor [6], which are the areas that generally receive the highest dose. In both the average intensity and percentage change plots, it is interesting how closely the pre- and mid-treatment estimates are correlated while the 3-month and 1-year post-treatment plots also are closely correlated to each other. While this is not all together surprising, the only noticeable feature in the mid-treatment dose-response is the functional increase in the high dose bins. Based on the observations in the individual patient dose-response curves, it is known that the relative dose-response quantification overestimates the average change in these scenarios, but given that the average intensities at mid-treatment in these high dose bins is also presented to be higher than the pre-treatment estimates, it is suggestive that reperfusion and reventilation does tend to occur in this patient population.

Figure 5.35 presents the average intensity and functional change in the global lungs, but these plots can also be generated for the ipsilateral and contralateral lungs. However, because the ipsilateral lung received the majority of the dose, the global lungs and ipsilateral lung curves are very similar, but the contralateral lung average intensity and percent change appear drastically different as shown in Figure 5.36. Because the contralateral lung plots are quantified within 1 Gy dose bins instead of 5 Gy dose bins, there is a bit more uncertainty in the curves. This is explicitly observed in the low average intensity in the 0-1 Gy dose bin, which is indicative that these voxels receiving essentially no dose are often located on the periphery of the lung contour where there may be a mismatch between the SPECT and CT images causing the appearance of a lower intensity. As previously mentioned, this effect was remedied by incorporating a 4mm inner boundary on the Lungs-GTV structure in subsequent analyses, i.e. the risk assessment. Outside of this artifact, the functional intensity in the contralateral lung remains above 0.8, which was the high point within

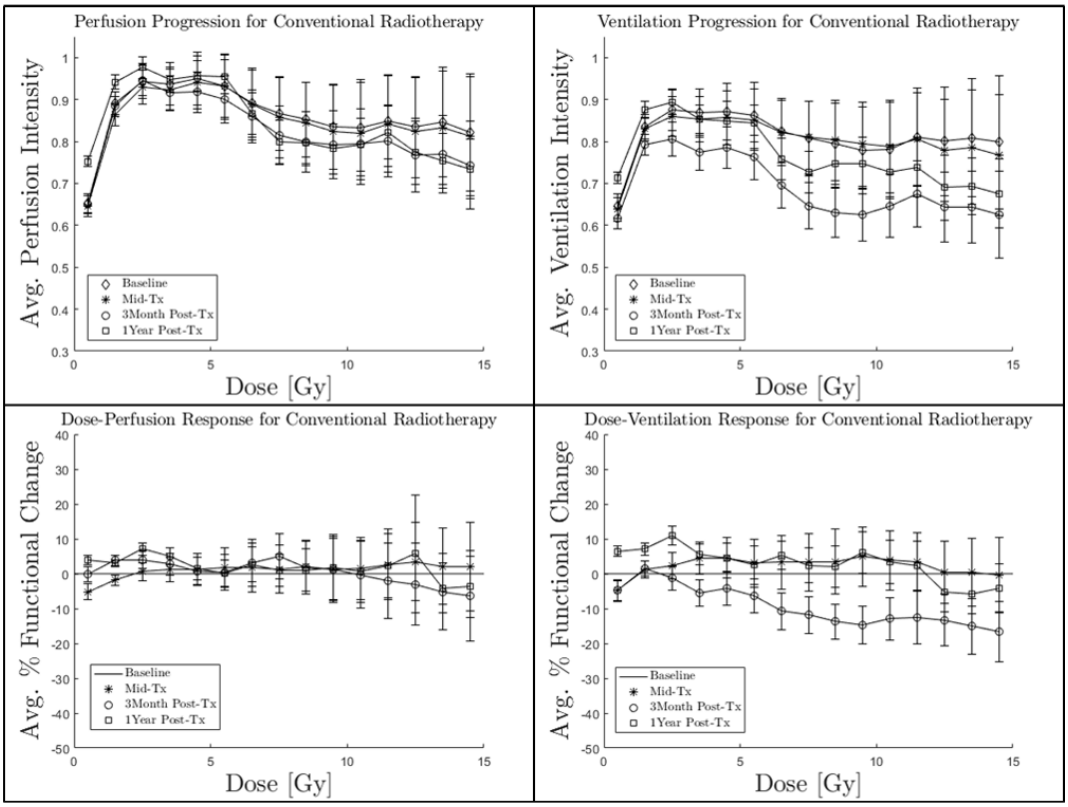

Figure 5.36: Perfusion (left) and ventilation (right) average functional intensity (top) and percent change (bottom) in the contralateral lung of 60 NSCLC patients treated with conventionally-fractionated RT. Standard error values based on the number of voxels contributing for each patient are presented as the uncertainty estimates.

the global lungs. Furthermore, it is remarkable how stable the perfusion intensity is in terms of longitudinal functional change. Effectively, the population-averaged dose-response does not vary more than 10% in either direction when delivered below 15 Gy.

The average functional intensity and percent change plots, within the global lungs, can also be generated for the 21 patients that received SBRT as shown in Figure 5.37. Based on the average perfusion intensity plot, it can be inferred that these patients present for treatment with a better pulmonary condition, which is not surprising given that SBRT is typically reserved for patients with smaller tumors. However, it appears that the ventilation intensity is rather impacted relative to the conventionally-fractionated RT patients. One reason for this reduction in ventilation intensity, given that these scans are known to have more uncertainty, is that 5 Gy dose bins were used to quantify this data even though the maximum EQD2 dose for these SBRT patients is much higher,

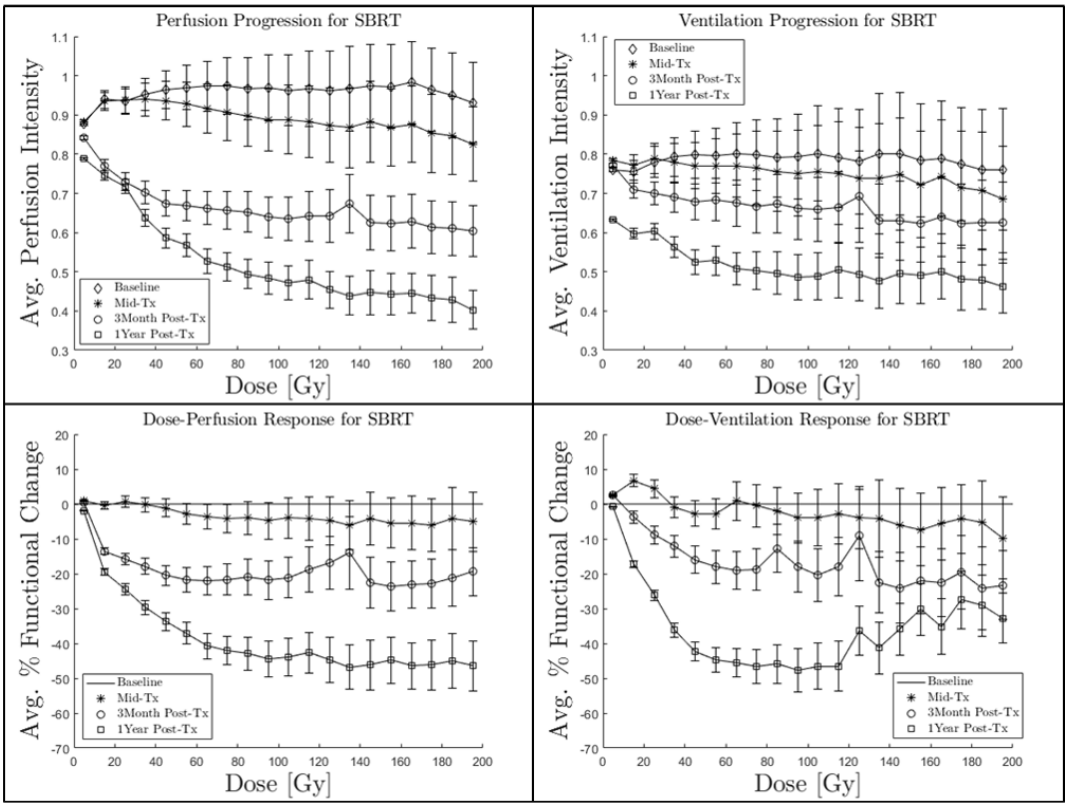

Figure 5.37: Perfusion (left) and ventilation (right) average functional intensity (top) and percent change (bottom) in the global lungs of 21 NSCLC patients treated with SBRT. Standard error values based on the number of voxels contributing for each patient are presented as the uncertainty estimates.

which results in less voxels contributing per dose bin resulting in less stability in the average intensity estimates. In terms of the dose-response, distinct logistic shapes are apparent at both of the post-treatment timepoints, and a slight reduction in intensity is observed at mid-treatment. It can also be observed that the functional intensity does not tend to progressively decrease past $\sim$60 Gy, suggesting a asymptote at a much lower dose than suggested in the Duke or NKI dose-response models [62].

The previous plots were generated using a simple average to calculate the dose-response for each cohort. In Figure 5.38, the dose-response is calculated based on a weighted-average that scales the each patient's response by the relative number of voxels contributed in the dose bin. Furthermore, instead of the standard error, the standard deviation was plotted as the uncertainty estimates. Clearly, a large variation in the responses exists, which is explicitly demonstrated by the

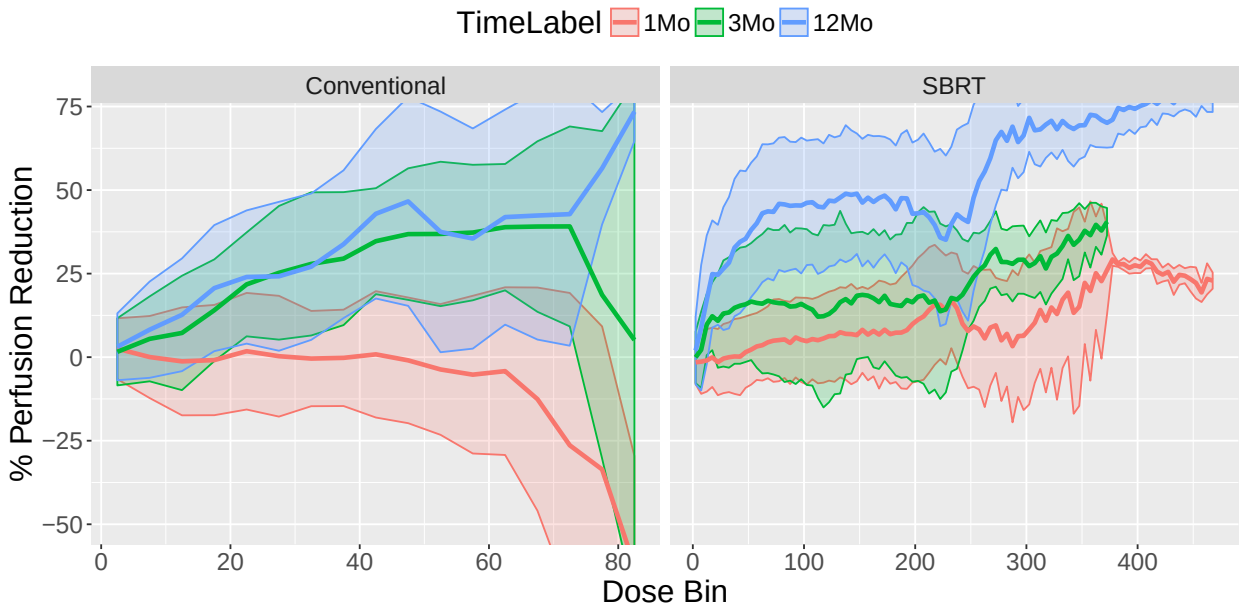

Figure 5.38: Conventional RT (left) and SBRT (right) perfusion dose-response calculated using a weighted-average based on the number of voxels contributing from each patient within each dose bin at mid-treatment (red), 3-months post-treatment (green), and 1-year post-treatment (blue). The shaded regions represent the standard deviation for each population-averaged curve.

individual patient dose-response curves shown in Figure 5.39, where the overlaid weighted-average curves are the same as the bolded lines in Figure 5.38.

Overall, the response curves at the post-treatment timepoints exhibit a logistic shape for the SBRT patients with maximal functional reduction at 1-year post-RT. In the conventional RT cohort, the post-treatment response appears more linear when using the simple average, but the responses appear to exhibit logistic characteristics when using the weighted-average calculation. It can also be observed that in each of the population-averaged plots, there is a increased variation in the high dose bins due to the limited number of voxels and patients contributing in these regions. While this effect is exacerbated in the high dose regions, it is indicative of the vulnerability associated with this simple averaging method. Therefore, to improve the estimates of the population-averaged response, an enhance modeling method is needed. Furthermore, because these plots are generated to represent functional damage, which in itself is indicative of cell death, and the individual patient responses were determined to exhibit a logistic response especially in the well-functioning lung, a logistic model was chosen as the best fit.

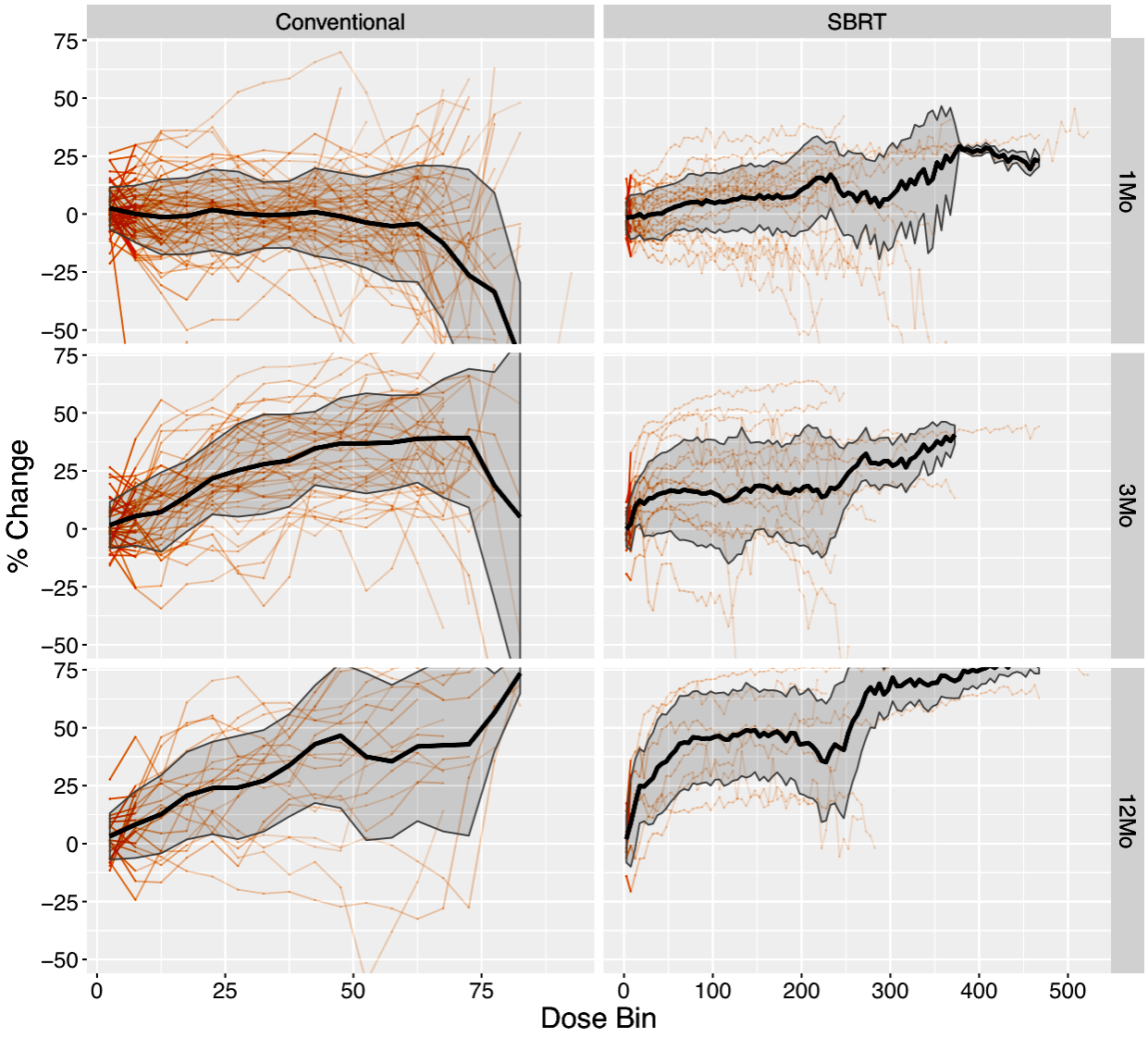

Figure 5.39: Conventional RT (left) and SBRT (right) perfusion dose-response calculated using a weighted-average accompanied with each individual patient's response at mid-treatment (top), 3-months post-treatment (middle), and 1-year post-treatment (bottom). The shaded regions represent the standard deviation for each population-averaged curve.

5.7 Patient-Specific Dose-Function Response Modeling

To account for inter-dependencies within an individual patient's dose-function response, the 3-parameter logistic model described by Scheenstra et al [39] was expanded to allow for a patient-specific asymptote (α_j, maximum possible reduction) and midpoint (μ_j; i.e. the dose at which 50% of the maximum reduction occurs). This is a common analytic approach for correlated data

and is also called a nonlinear mixed effects model, which refers to the mixture of population- and patient-specific parameters [136]. As such, the reduction in baseline intensity for patient j at dose bin i is modeled as:

$$\text{Patient-specific logistic model:} \frac{\alpha_j}{1+e^{(\mu_j - d_i)/\gamma}} \tag{5.8}$$

A non-patient-specific (i.e., population-averaged) inverse of the dose-effect slope at midpoint (γ) was set for all patients because of instability in fitting a patient-specific slope parameter. Using Equation 5.8, each patient's average dose-function response data points were fit to obtain the patient-specific model parameters. Because the patient-specific effects are assumed to be centered around global means, the population-average midpoint (μ) and maximum possible reduction (α) were calculated by averaging the patient-specific model parameters obtained from the cohort. As such, the population-level model takes the following form:

$$\text{Population-level logistic model:} \frac{\alpha}{1+e^{(\mu - d_i)/\gamma}} \tag{5.9}$$

where d_i is the dose at the center of dose bin i. By allowing each patient's dose-function response to be represented through a logistic function, the derived population-averaged logistic model better represents a patient's coherent functional reduction over all dose bins.

The patient-specific logistic function was further modified to characterize dose response stratified by baseline intensity, as shown:

$$\text{Stratified patient-specific model:} \frac{\alpha_j + \omega_k}{1+e^{(\mu_j - d_i)/\gamma}} \tag{5.10}$$

where k=$\{1,2,3,4\}$ denotes one of four baseline intensity groups, and $a_j + \omega_k$ denotes the patient-specific asymptote for voxels in group k. For identifiability, ω_4 was set to zero. The model shown in Equation 5.10 was used to describe the population-level response in each functional category. Voxels were grouped with respect to baseline perfusion. Specifically, the groups included all voxels with baseline intensity, expressed as a percent of the maximum normal-tissue intensity, in the

following ranges:

k=1: 10% *to* 30% *of baseline max*;

k=2: 30% *to* 50% *of baseline max*;

k=3: 50% *to* 75% *of baseline max*;

k=4: 75% *to* 100% *of baseline max*;

Voxels below 10% of the maximum intensity were excluded from the analysis on the basis of the low number of counts. The four functional categories, which roughly correspond to quartiles, were chosen before performance of the statistical analysis. The standard deviation in the reduction of function from baseline was allowed to vary with the number of voxels:

$$\text{Standard deviation: } \sigma(m_{ij})^{\lambda} \tag{5.11}$$

where m_{ij} is the number of voxels in dose bin i for patient j, σ is a scale parameter that describes the deviation between the patient-specific parameters and their population-level means, and λ modifies the deviation based on the number of voxels in that dose bin. Typically λ is negative, which corresponds to a reduction in variance with an increasing number of voxels. These models were fit using the nlme package in R [137].

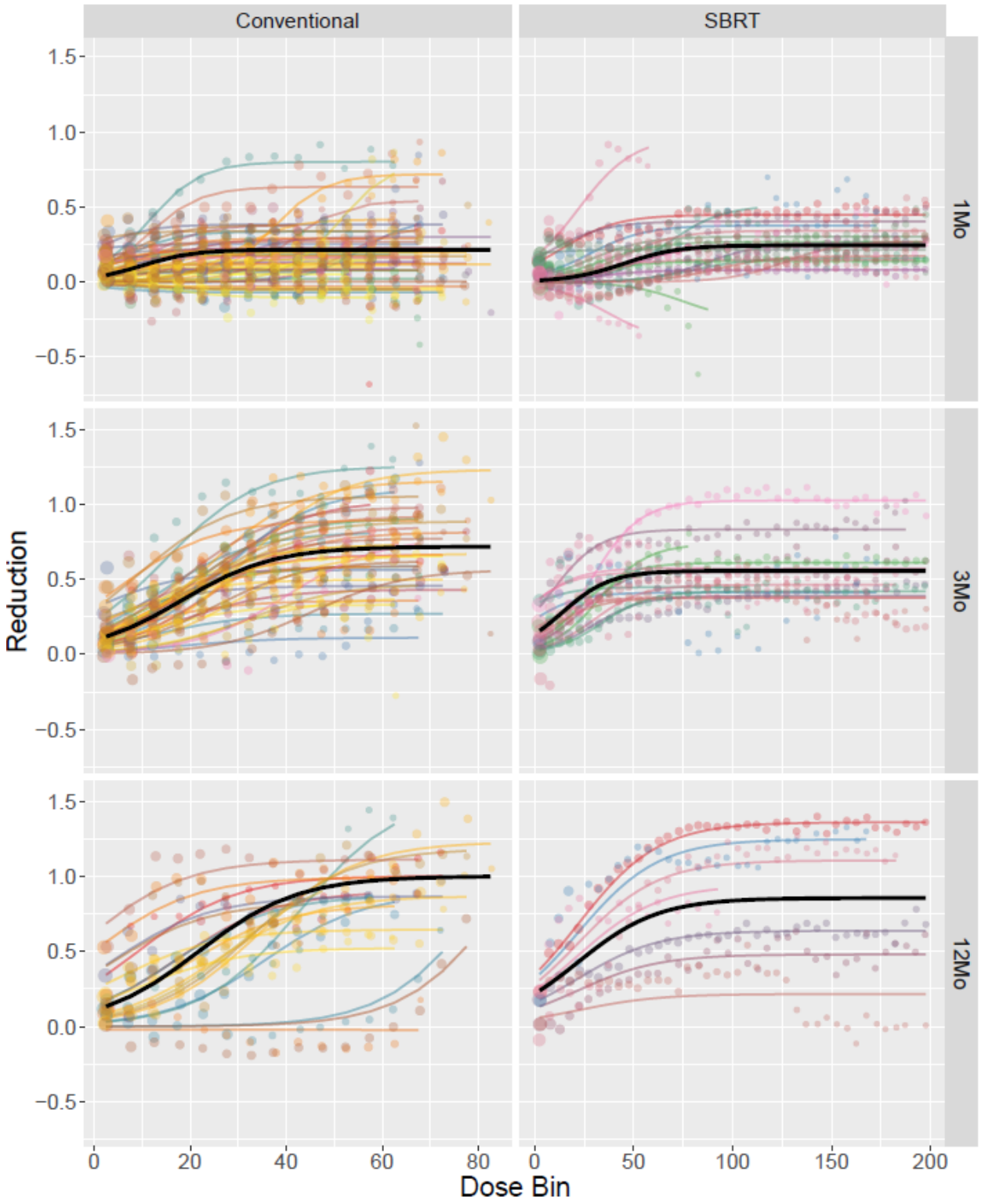

Figure 5.40: Individual patient dose-function response bin averages (colored points) and patient-specific model fits (colored lines) overlaid with the population-level model fit (solid) for initially well-perfused voxels. *Abbreviations*: 1Mo = midcourse treatment; 3Mo = 3 months post-treatment; 12Mo = 1 year post-treatment.

Voxelwise reduction in normalized perfusion intensity was modeled using a patient-specific logistic function. Functional reduction was measured and modeled as the decrease in normalized perfusion intensity, meaning a $d_{f,t,j,i}$ of -0.5 signifies a reduction of 0.5 normalized perfusion intensity units in that voxel. The presented models are graphically represented accordingly. For each patient, a normalized intensity of 1.0 signifies the average perfusion intensity of functioning voxels in the low-dose region of the contralateral lung. The population-level model parameters and standard deviations describing dose-perfusion response for the conventional RT and SBRT cohorts at each imaging time point are listed in Table 5.11 and Table 5.12.

5.8 Modeling Patient-Specific Dose-Response in Well-Perfused Voxels

Only well-perfused voxels were considered for the patient-specific and population-level dose-response curves shown in Figure 5.40. The color data points represent the average functional change in that dose bin for each patient. Each individual patient's data points are coherently modeled, as shown by the color-matched, shaded lines, using the logistic function shown in Equation 5.8. The patient-specific models are used to develop the bolded population-level dose-function response curves, as described by Equation 5.9. The population-level model fits and the associated uncertainty are explicitly tabulated in Table 5.11 and graphically shown in Figure 5.41A. The shaded 95% confidence intervals are a function of both the spread in the distribution of patient-specific responses and the number of voxels contributing to the data, as shown in Equation 5.11. A significant longitudinal increase in perfusion reduction is clearly observed, suggesting that lung function continues to degrade up to 1 year post-treatment. The maximal possible reduction asymptote ranged from approximately 30 to 60 Gy (EQD2), depending on the time point and treatment type. The patient- specific population-level models were compared with the population-level voxel-weighted average data points and non-patient-specific logistic models (i.e. simply fitting Equation 5.9 to the population-averaged data points), as shown in Figure 5.41B.

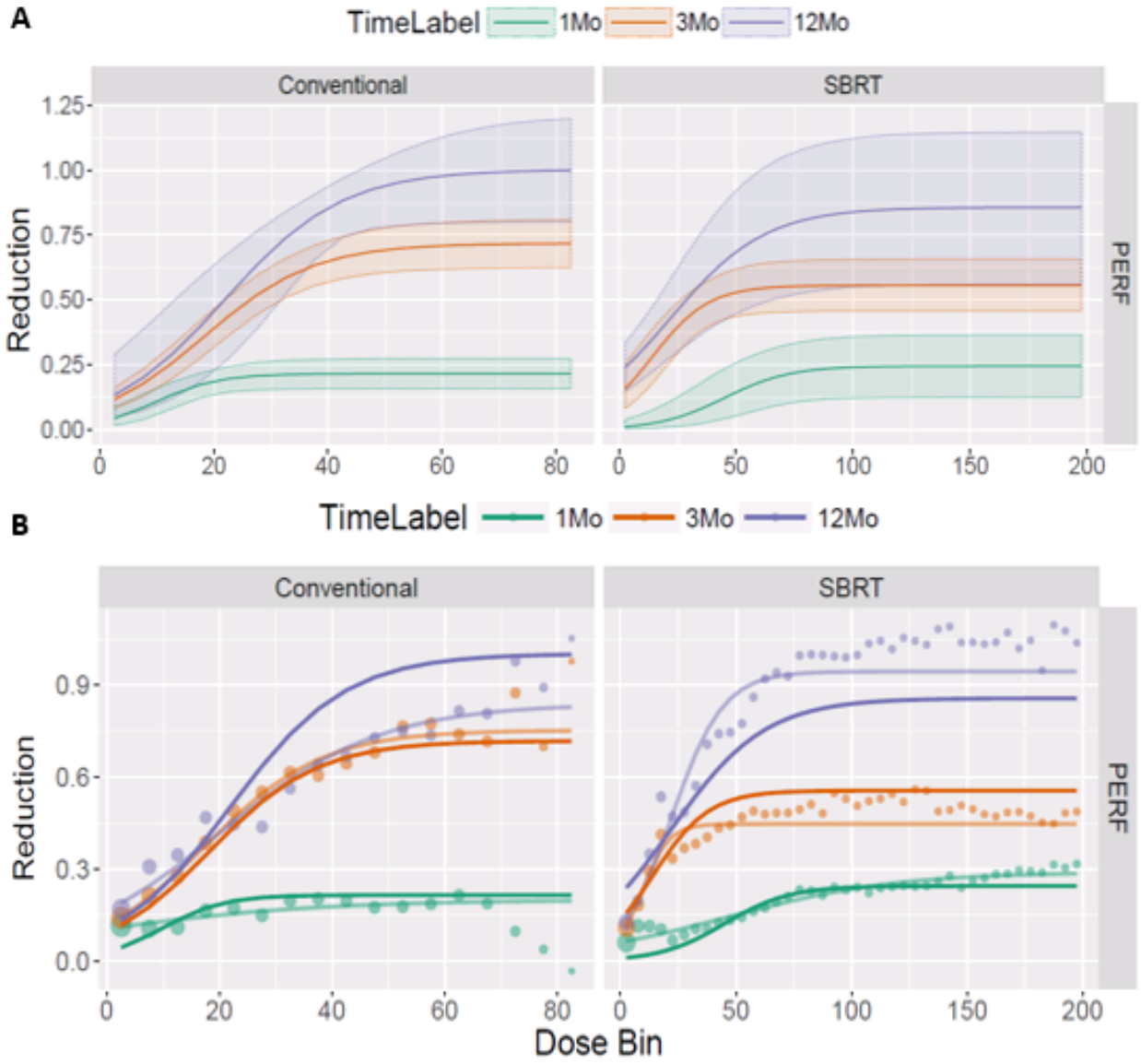

Figure 5.41: (A) Dose-perfusion response at mid-treatment (Mid-Tx) (green), 3 months post-treatment (3Month Post-Tx) (red), and 1 year post-treatment (1Year Post-Tx) (purple), fit using a patient-specific logistic model. The 95% confidence intervals are represented by the shaded region. B) Patient-specific logistic model fits (solid lines) compared with the voxel-weighted average data (points) and non-patient-specific logistic model fits (shaded lines). *Abbreviations*: Conventional = conventional radiation therapy; SBRT = stereotactic body radiation therapy.

Dose-Function Response in Well-Perfused Lung Model Parameters

RT Modality / Timepoint	n	$E[\alpha_j]=\alpha$	sd[α_j]	$E[\mu_j]=\mu$	sd[μ_j]
Conventional RT / Mid-Tx	54	0.22 (0.16,0.27)	0.21 (0.17,0.26)	9.8 (4.1,15.5)	17.9 (13.9,23.1)
Conventional RT / 3Month Post-Tx	37	0.72 (0.62,0.81)	0.28 (0.22,0.35)	18.2 (14.4,22.1)	10.9 (8.2,14.4)
Conventional RT / 1Year Post-Tx	19	1.00 (0.80,1.21)	0.44 (0.28,0.69)	21.8 (8.9,34.7)	28.1 (19.8,40.0)
SBRT / Mid-Tx	20	0.24 (0.12,0.37)	0.27 (0.18,0.40)	45.0 (28.9,61.2)	35.3 (24.5,50.9)
SBRT / 3Month Post-Tx	14	0.56 (0.46,0.66)	0.19 (0.13,0.27)	13.9 (4.4,23.3)	17.0 (10.8,26.7)
SBRT / 1Year Post-Tx	7	0.86 (0.56,1.15)	0.39 (0.23,0.67)	21.8 (18.3,25.3)	-

RT Modality / Timepoint	γ	σ	λ
Conventional RT / Mid-Tx	5.4 (4.0,6.8)	0.22 (0.19,0.26)	-0.11 (-0.13,-0.08)
Conventional RT / 3Month Post-Tx	9.6 (8.5,10.7)	0.32 (0.24,0.41)	-0.13 (-0.17,-0.10)
Conventional RT / 1Year Post-Tx	10.3 (8.7,12.0)	0.16 (0.10,0.25)	-0.03 (-0.10,0.03)
SBRT / Mid-Tx	14.0 (11.5,16.5)	0.10 (0.09,0.11)	-0.06 (-0.07,-0.04)
SBRT / 3Month Post-Tx	12.1 (9.9,14.4)	0.11 (0.10,0.13)	-0.01 (-0.04,0.01)
SBRT / 1Year Post-Tx	20.4 (16.4,24.3)	0.12 (0.09,0.15)	0.03 (-0.03,0.08)

Abbreviations: Mid-Tx = midcourse treatment; 3Month Post-Tx = 3 months post-treatment; 1Year Post-Tx = 1 year post-treatment; SBRT = stereotactic body radiation therapy

Models with "-" listed in the sd[μ_j] column were unable to converge using patient-specific midpoints, and thus, the same population-level midpoint was given to all patient in that cohort.

Table 5.11: Population-level model parameters and standard deviations describing the expected dose-function response in well-perfused voxels at baseline (95% confidence intervals).

5.9 Stratified Dose-Function Response Given Baseline Perfusion Intensity

The patient-specific voxelwise reduction in normalized perfusion intensity with respect to planned dose was modeled for each stratified baseline intensity level using Equation 5.10. The population-level models can be interpreted as a prediction for voxelwise functional reduction in an arbitrarily selected patient given the voxel's planned dose and functional categorization at baseline. The numerical results are given in Table 5.12 and graphically depicted in Figure 5.42. From these results, we observe that the population-average maximal reduction in each voxel group is longitudinally increasing (i.e. $\omega_1 < \omega_2 < \omega_3 < \omega_4 = 0$), and at the 3- and 12-month post-treatment time points, the confidence intervals for each parameter are non-overlapping. This trend between perfusion reduction and baseline function in both cohorts suggests that higher functioning voxels at baseline are damaged at a greater rate than lower functioning voxels.

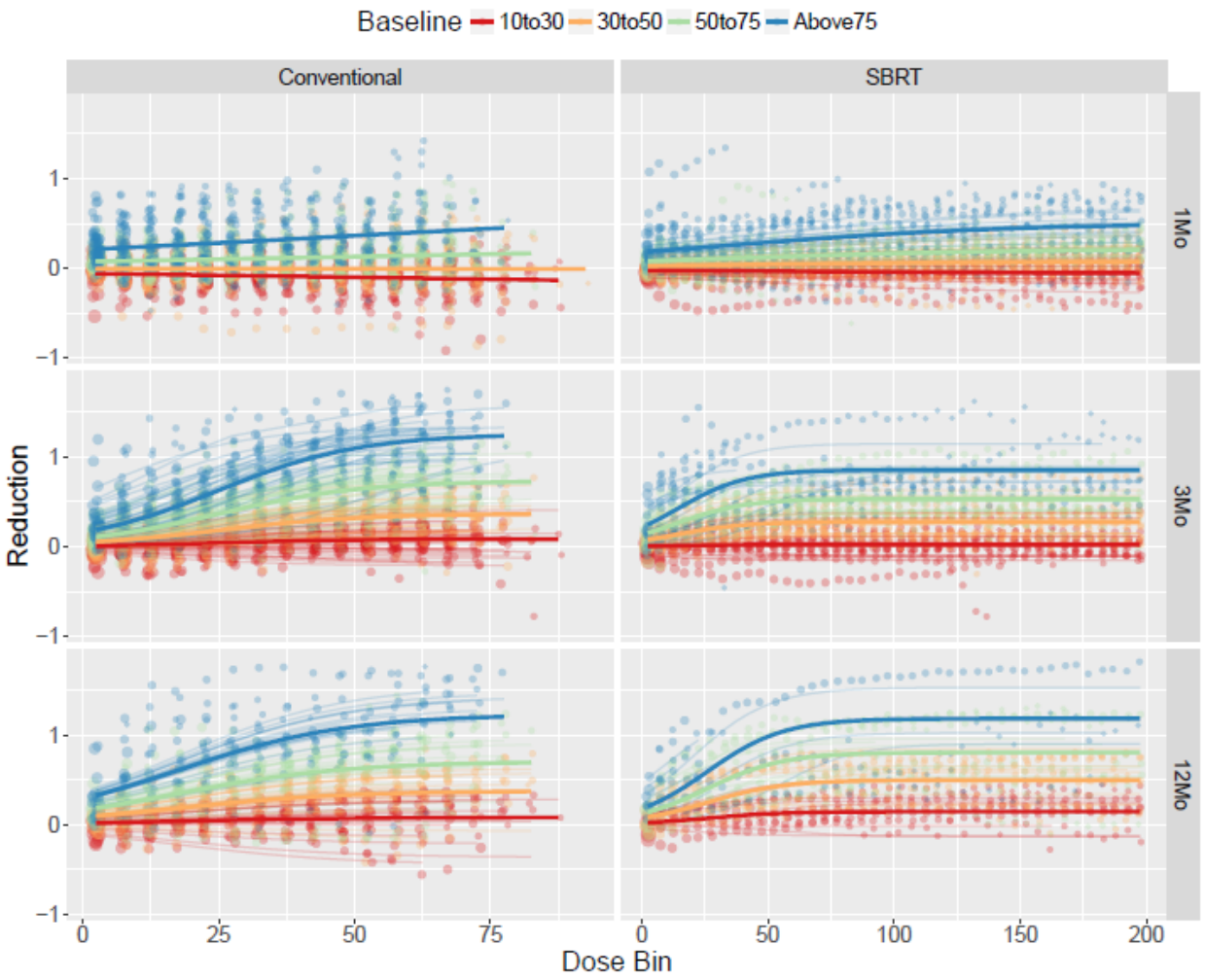

Figure 5.42: Stratified dose-perfusion response for voxels in each normalized baseline intensity level: 10% to 30% (red), 30% to 50% (orange), 50% to 75% (green), and >75% (blue) of the maximum intensity. Abbreviations: Conventional = conventional radiation therapy; SBRT = stereotactic body radiation therapy.

Dose-Function Response Stratified by Baseline Perfusion Intensity Model Parameters

RT Modality / Timepoint	$E[\alpha_j]=\alpha$	$sd[\alpha_j]$	$E[\mu_j]=\mu$	$sd[\mu_j]$	γ
Conventional RT / Mid-Tx	0.71 (-0.25,1.66)	–	46.6 (-102.6,195.8)	–	53.8 (-5.4,113.1)
Conventional RT / 3Month Post-Tx	1.26 (1.19,1.33)	0.16 (0.13,0.21)	25.1 (20.6,29.6)	13.2 (10.3,16.9)	13.0 (11.9,14.1)
Conventional RT / 1Year Post-Tx	1.23 (1.10,1.37)	0.23 (0.16,0.32)	17.9 (14.9,20.9)	–	15.4 (12.6,18.1)
SBRT / Mid-Tx	0.51 (0.43,0.59)	0.13 (0.09,0.18)	34.2 (19.1,49.3)	–	58.4 (41.5,75.2)
SBRT / 3Month Post-Tx	0.86 (0.77,0.94)	0.16 (0.11,0.23)	14.6 (4.0,25.1)	19.8 (13.4,29.2)	13.3 (11.6,15.1)
SBRT / 1Year Post-Tx	1.19 (1.02,1.36)	0.22 (0.13,0.38)	26.0 (14.1,37.9)	15.8 (9.1,27.2)	15.1 (13.3,16.9)
RT Modality / Timepoint	ω_1	ω_2	ω_3	σ	λ
Conventional RT / Mid-Tx	-0.90 (0.32,-2.12)	-0.72 (0.26,-1.69)	-0.45 (0.16,-1.07)	0.51 (0.46,0.57)	-0.15 (-0.17,-0.14)
Conventional RT / 3Month Post-Tx	-1.17 (-1.13,-1.22)	-0.89 (-0.85,-0.93)	-0.53 (-0.49,-0.56)	0.29 (0.25,0.32)	-0.10 (-0.12,-0.08)
Conventional RT / 1Year Post-Tx	-1.15 (-1.06,-1.24)	-0.85 (-0.77,-0.93)	-0.53 (-0.46,-0.59)	0.44 (0.37,0.53)	-0.12 (-0.14,-0.09)
SBRT / Mid-Tx	-0.57 (-0.50,-0.63)	-0.43 (-0.38,-0.49)	-0.29 (-0.25,-0.33)	0.21 (0.20,0.22)	-0.09 (-0.10,-0.08)
SBRT / 3Month Post-Tx	-0.83 (-0.81,-0.86)	-0.58 (-0.55,-0.60)	-0.32 (-0.30,-0.35)	0.17 (0.16,0.18)	-0.07 (-0.08,-0.05)
SBRT / 1Year Post-Tx	-1.04 (-0.98,-1.09)	-0.69 (-0.64,-0.73)	-0.38 (-0.33,-0.43)	0.27 (0.25,0.30)	-0.13 (-0.14,-0.11)

Abbreviations: Mid-Tx = midcourse treatment; 3Month Post-Tx = 3 months post-treatment; 1Year Post-Tx = 1 year post-treatment; SBRT = stereotactic body radiation therapy

Models with "-" listed in the $sd[\mu_j]$ column were unable to converge using patient-specific midpoints, and thus, the same population-level midpoint was given to all patient in that cohort. The number of patients contributing to each model is the same as shown in Table II.

Table 5.12: Population-level model parameters and standard deviations describing the expected dose-function response stratified by functional categorization at baseline (95% confidence intervals).

5.10 Discussion

This study quantified the voxelwise reduction in perfusion during and after radiation treatment by measuring the longitudinal change in normalized SPECT intensity, similar to methods in previous works. However, this analysis aimed to enhance the characterization of personalized functional changes by applying a patient-specific modeling approach that explicitly accounts for interdependencies within an individual patient's dose-function response. Using this methodology, population-averaged dose-function response curves and their uncertainties were calculated for patients with NSCLC undergoing conventional RT and SBRT.

From age to chemotherapy to comorbidities, many patient-, treatment-, and disease-related factors explicitly affect an individual's dose-function response [138–140]. Each patient has a unique signature that inherently creates a distinct treatment response curve. As such, the voxels and the corresponding dose effect from one patient are more closely related to each other than to voxels from a different patient. Although the dose effect has classically been modeled by fitting population-averaged data points, it is proposed that a patient-specific model can more accurately

describe the coherent dose-function response in an individual patient.

Logistic models have classically been used to describe dose-effect relations for cell survival. Boersma et al first proposed using the logistic model to describe changes in vascular subunits within the lung [34]. Scheenstra et al recently showed that local functional changes in patients undergoing SBRT were best represented through a logistic model driven by 3 parameters: (1) maximal reduction effect (asymptote); (2) dose to obtain 50% of maximal effect (midpoint); and (3) slope of the linear dose effect [39]. However, because a patient's signature effects the dose-function response over all dose bins, there is an inherent correlation among data points contributed by each patient. As a consequence of Jensen's inequality, averaging each dose bin across patients would introduce bias in the resulting estimated population-average curve [141]. Therefore, a mixed-effects nonlinear regression model was used in this analysis to allow for a patient-specific maximal effect and midpoint dose, as shown in Equation 5.8. With this approach, each patient's dose-perfusion response assumed a unique form, and population-level trends were derived, as shown in Figure 5.40. With application of a logistic function to each individual patient's data (as opposed to averaging each dose bin separately), the derived population-level model will better estimate the dose-function response for a future, arbitrarily selected patient.

Only minimal reductions in the high-dose regions were observed during treatment, whereas increasing longitudinal reductions occurred in these same areas after treatment. Furthermore, both patients undergoing conventional RT and those receiving SBRT consistently reached an asymptote in functional reduction near the target dose, suggesting that the maximal reduction effect occurs at a lower dose in conventionally fractionated RT. Although nearly all patients exhibit perfusion reduction at 3Month Post-Tx, 3 patients in both the conventional RT and SBRT cohorts exhibit markedly better response at 1Year Post-Tx than the rest of their cohort. This suggests a recovery pathway and illustrates the need for patient-specific modeling.

Random effects were assumed to vary around population-level global means. Standard deviations were calculated to account for both the deviation from the mean and the statistical uncertainty associated with each data point. Therefore, the 95% confidence intervals represent the bounds of

measured dose response for the conventional RT and SBRT cohorts. Analogously, these intervals can be interpreted as the uncertainty in predicting the voxelwise reduction in function from an arbitrarily selected patient given the planned dose.

Previous works have mostly focused on analyzing functional response in well-perfused and well-ventilated regions. This focus stems from the idea that limiting dose to functioning lung can reduce toxicity by maintaining a patient's functional reserve. However, the well-perfused regions have not been consistently defined and only consist of a small portion of the lung receiving a high dose. This study modeled the well-perfused dose response for comparison with previous modeling techniques, as shown in Figure 5.41B. However, this is the first study to differentially characterize dose-function response based on pre-treatment functional status across all functioning voxels. Although deviations from the population-level models are observed, the consistent differential treatment response suggests that initially higher functioning voxels exhibit a higher rate of perfusion loss, as shown in Figure 5.42.

Functional categorizations were chosen based on guidance from previous work [23, 36]. Furthermore, the ranges were kept broad to ensure sufficient normal lung volume and limited statistical uncertainty in each category. However, because these categorizations were arbitrarily selected to represent functional capabilities, the bins may distinguish between regions that are not meaningfully different in their ability to exchange gas. Our results suggest that the voxelwise reduction in perfusion is a nonlinear function of baseline perfusion, in addition to being a nonlinear function of dose, which makes numerical fitting of this model substantially more difficult.

The amount of reperfusion has been shown to be directly proportional to perfusion deficiency [36], suggesting that perfusion reduction in initially poorly functioning regions is diminished by a reperfusion effect that is inversely proportional to baseline intensity. The response was quantified in all functioning voxels because it is hypothesized that any portion of lung that is functioning at baseline can consequently become damaged and contribute to the loss of functional reserve. Future studies aim to further investigate the reperfusion effect and alternatively model the potential for functional improvement.

Although SPECT/CT is generally considered the gold standard for functional lung imaging, challenges regarding limited spatial resolution and presence of artifacts have been well documented. Because each frame of the SPECT image is acquired over a time period that typically en- compasses several cardiac and breathing cycles, physiological motion will lead to spatial blurring of the signals. Although this may introduce errors in individual voxel intensities, the large binning of voxels reduced the impact of decreased spatial resolution. Average functional change was tallied within 5 Gy isodose volumes (i.e., dose bins) such that numerous voxels contribute within each region. Although the use of rigid registration for functional image characterization can result in uncertainties, especially in areas of large motion and deformation, deformable image registration has typically not been applied to SPECT imaging because of low spatial resolution. Future studies using SPECT images may be improved by adjusting the acquisition parameters to better match the breathing states between the SPECT/CT and the planning CT image.

In many functional imaging modalities, such as SPECT/CT, normalization is required to quantitatively analyze longitudinal change. Most prior studies analyzing perfusion changes using SPECT/CT have normalized intensities using the average value of the functioning voxels in the low-dose region of the contralateral lung [1, 37, 38]. Although the specific definition of the low-dose region has varied, the technique is generally well accepted because minimal functional changes are expected in voxels receiving a low dose. We have yet to apply a patient-specific modeling approach to the contralateral lung, but this assumption was supported by the finding that the population-averaged functional change in the contralateral lung did not decrease significantly below 15 Gy, as shown in Figure 5.36.

Because these clinical data were gathered between 2007 and 2013, patients were treated with a conventionally-fractioned 3-dimensional conformal RT approach instead of the modern intensity modulated RT techniques currently used in the clinic. Many of these patients who received 3-dimensional conformal treatment would now be treated with volumetric modulated arc therapy, which would further change the dose-volume histogram profile. In an attempt to standardize the radiation effect between the treatment fractionation schemes, all doses were converted to EQD2

dose values. Furthermore, although some patient falloff occurred at the 3- and 12-month time points, we would not expect this loss of data to depend on the patient's unobserved voxelwise dose-response curve; therefore, it should not cause bias in our estimated regression coefficients.

By characterizing the patient-specific dose-function response in all baseline functioning voxels, this work provides specific population-level estimates for the expected voxelwise reduction in perfusion at mid-treatment, 3-month post-treatment, and 1-year post-treatment. These models allow for enhanced prediction of personalized functional damage by developing the population-level response through individual patient assessment and by segmenting the expected functional reduction based on a patient's pre-treatment functional status. In theory, by applying the generated dose-response incidence models, the cumulative functional lung damage for an arbitrarily selected patient could be predicted and used to support functional-guided RT plans by weighting voxels based on their risk of functional damage.

5.11 Conclusion

A patient-specific modeling approach was applied to quantify the dose-function response using perfusion SPECT/CT images in patients with NSCLC undergoing conventional RT and SBRT. By deriving functional response from patient-specific assessment, the population- level models presented in this analysis can be used to better predict functional lung damage in an arbitrarily selected patient. Differential treatment responses were observed based on the functional status of the voxel at baseline, suggesting that the highest functioning voxels are damaged at the highest rate. Although further refinement is required to implement personalized predictions of functional damage in the clinic, this work provides a simple methodology, applicable to any functional imaging modality, to more accurately model dose-function response.

CHAPTER VI

Analyzing the Dose-Function Toxicity Pathways

6.1 Summary

While dose to normal lung has commonly been linked with radiation-induced lung toxicity (RILT) risk, it has been hypothesized that including functional lung metrics in treatment planning may help to further optimize dose delivery and reduce RILT incidence. The purpose of this study was to investigate the impact of dose delivered to functional lung regions by analyzing perfusion (Q), ventilation (V), and combined VQ SPECT dose-function metrics with regard to RILT risk in non-small cell lung cancer (NSCLC) patients that received radiation treatment (RT). Patients with 3-month post-RT SPECT scans were also analyzed to assess the amount of total functional damage following treatment and its effect on RILT incidence. Specifically, this research integrated the post-treatment functional damage and quantified the delivered dose to functional lung categorizations in an attempt to identify dose-function trends that are associated with Grade 2+ radiation pneumonitis and fibrosis incidence.

V/Q SPECT images acquired from 88 locally-advanced NSCLC patients prior to undergoing conventionally-fractionated RT were retrospectively analyzed. A subset of 37 of these patients had 3-month post-treatment SPECT scans available. Dose was converted to equivalent dose per 2 Gy fraction (EQD2), and regional lung segments were defined as follows: upper lung above the carina, lower lung below the inferior pulmonary vein, and middle lung between the two. Three functional categorizations were defined to represent low-functioning, normal-functioning, and high-

functioning lung. The percent of functional lung category receiving $\geq$20 Gy (LF20/F20/HF20 or lowVQ20/midVQ20/highVQ20 for combined VQ metrics) and average functional intensity receiving $\geq$20 Gy (iV20) were calculated. The damage fraction was defined as the total reduction in functional intensity at the given timepoint relative to the total baseline intensity. RILT was defined as Grade 2+ radiation pneumonitis and/or clinical radiation fibrosis. Univariable and multivariable logistic regression were used to evaluate the association between dose-function metrics and the risk of RILT.

By analyzing V/Q normalized intensities and functional distributions across the population, a wide range in functional capability, especially in the ipsilateral lung, was observed in NSCLC patients prior to RT. Through multivariable regression models, global lung average dose to lower region of lung structure (ADL) was found to be significantly associated with RILT, while perfusion and ventilation iV20 were correlated with RILT when using ipsilateral lung metrics. Through ROC analysis, the intersection volume between low-function ventilation and low-function perfusion receiving $\geq$20 Gy, as a percentage of total lung structure volume (lowVQ20) in the ipsilateral lung was found to be the best predictor (AUC=0.79) of RILT risk. Irradiation of the inferior lung appears to be a locational sensitivity for RILT risk. The multivariable correlation between ipsilateral lung iV20 and RILT, as well as the association of lowVQ20 and RILT, suggest that irradiating low-functioning lung, which is indicative of pulmonary dysfunction, may lead to higher toxicity rates. Furthermore, a significant correlation was found between the amount of total functional damage that occurred at the 3-month post-treatment and RILT incidence.

6.2 Introduction

Radiation-induced lung toxicity is a common side effect in non-small cell lung cancer patients undergoing radiation treatment due to the high prescription doses and large volumes of normal lung incident in the radiation field. As local failure remains a significant hazard in the management of NSCLC, it has long been a goal to increase tumor control, while limiting RILT risk. In a secondary analysis of the RTOG-0617 randomized trial, the use of IMRT compared with 3D conformal RT

planning was associated with lower rates of severe radiation pneumonitis (RP), suggesting that dose modulation can help to reduce toxicity [142]. As such, ongoing clinical trials, including RTOG-1106, have aimed to improve local control through the use of PET adaptive RT planning to specifically increase dose to actively growing tumor [143].

Another strategy hypothesized to improve the therapeutic ratio is to preferentially limit dose to functional lung to reduce the risk of RILT. This has been an area of investigation since the early 1990s, when studies from NKI [5] and Duke University [4] first investigated the use of functional lung imaging in radiation treatment planning. Both Boersma et al. [34] and Marks et al. [1] successfully used SPECT to quantify functional lung changes following radiation treatment, which motivated the potential to inversely incorporate perfusion and/or ventilation metrics in RT planning [6]. In 2002, Seppenwoolde et al. theorized that radiation treatment plans could be optimized to maximize lung function after treatment by sparing well-perfused lung tissue [8], which has formed the basis for functional-avoidance RT planning in lung cancer patients. However, this recommendation was based on the inability for bullous lung (i.e. regions of poor perfusion and ventilation) to reperfuse following RT and was not based on the study of its direct impact to patient outcome [36]. Although functional-avoidance may play a vital role in the treatment of some patients, an enhanced understanding for the dose-function metrics that are associated with RILT is needed to ensure optimal patient-specific dose delivery.

Currently, most RT plans designed for NSCLC patients are developed solely to limit physical dose metrics, such as mean lung dose (MLD) and volume of lung receiving ≥ 20 Gy (V20). While these volumetric dosimetrics treat all lung as functionally-equivalent, in practice there is wide variation in the functional distribution both within a patient's lungs as well as between patients. Recently, CT-based functional imaging has gained interest as a possible tool for functional lung mapping due to its ability to quantify ventilation-based metrics and its wide-availability in the clinic. Vinogradskiy et al has observed extensive functional defects in stage III NSCLC patients [19] and has also demonstrated functional-avoidance RT techniques using 4DCT ventilation maps [27]. Based on this research [26] and various other studies [20, 13], functional-avoidance clinical

trials are underway at numerous institutions [82, 144–146].

In theory, functional imaging allows for personalized RT planning that can minimize damage, and ultimately, can reduce the risk of RILT. Despite this potential, there is little clinical data to validate that it is an effective approach to reducing toxicity, and specifically that shifting dose from high-functioning regions into low-functioning regions in patients with heterogeneous lung function reduces the incidence or severity of RILT. The purpose of this study was to investigate the utility of functional lung images in RT planning by analyzing the correlation between V/Q SPECT-based dose-function metrics and the incidence of RILT. Specifically, we defined functional lung categorizations based on perfusion, ventilation, and combined perfusion and ventilation and quantified the delivered dose to these various functional lung regions in an attempt to identify dose-function metrics associated with grade 2+ RILT incidence. Through this study, we aim to better understand the implications of redistributing dose in the lung and to identify functional targets that may be used to mitigate RILT incidence through functional-guided RT planning.

6.3 Methods

6.3.1 Patient Cohort

A total of 88 NSCLC patients treated with conventionally fractionated RT, with (n=76) and without (n=13) concurrent chemotherapy, from two separate institutional review board (IRB)- approved studies (2006.040: n=58, treated 2007–2013; 2015.035: n=30, treated 2015–2019) were retrospectively analyzed. The prescription dose in both cohorts was typically 60 – 74 Gy over 30 fractions. However, the latter cohort was primarily treated with volumetric modulated arc therapy (VMAT), as opposed to 3D conformal RT, and functional-avoidance RT planning and re-planning, i.e. adaptive RT at mid-treatment, was implemented to limit dose to above-average V/Q SPECT functional intensity. In this study, RILT was defined as grade 2+ RP and/or grade 2+ clinical pulmonary fibrosis. RP and pulmonary fibrosis were diagnosed and graded prospectively according to a pre-specified system [134], with a grading scale consistent with that of the common

terminology criteria for adverse events (CTCAE) v3.0 and the maximal grade was reported [135]. While these pathologies are often considered distinct clinical processes, RILT was used because it encompasses the primary dose-limiting pulmonary complications that impact patient survival and quality of life and some evidence suggests these toxicities may be linked [103, 101].

6.3.2 Data Processing

V/Q SPECT/CT scans (voxel size: 3. 5 mm x 3.5 mm x 2 mm) were obtained from each patient (Symbia T6, Siemens Medical Solutions, Malvern, PA) prior to RT with the patient supine and immobilized using a standard thorax support device. Each patient was first imaged for pulmonary ventilation by inhaling aerosolized 99mTc-diethylenetriaminepentaacetic from an 1850 MBq reservoir and subsequently imaged for pulmonary perfusion after intravenous injection of 185 MBq of 99mTc-labeled macroaggregated albumin particles. Each SPECT scan was rigidly registered to the treatment planning CT using an alignment tool embedded in a commercial treatment planning system (Eclipse, Varian Medical Systems, Palo Alto, CA). Through the application programming interface within this treatment planning system, a novel program (C#) was implemented to process and analyze the spatially aligned dose-function data. Saturation artifacts were cleansed from the SPECT images by removing any voxel with functional intensity greater than three standard deviations above the mean of the normal-functioning region. Raw SPECT intensities (f_i) were normalized to the average intensity in the low-dose ($\leq$5 Gy), normal-functioning region of the contralateral lung ($\mathbb{N}$), shown in Equation 3.1, as this region was assumed to be stable against radiation-induced longitudinal functional changes.

This normalization was performed to equalize functional values such that a normalized functional intensity of 1.0 equates to the average intensity of normal-functioning lung for all patients. Normalized perfusion and ventilation SPECT intensities were used as a direct surrogate for lung function and dose values were converted to the nominal EQD2 to biologically correct for fractionation of the RT dose (α/β=2.5 Gy) [130].

Three functional categorizations were created to represent low-function lung (LF), normal-

function lung (F), and high-function lung (HF) lung. Each voxel with normalized functional intensity $f_i^{\mathbb{N}}$ was assigned a functional categorization based on its intensity relative to the maximum intensity $f_{maximum}^{\mathbb{N}}$ the schema shown in Table 3.2. The functional categorization limits were chosen based on previous guidance [36, 23] and were determined prior to any statistical modeling. An example image of the functional categorizations is shown in Figure 6.1. For this study, patients with $< 5\%$ LF lung were considered to have no functional defects.

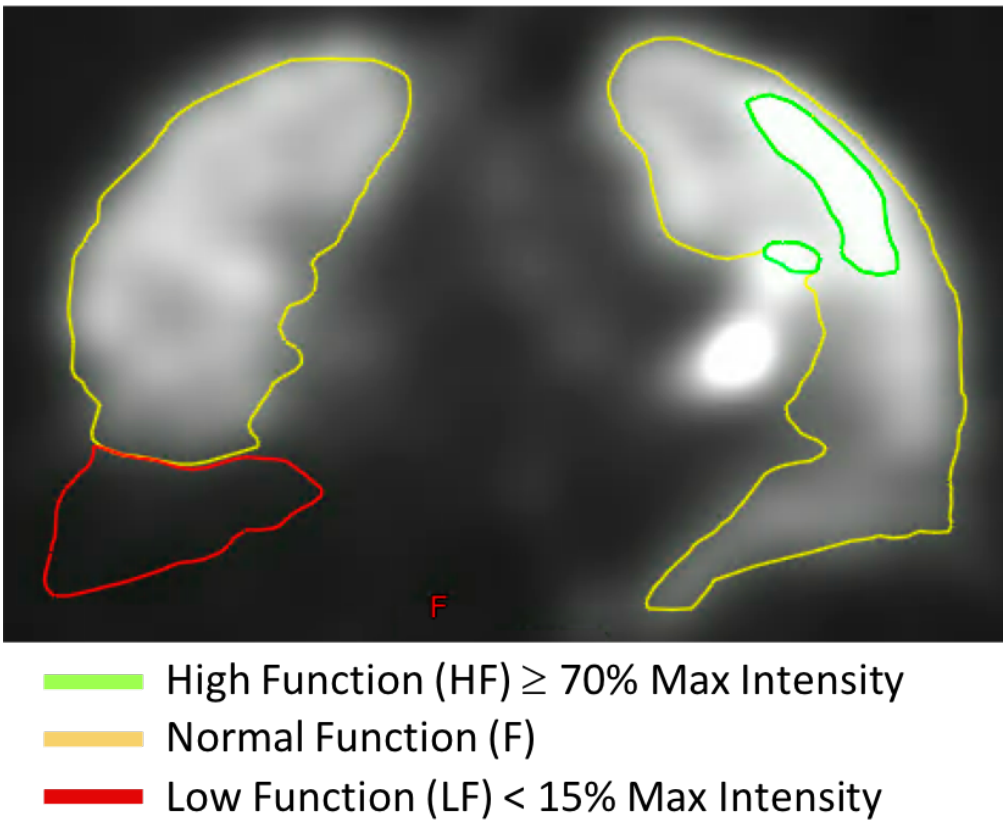

Figure 6.1: Example perfusion SPECT image demonstrating the functional categorizations for example patient UM025.

Pre-treatment dose-function metrics were calculated within the global lungs, ipsilateral lung (i.e., individual lung structure receiving the higher mean dose), and contralateral lung using clinically-defined lung contours, excluding the GTV and a 4mm inner boundary ($\sim$voxel width) to reduce the partial volume effect. Regional lung segments were defined as follows: upper lung above the carina, lower lung below the inferior pulmonary vein, and middle lung between the upper and

lower segments as shown in Figure 6.2. The number of patients with primary tumor involvement in the given lung sextant, with grade 2+ RILT cases in parentheses, were as follows: right upper lung=33(2); right middle lung=10(2); right lower lung=8(4); left upper lung=23(4); left middle lung=11(2); left lower lung=3(1). However, it should be noted there was significant tumor involvement in the mediastinum for many of these cases.

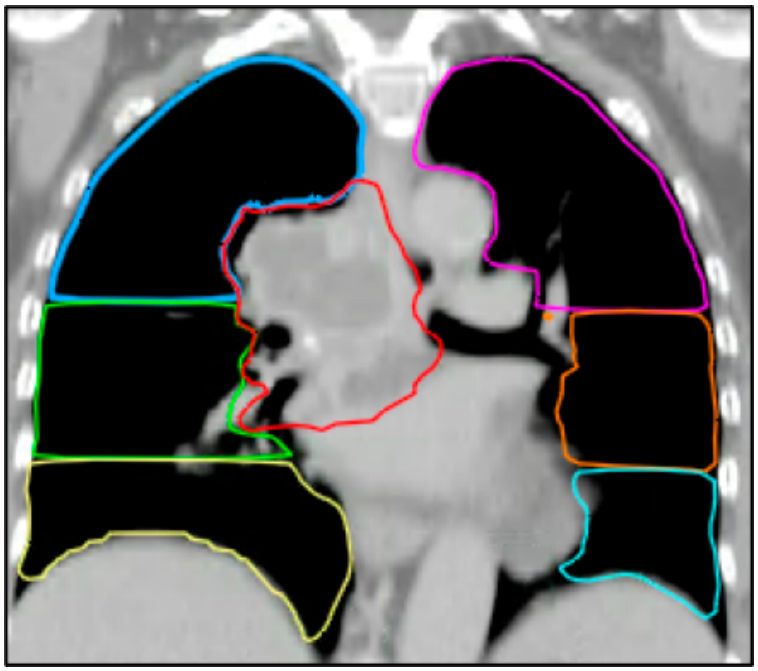

Figure 6.2: Example of regional lung sectioning that produced the following lung segments: RUL=Right Upper Lung (blue); RML=Right Middle Lung (green); RLL=Right Lower Lung (yellow); LUL=Left Upper Lung (pink); LML=Left Middle Lung (orange); LLL=Left Lower Lung (teal).

Patient age, normal lung volume, and volumetric dosimetrics, including mean lung dose, volume of lung receiving $\geq$ 5 Gy (V5), and V20, were calculated for each patient. The average dose to each regional lung segment was quantified. Functional metrics including mean intensity, average functional intensity receiving $\geq$5 Gy (iV5), iV20, and percent of functional lung category receiving $\geq$20 Gy (LF20/F20/HF20) were calculated. The mean intensity receiving greater than dose d was calculated using Equation 6.1:

$$iVd = if\ d_i \geq d \implies \sum_{i=1}^{N_d} \frac{f_i^{\mathbb{N}}}{N_d} \tag{6.1}$$

where d_i is the EQD2 dose in the ith voxel and N_d is the total number of voxels receiving a dose greater than the threshold dose d. The percent of functional lung category F receiving threshold dose d was calculated as shown in Equation 6.2:

$$Fd = if\ f_i^{\mathbb{N}} \ni F\ \&\ d_i \geq d \implies \frac{N_{F>d}}{N} \tag{6.2}$$

where $N_{F>d}$ is the number of voxels in the functional category F that received at least dose d and N is the total number of voxels in the structure. The F_d metric was calculated in terms of perfusion, ventilation, and perfusion combined with ventilation (VQ), i.e. meaning both perfusion and ventilation intensities were considered for the functional categorization of each voxel. For example, a given voxel must have both low-functioning perfusion and low-functioning ventilation to be considered a combined VQ low-functioning voxel.

The total functional intensity loss incurred within the lungs of each patient, divided by the patient's total functional intensity at baseline, was defined as the damage fraction and was calculated as shown in Equation 6.3. Therefore, a positive damage fraction indicates an overall increase in functional intensity, whereas a negative damage fraction indicates a loss of total functional intensity, following RT.

$$Damage\ Fraction = \frac{(Total\ Intensity\ at\ 3{-}Months\ Post{-}Tx){-}(Total\ Intensity\ at\ Pre{-}Tx)}{Total\ Intensity\ at\ Pre{-}Tx} \tag{6.3}$$

Only voxels in the lungs with an intensity $\geq$10% of the maximum intensity were included in the damage fraction calculation.

6.3.3 Statistical Modeling

Ventilation, perfusion, and combined ventilation/perfusion functional metrics were calculated in 88 patients. Spearman correlation coefficients were calculated for volumetric dosimetrics and combined VQ functional metrics as shown in Figure 6.3. The correlation between voxelwise perfusion and ventilation intensities in each patient were also calculated using a Spearman analysis. A paired t-test was used to assess significant differences in metrics between patient cohorts. Patient, dose, and functional metrics were tested for their association with the incidence of grade 2+ radiation pneumonitis or pulmonary fibrosis (i.e. RILT) using the odds ratios (ORs) from univariate and multivariable logistic regression analyses. Normal lung volume, V20, average dose to lower region of lung structure (ADL), and iV20 were chosen for inclusion in the multivariable model, based on univariate association, to represent patient, dose, location, and functional sensitivities that may independently influence RILT incidence. Receiver operating characteristic curves were generated and the area under the curve (AUC) values were calculated using the logistic regression models. The 95% confidence intervals were calculated for purposes of measuring uncertainty and assessing metric stability. Five-fold cross-validation was used to minimize overly optimistic bias. For all analyses, two-sided P values of <0.05 were considered statistically significant and values <0.1 were considered a marginal association. Analyses were performed using R (version 3.6.1) and MATLAB (version 9.4).

6.4 Results

This study combined data from two IRB-approved clinical trials (2006.040 & 2015.035) in which V/Q SPECT images were obtained from 88 NSCLC patients prior to undergoing RT. Patient characteristics and voxelwise metrics quantifying volumetric dose, functional lung, and dose delivered to functional lung for both patient cohorts are summarized in Table 6.1. Similar functional lung distributions were observed in each patient cohort as shown in Figure C.1. The latter cohort was primarily treated with VMAT, as opposed to 3D conformal RT in the former cohort,

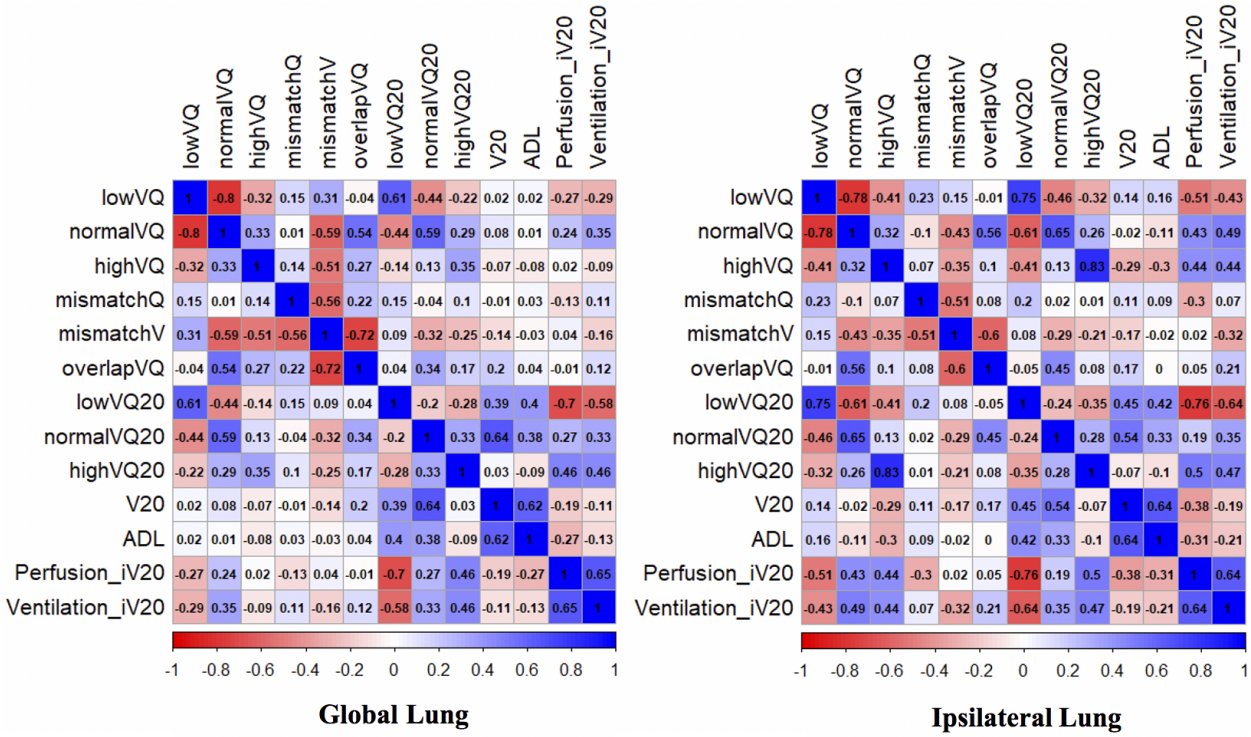

Figure 6.3: Bivariate spearman correlation coefficients for pre-treatment patient-averaged metrics.

which is reflected by the significantly higher V5 and fV5 values caused by the larger low-dose bath associated with modulated RT. Above-average perfusion and ventilation were used as functional-avoidance priorities in the latter cohort, and yet, no other metrics were found to significantly differ between the cohorts.

For the 37 NSCLC patients with SPECT scans available, the probability of RILT incidence (n=8/37) based on a patient's 3-month post-treatment damage fraction was calculated using a logistic regression of the form:

$$Pr(Tox|damage) = \frac{1}{1+e^{-\alpha-\beta*damage}} \tag{6.4}$$

Through this analysis, a significant correlation between the damage fraction in the total lungs at 3-month post-treatment, as measured by perfusion SPECT, and RILT incidence was found (p=0.010). The 3Month post-treatment ventilation-based damage fraction was not found to be associated with RILT (p=0.721). The complete model parameters are shown in Figure 6.4.

Patient Characteristics and SPECT Dose-Function Metrics for Each Patient Cohort

	2006.040 Cohort (n = 58)	2015.035 Cohort (n = 30)	p-value
Gender			
Male	46 (78%)	18 (60%)	
Female	12 (22%)	12 (40%)	
Radiation Delivery			
3D Conformal RT	58	0	
Volumetric Arc Therapy (VMAT)	0	29	
Intensity-Modulated RT (IMRT)	0	1	
Concurrent Chemotherapy			
Yes	45 (78%)	30 (100%)	
No	13 (22%)	0 (0%)	
Tumor Stage			
Stage I	8 (13%)	0	
Stage II	4 (7%)	1 (3%)	
Stage III	46 (80%)	28 (94%)	
Stage IV	0	1 (3%)	
RILT Grade			
Grade 0-1	49 (85%)	24 (80%)	
Grade 2-5	9 (15%)	6 (20%)	
Age [years] Mean (SD)	68 (9)	65 (9)	0.46
Volume [cc] Mean (SD)	2888 (961)	2535 (666)	0.08
Mean Dose [Gy] Mean (SD)	12.4 (3.3)	13.1 (3.7)	0.32
V5 [%] Mean (SD)	44.0 (13.0)	54.5 (13.9)	**0.001**
V20 [%] Mean (SD)	21.2 (6.9)	21.6 (7.6)	0.79
Average Dose to Lower (ADL) Mean (SD)	4.5 (5.9)	4.8 (5.3)	0.77
Average Dose to Middle (ADM) Mean (SD)	14.4 (5.1)	15.1 (5.7)	0.58
Average Dose to Upper (ADU) Mean (SD)	17.5 (7.7)	18.1 (7.1)	0.72
Perfusion fV5 [%] Mean (SD)	42.5 (13.8)	51.6 (15.3)	**0.006**
Perfusion fV20 [%] Mean (SD)	19.1 (7.3)	17.2 (6.9)	0.24
Perfusion iV5 [%] Mean (SD)	0.88 (0.21)	0.88 (0.24)	0.90
Perfusion iV20 [%] Mean (SD)	0.83 (0.26)	0.79 (0.32)	0.54
Perfusion Mean Intensity Mean (SD)	0.90 (0.13)	0.91 (0.15)	0.61
Ventilation Mean Intensity Mean (SD)	0.86 (0.15)	0.88 (0.16)	0.68
Perfusion Low Function (LF) [%] Mean (SD)	11.1 (10.0)	10.7 (11.8)	0.89
Ventilation Low Function (LF) [%] Mean (SD)	19.0 (15.7)	16.2 (15.9)	0.42
Perfusion Normal Function (F) [%] Mean (SD)	78.9 (8.5)	77.1 (12.2)	0.40
Ventilation Normal Function (F) [%] Mean (SD)	74.8 (13.6)	75.6 (14.5)	0.77
Perfusion High Function (HF) [%] Mean (SD)	10.0 (5.6)	12.2 (6.3)	0.09
Ventilation High Function (HF) [%] Mean (SD)	6.2 (3.5)	8.2 (7.3)	0.09
Perfusion Low Function ≥20 Gy (LF20) [%] Mean (SD)	3.3 (3.7)	5.1 (7.1)	0.12
Ventilation Low Function ≥20 Gy (LF20) [%] Mean (SD)	4.9 (4.7)	5.8 (7.0)	0.44
Perfusion Normal Function ≥20 Gy (F20) [%] Mean (SD)	16.5 (6.6)	15.2 (6.8)	0.37
Ventilation Normal Function ≥20 Gy (F20) [%] Mean (SD)	15.0 (6.6)	14.4 (6.9)	0.70
Perfusion High Function ≥20 Gy (HF20) [%] Mean (SD)	1.3 (1.5)	1.3 (1.3)	0.91
Ventilation High Function ≥20 Gy (HF20) [%] Mean (SD)	1.3 (1.2)	1.3 (1.6)	0.79

V5=Volume of lung structure receiving ≥5 Gy, as a percent of total lung volume
V20=Volume of lung structure receiving ≥20 Gy, as a percent of total lung volume
fV5= Functional intensity receiving ≥5 Gy, as a percent of total functional intensity
fV20=Functional intensity receiving ≥20 Gy, as a percent of total functional intensity
iV5=Average normalized functional intensity receiving ≥5 Gy in arbitrary units
iV20= Average normalized functional intensity receiving ≥20 Gy in arbitrary units

Table 6.1: Patient characteristics and dose-function metrics for each patient cohort included in this study.

By separating the fitted probabilities of Grade $\geq$2 RILT into quartiles, a comparison was made between the expected and observed number of RILT incidences based on the measured perfusion damage fraction as shown in Figure 6.5.

Predicting occurrence of Grade 2+ lung toxicity as a function of damage fraction at 3 months post-treatment

Modality	Number of Patients	Variable	Estimate	Std. Error	p-value
Perfusion	37	α	-2.70	0.84	0.000
		β	-12.44	4.81	0.010
Ventilation	37	α	-1.41	0.53	0.000
		β	0.99	2.78	0.721

Figure 6.4: Logistic regression model parameters and results for the association between the perfusion and ventilation 3-month post-treatment damage fraction and RILT incidence (n=8).

Expected Versus Observed RILT Incidence Based on Post-Treatment Perfusion Damage Fraction

Modality	Number of Patients	Avg. Damage Fraction	Avg. RILT Probability	Expected # RILT Cases	Observed # RILT Cases
Perfusion	10	0.058	0.033	0.332	0
	9	-0.015	0.078	0.702	1
	9	-0.117	0.226	2.038	3
	9	-0.234	0.548	4.929	4

Figure 6.5: A measure of the expected versus observed grade $\geq$2 RILT cases separated into equal quartiles based on the range of observed perfusion damage fractions.

Because 20 Gy is considered to cause cellular damage, the 3-month post-treatment damage fraction was plotted against the global lung V20 (shown in Figure 6.6) in an effort to understand the relationship between the variables.

Individual patient and population-averaged (n=88) perfusion and ventilation functional distributions prior to RT are shown in Figure 6.7. For reference, a functional intensity of 1.0 is considered the average value of normal function, and a normal distribution around 1.0 is expected for a healthy individual. These normal distributions are largely exemplified by the 38 patients with $<$5% perfusion LF as shown in Figure 6.8. As another reference, the population-average perfusion (ventilation) low-functioning and high-functioning categorization thresholds, in absolute intensity, were 0.32 (0.38) and 1.49 (1.76), respectively. Mean perfusion and ventilation intensities in various regions of the lung are depicted in Figure 6.9 to demonstrate the range of functional capability

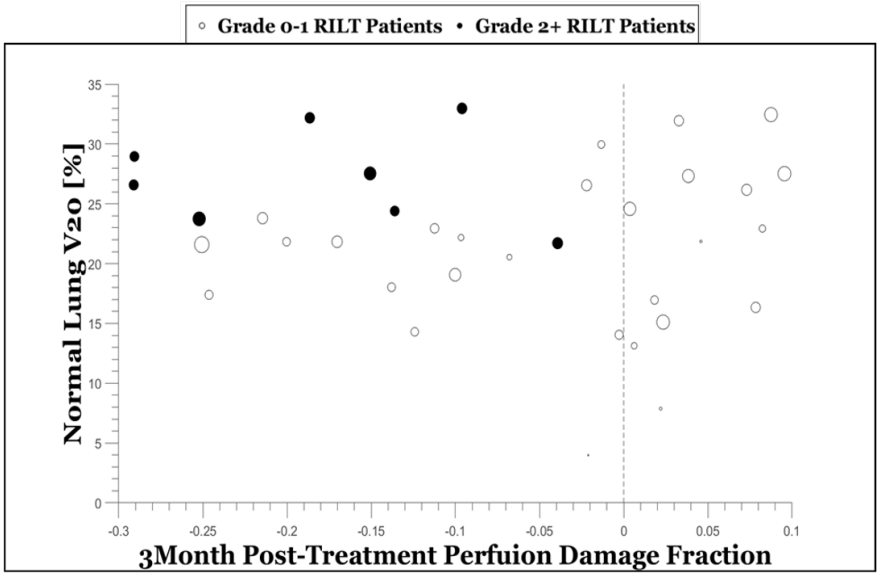

Figure 6.6: Scatter plot demonstrating the relationship between global lung percent volume receiving $\geq$20 Gy (V20) and 3Month post-treatment perfusion damage fraction in patients that incurred grade $\geq$2 (filled circles) and those that did not incur toxicity (open circles), with marker size relative to the pre-treatment AD2LF in the ipsilateral lung.

observed. Across the population, mean perfusion (ventilation) intensity in the global lungs, ipsilateral lung, and contralateral lung were found to be 0.90 (0.87), 0.82 (0.81), and 0.96 (0.91), respectively. In patients exhibiting $<$5% LF, the mean global perfusion (n=38) and ventilation (n=21) intensity were 0.96 and 0.95, respectively.

On the contrary, 50 patients were found to have $>$5% perfusion LF and 67 patients were found to have $>$5% ventilation LF, which corresponded to a global average perfusion and ventilation of 0.86 and 0.84, respectively. In patients that incurred RILT (n=15), the average perfusion and ventilation intensity in the ipsilateral lung was found to be 0.68 and 0.66, respectively, signifying a large presence of functional defects in these patients. Additionally, for both perfusion and ventilation, the population-averaged iV20 was less than the average functional intensity in the RILT cohort, demonstrating that high dose was primarily funneled through below-average functioning lung (inadvertently so in the former cohort) in the patients that incurred RILT.

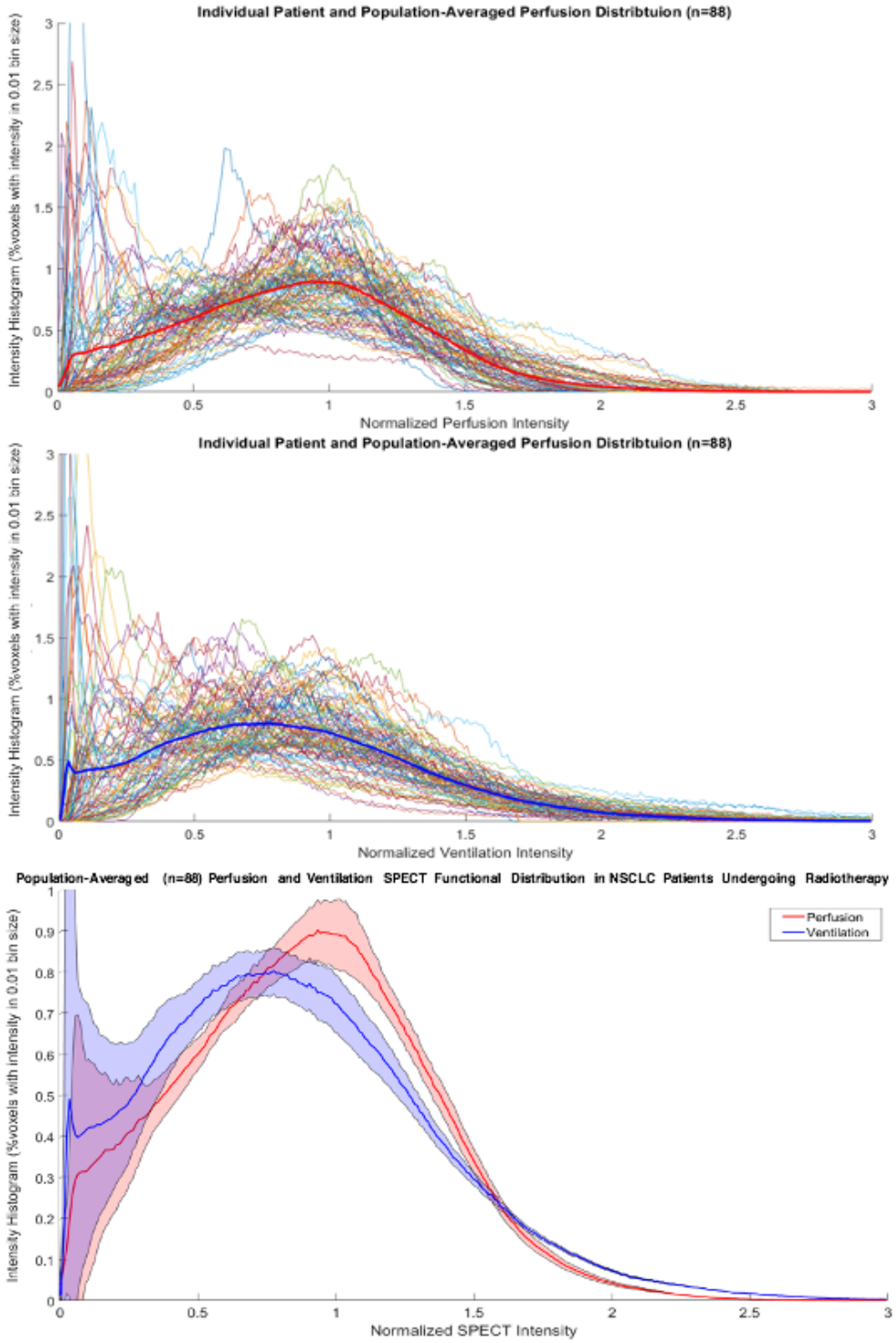

Figure 6.7: A) Perfusion SPECT and B) ventilation SPECT individual (colored) and population-average (bold) normalized functional distributions for 88 NSCLC patients prior to RT. C) Perfusion (red) and ventilation (blue) population-average normalized functional distributions accompanied by the standard deviations (shaded).

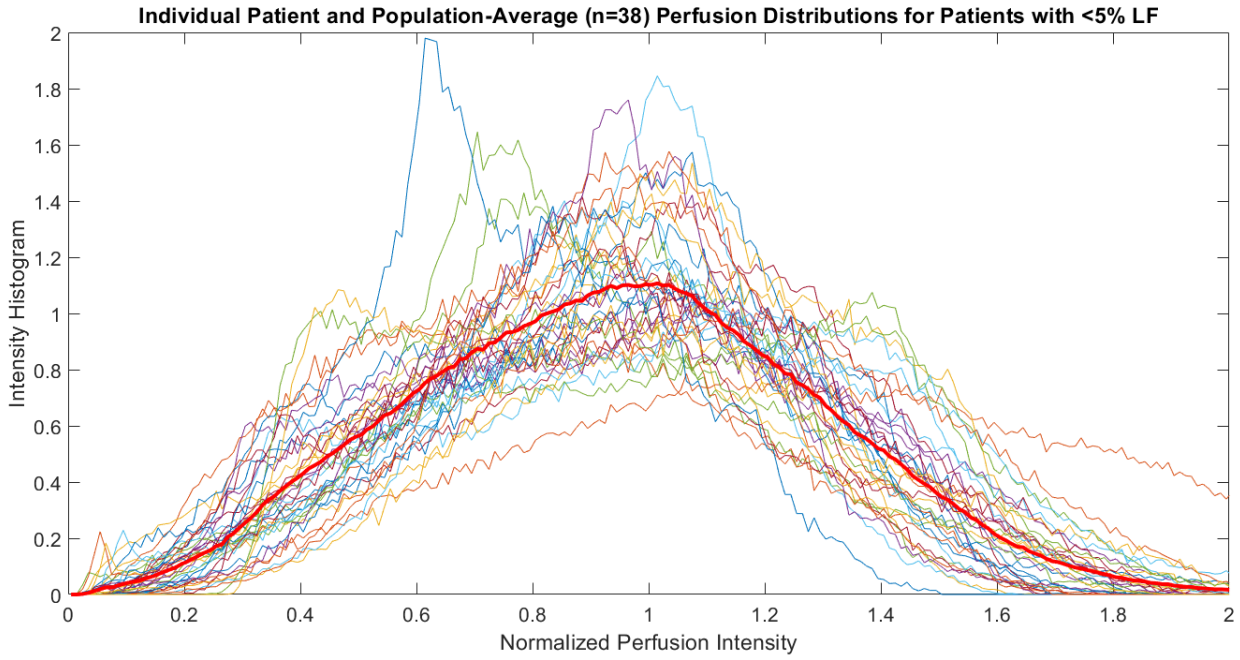

Figure 6.8: Individual patient (colored) and population-averaged (bold red) perfusion SPECT functional distributions for the n=38 NSCLC patients with ¡5% low-function.

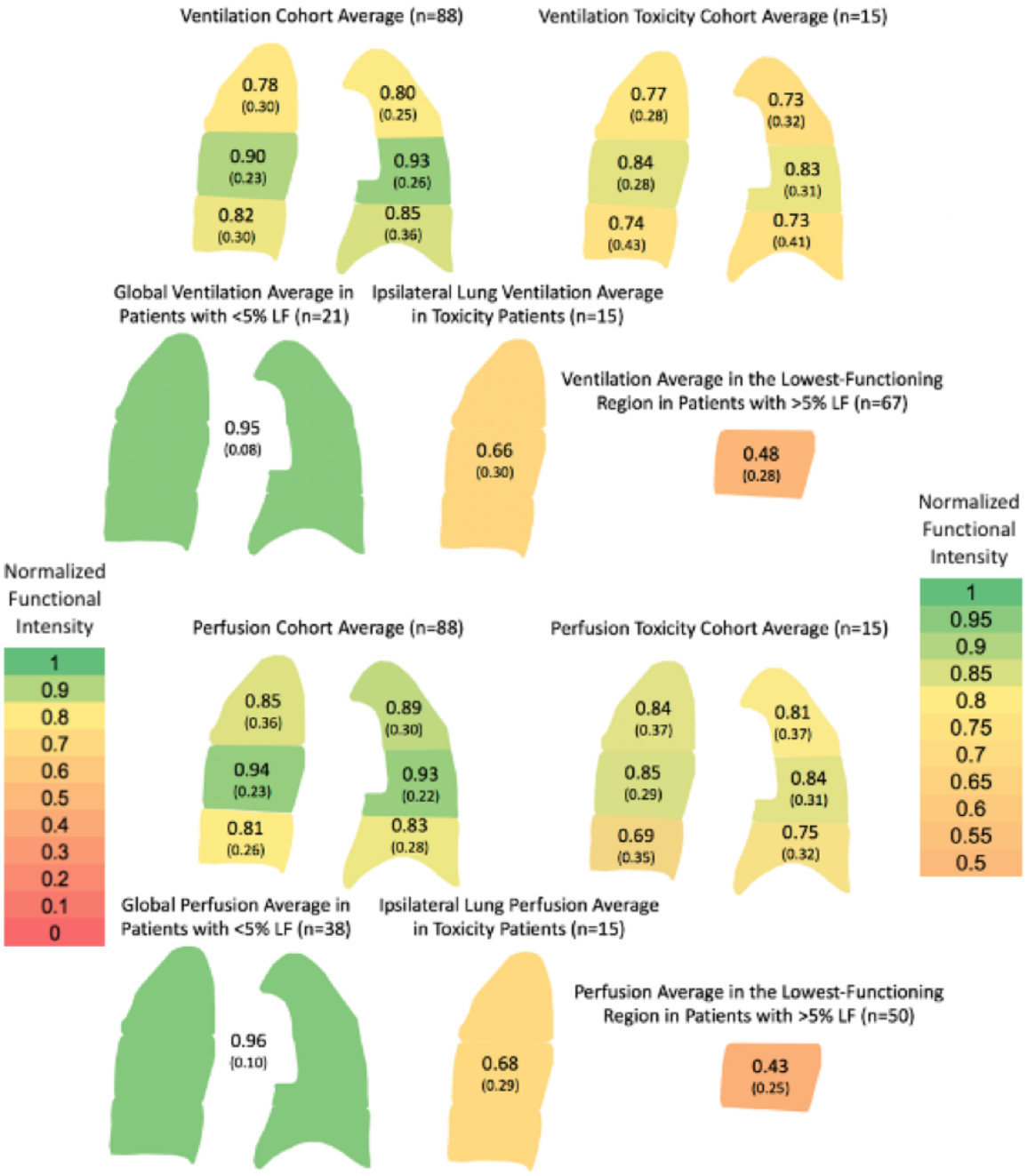

Figure 6.9: Mean perfusion and ventilation normalized functional intensities (and standard deviations) observed for various regions of the lung and subcohorts of patients.

Univariable Logistic Regression Estimates for Association Between Pre-Treatment SPECT Dose-Function Metrics and RILT

Metric	Global Lung				Ipsilateral Lung				Contralateral Lung			
	Mean (SD)	Odds Ratio	95% CI	p	Mean (SD)	Odds Ratio	95% CI	p	Mean (SD)	Odds Ratio	95% CI	p
Volume [cc]	2768 (884)	0.79	0.39–1.50	0.49	1271 (469)	0.34	0.08–1.20	0.11	1480 (530)	1.18	0.40–3.29	0.76
Mean Dose [Gy]	12.6 (3.4)	1.18	0.99–1.45	0.09	21.8 (7.7)	1.06	0.99–1.14	**0.05**	5.2 (2.7)	1.08	0.88–1.31	0.46
V5 [%]	47.6 (14.2)	1.04	1.00–1.09	0.06	65.6(18.8)	1.04	1.01–1.08	**0.01**	32.7 (17.6)	1.01	0.98–1.05	0.38
V20 [%]	21.5 (7.1)	1.11	1.02–1.22	**0.03**	42.7 (16.4)	1.05	1.02–1.10	**0.008**	34.0 (5.5)	1.01	0.91–1.11	0.84
ADL [Gy]	4.6 (5.7)	1.15	1.05–1.26	**0.003**	9.3 (13.3)	1.06	1.02–1.10	**0.004**	1.7 (1.5)	1.49	1.05–2.14	**0.02**
ADM [Gy]	14.6 (5.3)	1.08	0.96–1.22	0.21	25.1 (11.2)	1.04	0.99–1.10	0.12	5.9 (3.4)	1.06	0.90–1.23	0.48
ADU [Gy]	17.7 (7.5)	0.97	0.89–1.04	0.39	32.7 (17.3)	1.00	0.96–1.03	0.79	7.5 (4.9)	1.01	0.90–1.12	0.85
Perfusion Mean Intensity [a.u.]	0.90 (0.14)	0.72	0.47–1.10	0.13	0.82 (0.24)	0.75	0.58–0.94	**0.02**	0.96 (0.11)	1.22	0.74–2.17	0.46
Perfusion fV5 [%]	45.6 (14.9)	1.02	0.99–1.06	0.24	65.0 (20.0)	1.03	1.00–1.07	**0.04**	33.0 (19.6)	1.01	0.98–1.04	0.41
Perfusion fV20 [%]	18.5 (7.2)	1.02	0.94–1.11	0.62	41.2 (17.2)	1.04	1.01–1.08	**0.03**	3.9 (6.3)	1.02	0.93–1.10	0.65
Perfusion iV5 [a.u.]	0.88 (0.22)	0.08	0.00–1.18	0.08	0.81 (0.27)	0.05	0.00–0.42	**0.01**	0.96 (0.26)	0.60	0.07–5.27	0.64
Perfusion iV20 [a.u.]	0.82 (0.28)	0.07	0.01–0.60	**0.02**	0.80 (0.29)	0.04	0.00–0.38	**0.007**	0.61 (0.43)	1.16	0.31–4.35	0.83
Perfusion LF [%]	11.0 (10.6)	1.03	0.98–1.09	0.16	15.7 (18.6)	1.03	1.00–1.06	**0.02**	7.4 (10.0)	0.98	0.90–1.03	0.50
Perfusion F [%]	78.3 (9.9)	0.96	0.91–1.01	0.12	77.5 (17.1)	0.97	0.94–1.00	**0.05**	78.9 (9.7)	0.99	0.94–1.05	0.71
Perfusion HF [%]	10.7 (5.9)	1.01	0.91–1.10	0.89	6.8 (6.3)	0.89	0.78–1.00	0.07	13.8 (9.3)	1.03	0.97–1.09	0.27
Perfusion LF20 [%]	4.0 (5.1)	1.11	1.01–1.23	**0.03**	8.6 (12.0)	1.06	1.01–1.10	**0.01**	0.48 (1.11)	0.83	0.29–1.39	0.61
Perfusion F20 [%]	16.1 (6.7)	1.04	0.95–1.13	0.40	31.8 (15.4)	1.02	0.98–1.05	0.31	3.1 (4.4)	1.02	0.89–1.14	0.73
Perfusion HF20 [%]	1.3 (1.4)	0.63	0.31–1.08	0.15	2.4 (2.9)	0.83	0.58–1.06	0.23	0.42 (0.99)	1.01	0.49–1.66	0.98
Ventilation Mean Intensity [a.u.]	0.87 (0.15)	0.80	0.55–1.16	0.25	0.81 (0.27)	0.77	0.60–0.95	**0.02**	0.91 (0.13)	1.28	0.82–2.15	0.31
Ventilation fV5 [%]	46.3 (14.8)	1.02	0.98–1.06	0.33	66.0 (19.7)	1.04	1.01–1.08	**0.02**	32.6 (19.4)	1.01	0.98–1.04	0.54
Ventilation fV20 [%]	19.4 (7.7)	1.02	0.95–1.10	0.63	42.3 (17.2)	1.04	1.01–1.08	**0.01**	3.8 (6.0)	1.02	0.93–1.11	0.59
Ventilation iV5 [a.u.]	0.86 (0.21)	0.07	0.00–1.05	0.06	0.81 (0.27)	0.05	0.00–0.44	**0.01**	0.89 (0.24)	0.56	0.06–5.61	0.62
Ventilation iV20 [a.u.]	0.82 (0.27)	0.09	0.01–0.72	**0.03**	0.81 (0.28)	0.05	0.00–0.43	**0.009**	0.70 (0.35)	1.62	0.27–9.49	0.59
Ventilation LF [%]	18.1 (15.7)	1.01	0.97–1.04	0.58	23.1 (22.0)	1.02	1.00–1.05	**0.04**	14.4 (15.3)	0.97	0.92–1.01	0.24
Ventilation F [%]	75.1 (13.8)	0.99	0.95–1.03	0.47	70.8 (19.6)	0.97	0.95–1.00	**0.04**	78.0 (13.6)	1.02	0.98–1.08	0.38
Ventilation HF [%]	6.9 (5.2)	1.01	0.90–1.12	0.80	6.1 (5.9)	0.94	0.82–1.04	0.31	7.6 (6.4)	1.04	0.96–1.13	0.33
Ventilation LF20 [%]	5.2 (5.6)	1.11	1.01–1.21	**0.03**	11.3 (14.5)	1.04	1.01–1.08	**0.03**	0.80 (1.55)	0.97	0.59–1.35	0.89
Ventilation F20 [%]	14.8 (6.7)	1.01	0.93–1.10	0.76	28.8 (14.1)	1.01	0.97–1.05	0.52	2.9 (4.2)	1.00	0.86–1.13	0.97
Ventilation HF20 [%]	1.3 (1.4)	1.08	0.70–1.57	0.68	2.5 (2.7)	1.02	0.81–1.22	0.88	0.26 (0.70)	1.39	0.66–2.77	0.32

Table 6.2: Univariable logistic regression analysis for dose, perfusion, and ventilation metrics.

Through univariable logistic regression analysis, ipsilateral lung perfusion and ventilation LF were significantly associated with RILT incidence as shown in Table 6.2. Normal-function (F) perfusion and ventilation were also found to be associated with RILT, but inversely correlated, suggesting patients with less normal-functioning lung were at a higher risk. For both perfusion and ventilation, the ipsilateral lung tended to exhibit a lower mean intensity and higher percent of LF than the contralateral lung. Ipsilateral lung volumetric dosimetrics (including V20 and mean dose) and dose-function metrics (including iV20 and ventilation or perfusion low-function volume receiving $\geq$20 Gy, as a percent of total lung structure volume (LF20)) were also correlated with RILT on univariate analysis. Both iV20, a continuous metric that quantifies the average functional intensity delivered $\geq$20 Gy, and LF20, the percent of total volume that received $\geq$20 Gy to low-functioning lung, correlations suggest that patients receiving more dose to dysfunctional lung may be most at-risk for RILT.

The only contralateral lung metric associated with RILT was average dose to lower region of lung structure (ADL). While 65% of patients were found to have primary tumor involvement located in the upper lung sextants, only 11% of these patients incurred RILT. Conversely, 11 patients exhibited primary tumor involvement in the lower lung sextants and 5 of these patients incurred RILT. Through a multivariable logistic regression model that included normal lung volume, V20, ADL, and ventilation or perfusion iV20, ADL was most prominently associated with RILT incidence within the global lungs and contralateral lung as shown in Table 6.3. However, perfusion and ventilation iV20 were found to be most correlated with RILT in the ipsilateral lung.

To better understand the interplay between perfusion and ventilation functional distributions within the lung and its effect on RILT risk, combined perfusion and ventilation (VQ) metrics were quantified and analyzed as shown in Table 6.4. For a voxel to be considered for a combined VQ categorization, it must have the same functional classification for perfusion as for ventilation. In total, an average of 77% of voxels were found to have overlapping perfusion and ventilation functional categorizations, with moderate dice similarity coefficient (DSC), a measure of spatial overlap, in the low-functioning and normal- functioning regions. Poor overlap was found in the high function-

Multivariable Logistic Regression Modeling for Association Between Dose-Function Metrics and RILT

Modality	Timepoint	*n*	Structure	Metric	Odds Ratio	95% CI	P-value
Perfusion	**Pre-Treatment**	88	Lungs-GTV	Volume [cc]	1.02	0.50–2.01	0.95
				V20 [%]	1.05	0.94–1.17	0.39
				ADL [Gy]	1.12	1.02–1.25	**0.02**
				iV20 [a.u.]	0.08	0.01–0.91	**0.05**
			Ipsilateral Lung-GTV	Volume [cc]	0.85	0.16–4.05	0.84
				V20 [%]	1.01	0.96–1.07	0.66
				ADL [Gy]	1.05	1.00–1.10	0.07
				iV20 [a.u.]	0.05	0.00–0.69	**0.03**
			Contralateral Lung-GTV	Volume [cc]	0.91	0.25–2.97	0.87
				V20 [%]	1.00	0.86–1.15	0.95
				ADL [Gy]	1.52	1.06–2.23	**0.03**
				iV20 [a.u.]	0.82	0.13–4.88	0.83
Ventilation	**Pre-Treatment**	88	Lungs-GTV	Volume [cc]	1.00	0.49–1.98	0.99
				V20 [%]	1.06	0.95–1.19	0.29
				ADL [Gy]	1.14	1.03–1.26	**0.01**
				iV20 [a.u.]	0.06	0.00–0.64	**0.02**
			Ipsilateral Lung-GTV	Volume [cc]	0.87	0.17–3.99	0.86
				V20 [%]	1.02	0.97–1.08	0.39
				ADL [Gy]	1.05	1.00–1.10	0.08
				iV20 [a.u.]	0.06	0.00–0.61	**0.03**
			Contralateral Lung-GTV	Volume [cc]	1.47	0.41–5.10	0.54
				V20 [%]	0.99	0.85–1.12	0.88
				ADL [Gy]	1.36	0.92–2.01	0.12
				iV20 [a.u.]	1.24	0.15–9.27	0.83

Volume = Normal lung volume excluding gross tumor volume
V20 = Volume of lung structure receiving ≥20 Gy, as a percent of total lung structure volume
ADL = Average dose to lower region of lung structure in Gy
iV20 = Average normalized functional intensity receiving ≥20 Gy in arbitrary units

Table 6.3: Multivariable logistic regression analysis using normal lung volume, V20, ADL, and pre-treatment perfusion or ventilation iV20 in the global lungs, ipsilateral lung, and contralateral lung.

ing region. Mismatched defect categorizations were also defined but did not appear to be significant in terms of RILT incidence on univariable analysis. The DSC for low-functioning lung was statistically significant in the global lung and ipsilateral lung and the DSC for normal-functioning lung was found to be negatively correlated. Using combined VQ categorizations, both low-functioning V/Q (lowVQ20) and normal-functioning V/Q (intersection volume between normal-function ventilation and normal-function perfusion receiving $\geq$20 Gy, as a percentage of total lung structure

volume (midVQ20)) were found to correlate with RILT incidence, while intersection volume between high-function ventilation and high-function perfusion receiving $\geq$20 Gy, as a percentage of total lung structure volume (highVQ20) was not significantly associated. However, the midVQ20 odds ratio $<$1 suggests patients with less midVQ20 are at a higher risk for RILT.

Univariable Logistic Regression Estimates for Association Between Pre-Treatment Combined VQ Dose-Function Metrics and RILT

Metric	Global Lung				Ipsilateral Lung				Contralateral Lung			
	Mean (SD)	Odds Ratio	95% CI	p	Mean (SD)	Odds Ratio	95% CI	p	Mean (SD)	Odds Ratio	95% CI	p
Low VQ [%]	15.7 (11.1)	1.05	1.00–1.10	0.06	19.6 (15.5)	1.06	1.02–1.10	**0.004**	12.6 (11.3)	1.00	0.95–1.05	0.96
Normal VQ [%]	59.4 (14.1)	0.99	0.95–1.02	0.44	55.5 (19.6)	0.97	0.94–1.00	**0.02**	62.4 (14.2)	1.02	0.98–1.07	0.36
High VQ [%]	1.9 (1.7)	1.14	0.81–1.54	0.42	1.3 (1.7)	0.63	0.33–0.99	0.09	2.4 (2.5)	1.18	0.97–1.43	0.09
Mismatch Q [%]	3.5 (3.6)	1.04	0.89–1.19	0.55	5.0 (8.0)	1.02	0.96–1.09	0.40	2.4 (2.3)	1.02	0.78–1.28	0.87
Mismatch V [%]	11.1 (10.7)	0.97	0.89–1.02	0.32	12.3 (13.3)	1.00	0.95–1.04	0.93	10.2 (10.3)	0.93	0.83–1.00	0.11
Overlap VQ [%]	77.0 (9.8)	1.05	0.98–1.15	0.21	76.4 (12.1)	1.00	0.96–1.06	0.88	77.4 (9.7)	1.09	1.01–1.22	0.07
DSC Low [%]	64.6 (16.2)	1.06	1.01–1.11	**0.02**	64.7 (19.0)	1.04	1.00–1.08	**0.05**	60.8 (17.7)	1.00	0.97–1.04	0.77
DSC Normal [%]	82.8 (10.2)	1.02	0.96–1.10	0.61	79.0 (19.2)	0.97	0.95–1.00	**0.04**	83.7 (9.5)	1.08	0.99–1.22	0.14
DSC High [%]	28.2 (15.8)	1.03	0.99–1.07	0.14	20.7 (17.8)	0.97	0.93–1.01	0.12	28.2 (17.9)	1.03	1.00–1.07	0.06
Low VQ ≥20 Gy [%]	4.5 (4.5)	1.18	1.06–1.34	**0.004**	9.0 (9.6)	1.10	1.04–1.17	**0.001**	0.84 (1.31)	0.97	0.54–1.42	0.88
Normal VQ ≥20 Gy [%]	12.0 (5.9)	1.00	0.91–1.10	0.94	22.2 (12.1)	1.00	0.96–1.05	0.89	2.8 (3.7)	1.00	0.85–1.16	0.96
High VQ ≥20 Gy [%]	0.24 (0.32)	0.24	0.01–1.85	0.26	0.43 (0.69)	0.46	0.08–1.32	0.26	0.07 (0.22)	1.29	0.05–10.4	0.83

DSC = Dice similarity coefficient

Table 6.4: Univariable logistic regression analysis using combined VQ metrics in the global lungs, ipsilateral lung, and contralateral lung.

Global lung and ipsilateral lung percent of low VQ receiving $\geq$20 Gy (lowVQ20) were both found to be significantly associated with RILT incidence on univariate analysis. In patients that incurred RILT, the mean percent of lowVQ20 and lowVQ20 in ipsilateral lung was 32% and 17%, respectively, corresponding to an average of 161cm^3 of combined V/Q low-functioning lung of which 88cm^3 received $\geq$20 Gy. Conversely, the mean ipsilateral lowVQ20 and lowVQ20 in patients without toxicity was found to be 17% and 7%, respectively, corresponding to an average of 164cm^3 of combined V/Q low-functioning lung of which 69cm^3 received $\geq$20 Gy. Therefore, while the volume of low-function lung was similar, the patients that incurred RILT were delivered 20 Gy or more to an additional 19cm^3 of low-functioning lung on average. In a univariable ROC analysis, lowVQ20 was the best predictor of RILT incidence for both the global lung (AUC=0.76) and ipsilateral lung (AUC=0.79) compared to V20, perfusion iV20, and ventilation iV20 as shown in Table 6.5. Furthermore, all ipsilateral lung metrics had higher AUC values than their global lung counterparts. Based on the results of the multivariable logistic regression, lowVQ20, the selected functional metric, was combined with ADL, the representative locational metric, in a multivariate ROC analysis, but no additional predictive power was observed.

Despite this result, the angle of the 20% RILT risk line based on lowVQ20 versus ADL in the ipsilateral lung, as shown in Figure 6.10, demonstrates influence from both metrics, suggesting independent vulnerabilities that lead to RILT based on dose to low-functioning lung and dose to lower lung. By assigning limits of 20 Gy to lower lung and 15% lowVQ20 that generally represent $>$20% RILT risk, there appears to be 4 RILT cases in each of the three labeled sections, demonstrating the independent and overlapping vulnerabilities. Full results from the multivariate models are provided in Table 6.6. Interestingly, both patients that incurred Grade 5 RILT in this cohort presented with lower lung tumors with an adjacent combined VQ functional defect that received a large portion of high dose, as shown in Figure 6.11. Furthermore, although the depicted treatment planning CT scans are of limited diagnostic quality, both patients appear to exhibit significant pulmonary fibrosis prior to RT.

ROC Analysis for Perfusion, Ventilation, and Combined Ventilation+Perfusion Logistic Regression Models to Predict RILT Incidence

Structure	Metric	AUC	95% CI
Lungs-GTV	V20 [%]	0.69	0.55–0.82
	Perfusion iV20 [a.u.]	0.67	0.54–0.79
	Ventilation iV20 [a.u.]	0.68	0.56–0.81
	Low-Functioning Ventilation+Perfusion Receiving ≥20 Gy [%]	0.76	0.65–0.87
	ADL [Gy] † Low VQ ≥20 [%] †	0.65	0.52–0.78
Ipsilateral Lung-GTV	V20 [%]	0.74	0.62–0.85
	Perfusion iV20 [a.u.]	0.7	0.58–0.82
	Ventilation iV20 [a.u.]	0.74	0.63–0.85
	Low VQ ≥20 [%]	0.79	0.65–0.87
	ADL [Gy] † Low VQ ≥20 [%] †	0.75	0.63–0.87
Contralateral Lung-GTV	V20 [%]	0.35	0.21–0.48
	Perfusion iV20 [a.u.]	0.33	0.18–0.49
	Ventilation iV20 [a.u.]	0.34	0.18–0.51
	Low VQ ≥20 [%]	0.37	0.22–0.52
	ADL [Gy] † Low VQ ≥20 [%] †	0.31	0.14–0.48

† Multivariate logistic regression model
V20=Volume of lung structure receiving ≥20 Gy, as a percent of the total lung structure volume
ADL=Average dose to lower region of lung structure in Gy
iV20=Average normalized functional intensity receiving ≥20 Gy in arbitrary units
Low VQ ≥20 = V/Q low-function volume, defined as the intersection between low-function perfusion and low-function ventilation, that received ≥20 Gy, as a percent of the total lung structure volume

Table 6.5: Univariable logistic regression analysis using combined VQ metrics in the global lungs, ipsilateral lung, and contralateral lung.

6.5 Discussion

The goal of this study was to analyze V/Q SPECT functional lung images to better understand the interplay between dose delivery and functional lung distribution with regards to RILT incidence in NSCLC patients treated with RT. By utilizing novel methods for quantification of absolute functional intensity and combined VQ functional lung categorization, patient-specific functional distributions and dose-function metrics were generated to characterize pulmonary condition and dose delivered to various functional lung regions. These methods were applied to V/Q SPECT scans from 88 NSCLC patients accrued in two separate clinical trial cohorts. Through this analysis, a wide range in functional capability, including a large presence of functional defects primarily located in the ipsilateral lung, was observed. While the lungs are known to act as a parallel organ,

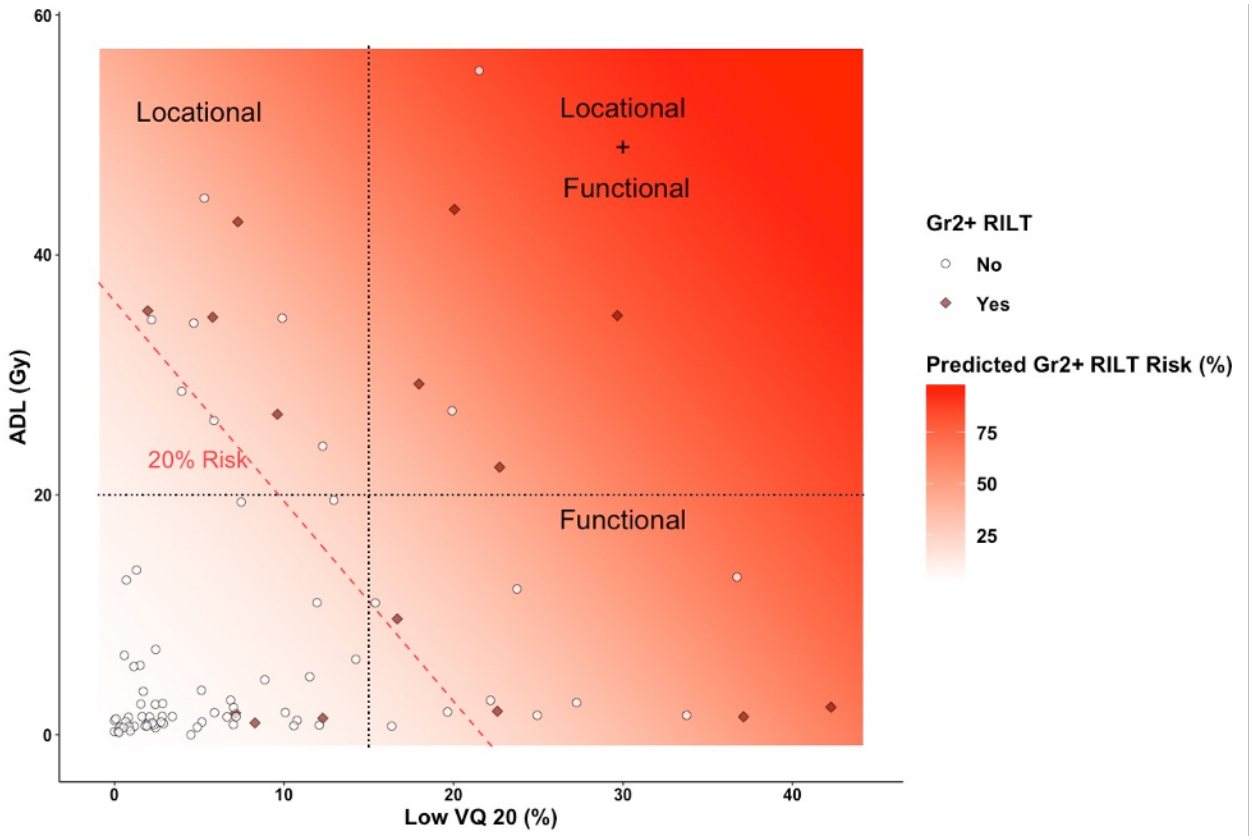

Figure 6.10: Scatter plot of percent of ipsilateral lung with combined VQ low-function receiving $\geq$20 Gy (lowVQ20) and average dose to lower ipsilateral lung (ADL) for patients with Grade 0-1 RILT (white circles) versus Grade 2-5 RILT (red diamonds). The estimated RILT risk based on logistic regression analysis is overlaid (shaded red) and the 20% risk threshold is explicitly shown (dotted red line). Independent functional (lowVQ20$>$15%) and locational (ADL$\geq$20 Gy) radiation sensitivities are hypothesized based on these results.

NSCLC tumors are often primarily located within one lung, which can lead to a large imbalance in functional capacity between the ipsilateral and contralateral lungs. Previous work has suggested that individual lung metrics may provide deeper insight into the relationship between dose, function, and toxicity [147].

Through the study of post-treatment reduction in functional intensity, a strong association between negative perfusion damage fractions and RILT incidence was found. Damage fraction measures a patient's global functional reduction relative to their baseline functional capacity, effectively quantifying the fractional amount of functional lung that was damaged, or recovered, following radiation treatment. Therefore, this association suggests that patients who incur the most functional

ROC Analysis for Combined Perfusion/Ventilation + Dose Multivariate Model

Structure	Metric	Odds Ratio	95% CI	p	AUC (95% CI)
Lungs-GTV	ADL [Gy]	1.15	1.05–1.27	**0.004**	0.65 (0.52–0.78)
	Low VQ ≥20 Gy [%]	1.19	1.06–1.36	**0.006**	
Ipsilateral Lung-GTV	ADL [Gy]	1.06	1.01–1.10	**0.011**	0.75 (0.63–0.87)
	Low VQ ≥20 Gy [%]	1.10	1.04–1.17	**0.002**	
Contralateral Lung-GTV	ADL [Gy]	1.51	1.06–2.17	**0.022**	0.31 (0.14–0.48)
	Low VQ ≥20 Gy [%]	0.90	0.44–1.37	0.687	

ADL=Average dose to lower region of lung structure in Gy
Low VQ ≥20 = V/Q low-function volume, defined as the intersection between low-function perfusion and low-function ventilation, that received ≥20 Gy, as a percent of the total lung structure volume

Table 6.6: ROC analysis results using a multivariable model consisting of lowVQ20 and ADL in the global lungs, ipsilateral lung, or contralateral lung.

damage at 3 months post-treatment are at the highest risk to develop RILT and supports the theory that limiting functional damage can reduce toxicity rates. While post-treatment metrics are not necessarily valuable in terms of RT planning, the strong association between functional damage and RILT incidence provides merit to the use of functional imaging in RT assessment and can serve as motivation to enhance our understanding for the dose-function response in NSCLC patients undergoing RT in an effort to predict functional damage and optimize dose delivery.

In terms of the pre-treatment analysis, dose-function metrics in the ipsilateral lung and average dose to lower region of lung structure (ADL) were found to have the highest correlation with RILT incidence. The correlation between ADL and RILT suggests a physiological radiosensitivity in the lower lung, which is consistent with previous studies that have reported on the increased vulnerability of the inferior lung [69, 100]. Moreover, ipsilateral lung perfusion and ventilation mean intensity receiving $\geq$20 Gy (iV20) were both associated with RILT. Because the estimated odds ratios for these associations were found to be less than unity, these results suggest that patients receiving $\geq$20 Gy to a lower average functional intensity are at an increased risk to incur RILT. To further investigate this functional sensitivity, combined VQ metrics were generated by considering both the perfusion and ventilation intensities in the voxelwise functional categorization. Similar

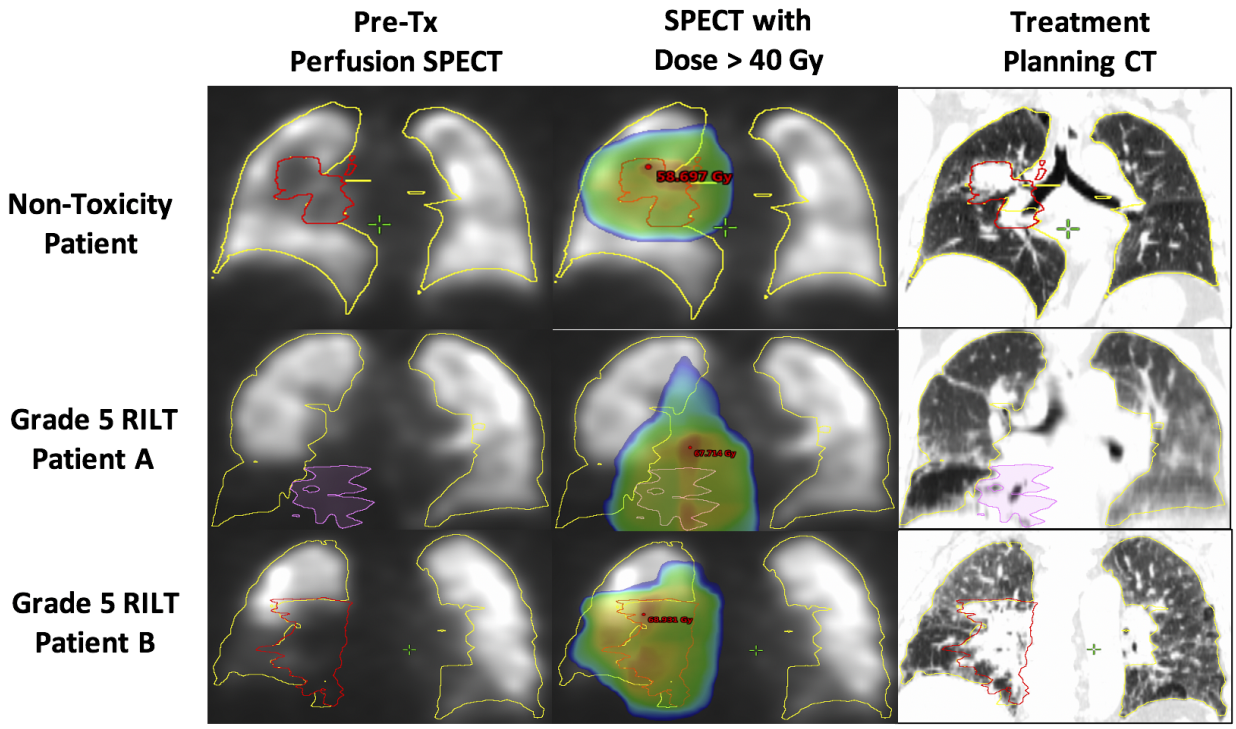

Figure 6.11: Pre-treatment perfusion scans (left column), overlaid with dose ¿40 Gy (middle column), and the treatment planning CT (right column) for a non-toxicity patient (top row), Grade 5 Patient A (middle row), and Grade 5 Patient B (bottom row).

to the individual V/Q analysis, patients receiving $\geq$20 Gy to a large percentage of combined VQ low-functioning lung were found to be at the highest risk for RILT.

These results were surprising based on previous literature. Various studies have reported on the time-dependent reduction in normal lung [37, 38], in which functional damage occurs at a higher rate in higher functioning lung [74]. Moreover, many studies have reported that dose to a higher percent of functional intensity is associated with RILT [65]. Although normal lung doses should clearly be kept to a minimum to reduce functional damage, measuring the fraction of perfusion/ventilation intensity receiving $\geq$20 Gy (fV20), in theory, only significantly differs from V20 in patients with heterogeneous lung function. In these cases, where the total intensity – the denominator of fV20 – is compromised relative to the rest of the cohort, the amount of functional intensity irradiated – the nominator of fV20 – is less for a given fV20 value than in a patient with homogeneous lung function. Thus, fV20 effectively downplays the dose-effect in low- functioning

lung. As shown in Figure 6.12C and Figure 6.12D, many of the patients with large ipsilateral perfusion fV20 values were also delivered high dose to a large portion of ipsilateral low-functioning lung.

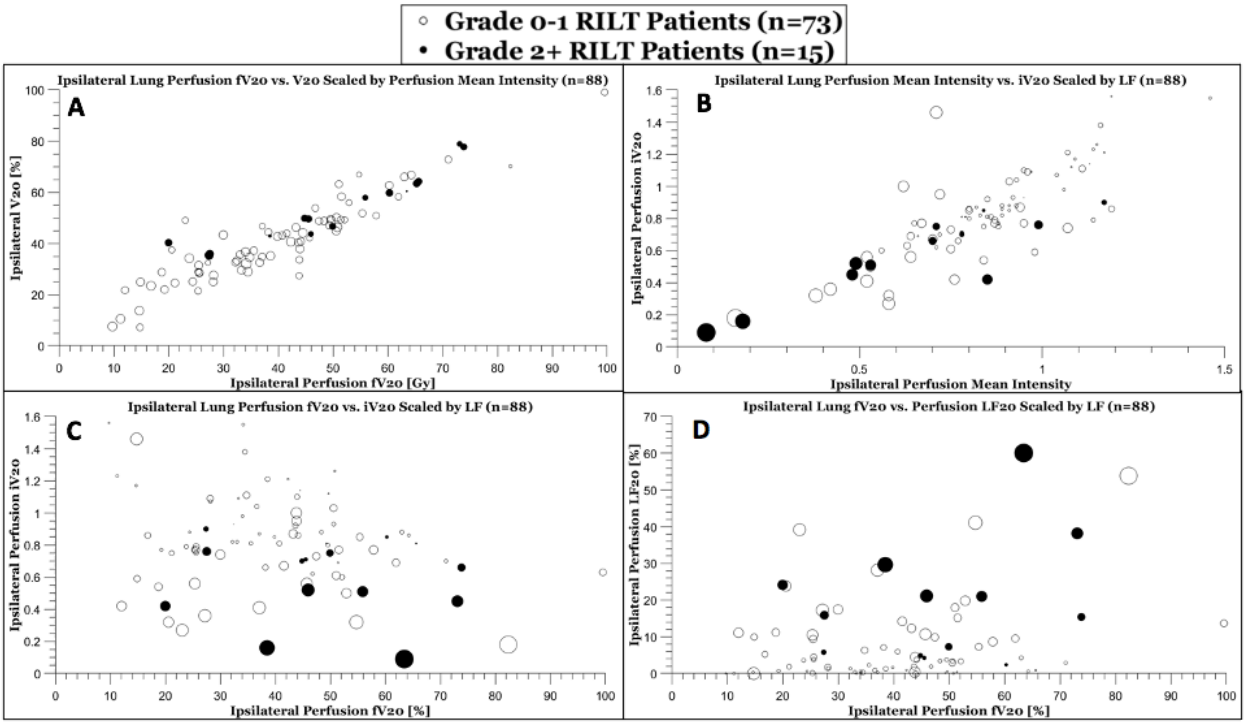

Figure 6.12: Scatterplots of ipsilateral lung metrics (with marker size scaled by the percent of perfusion low-function) including: A) fraction of perfusion intensity receiving $\geq$20 Gy (fV20) vs. fraction of volume receiving $\geq$20 Gy (V20); B) mean perfusion intensity vs. mean perfusion intensity receiving $\geq$20 Gy (iV20); C) perfusion fV20 vs. perfusion iV20; D) perfusion fV20 vs. perfusion low-function receiving $\geq$20 Gy (LF20).

To better quantify the interplay between the dose delivery and patient-specific functional lung distributions, the amount of each functional lung categorization delivered $\geq$20 Gy (LF20/F20/HF20) was calculated as a percent of the total lung structure volume. Although the amount of low- and high-functioning perfusion in the global lung was similar, LF20 was found to be nearly 4 times higher than ventilation or perfusion high-function volume receiving $\geq$20 Gy, as a percent of total lung structure volume (HF20), meaning high dose was more likely to be directed through low-functioning perfusion than high-functioning perfusion. A higher prevalence of LF in the ipsilateral lung also suggests low-functioning lung was primarily located near the tumor, whereas

high-functioning lung was generally more concentrated in the contralateral lung. A recent study suggested that dose to 4DCT highly-ventilated lung is most predictive of RP [32], however, it is unclear how well deformation-based ventilation metrics correlate with pulmonary function. Similarly, high-functioning lung can be hard to interpret physiologically. In terms of SPECT imaging, the HF regions signify accumulated intensity that may be caused by patient geometry or saturation artifacts. The poor DSC between perfusion and ventilation high-functioning lung found in these patients suggest the HF regions were not well-related. Alternatively, low- and normal-functioning lung were found to have more perfusion/ventilation spatial overlap and volume.

Combined VQ functional categorizations were quantified to improve confidence in the determination of functional lung versus dysfunctional lung [148]. In this context, combined VQ normal- and high-functioning lung represent regions of functional gas exchange, and combined VQ low-functioning lung represents regions with matching V/Q defects. Furthermore, an aggressive low-functioning lung bound ($<$15% of max intensity) was implemented to capture the most significant defects. While the specific cause of the functional defect is unknown, pulmonary dysfunction in these patients is primarily attributed to either: 1) tumor burden or 2) lung disease [58, 59]. Therefore, it is possible that irradiating these functional defects could cause 1) a large dose to reperfused/reventilated lung or 2) an exacerbation of pulmonary comorbidities, which may be an explanation for the increased radiosensitivity in the low-functioning lung found in this study.

Numerous studies have previously reported a strong connection between pre-existing pulmonary comorbidities and radiation-induced lung toxicity [84, 85]. Specifically, recent studies have suggested patients with interstitial lung disease (ILD) [88, 87] or idiopathic pulmonary fibrosis (IPF) [149, 89] prior to RT are disproportionately prone to developing severe toxicity. Despite this known risk factor, low-functioning lung, which may be indicative of disease, is generally deemed less important in the dose-function response than high-functioning lung. However, there are indications that severe RILT is linked with a rapid progression of out-of-field radiographic changes that may be indicative of a global lung immune response [150]. As stated by Makimoto et al. in 1999 [151],

Baseline impairment of pulmonary function will add to radiation damage and cause symptoms with smaller radiation volumes than in patients with normal function [152, 153].

The two grade 5 RILT cases in this study both presented with matching V/Q functional defects in the inferior region of the ipsilateral lung, appeared to exhibit pulmonary fibrosis on the treatment planning CT, and ultimately, died of hypoxic respiratory failure. Therefore, while further study is needed, this course of failure could be indicative of an immunological response [112], potentially caused by a cascade of inflammatory cytokines [102], that is initiated due to radiation-induced exacerbation of pulmonary disease [154]. Ideally, if the presence of IPF or ILD was clinically confirmed, these comorbidities would have been addressed or the patients would have been excluded from treatment, which demonstrates the need to screen NSCLC patients for comorbidities prior to RT. While the grade 5 RILT cases represent the most severe negative response, the pattern of irradiating large portions of low-functioning lung is consistently observed in RILT cases from both cohorts.

Functional-guided RT has primarily been employed to shape radiation fields to avoid functional lung and funnel dose through low-functioning regions. A functional-avoidance technique was employed in the latter patient cohort (n=30) to protect against irradiating above- average perfusion and ventilation. Despite these included functional priorities in treatment planning, perfusion functional intensity receiving $\geq$ 5 Gy (fV5) was the only dose-function metric found to significantly differ between the patient cohorts, suggesting the ability to significantly shift dose to spare functional lung was limited. Out of the eight RILT cases that received lowVQ20 to greater than 15% of the ipsilateral lung, half were from the former cohort and half from the latter cohort, suggesting the functional sensitivity of low-functioning lung was similar in each cohort despite the use of functional- avoidance RT in the latter cohort. Patients with compromised lung function prior to RT are generally thought to be more prone to toxicity [118]. Increased FDG-PET uptake in the normal lung, a marker of pulmonary inflammation, has been shown to correlate with RP incidence [98], especially in patients also receiving a high mean lung dose [155]. Similarly, in 2018, Otsuka

et al published a study that concluded high dose to poorly functioning regions, as determined by 4DCT ventilation, was associated with the highest risk of toxicity [99]. However, dysfunctional lung sensitivity to RT has never been shown on V/Q SPECT imaging.

As SPECT is a direct measure of perfusion or ventilation intensity, such that combined V/Q represents functional gas exchange, it is considered the gold standard in functional lung imaging but is non-specific for regions of dysfunction. Alternatively, normal lung PET imaging can measure pulmonary inflammation and CT can measure parenchymal density, which may be related to lung disease. Consequently, these imaging modalities are often used in the context of quantifying dysfunctional lung, as opposed to SPECT which is primarily used for functional lung quantification. As such, there has been limited investigation into the dose-effect in SPECT-based low-functioning lung regions. And yet, because the patients who will benefit most from functional-guided RT are those with functional defects, further work is needed to understand the underlying pathology of these defected regions and its effect on the biological makeup in the lung prior to RT. In other words, limiting dose to normal lung is suggested in all cases, but identifying the patients with increased risk for severe RILT prior to RT should be the highest priority. Especially with concurrent immunotherapy becoming standard of care in NSCLC patients undergoing RT, patient-specific functional estimates are needed to identify patients with compromised lung function. Ultimately, further research is paramount to understand the immune reaction to RT such that the individual response can be optimized [156].

While the results of this study are suggestive that irradiating low-functioning tissue plays a role in the onset of RILT, there are many challenges in the quantification of V/Q SPECT. A cleansing methodology was implemented to remove saturation artifacts, but in many cases, it can be difficult to decipher true functional intensity from an artifact. Because the resolution of SPECT images is limited, combined VQ functional categorizations were implemented to represent regions with high probability of pulmonary dysfunction but of unknown etiology. Similarly, regional lung segments and individual lung structures were used to refine the area of interest, yet better functional localization could further improve risk estimates. Functional imaging is challenging to quantify

and even more challenging to compare due to the complexities of the lungs and the various imaging modalities. However, by implementing three functional lung categorizations (low, normal, high) and establishing an average normalized functional intensity of 1.0 for normal lung, this study aimed to provide a template for standardization that can be expanded upon to improve our understanding for the role of irradiating functional lung in the onset of RILT.

6.6 Conclusion

This study evaluated perfusion, ventilation, and combined V/Q SPECT functional metrics in 88 NSCLC patients treated with conventionally fractionated RT. Through this analysis, patients at the highest risk for RILT were found to be those who received a high dose to lower lung or low-functioning regions of the ipsilateral lung at baseline. This result runs counter to the hypothesis that redistributing dose from high- to low-functioning regions of lung is a strategy likely to decrease toxicity. Future studies are warranted to better characterize the effect of irradiating dysfunctional lung, and to determine the appropriate role for functional imaging-guided treatment planning for NSCLC patients with heterogeneously distributed lung function.

CHAPTER VII

Transition to CT-Based Parametric Response Mapping

7.1 Summary

Currently, no standard protocol exists to measure pulmonary dysfunction in lung cancer patients prior to radiation treatment (RT). Parametric response mapping (PRM) of high-resolution inhale/exhale CT is a promising solution that offers the ability to quantify and characterize pulmonary disease – including small airway disease, emphysema, and parenchymal disease – on a patient-specific basis. The aims of this investigation were: 1) to establish the expected PRM metrics in lung cancer patients prior to RT and 2) to analyze PRM metrics in patients that incurred radiation pneumonitis. Quantitative analysis of high-resolution inhale/exhale CT scans, through Jacobian-based deformation and PRM classification, has the potential to readily provide functional lung and pulmonary disease metrics and should be further investigated for use in RT treatment planning.

7.2 Introduction

Despite major paradigm shifts in radiation treatment (RT) planning and delivery over the past decade, radiation-induced lung toxicity (RILT) continues to be a major obstacle in the successful treatment and management of advanced lung cancer patients. Symptomatic radiation pneumonitis (RP) requiring medical intervention (Grade 2) can occur in roughly 20-30% of lung cancer patients

receiving RT and the prognosis significantly worsens for patients who incur severe cases (Grade 3 and above) of RP [157–160]. To address this sequela of radiotherapy, efforts are being made to incorporate risk factors, such as patient characteristics, treatment and biological markers, in treatment planning and assessment to improve patient outcome. Nevertheless, RILT continues to hinder successful clinical management of lung cancer patients treated with RT.

Lung cancer patients are known to suffer from pulmonary comorbidities, such as chronic obstructive pulmonary disease (COPD) or interstitial lung disease (ILD), which can diminish their ability to recover from radiation treatment [161, 162, 134]. And yet, standard practice RT treatment planning for lung cancer patients does not include any patient-specific assessment of pulmonary condition. Functional imaging techniques such as single-photon emission computed tomography (SPECT), hyperpolarized xenon magnetic resonance imaging (MRI), dual-energy computed tomography (CT), and four-dimensional computed tomography (4DCT) have been studied for use in assessing lung function and have demonstrated the potential to incorporate functional lung information in RT planning [5, 24, 163, 164]. However, because these imaging techniques provide measures of perfusion and ventilation, they are unable to identify pre-existing pulmonary comorbidities. Recent studies have found that increased uptake of fluorodeoxyglucose positron emission tomography (FDG-PET), a marker of pulmonary inflammation, in non-cancerous lung parenchyma was correlated with RP incidence [98]. As such, this work replicated the findings of Petit et. al, which demonstrated a relationship between high dose to regions with increased FDG uptake prior to RT and RILT incidence [165]. While these studies are encouraging, the authors were unable to determine the type and extent of pulmonary abnormality using PET imaging.

Parametric response mapping (PRM) is an analytical technique based on deformable mapping of inspiration/expiration CT scans that is capable of differentiating and displaying pulmonary abnormality subtypes as a spatially-resolved patient-specific map. First introduced in 2012, PRM has since been shown to improve phenotyping of COPD [166]. Recent studies have demonstrated that PRM-based estimates for small airways disease (SAD) are significant predictors of disease progression [167] and have been validated as a quantitative measure of SAD in COPD patients [168].

In addition to COPD, the PRM analysis of clinical CT scans has been shown to detect infection and pneumonitis in bone marrow transplant recipients [169, 170] and fibrosis in lung transplant recipients [171] even in the presence of obstructive lung disease. The purpose of this chapter was to investigate the incidence of pulmonary abnormalities, as identified by PRM analysis, in lung cancer patients presenting for RT. Furthermore, voxel-wise PRM classifications for normal and abnormal lung were quantified on a global and regional basis and were evaluated in patients that incurred Grade 2 RP.

7.3 Methods

7.3.1 Patient Population

Twenty-four lung cancer patients undergoing RT were accrued as part of a single-site, IRB-approved clinical trial to determine the feasibility of PRM for use in radiation treatment planning. Patients with histologically-verified lung cancer scheduled for RT were eligible for enrollment. Informed written consent was obtained from each patient. Patients were treated with 3-dimensional conformal RT (n=5), intensity-modulated RT (n=4), or volumetric arc therapy (n=15) based on tumor size, location, and geometry. The prescription dose was generally 60 or 66 Gy, and seven patients received functional-adaptive RT, i.e. dose fields were shaped to limit dose to ventilation/perfusion (V/Q) SPECT-based functional lung at mid-treatment. Radiation pneumonitis (RP) was graded using the Common Terminology Criteria for Adverse Events (CTCAE) v4.0 and RP Grade $\geq$2 was used as the toxicity endpoint [135]. In 24 lung cancer patients with a median follow up of 16 months, 4 patients were graded to have incurred Grade 2 RP. Patient characteristics are provided in Table 7.1.

7.3.2 X-Ray Computed Tomography

Inspiration and expiration CT scans were performed at total lung capacity and functional residual capacity, respectively, and were acquired prior to any treatment. CT acquisition and recon-

Patient Characteristics and Whole-Lung Pre-Treatment PRM Metrics

	Total Cohort (n = 24)	Non-Toxicity Cohort (n=20)	Toxicity Cohort (n=4)
Histology			
Adenocarcinoma	13	10	3
Squamous Cell Carcinoma	8	7	1
Small Cell Lung Cancer	2	2	0
Non-small Cell Lung Cancer	1	1	0
Age [years]			
Median	59	57	61
Range	42 – 86	42 – 86	57 – 77
Gender			
Male	17	15	2
Female	7	5	2
Tumor Stage			
Stage 2	1	1	0
Stage 3	19	16	3
Stage 4	4	3	1
Clinically-Verified Pulmonary Comorbidity			
Emphysema	1	1	0
COPD	3	3	0
Fibrosis	0	0	0
Concurrent Chemotherapy			
Yes	20	17	3
No	4	3	1
Volume [cc]			
Median	3433	3531	3119
Range	1880 – 5296	1880 – 5296	2369 – 3344
Mean Lung Dose [Gy]			
Median	14.5	13.4	18.1
Range	2.2 – 23.9	2.2 – 23.9	15.0 – 20.1
PRM Normal			
Median	66.5	69.1	57.9
Range	11.8 – 90.8	31.7 – 90.8	11.8 – 61.7
PRM PD			
Median	17.4	16.1	25.0
Range	6.9 – 85.4	6.9 – 60.4	8.6 – 85.4
PRM SAD			
Median	6.7	6.4	15.8
Range	0.3 – 30.3	0.4 – 30.3	0.3 – 22.6

Table 7.1: Patient characteristics and global lung pre-treatment PRM metrics.

struction parameters are listed in Table 7.2. Lung volumes, excluding the gross tumor volume, were segmented using in-house software from the thoracic cavity. Segmented lungs were regionally divided into sextants as defined: upper lung sextants were defined above the carina, lower lung sextants were defined below the inferior pulmonary vein, and middle lung sextants were defined between the upper and lower sextants Figure 6.2.

High-Resolution Inspiration/Expiration CT Acquisition Parameters	
Manufacturer	Philips
Model	Brilliance Big Bore
Scan Options	HELIX
Reconstruction	Convolution Kernel B
Filter Type	B
Tube Voltage	120 kV
Tube Current	407 mA
Exposure	250 mAs
Slice Size	512 x 512
Slice Thickness	1 mm

Table 7.2: High-resolution inspiration/expiration CT acquisition parameters.

7.3.3 Parametric Response Mapping

PRM was applied to all paired CT scans as previously described [166, 172]. As illustrated in Figure 7.1A, PRM was performed by spatially aligning the inspiration CT scan to the expiration CT scan using Elastix, an open-source, intensity-based deformable image registration (DIR) algorithm [173, 174]. Once the paired CT scans were aligned, individual voxels were classified based on the paired CT Hounsfield units (HU) as shown in FFigure 7.1B. The discrete thresholds that are applied to the spatially aligned paired CT scans have been previously reported, and in some cases validated [168, 175–177]. The percent volume of each PRM classification was calculated by normalizing the sum of all like-classified voxels by the sum of all voxels in the lungs structure and multiplying by 100. PRM analysis was performed using in-house algorithms developed in a technical computing language (MATLAB v. R2016a, MathWorks Inc., Natick, MA).

7.3.4 Statistical Analysis

Summary statistics of PRM metrics were generated over the whole-lung and regional lung sextants. The average dose to each PRM classification was quantified for 23 patients – as the voxelwise dose was unavailable for one patient – using the Eclipse treatment planning system (Varian Medical Systems, Palo Alto, CA). Correlations between PRM metrics and patient characteristics were analyzed using a paired t-test. Due to minimal levels of emphysema present in this patient population (cohort average $<0.3\%$), only parenchymal disease (PD) and SAD were reported as

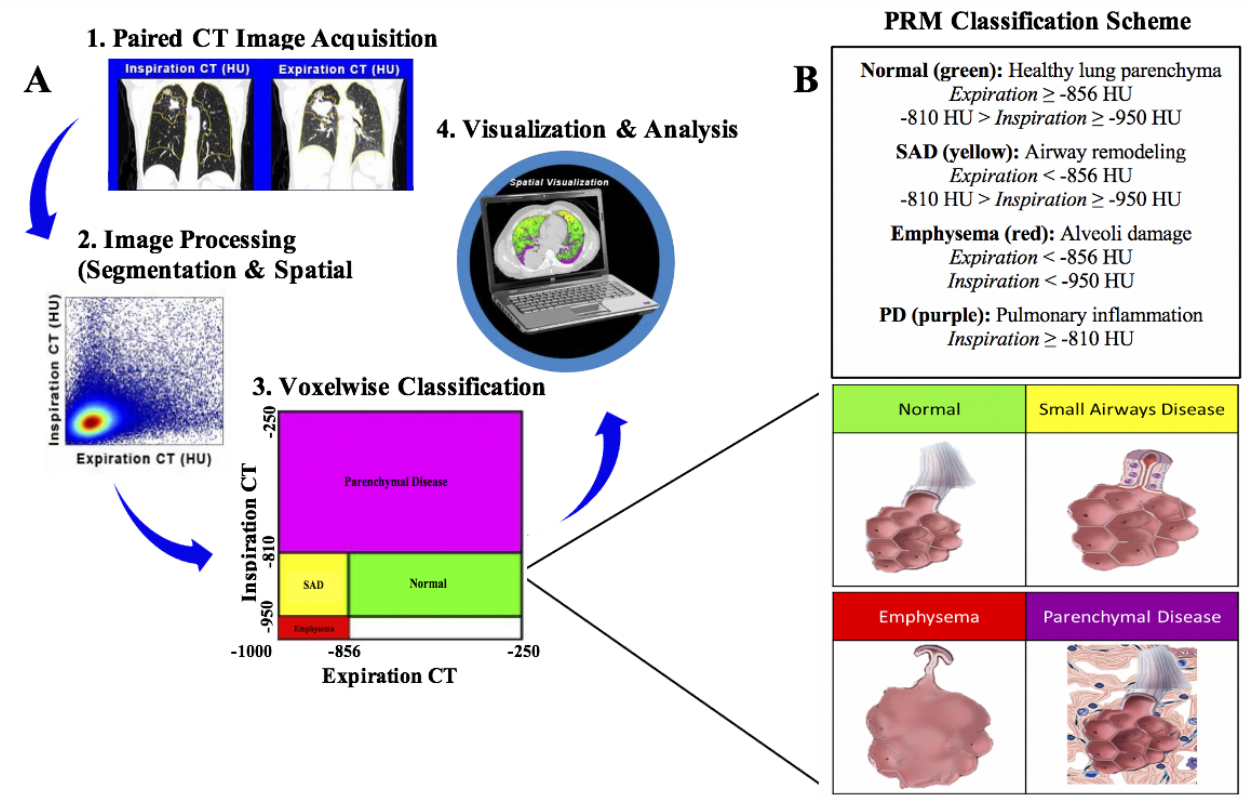

Figure 7.1: A) The workflow used for PRM analysis data acquisition and processing. B) Illustration of the pulmonary abnormalities identified by PRM analysis (bottom) and the classification schema (top) based on inspiration/expiration CT lung densities accompanied with clinical interpretations for each PRM category.

PRM abnormalities. Individual sextants for each case were stratified based on elevated levels of SAD and PD in the volume. Based on previously published work, SAD>20% and PD>20% are considered significantly elevated and indicate the presence of a pulmonary abnormality [169, 171]. All cases were stratified based on these criteria to determine frequency of elevated SAD and/or PD by lung location (i.e. sextant). A paired t-test was performed to determine if elevated SAD and/or PD occur in close proximity of the tumor (i.e. sextant where the tumor resides). Univariate logistic regression analyses were used to test the association between PRM metrics and the incidence of grade 2 radiation pneumonitis. The 95% confidence intervals were computed to quantify uncertainty and metric stability. For all analyses, two-sided p-values of <0.05 were considered statistically significant and p-values <0.1 were considered a marginal association.

7.4 Results

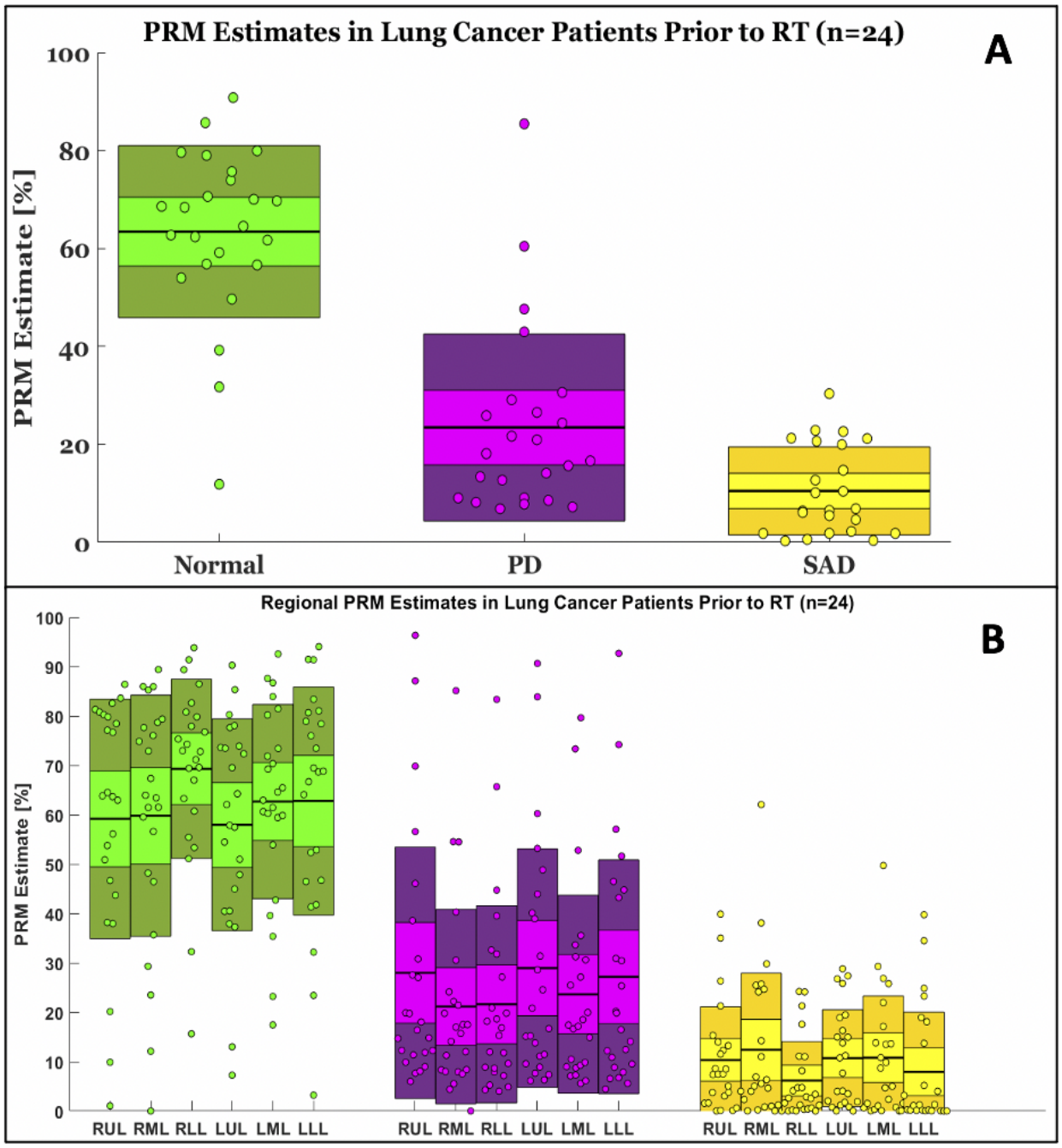

Figure 7.2: A) Global and B) regional PRM classification metrics for normal, small airways disease (SAD), and parenchymal disease (PD) in 23 NSCLC patients prior to receiving RT.

The distribution of pre-treatment whole-lung PRM metrics are shown in Figure 7.2A, which corresponded to a cohort average of 63%±18% normal lung, 23%±19% PD, and 10%±9% SAD.

When comparing PRM metrics to patient characteristics and pulmonary function tests, only a marginal negative correlation was found between age and normal PRM (r=-0.39; p=0.06). All PRM metrics demonstrated negligible correlations with gender, smoking status, concurrent chemotherapy, or pre-treatment FEV1/FVC. Elevated levels of PD were found to be inversely correlated to normal parenchyma (r=-0.87; Figure 7.3A), which was not observed for SAD (r=-0.11; Figure 7.3B).

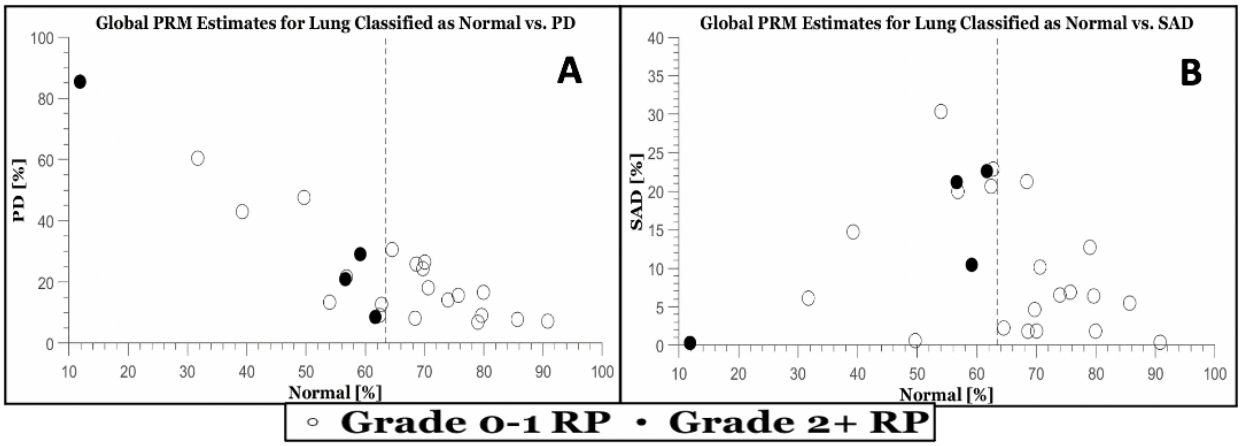

Figure 7.3: A) Normal vs. parenchymal disease (PD); B) Normal vs. small airways disease (SAD) relative to the average amount of PRM-classified normal lung (dashed line) for patients that incurred Grade 2 RP (filled circles) versus patients that incurred Grade 0-1 RP (open circles).

Analysis of PRM metrics over each regional sextant resulted in similar distributions to those observed over the whole-lung as shown in Figure 7.2B. In the region with primary tumor involvement, average PRM values were found to be 59%±26% normal, 29%±27% PD, and 9%±11% SAD. These values were not found to be significantly different from other regions of the lungs. Although this patient population had a high incidence of elevated levels of PD and SAD, as defined as lung sextants with SAD and/or PD >20%, these abnormalities were not found to be correlated to any specific lung sextant or tumor location Table 7.3.

Applying the elevated abnormality criteria of >20% over the entire lung volume, 16 patients exhibited elevated pulmonary SAD (n=6) or PD (n=11), and all of these patients exhibited elevated abnormalities within multiple sextants in the lungs. Of the eight patients without elevated global disease, five patients were found to have local elevated SAD or PD, and only three patients in

Frequency of tumor involvement with elevated SAD and PD

Lung Sextant	Primary Tumor Involvement	Elevated SAD	Elevated PD
RUL	9	3 (4)	2 (9)
RML	4	1 (7)	2 (8)
RLL	0	0 (3)	0 (8)
LUL	7	0 (4)	5 (12)
LML	1	0 (5)	0 (9)
LLL	3	0 (4)	1 (11)

Note: Frequency values for SAD and PD represent the number of cases with SAD>20% and PD>20% within the tumor bearing lung volume. Parentheses values represent all cases with elevated SAD or PD in any sextant. Volumes of the lungs are presented as RUL for right upper lung, RML for right middle lung, RLL for right lower lung, LUL for left upper lung, LML for left middle lung, and LLL for left lower lung.

Table 7.3: Frequency of tumor involvement with elevated SAD and PD.

this cohort did not exhibit elevated disease in any of the lung regions. Nevertheless, 13 of the 24 patients (54%) exhibited either elevated SAD or PD in the region with primary tumor involvement. Only one patient (RP Patient C; Figure 7.4) exhibited both elevated SAD (30%) and PD (22%) in the tumor region.

As shown in Figure 7.4, all four RP cases demonstrated pulmonary abnormalities in close proximity to the tumor, of which two had elevated PD, one had elevated SAD, and one had elevated PD and SAD. The extent of pulmonary abnormality within the global lung was most pronounced in RP Case A, with 85% of the entire lungs classified as PD. As observed in Figure 7.3, the four RP cases were all estimated to have below-average amount of PRM-classified normal lung prior to RT, where the dashed line represents the population-average for PRM-classified normal lung. The RP cases, on average, also received a higher mean lung dose than the total cohort (Table 7.1). While none of the tested metrics were found to significantly correlate with Grade 2 RP incidence, normal PRM ($p=0.08$) and mean lung dose ($p=0.08$) were found to be marginally associated with Grade 2 RP using univariate logistic regression as shown in Table 7.4.

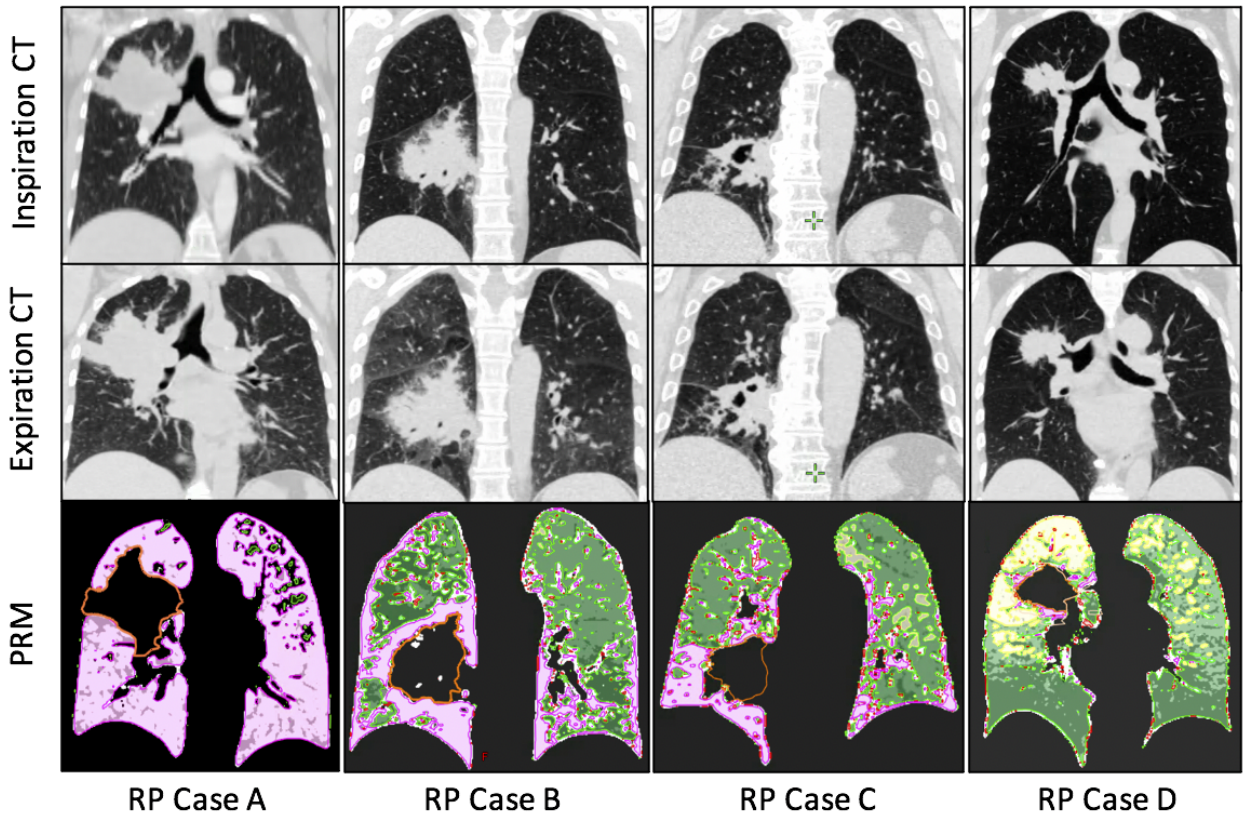

Figure 7.4: Single slice images for the inspiration (top row) and expiration (middle row) CT scans and PRM classification distributions (bottom row) showing normal parenchyma (green), small airways disease (yellow), and parenchymal disease (purple) in the four lung cancer patients that incurred Grade 2 RP.

Univariable Logistic Regression for Association Between Pre-Treatment Metrics and RP

	Whole-Lung			
Metric	**Mean (SD)**	**Odds Ratio**	**95% CI**	**p**
Lung Volume [cc]	3713 (1084)	1.29	0.45–3.37	0.60
Age [yr]	61.6 (10.7)	1.03	0.93–1.14	0.51
Concurrent Chemotherapy	--	0.53	0.05–12.7	0.63
FEV1/FVC [%]	72.5 (6.3)	1.02	0.86–1.24	0.85
Jacobian	1577 (304)	0.15	0.00–6.21	0.35
Lung Dose [Gy]	13.8 (3.8)	1.63	1.07–3.36	0.08
Normal PRM [%]	63.4 (17.6)	0.94	0.87–1.00	0.08
Small Airway Disease PRM [%]	10.5 (9.0)	1.05	0.93–1.19	0.44
Parenchymal Disease PRM [%]	23.5 (19.1)	1.04	0.98–1.10	0.18

Table 7.4: Univariable logistic regression analysis between baseline global lung metrics and grade 2 RP incidence.

7.5 Discussion

Patients with advanced lung cancer often present for RT with various pulmonary comorbidities, such as COPD and idiopathic pulmonary fibrosis (IPF). In fact, studies have found that 40-70% of patients diagnosed with lung cancer have shown a prevalence of COPD [178]. And while IPF is generally less common (10-20%), the outlook for patients with pre-existing IPF is dismal both in terms of survival [89] and incidence of severe toxicity [149, 94]. Furthermore, recent studies have found that pulmonary comorbidities in lung cancer patients are often clustered due to the shared risk factor of smoking and that patients with combined emphysema and fibrosis had the worst prognosis [179, 180]. Despite these comorbidities being a known risk factor for the incidence of RILT and a poor prognostic factor for overall survival, their presence and severity is often unknown to the radiation oncology team. Given this lack of information, there have been numerous calls for a better approach to account for comorbidities and functional condition in the treatment management and risk assessment of lung cancer patients [181, 182].

As an established diagnostic imaging technique used to identify and quantify lung-related disease, PRM analysis of inspiration/expiration CT scans allows for improved detection and quantification of pulmonary abnormalities that may be compromising a patient's functional condition. In this thesis, PRM analysis was used to generate global and regional estimates of pulmonary abnormalities in 24 lung cancer patients prior to RT. A large deviation in the extent of these pulmonary abnormalities was observed, suggesting a wide variation in pulmonary condition. Toxicity Case A in Figure 7.4 was identified as an extreme case. Given the complete bronchial obstruction to the ipsilateral lung observed on V/Q SPECT, the excessive global PD estimate is thought to be evident of the patient's inability to reach complete inspiration, which caused an irregular scan. However, based on this cohort, 21 out of 24 patients exhibited some form of local elevated pulmonary abnormality. As such, these findings suggest a high prevalence of pulmonary disease, that varies in location on a patient-specific basis, is present in advanced lung cancer patients prior to RT.

While there is a high prevalence of PRM-derived lung abnormalities, these conditions do not appear to be associated with tumor location. Yet, all 4 patients that incurred Grade 2 RP were

estimated to have below-average values of PRM-classified normal lung, indicating an elevated presence of pulmonary abnormalities in these cases. Upon closer examination (Figure 7.4), three of the four RP cases had elevated PD and one had elevated SAD. While no PRM metrics were found to be significantly associated with toxicity incidence, patients that incurred grade 2 RP tended to have less PRM normal lung and received a higher mean lung dose. With only four RP cases, it is difficult to draw any meaningful conclusions, however, based on known risk factors, it is expected that patients with pre-existing pulmonary comorbidities and a higher mean lung dose are at the highest risk for RP [84].

PRM of CT scans was used as an indicator for a subset of pulmonary comorbidities. The strength of PRM is its ability to classify individual voxels as normal, SAD, emphysema, and PD using high-resolution inspiratory and expiratory CT scans (Figure 7.1). In contrast to emphysema and SAD, PRM-derived PD, which is classified based on -810 HU at full inflation, is less specific. This quantitative index signifies a high attenuation area (HAA) initially used to account for the presence of infection in hematopoietic stem cell transplantation recipients that develop bronchiolitis obliterans syndrome [169]. Subsequently, the PD classification has been applied to quantify fibrosis and pulmonary pneumonitis [170, 171]. This interpretation of PD is similar to other previously published work using similar strategies to evaluate pulmonary inflammation using HAA on CT scans [183].

The increased lung attenuation, i.e. PRM-derived PD, observed in this cohort can be considered to be an indirect readout of local inflammation within the lung parenchyma. This would be consistent with two studies that attributed local inflammation to elevated levels of FDG-PET in advanced lung cancer patients that developed RP following RT [98, 155]. While the Castillo et al study did not find any association between CT-based lung density and RP incidence, other studies have found baseline lung density as a determinant of radiation-induced lung damage and have proposed personalizing RT to avoid high density lung as a way to improve patient outcome [184, 185]. Furthermore, numerous other studies have previously reported the presence of pulmonary comorbidities as a significant risk-factor in the development of radiation-induced lung toxicity following

RT [84, 85, 88, 87]. Thus, while most functional imaging modalities have relied on quantifying perfusion and/or ventilation as a surrogate for lung function, it is possible that utilizing PRM-based classifications may provide an enhanced understanding regarding the patient-specific risk for developing RP.

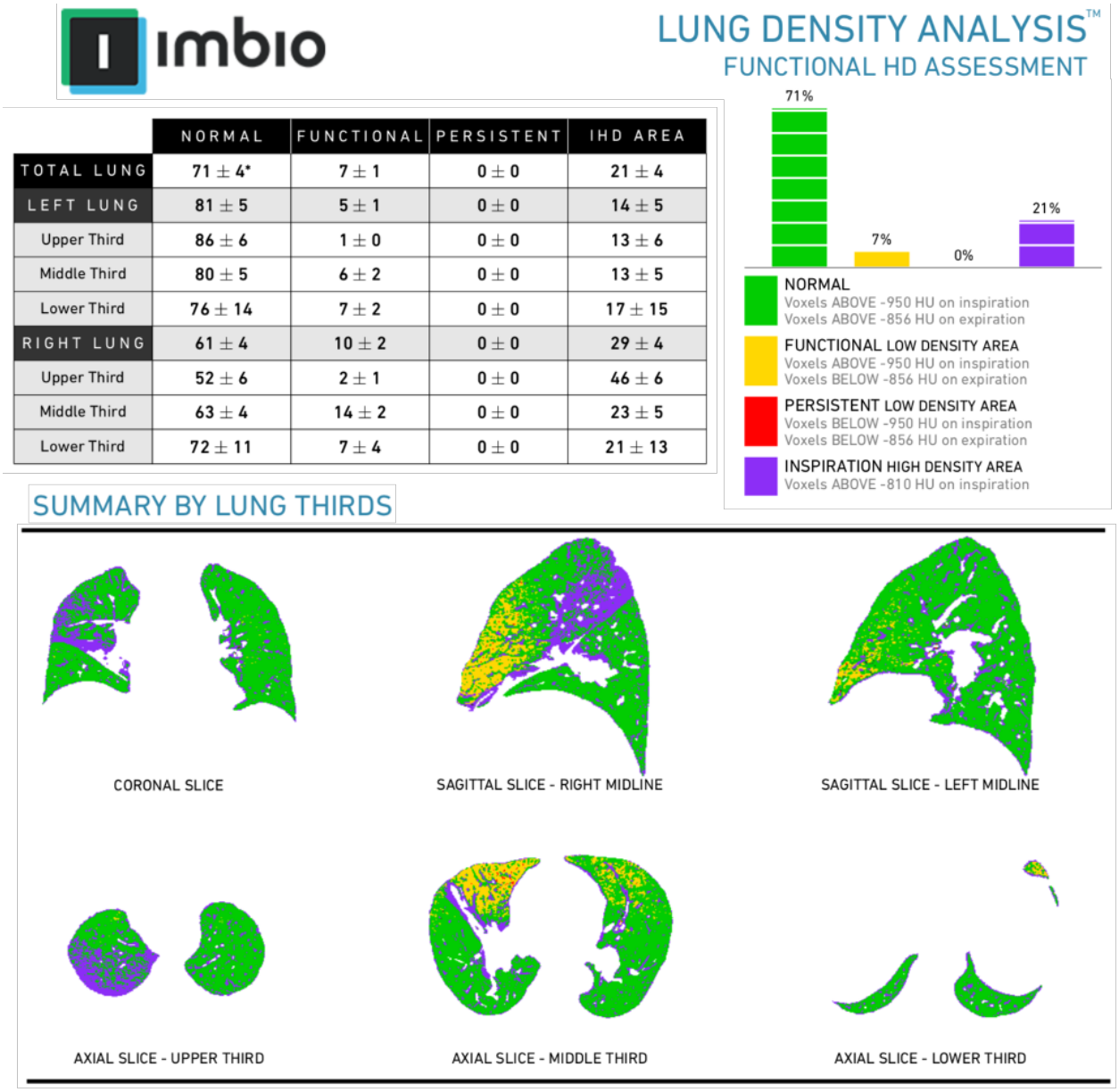

	NORMAL	FUNCTIONAL	PERSISTENT	IHD AREA
TOTAL LUNG	71 ± 4*	7 ± 1	0 ± 0	21 ± 4
LEFT LUNG	81 ± 5	5 ± 1	0 ± 0	14 ± 5
Upper Third	86 ± 6	1 ± 0	0 ± 0	13 ± 6
Middle Third	80 ± 5	6 ± 2	0 ± 0	13 ± 5
Lower Third	76 ± 14	7 ± 2	0 ± 0	17 ± 15
RIGHT LUNG	61 ± 4	10 ± 2	0 ± 0	29 ± 4
Upper Third	52 ± 6	2 ± 1	0 ± 0	46 ± 6
Middle Third	63 ± 4	14 ± 2	0 ± 0	23 ± 5
Lower Third	72 ± 11	7 ± 4	0 ± 0	21 ± 13

Figure 7.5: Lung Density Analysis (LDA) visualization provided through collaboration with Imbio, LLC. Quantitative estimates are shown for the global and regional lung structures (top), and the spatial distribution is displayed across various slice orientations (bottom).

To better understand and act upon these specific abnormalities in individual patients, three-

dimensional voxel-wise maps of PRM classifications can be generated on a patient-specific basis and presented to the radiation oncology team as tool for both qualitative and quantitative assessment of pulmonary condition. Through a collaboration with Imbio, LLC, a cloud-based solution has been implemented at the University of Michigan to generate PRM images and metrics (Figure 7.5), which successfully demonstrates the translation of this established diagnostic technique in therapeutic applications. It is also possible to produce volume density maps for each PRM classification for use in PRM-guided treatment planning (Figure 7.6). The Jacobian determinant between the inspiration and expiration scan, a measure of biomechanical deformation, can also be quantified to provide an additional metric to assess ventilation and compare to other functioning imaging modalities, e.g. V/Q SPECT. Although larger scale studies are needed to decipher the true benefit of these PRM metrics in the management and risk assessment of lung cancer patients undergoing RT, this chapter provides a blueprint for an exciting new approach to quantify pulmonary abnormalities in lung cancer patients prior to, during, and following treatment.

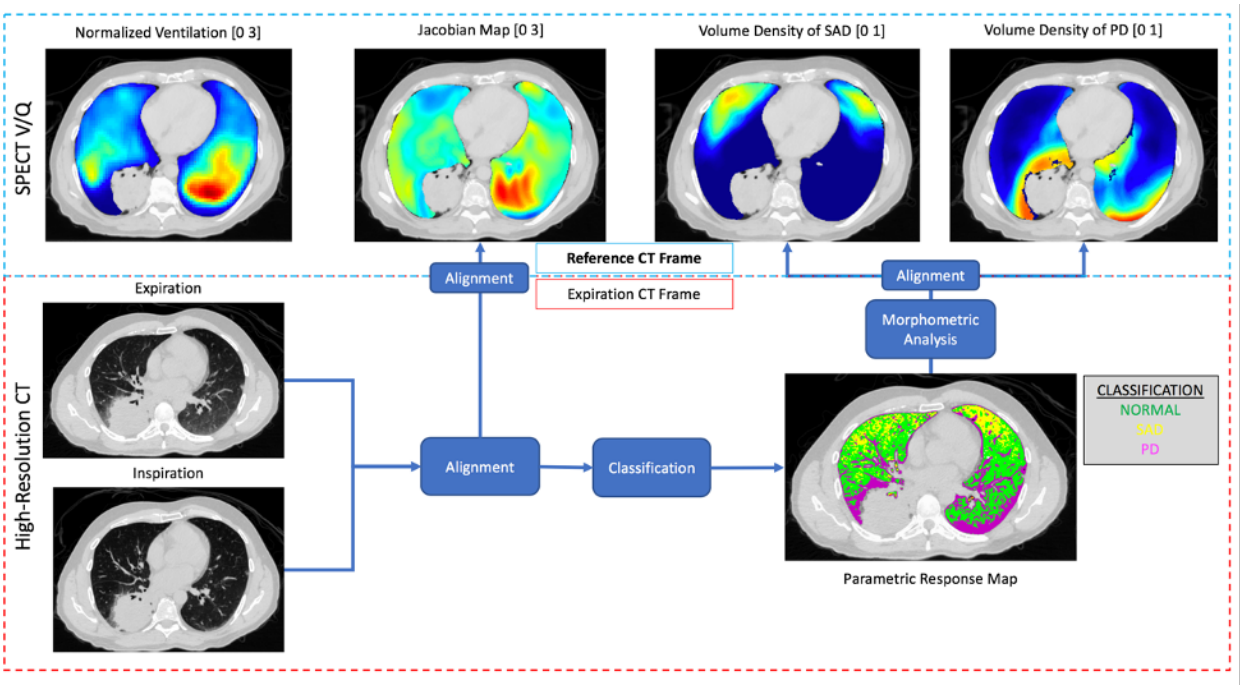

Figure 7.6: Workflow used to process and spatially align high-resolution inhale/exhale CT scans to the treatment planning CT and V/Q SPECT images. PRM metrics for normal and dysfunctional lung can be visualized through voxelwise classifications (bottom) or volume density maps (top).

Although larger scale studies are needed to decipher the true benefit of these PRM metrics in the management and risk assessment of lung cancer patients undergoing RT, this chapter provides a blueprint for an exciting new approach to quantify pulmonary abnormalities in lung cancer patients.

Several limitations of this imaging technique must be explicitly noted. First, the limited number of cases included resulted in insufficient statistical power to conclusively demonstrate PRM metrics as predictive of RILT. Nonetheless, these findings provided some indication of the potential of PRM metrics to identify at-risk patients. In addition, the spatially retained information in PRM provides an opportunity to incorporate this approach into radiation dose planning to avoid regions of lung abnormalities that may, upon irradiation, stimulate RILT onset. Secondly, advanced lung cancer patients may have difficulties in performing the required breath holds, sometimes up to 30 seconds, during CT acquisitions, required for PRM. This could result in insufficient inflation or deflation of lungs altering the lung densities on the CT scans, which would affect the PRM quantitative measurements. Although there is a possibility for error, the protocols used in this method are standard for evaluating patients with chronic lung disease, such as COPD, by CT in thoracic radiology and the feasibility of acquiring paired CT has been demonstrated in many large clinical trials [186, 187]. Furthermore, all patients enrolled in the trial were able to complete the breath-hold requirements.

7.6 Conclusion

High-resolution, inspiration/expiration paired-CT scans were used to quantify pulmonary abnormalities, through parametric response mapping (PRM), in lung cancer patients prior to undergoing RT. As such, this investigation demonstrated the use of PRM analysis as an alternate imaging modality with the potential to provide pulmonary disease information for lung cancer patients prior to RT. Ultimately, this standard imaging approach may prove useful in the radiation oncology clinic as the basis for spatial prioritization in personalized treatment planning and risk assessment of RP incidence, and future studies in these areas are ongoing.

CHAPTER VIII

Conclusions and Future Work

8.1 Summary of Findings

Based on the results of this thesis, we propose three separate dose-function pathways that lead to radiation-induced lung toxicity: 1) Excessive functional damage in the lung exceeds the capability of the functional reserve to maintain normal respiration, 2) high dose to the lower lung region aggravates an anatomical sensitivity, and 3) high dose to diseased regions provokes a negative reaction due to the exacerbation of pulmonary comorbidities.

In patients with homogeneous lung function or a pronounced lack of pulmonary comorbidities, it is clear that dose should be delivered sparingly to the normal tissue such that functional damage is minimized, given that normal- and high-functioning lung is damaged at the highest rate. However, it is also important to consider the delivered dose to each individual lung, not just the global lung dose constraints, to ensure the ipsilateral lung is not overwhelmed, such that it cannot sufficiently perform gas exchange and can no longer maintain an effective oxygen capacity.

Alternatively, understanding the effect of dose to low-functioning lung is critical in non-small cell lung cancer patients who commonly present with comorbidities and other pulmonary defects that change during the course of fractionated radiation treatment. In fact, we hypothesize that the optimal radiation prescription varies on a patient-specific basis and is a delicate balance between limiting functional damage and avoiding diseased lung, which may be hypersensitive to radiation and cause excessive damage outside of the high dose regions. Further work in this area is required

to understand the underlying factors that may be contributing to these various responses, and it is suggested that imaging techniques that can combine information regarding pulmonary function, biological factors, such as cytokines and mRNAs, as well as pre-existing disease will all be crucially important to better understand optimal patient-specific strategies for treating NSCLC patients with radiation.

8.2 Future Work

While this type of precision discovery is elemental in understanding how patients respond to treatment, the ultimate goal in cancer medicine are individualized treatments informed by personalized parameters. In their 2000 work titled "The Hallmarks of Cancer", Hanahan and Weinberg stated:

> We forsee cancer research developing into a logical science, where the complexities of the disease, described in the laboratory and clinic, will become understandable in terms of a small number of underlying principles

Ultimately, this sentiment regarding the treatment of cancer can be equally applied to reducing toxicity, and as a next step in this research, I believe it is imperative to further develop and test The Hallmarks of Toxicity, i.e. a small number of principles, or pathways, that describe the primary factors leading to toxicity incidence. While these hallmarks could be determined for any disease site or treatment modality, this research specifically identified three separate hallmarks of radiation-induced lung toxicity $\{$1) large functional damage fraction, 2) high dose to lower lung, and 3) high dose to low-functioning lung$\}$, and the best way to vet and further develop these findings is to continue to gather data regarding these vulnerabilities. And while there are a myriad of confounding factors that may ultimately contribute, it is necessary to make assumptions to identify the properties that are most prominent and easy to act upon. To this end, Figure 8.1 demonstrates a proposed mechanism, "The Data Box", in which the principles of RILT, and the metrics that describe them, can be gathered, applied, and adjusted through a continuous process that will allow

for each patient's risk to be assessed against the current hallmarks and stored for future modification. Furthermore, the hallmarks for RILT must be weighed against the risk of tumor recurrence, given that reducing toxicity incidence is only a piece of the cancer puzzle.

Although SPECT imaging has proven to be challenging to obtain in the Radiation Oncology clinic, limiting the predicted functional lung damage during the treatment planning process, based on the derived patient-specific dose-function response estimates, has the potential to reduce the incidence of toxicity following radiotherapy. Therefore, these dose-function models should be further refined (especially in regard to incorporating a component of reperfusion) and implemented to model individual outcomes. It may also be possible to include a quantitative risk metric to weight the locational sensitivity of the delivered radiation. To further examine our finding that patients with pulmonary dysfunction were at an increased risk for toxicity incidence, we propose further testing the potential for parametric response mapping to quantify specific phenotypes of pulmonary disease, including SAD, fibrosis, and emphysema. Whether through SPECT or PRM analysis, quantifying global and regional metrics within a larger patient population may help to contribute a precision database that can characterize the expected health and homogeneity expected for normal and abnormal patients. Based on the results of this proposed research, a functional normal tissue complication probability risk assessment could be developed to account for patient-specific pulmonary sensitivities and expected functional lung damage to enhance the prescription and development of personalized radiation treatment plans for NSCLC patients.

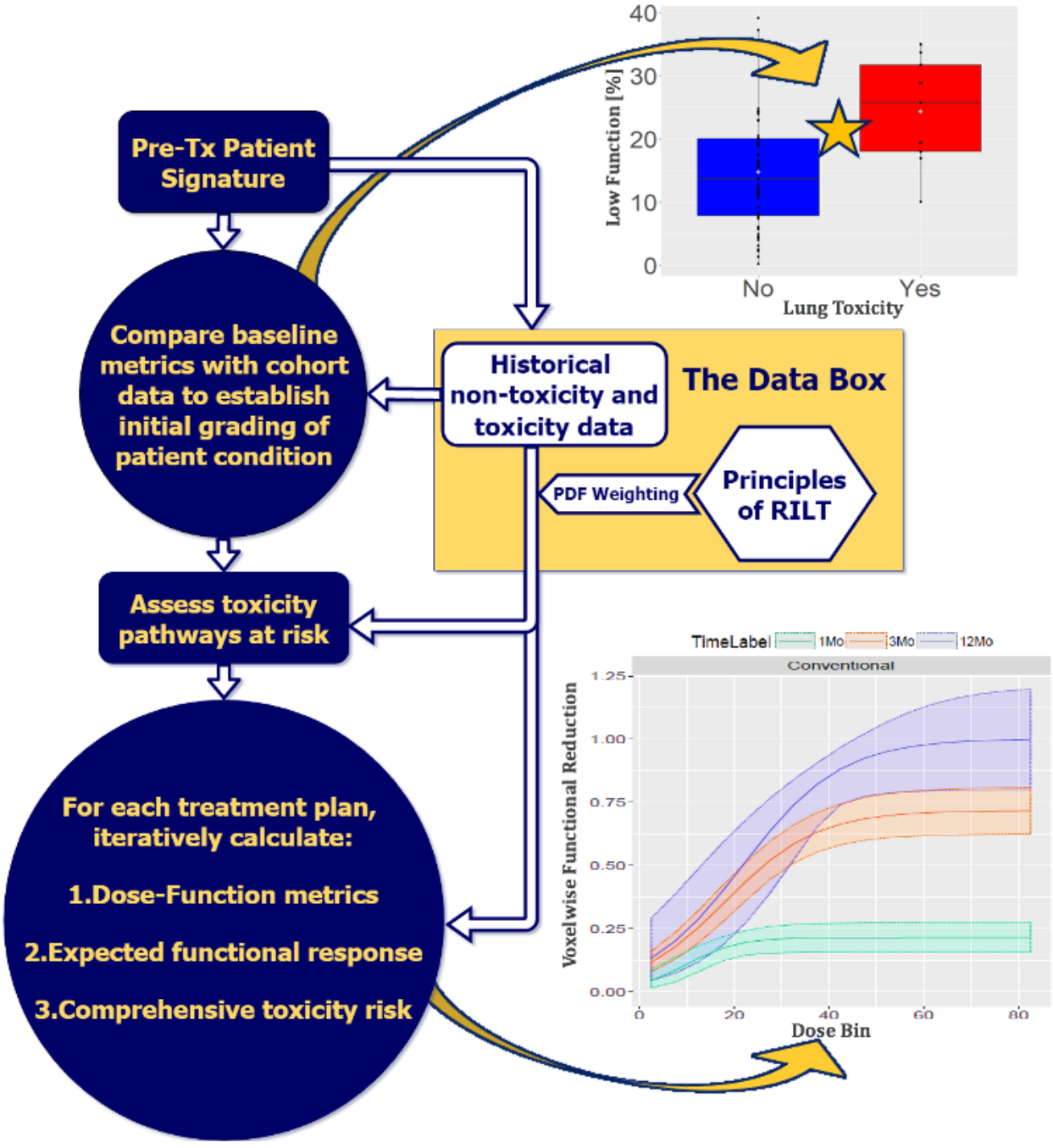

Figure 8.1: A theoretical approach to utilize functional lung metrics and models to enhance patient-specific radiation treatments using a historical database that tracks successes and failures and implements weighting based on the established principles of RILT.

APPENDICES

APPENDIX A

Dose-Function Analysis Batch Code Input File

UN	EclipseID	Course	Plan Type	Plan Name	SBRT	CT Study	CT Series
1	$2006040_VA001	Eclipse	PlanSum	AAA PLN 34	No	none	Series
2	$2006040_UM001	Eclipse	ExternalBeam	AAA PLN 3	No	none	Series
3	$2006040_UM002	Eclipse	ExternalBeam	AAA PLN 1	Yes	none	Series
4	$2006040_VA002	Eclipse	ExternalBeam	AAA PLN 1	No	none	Series
5	$2006040_VA004	Eclipse	PlanSum	Plan Sum	No	none	Series 1607
6	$2006040_UM004	Eclipse	PlanSum	AAA PLN 2223	No	none	Series
7	$2006040_VA005	Eclipse	PlanSum	AAA PLN 34	No	none	Series
8	$2006040_UM005	Eclipse	ExternalBeam	AAA PLN 1	No	none	Series
9	$2006040_VA006	Eclipse	PlanSum	AAA PLN 34	No	none2	Series 4743
10	$2006040_UM006	Eclipse	PlanSum	AAA PLN 45	No	none1	Series
11	$2006040_VA007	Eclipse	ExternalBeam	AAA PLN 2	No	none	Series
12	$2006040_UM007	Eclipse	PlanSum	Plan Sum	Yes	none	Series
13	$2006040_VA008	Eclipse	ExternalBeam	AAA PLN 2	No	none	Series
14	$2006040_UM008	Eclipse	ExternalBeam	AAA PLN 3	Yes	none	Series
15	$2006040_VA009	Eclipse	PlanSum	AAA PLN 34	No	none	Series
16	$2006040_UM009	Eclipse	ExternalBeam	AAA PLN 1	Yes	none	Series
17	$2006040_UM010	Eclipse	PlanSum	AAA PLN 12	No	none	Series
18	$2006040_VA011	Eclipse	ExternalBeam	AAA PLN 2	No	none	Series
19	$2006040_UM011	Eclipse	ExternalBeam	AAA PLN 1	No	none	Series
20	$2006040_UM012	Eclipse	ExternalBeam	AAA PLN 6	No	none	Series
21	$2006040_VA013	Eclipse	PlanSum	AAA PLN 34	No	none	Series
22	$2006040_UM013	Eclipse	ExternalBeam	AAA PLN 1	Yes	none	Series
23	$2006040_VA014	Eclipse	PlanSum	AAA PLN 34	No	none	Series
24	$2006040_VA015	Eclipse	ExternalBeam	AAA PLN 2	No	none	Series
25	$2006040_UM015	Eclipse	ExternalBeam	AAA PLN 1	No	none	Series
26	$2006040_VA016	Eclipse	ExternalBeam	AAA PLN 2	No	none	Series
27	$2006040_VA017	Eclipse	PlanSum	AAA PLN 23	No	none	Series
28	$2006040_VA018	Eclipse	ExternalBeam	AAA PLN 2	No	none	Series
29	$2006040_VA019	Eclipse	ExternalBeam	AAA PLN 2	No	none	Series
30	$2006040_UM019	Eclipse	ExternalBeam	AAA PLN 1	No	none	Series
31	$2006040_VA020	Eclipse	ExternalBeam	AAA PLN 2	No	none	Series
32	$2006040_UM020	Eclipse	PlanSum	AAA PLN 12	No	none1	Series
33	$2006040_VA021	Eclipse	PlanSum	AAA PLN 45	No	none	Series
34	$2006040_UM021	Eclipse	ExternalBeam	AAA PLN 1	No	none	Series
35	$2006040_VA022	Eclipse	ExternalBeam	AAA PLN 2	No	none	Series
36	$2006040_UM023	Eclipse	PlanSum	AAA PLN 12	Yes	none3	Series
37	$2006040_VA024	Eclipse	PlanSum	AAA PLN 34	No	none	Series
38	$2006040_UM024	Eclipse	ExternalBeam	AAA PLN 1	Yes	none4	Series
39	$2006040_VA025	Eclipse	PlanSum	AAA PLN 456	No	none	Series
40	$2006040_UM025	Eclipse	PlanSum	AAA PLN 23	No	none	Series
41	$2006040_VA026	Eclipse	PlanSum	AAA PLN 34	No	none	Series
42	$2006040_UM026	Eclipse	PlanSum	AAA PLN 25	No	none	Series
43	$2006040_VA027	Eclipse	PlanSum	AAA PLN 456	No	none	Series
44	$2006040_UM027	Eclipse	ExternalBeam	AAA PLN 1	No	none	Series
45	$2006040_VA028	Eclipse	PlanSum	AAA PLN 2122	No	none	Series
46	$2006040_UM028	Eclipse	ExternalBeam	AAA PLN 1	Yes	none	Series

Figure A.1: Dose Function Analysis Batch Code Input File

UN	EclipseID	Course	Plan Type	Plan Name	SBRT	CT Study	CT Series
47	$2006040_VA029	Eclipse	PlanSum	AAA PLN 34	No	none	Series
48	$2006040_VA030	Eclipse	PlanSum	AAA PLN 45	No	none	Series
49	$2006040_UM030	Eclipse	ExternalBeam	AAA PLN 1	Yes	none	Series
50	$2006040_VA031	Eclipse	ExternalBeam	AAA PLN 2	No	none	Series
51	$2006040_UM031	Eclipse	ExternalBeam	AAA PLN 1	Yes	none	Series
52	$2006040_VA032	Eclipse	ExternalBeam	AAA PLN 2	No	none	Series
53	$2006040_UM032	Eclipse	PlanSum	AAA PLN 12	No	none	Series
54	$2006040_VA033	Eclipse	ExternalBeam	AAA PLN 2	No	none	Series
55	$2006040_UM033	Eclipse	ExternalBeam	AAA PLN 1	Yes	none	Series
56	$2006040_VA034	Eclipse	PlanSum	AAA PLN 34	No	none	Series
57	$2006040_VA035	Eclipse	PlanSum	Plan Sum	No	none	Series
58	$2006040_UM035	Eclipse	ExternalBeam	AAA PLN 1	Yes	none	Series
59	$2006040_VA036	Eclipse	PlanSum	AAA PLN 34	No	none	Series
60	$2006040_UM036	Eclipse	ExternalBeam	AAA PLN 1	Yes	none	Series
61	$2006040_UM037	Eclipse	ExternalBeam	AAA PLN 3	No	none	Series
62	$2006040_VA038	Eclipse	ExternalBeam	AAA PLN 2	No	none	Series
63	$2006040_UM039	Eclipse	PlanSum	AAA PLN 25	No	none	Series
64	$2006040_VA040	Eclipse	PlanSum	AAA PLN 45	No	none	Series
65	$2006040_UM040	Eclipse	ExternalBeam	AAA PLN 1	No	none	Series
66	$2006040_VA041	Eclipse	ExternalBeam	AAA PLN 6	No	none	Series
67	$2006040_UM042	Eclipse	ExternalBeam	AAA PLN 1	No	none	Series
68	$2006040_UM043	Eclipse	ExternalBeam	AAA PLN 2	No	none	Series
69	$2006040_VA044	Eclipse	ExternalBeam	AAA PLN 8	No	none	Series 2654
70	$2006040_UM044	Eclipse	PlanSum	Plan Sum	No	none	Series
71	$2006040_VA045	Eclipse	ExternalBeam	AAA PLN 19	Yes	none	Series 2659
72	$2006040_UM045	Eclipse	PlanSum	Plan Sum	No	none	Series
73	$2006040_UM046	Eclipse	ExternalBeam	AAA PLN 1	No	none	Series
74	$2006040_VA047	Eclipse	ExternalBeam	AAA PLN 6	Yes	none	Series 3111
75	$2006040_UM047	Eclipse	ExternalBeam	AAA PLN 2	Yes	none	Series
76	$2006040_VA048	Eclipse	ExternalBeam	AAA PLN 13	Yes	none	Series 2360
77	$2006040_UM048	Eclipse	ExternalBeam	AAA PLN 1	No	none	Series
78	$2006040_VA049	Eclipse	ExternalBeam	AAA PLN 2	Yes	none	Series
79	$2006040_UM049	Eclipse	ExternalBeam	AAA PLN 3	No	none	Series
80	$2006040_VA050	Eclipse	ExternalBeam	AAA PLN 4	Yes	none	Series
81	$2006040_VA051	Eclipse	PlanSum	AAA PLN 78	Yes	none	Series
82	$2006040_VA054	Eclipse	ExternalBeam	AAA PLN 3	No	none	Series
83	$2006040_VA055	Eclipse	ExternalBeam	AAA PLN 2	Yes	none	Series
84	$2015035_UM001	Eclipse	PlanSum	Plan Sum	No	none	Series29
85	$2015035_UM002	Eclipse	PlanSum	Plan Sum	No	none	Series2
86	$2015035_UM003	Eclipse	PlanSum	Plan Sum	No	none	Series11
87	$2015035_UM004	Eclipse	PlanSum	Plan Sum	No	none	Series33
88	$2015035_UM005	Eclipse	PlanSum	Plan Sum	No	none	Series28
89	$2015035_UM006	Eclipse	PlanSum	Plan Sum	No	none1	Series21
90	$2015035_UM007	Eclipse	PlanSum	Plan Sum	No	none	Series
91	$2015035_UM008	Eclipse	PlanSum	Plan Sum	No	none6	Series
92	$2015035_UM009	Eclipse	PlanSum	Plan Sum	No	none	Series6

UN	EclipseID	Course	Plan Type	Plan Name	SBRT	CT Study	CT Series
93	$2015035_UM010	Eclipse	PlanSum	Plan Sum	No	none2	Series9
94	$2015035_UM011	Eclipse	ExternalBeam	Dose Plan	No	none	Series20
95	$2015035_UM012	Eclipse	PlanSum	Plan Sum	No	none2	Series11
96	$2015035_UM013	Eclipse	PlanSum	Plan Sum	No	none3	Series
97	$2015035_UM014	Eclipse	PlanSum	Plan Sum	No	none7	Series
98	$2015035_UM015	Eclipse	PlanSum	Plan Sum	No	none1	Series
99	$2015035_UM016	Eclipse	PlanSum	Plan Sum	No	none1	Series11
100	$2015035_UM017	Eclipse	PlanSum	Plan Sum	No	none	Series3
101	$2015035_UM018	Eclipse	PlanSum	Plan Sum	No	none	Series10
102	$2015035_UM019	Eclipse	PlanSum	Plan Sum	No	none1	Series
103	$2015035_UM022	Eclipse	PlanSum	Plan Sum	No	none	Series7
104	$2015035_UM023	Eclipse	PlanSum	Plan Sum	No	none	Series7
105	$2015035_UM024	Eclipse	PlanSum	Plan Sum	No	none2	Series8
106	$2015035_UM025	Eclipse	PlanSum	Plan Sum	No	none	Series21
107	$2015035_UM026	Eclipse	PlanSum	Plan Sum	No	none5	Series
108	$2015035_UM027	Eclipse	PlanSum	Plan Sum	No	none3	Series
109	$2015035_UM028	Eclipse	PlanSum	Plan Sum	No	none	Series7
110	$2015035_UM029	Eclipse	PlanSum	Plan Sum	No	none6	Series
111	$2015035_UM030	Eclipse	PlanSum	Plan Sum	No	none7	Series9
112	$2015035_UM031	Eclipse	PlanSum	Plan Sum	No	none	Series2
113	$2015035_UM032	Eclipse	PlanSum	Plan Sum	No	none1	Series3

UN	EclipseID	CT Image	PreTx Q SPECT Study	PreTx V SPECT Study
1	$2006040_VA001	IMAGE:CT	N/A	N/A
2	$2006040_UM001	CTSIM	Initial PERF	Initial VENT
3	$2006040_UM002	CTSIM	Initial PERF	Initial VENT
4	$2006040_VA002	IMAGE:CT	N/A	N/A
5	$2006040_VA004	IMAGE:CT	Initial PERF	Initial VENT
6	$2006040_UM004	CTSIM	Initial PERF	Initial VENT
7	$2006040_VA005	IMAGE:CT	Initial PERF	Initial VENT
8	$2006040_UM005	CTSIM	Initial PERF	Initial VENT
9	$2006040_VA006	IMAGE:CT	Initial PERF	Initial VENT
10	$2006040_UM006	CTSIM	Initial PERF	Initial VENT
11	$2006040_VA007	IMAGE:CT	Initial PERF	Initial VENT
12	$2006040_UM007	IMAGE:CTEX	Initial PERF	Initial VENT
13	$2006040_VA008	IMAGE:CTEX	Initial PERF	Initial VENT
14	$2006040_UM008	CTSIM	Initial PERF	Initial VENT
15	$2006040_VA009	IMAGE:CT	Initial PERF	Initial VENT
16	$2006040_UM009	CTSIM	Initial PERF	Initial VENT
17	$2006040_UM010	CTSIM	Initial PERF	Initial VENT
18	$2006040_VA011	IMAGE:CT	Initial PERF	Initial VENT
19	$2006040_UM011	CTSIM	Initial PERF	Initial VENT
20	$2006040_UM012	CTSIM	Initial PERF	Initial VENT
21	$2006040_VA013	IMAGE:CT	Initial PERF	Initial VENT
22	$2006040_UM013	CTSIM	Initial PERF	Initial VENT
23	$2006040_VA014	IMAGE:CTEX1	Initial PERF	Initial VENT
24	$2006040_VA015	IMAGE:CTEX	Initial PERF	Initial VENT
25	$2006040_UM015	CTSIM	Initial PERF	Initial VENT
26	$2006040_VA016	IMAGE:CTEX	Initial PERF	Initial VENT
27	$2006040_VA017	IMAGE:CT	Initial PERF	Initial VENT
28	$2006040_VA018	IMAGE:CT	Initial PERF	Initial VENT
29	$2006040_VA019	IMAGE:CT	Initial PERF	Initial VENT
30	$2006040_UM019	CTSIM	Initial PERF	Initial VENT
31	$2006040_VA020	IMAGE:CT	Initial PERF	Initial VENT
32	$2006040_UM020	CTSIM	Initial PERF	Initial VENT
33	$2006040_VA021	IMAGE:CT	Initial PERF	Initial VENT
34	$2006040_UM021	CTSIM	Initial PERF	Initial VENT
35	$2006040_VA022	IMAGE:CTEX	Initial PERF	Initial VENT
36	$2006040_UM023	CTSIM	Initial PERF	Initial VENT
37	$2006040_VA024	IMAGE:CT	Initial PERF	Initial VENT
38	$2006040_UM024	CTSIM	Initial PERF	Initial VENT
39	$2006040_VA025	IMAGE:CT	Initial PERF	Initial VENT
40	$2006040_UM025	CTSIM	Initial PERF	Initial VENT
41	$2006040_VA026	IMAGE:CTEX	Initial PERF	Initial VENT
42	$2006040_UM026	CTSIM	Initial PERF	Initial VENT
43	$2006040_VA027	IMAGE:CT	Initial PERF	Initial VENT
44	$2006040_UM027	CTSIM	Initial PERF	Initial VENT
45	$2006040_VA028	IMAGE:CT2	Initial PERF	Initial VENT
46	$2006040_UM028	CTSIM	Initial PERF	Initial VENT

UN	EclipseID	CT Image	PreTx Q SPECT Study	PreTx V SPECT Study
47	$2006040_VA029	IMAGE:CT	Initial PERF	Initial VENT
48	$2006040_VA030	IMAGE:CT	Initial PERF	Initial VENT
49	$2006040_UM030	CTSIM	Initial PERF	Initial VENT
50	$2006040_VA031	IMAGE:CT	Initial PERF	Initial VENT
51	$2006040_UM031	CTSIM	Initial PERF	Initial VENT
52	$2006040_VA032	IMAGE:CT	Initial PERF	Initial VENT
53	$2006040_UM032	CTSIM	Initial PERF	Initial VENT
54	$2006040_VA033	IMAGE:CT	Initial PERF	Initial VENT
55	$2006040_UM033	CTSIM	Initial PERF	Initial VENT
56	$2006040_VA034	IMAGE:CT	Initial PERF	Initial VENT
57	$2006040_VA035	IMAGE:CTEX	Initial PERF	Initial VENT
58	$2006040_UM035	CTSIM	Initial PERF	Initial VENT
59	$2006040_VA036	IMAGE:CT1	Initial PERF	Initial VENT
60	$2006040_UM036	IMAGE:CT	Initial PERF	Initial VENT
61	$2006040_UM037	CTSIM	Initial PERF	Initial VENT
62	$2006040_VA038	IMAGE:CT	Initial PERF	Initial VENT
63	$2006040_UM039	CTSIM	Initial PERF	Initial VENT
64	$2006040_VA040	IMAGE:CT	Initial PERF	Initial VENT
65	$2006040_UM040	IMAGE:CTUN	Initial PERF	Initial VENT
66	$2006040_VA041	IMAGE:CT2	Initial PERF	Initial VENT
67	$2006040_UM042	CTSIM	Initial PERF	Initial VENT
68	$2006040_UM043	CTSIM	Initial PERF	Initial VENT
69	$2006040_VA044	IMAGE:CT	Initial PERF	Initial VENT
70	$2006040_UM044	CTSIM	Initial PERF	Initial VENT
71	$2006040_VA045	IMAGE:CT	Initial PERF	Initial VENT
72	$2006040_UM045	CTSIM	Initial PERF	Initial VENT
73	$2006040_UM046	CTSIM	Initial PERF	Initial VENT
74	$2006040_VA047	IMAGE:CT	Initial PERF	Initial VENT
75	$2006040_UM047	IMAGE:CT	Initial PERF	Initial VENT
76	$2006040_VA048	IMAGE:CT	Initial PERF	Initial VENT
77	$2006040_UM048	CTSIM	Initial PERF	Initial VENT
78	$2006040_VA049	IMAGE:CT	Initial PERF	Initial VENT
79	$2006040_UM049	CTSIM	Initial PERF	Initial VENT
80	$2006040_VA050	IMAGE:CT1	Initial PERF	Initial VENT
81	$2006040_VA051	IMAGE:CT	Initial PERF	Initial VENT
82	$2006040_VA054	IMAGE:CTUT	Initial PERF	Initial VENT
83	$2006040_VA055	IMAGE:CTUT1	Initial PERF	Initial VENT
84	$2015035_UM001	20160106_UTP	none5	none2
85	$2015035_UM002	20160217_UTP	none4	none3
86	$2015035_UM003	20160217 UT P	none4	none2
87	$2015035_UM004	20160329 UT P	none4	none3
88	$2015035_UM005	20160426UT P AMP	none2	none1
89	$2015035_UM006	20161018 UT P	none5	none
90	$2015035_UM007	20161026 UT P2	none6	none4
91	$2015035_UM008	20161123LUNG2	none3	none5
92	$2015035_UM009	20170425CT_UT P	none6	none3

UN	EclipseID	CT Image	PreTx Q SPECT Study	PreTx V SPECT Study
93	$2015035_UM010	20170714_UTP	none3	none4
94	$2015035_UM011	20170711 UT P	none3	none2
95	$2015035_UM012	20170815CT_RP_Av	none5	none1
96	$2015035_UM013	20171110RTLUNG	none	none2
97	$2015035_UM014	20171115RLNGSDX	none4	none5
98	$2015035_UM015	20171204LUNGSDX2	none3	none2
99	$2015035_UM016	20180312_UTP2	none3	none
100	$2015035_UM017	20180423_UTP	none3	none4
101	$2015035_UM018	20180430 UTP2	none3	none1
102	$2015035_UM019	20180514RLUNGSDX	none3	none4
103	$2015035_UM022	20180608_UTP2	none1	none5
104	$2015035_UM023	20180626_UTP2	none4	none2
105	$2015035_UM024	20180731 UT P2	none3	none1
106	$2015035_UM025	20180814RLUNGSDX	none6	none1
107	$2015035_UM026	20180920RLUNGSDX	none	none2
108	$2015035_UM027	20180928LLUNGSDX	none2	none1
109	$2015035_UM028	20181113 UT P	none1	none4
110	$2015035_UM029	20181113 UT P	none3	none4
111	$2015035_UM030	20190117 UT P	none3	none4
112	$2015035_UM031	20190122 UTP2	none2	none6
113	$2015035_UM032	20190312_UTP2	none5	none3

UN	EclipseID	MidTx Q SPECT Study	MidTx V SPECT Study
1	$2006040_VA001	1Month PERF	1Month VENT
2	$2006040_UM001	1Month PERF	1Month VENT
3	$2006040_UM002	1Month PERF	N/A
4	$2006040_VA002	1Month PERF	1Month VENT
5	$2006040_VA004	1Month PERF	1Month VENT
6	$2006040_UM004	1Month PERF	1Month VENT
7	$2006040_VA005	1Month PERF	1Month VENT
8	$2006040_UM005	1Month PERF	1Month VENT
9	$2006040_VA006	1Month PERF	1Month VENT
10	$2006040_UM006	1Month PERF	1Month VENT
11	$2006040_VA007	1Month PERF	1Month VENT
12	$2006040_UM007	1Month PERF	1Month VENT
13	$2006040_VA008	1Month PERF	1Month VENT
14	$2006040_UM008	1Month PERF	1Month VENT
15	$2006040_VA009	1Month PERF	1Month VENT
16	$2006040_UM009	1Month PERF	1Month VENT
17	$2006040_UM010	1Month PERF	1Month VENT
18	$2006040_VA011	N/A	N/A
19	$2006040_UM011	1Month PERF	1Month VENT
20	$2006040_UM012	1Month PERF	1Month VENT
21	$2006040_VA013	1Month PERF	1Month VENT
22	$2006040_UM013	1Month PERF	1Month VENT
23	$2006040_VA014	1Month PERF	1Month VENT
24	$2006040_VA015	1Month PERF	1Month VENT
25	$2006040_UM015	1Month PERF	1Month VENT
26	$2006040_VA016	1Month PERF	1Month VENT
27	$2006040_VA017	1Month PERF	1Month VENT
28	$2006040_VA018	1Month PERF	1Month VENT
29	$2006040_VA019	1Month PERF	1Month VENT
30	$2006040_UM019	1Month PERF	1Month VENT
31	$2006040_VA020	1Month PERF	1Month VENT
32	$2006040_UM020	1Month PERF	1Month VENT
33	$2006040_VA021	1Month PERF	1Month VENT
34	$2006040_UM021	1Month PERF	1Month VENT
35	$2006040_VA022	1Month PERF	1Month VENT
36	$2006040_UM023	1Month PERF	1Month VENT
37	$2006040_VA024	1Month PERF	1Month VENT
38	$2006040_UM024	1Month PERF	1Month VENT
39	$2006040_VA025	1Month PERF	1Month VENT
40	$2006040_UM025	1Month PERF	1Month VENT
41	$2006040_VA026	1Month PERF	1Month VENT
42	$2006040_UM026	1Month PERF	1Month VENT
43	$2006040_VA027	1Month PERF	1Month VENT
44	$2006040_UM027	1Month PERF	1Month VENT
45	$2006040_VA028	1Month PERF	1Month VENT
46	$2006040_UM028	1Month PERF	1Month VENT

UN	EclipseID	MidTx Q SPECT Study	MidTx V SPECT Study
47	$2006040_VA029	1Month PERF	1Month VENT
48	$2006040_VA030	N/A	N/A
49	$2006040_UM030	1Month PERF	1Month VENT
50	$2006040_VA031	1Month PERF	1Month VENT
51	$2006040_UM031	1Month PERF	1Month VENT
52	$2006040_VA032	1Month PERF	1Month VENT
53	$2006040_UM032	1Month PERF	1Month VENT
54	$2006040_VA033	N/A	N/A
55	$2006040_UM033	1Month PERF	1Month VENT
56	$2006040_VA034	1Month PERF	1Month VENT
57	$2006040_VA035	1Month PERF	1Month VENT
58	$2006040_UM035	1Month PERF	1Month VENT
59	$2006040_VA036	N/A	N/A
60	$2006040_UM036	N/A	N/A
61	$2006040_UM037	1Month PERF	1Month VENT
62	$2006040_VA038	1Month PERF	1Month VENT
63	$2006040_UM039	N/A	N/A
64	$2006040_VA040	1Month PERF	1Month VENT
65	$2006040_UM040	N/A	N/A
66	$2006040_VA041	1Month PERF	1Month VENT
67	$2006040_UM042	1Month PERF	1Month VENT
68	$2006040_UM043	1Month PERF	1Month VENT
69	$2006040_VA044	1Month PERF	1Month VENT
70	$2006040_UM044	1Month PERF	1Month VENT
71	$2006040_VA045	1Month PERF	1Month VENT
72	$2006040_UM045	1Month PERF	1Month VENT
73	$2006040_UM046	1Month PERF	1Month VENT
74	$2006040_VA047	1Month PERF	1Month VENT
75	$2006040_UM047	1Month PERF	1Month VENT
76	$2006040_VA048	1Month PERF	1Month VENT
77	$2006040_UM048	1Month PERF	1Month VENT
78	$2006040_VA049	1Month PERF	1Month VENT
79	$2006040_UM049	1Month PERF	1Month VENT
80	$2006040_VA050	1Month PERF	1Month VENT
81	$2006040_VA051	1Month PERF	1Month VENT
82	$2006040_VA054	1Month PERF	1Month VENT
83	$2006040_VA055	1Month PERF	1Month VENT
84	$2015035_UM001	none3	none6
85	$2015035_UM002	none5	none2
86	$2015035_UM003	none1	none3
87	$2015035_UM004	none6	none5
88	$2015035_UM005	none4	none3
89	$2015035_UM006	none4	none6
90	$2015035_UM007	none3	none7
91	$2015035_UM008	none4	none2
92	$2015035_UM009	none5	none2

UN	EclipseID	MidTx Q SPECT Study	MidTx V SPECT Study
93	$2015035_UM010	none5	none7
94	$2015035_UM011	N/A	N/A
95	$2015035_UM012	none4	none6
96	$2015035_UM013	none4	none5
97	$2015035_UM014	none3	none6
98	$2015035_UM015	none4	none5
99	$2015035_UM016	none4	N/A
100	$2015035_UM017	none5	none6
101	$2015035_UM018	none4	none6
102	$2015035_UM019	none5	none2
103	$2015035_UM022	none3	none4
104	$2015035_UM023	none3	none5
105	$2015035_UM024	none5	none4
106	$2015035_UM025	none4	none5
107	$2015035_UM026	none3	none4
108	$2015035_UM027	none4	none5
109	$2015035_UM028	none5	none3
110	$2015035_UM029	none5	none2
111	$2015035_UM030	none2	none8
112	$2015035_UM031	none3	none4
113	$2015035_UM032	none4	none2

APPENDIX B

Dose-Function Modeling Supplementary Data

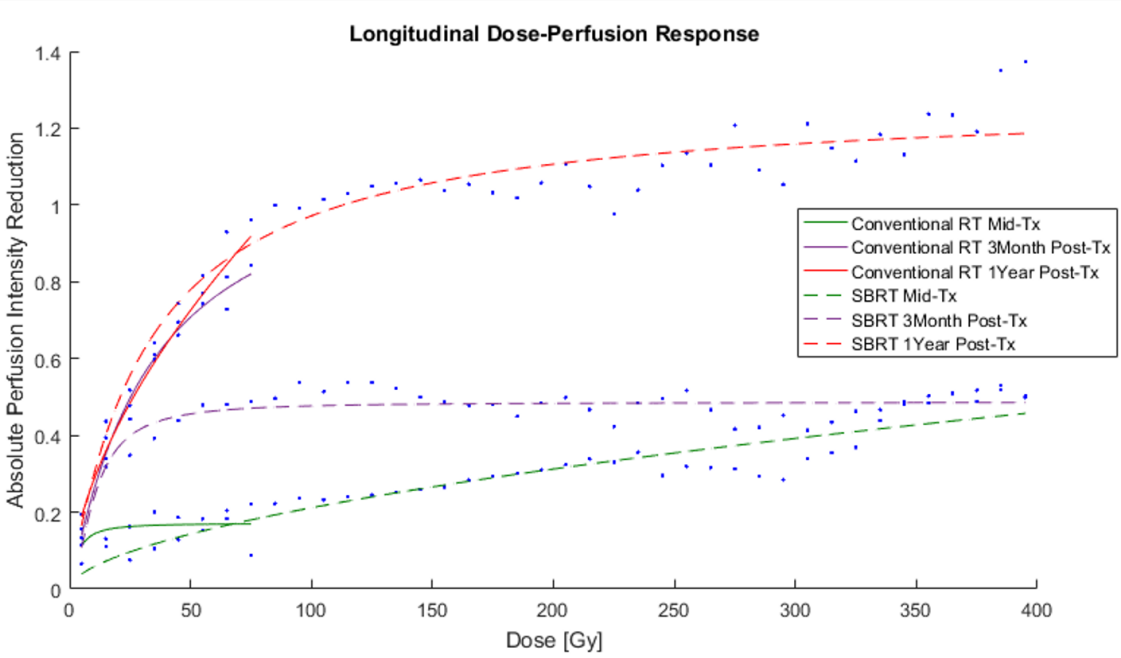

Figure B.1: Overlaid population-averaged data points and logistic models describing the perfusion dose-function response for conventional RT and SBRT patients.

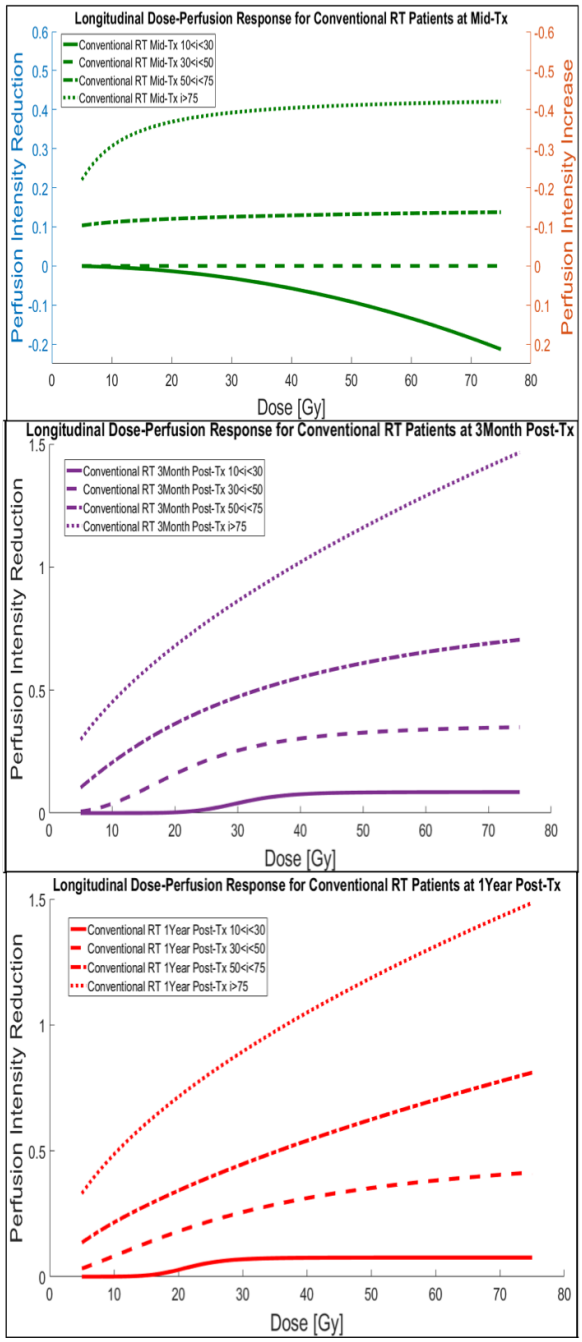

Figure B.2: Perfusion dose-function response models stratified by baseline intensity with included reperfusion allowed at mid-treatment.

APPENDIX C

Toxicity Analysis Supplementary Data

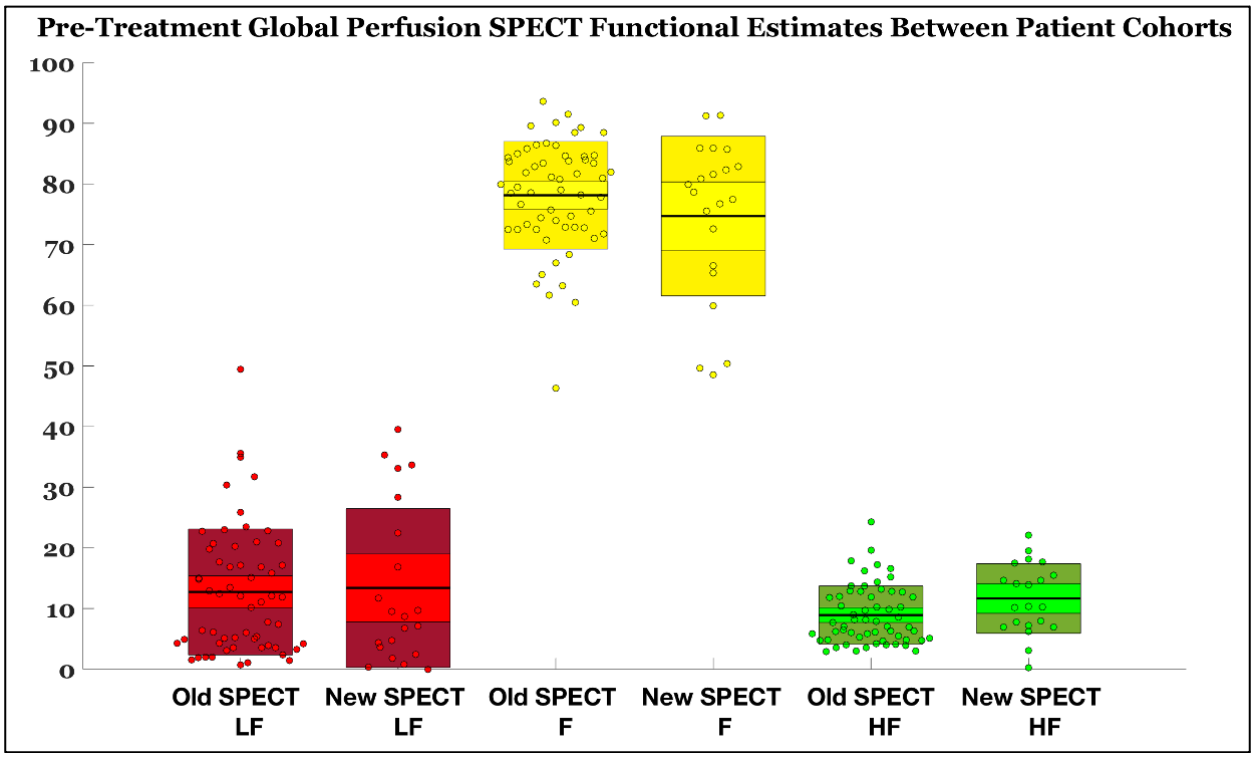

Figure C.1: Comparison between the functional categorizations within each patient in the 2006.040 "Old SPECT" cohort and the 2015.035 "New SPECT" cohort.

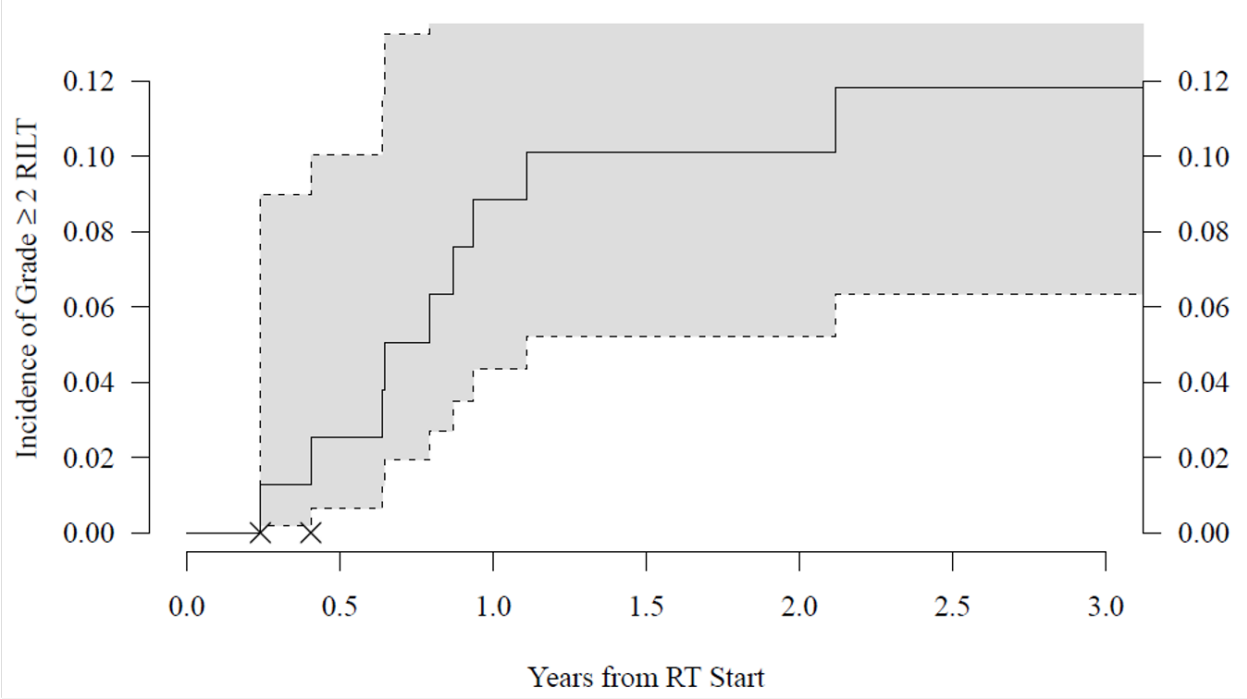

Figure C.2: Cox proportional hazard model for the time to toxicity in the 2006.040 cohort with 9 toxicity cases out of 76 total conventionally fractionated RT patients.

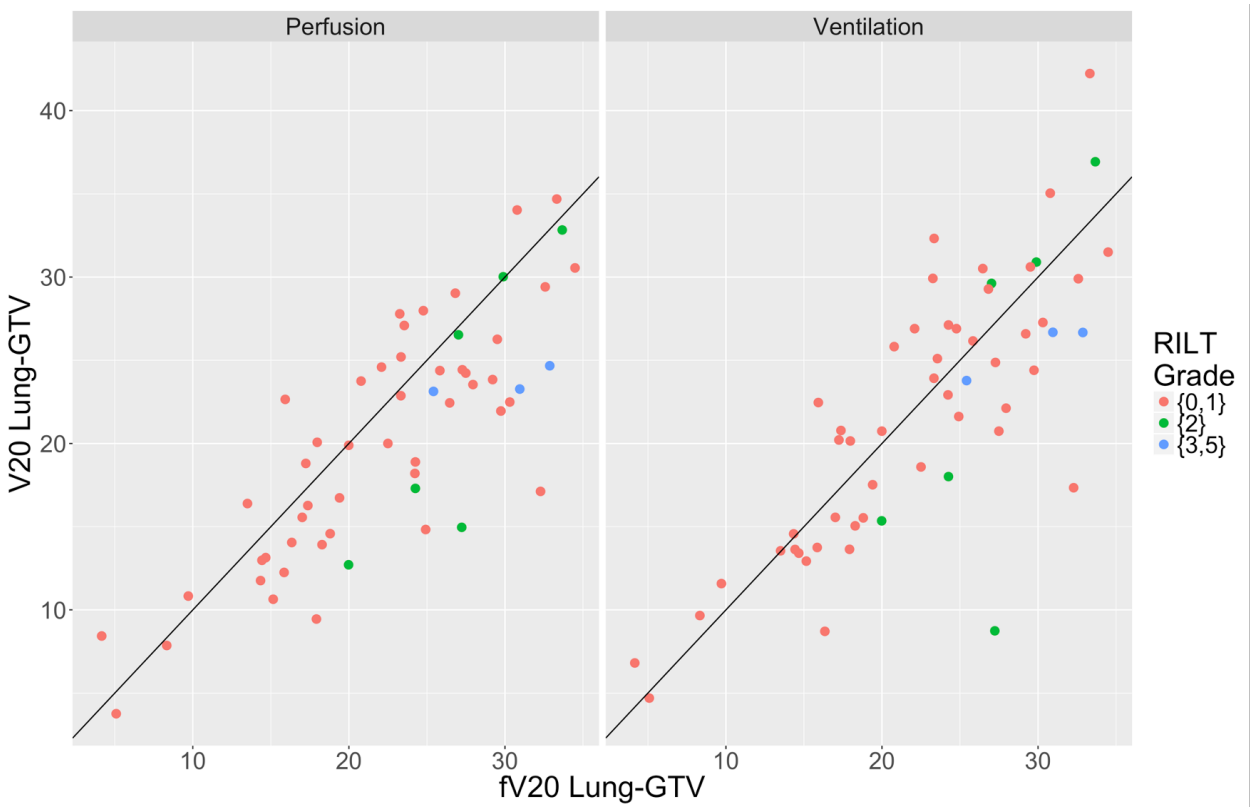

Figure C.3: Scatter plot of the V20 versus fV20 values in the 2006.040 cohort.

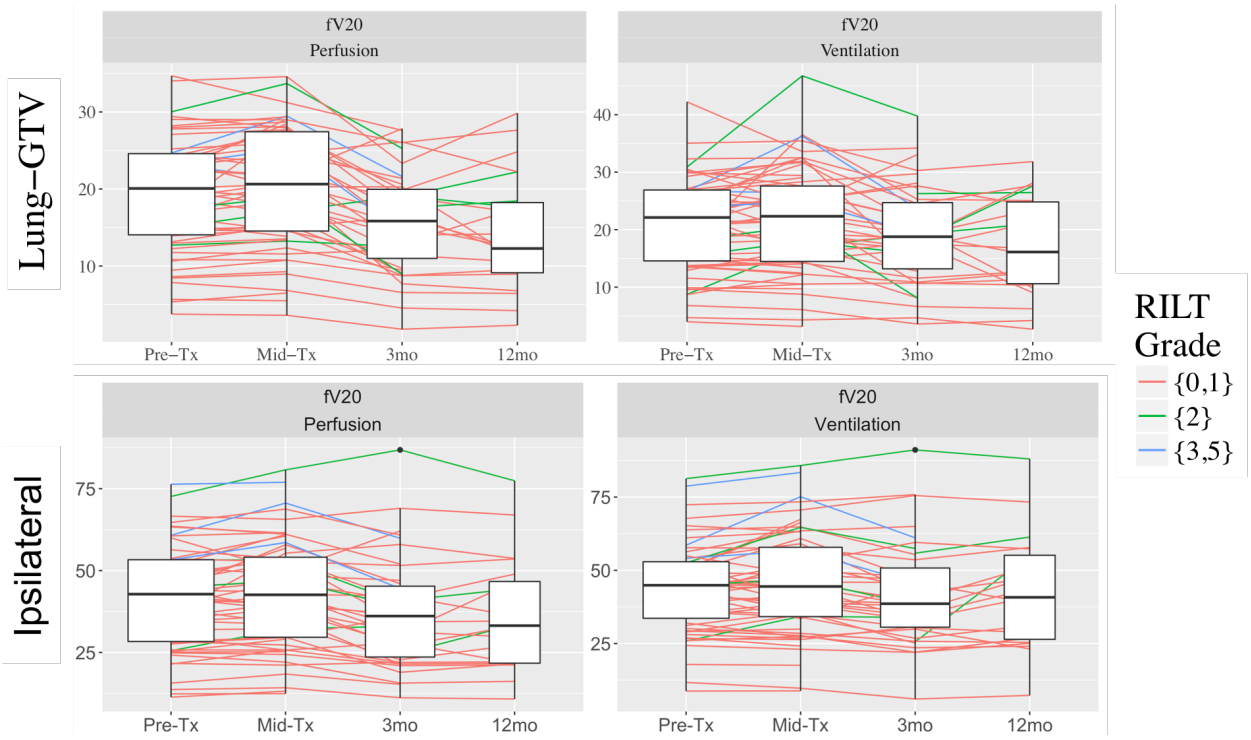

Figure C.4: Box plots demonstrating the longitudinal change in the fV20 metric within the global lungs (top) and ipsilateral lung (bottom) for patients in the 2006.040 cohort.

The gray level size zone matrix (GLSZM) features provide information on the size of homogeneous zones for each grey-level in 3-dimensions. and short-zone low gray-level emphasis (SZLGE) is the distribution of the short homogeneous zones with low gray-levels as given by:

$$SZLGE = \frac{1}{H}\sum_{i}\sum_{j}\frac{GLSZM(i,j)}{i^2 j^2} \tag{C.1}$$

where GLSZM(i,j) corresponds to the number of homogeneous zones of$j$ voxels with the intensity i and H is the total number of homogeneous zones.

The SZLGE feature increases when the texture is dominated by many short runs of low gray-level value. On the contrary, a low value of the SZLGE feature would suggest a lack of homogeneous short-zone low gray-level values.

Feature (p-value)	Small Zone Emphasis	Large Zone Emphasis	Gray-Level Non-uniformity	Zone Size Non-uniformity	Zone Percentage	Low Gray-Level Zone Emphasis	High Gray-Level Zone Emphasis	Small Zone Low Gray-Level Emphasis	Small Zone High Gray-Level Emphasis	Large Zone Low Gray-Level Emphasis	Large Zone High Gray-Level Emphasis	Gray-Level Variance	Zone Size Variance
LUNGS-GTV	0.546	0.705	0.480	0.395	0.519	0.092	0.645	0.038	0.894	0.351	0.675	0.878	0.191
LUNGS-GTV (Resampled at 3mm)	0.290	0.442	0.455	0.546	0.281	0.146	0.073	0.100	0.254	0.480	0.574	0.660	0.096
IPSILATERAL_LUNG-GTV	0.160	0.602	0.130	0.160	0.632	0.250	0.771	0.100	0.708	0.392	0.250	0.518	0.369
IPSILATERAL_LUNG-GTV (Resampled at 3mm)	0.392	0.392	0.835	0.917	0.337	0.066	0.209	0.030	0.201	0.771	0.147	0.884	0.505

Table C.1: Spearman correlation coefficients between GSZLM radiomics features and RILT was calculated using the treatment planning CT in 59 conventional RT patients from the 2006.040 cohort.

BIBLIOGRAPHY

BIBLIOGRAPHY

[1] Marks L.B., Munley M.T., Spencer D.P., et al. Quantification of radiation-induced regional lung injury with perfusion imaging. *Int J Radiat Oncol.* 1997;38(2):399-409.

[2] Society American Cancer. Lung Cancer - Non-Small Cell - Statistics. Accessed March 1, 2021. `www.cancer.net/cancer-types/lung-cancer-non-small-cell/statistics`.

[3] Sause W., Kolesar P., Taylor I.V., et al. Final results of phase III trial in regionally advanced unresectable non-small cell lung cancer: Radiation Therapy Oncology Group, Eastern Cooperative Oncology Group, and Southwest Oncology Group. *Chest.* 2000;117(2):358-364.

[4] Marks L.B., Spencer D.P., Bentel G.C., et al. The utility of SPECT lung perfusion scans in minimizing and assessing the physiologic consequences of thoracic irradiation. *Int J Radiat Oncol.* 1993;26(4):659-668.

[5] Boersma L.J., Damena E.M.F., de Boer R.W., et al. A new method to determine dose-effect relations for local lung-function changes using correlated SPECT and CT data. *Radiother Oncol.* 1993;29(2):110-116.

[6] Marks L.B., Spencer D.P., Sherouse G.W., et al. The role of three dimensional functional lung imaging in radiation treatment planning: The functional dose-volume histogram. *Int J Radiat Oncol.* 1995;33(1):65-75.

[7] Boersma L.J., Damen E.M., de Boer R.W., et al. Estimation of overall pulmonary function after irradiation using dose-effect relations for local functional injury. *Radiother Oncol.* 1995;36(1):15-23.

[8] Seppenwoolde Y., Engelsman M., De Jaeger K., et al. Optimizing radiation treatment plans for lung cancer using lung perfusion information. *Radiother Oncol.* 2002;63(2):165-177.

[9] McGuire S.M., Zhou S., Marks L.B., Dewhirst M., Yin F.F., Das S.K.. A methodology for using SPECT to reduce intensity-modulated radiation therapy (IMRT) dose to functioning lung. *Int J Radiat Oncol.* 2006;66(5):1543-1552.

[10] Shioyama Y., Jang S.Y., Liu H.H., et al. Preserving functional lung using perfusion imaging and intensity-modulated radiation therapy for advanced-stage non-small cell lung cancer. *Int J Radiat Oncol.* 2007;68(5):1349-1358.

[11] Wang D., Li B., Wang Z., et al. Functional dose-volume histograms for predicting radiation pneumonitis in locally advanced non-small cell lung cancer treated with late-course accelerated hyperfractionated radiotherapy. *Exp Ther Med.* 2011;2(5):1017-1022.

[12] Marks L.B., Sherouse G.W., Munley M.T., Bentel G.C., Spencer D.P.. Incorporation of functional status into dose-volume analysis. *Med Phys.* 1999;26(2):196-199.

[13] Yaremko B.P., Guerrero T.M., Noyola-Martinez J., et al. Reduction of normal lung irradiation in locally advanced non-small-cell lung cancer patients, using ventilation images for functional avoidance. *Int J Radiat Oncol.* 2007;68(2):562-571.

[14] St-Hilaire J., Lavoie C., Dagnault A., et al. Functional avoidance of lung in plan optimization with an aperture-based inverse planning system. *Radiother Oncol.* 2011;100(3):390-395.

[15] Yamamoto T., Kabus S., von Berg J., Lorenz C., Keall P.J.. Impact of four-dimensional computed tomography pulmonary ventilation imaging-based functional avoidance for lung cancer radiotherapy. *Int J Radiat Oncol.* 2011;79(1):279-288.

[16] Janssen-Heijnen M.L., Schipper R.M., Razenberg P.P., Crommelin M.A., Coebergh J.W.. Prevalence of co-morbidity in lung cancer patients and its relationship with treatment: a population-based study. *Lung Cancer.* 1998;21(2):105-113.

[17] Meng X., Frey K., Matuszak M., et al. Changes in functional lung regions during the course of radiation therapy and their potential impact on lung dosimetry for non-small cell lung cancer. *Int J Radiat Oncol.* 2014;89(1):145-151.

[18] Durham A.L., Adcock I.M.. The relationship between COPD and lung cancer. *Lung Cancer.* 2015;90(2):121-127.

[19] Vinogradskiy Y., Schubert L., Diot Q., et al. Regional Lung Function Profiles of Stage I and III Lung Cancer Patients: An Evaluation for Functional Avoidance Radiation Therapy. *Int J Radiat Oncol.* 2016;95(4):1273-1280.

[20] Lavrenkov K., Christian J.A., Partridge M., et al. A potential to reduce pulmonary toxicity: The use of perfusion SPECT with IMRT for functional lung avoidance in radiotherapy of non-small cell lung cancer. *Radiother Oncol.* 2007;83(2):156-162.

[21] Munawar I., Yaremko B.P., Craig J., et al. Intensity modulated radiotherapy of non-small-cell lung cancer incorporating SPECT ventilation imaging. *Med Phys.* 2010;37(4):1863-1872.

[22] Liss A.L., Marsh R.B., Kapadia N.S., et al. Decreased Lung Perfusion After Breast/Chest Wall Irradiation: Quantitative Results From a Prospective Clinical Trial. *Int J Radiat Oncol.* 2017;97(2):296-302.

[23] Lee E., Zeng J., Miyaoka R.S., et al. Functional lung avoidance and response-adaptive escalation (FLARE) RT: Multimodality plan dosimetry of a precision radiation oncology strategy. *Med Phys.* 2017;44(7):3418-3429.

[24] Huang T.C., Hsiao C.Y., Chien C.R., Liang J.A., Shih T.C., Zhang G.G.. IMRT treatment plans and functional planning with functional lung imaging from 4D-CT for thoracic cancer patients. *Radiother Oncol.* 2013;8(3).

[25] Yamamoto T., Kabus S., Bal M., Keall P., Benedict S., Daly M.. The first patient treatment of computed tomography ventilation functional image-guided radiotherapy for lung cancer. *Radiother Oncol.* 2016;118(2):227-231.

[26] Faught A.M., Yamamoto T., Castillo R., et al. Evaluating Which Dose-Function Metrics Are Most Critical for Functional-Guided Radiation Therapy. *Int J Radiat Oncol.* 2017;99(1):202-209.

[27] Waxweiler T., Schubert L., Diot Q., et al. A complete 4DCT-ventilation functional avoidance virtual trial: Developing strategies for prospective clinical trials. *J Appl Clin Med Phys.* 2017;18(3):144-152.

[28] Ireland R.H., Bragg C.M., McJury M., et al. Feasibility of Image Registration and Intensity-Modulated Radiotherapy Planning With Hyperpolarized Helium-3 Magnetic Resonance Imaging for Non–Small-Cell Lung Cancer. *Int J Radiat Oncol.* 2007;68(1):273-281.

[29] Bates E.L., Bragg C.M., Wild J.M., Hatton M.Q.F., Ireland R.H.. Functional image-based radiotherapy planning for non-small cell lung cancer: A simulation study. *Radiother Oncol.* 2009;93(1):32-36.

[30] Farr K.P., Kramer S., Khalil A.A., Morsing A., Grau C.. Role of perfusion SPECT in prediction and measurement of pulmonary complications after radiotherapy for lung cancer. *Eur J Nucl Med Mol I.* 2015;42(8):1315-1324.

[31] Faught A.M., Miyasaka Y., Kadoya N., et al. Evaluating the Toxicity Reduction With Computed Tomographic Ventilation Functional Avoidance Radiation Therapy. *Int J Radiat Oncol.* 2017;99(2):325-33.

[32] O'Reilly S., Jain V., Huang Q., et al. Dose to Highly Functional Ventilation Zones Improves Prediction of Radiation Pneumonitis for Proton and Photon Lung Cancer Radiotherapy. *Int J Radiat Oncol.* 2020.

[33] Damen E.M., Muller S.H., Boersma L.J., de Boer R.W., Lebesque J.V.. Quantifying local lung perfusion and ventilation using correlated SPECT and CT data. *J Nucl Med.* 1994;35(5):784-792.

[34] Boersma L.J., Damen E.M., de Boer R.W., et al. Dose-effect relations for local functional and structural changes of the lung after irradiation for malignant lymphoma. *Radiother Oncol.* 1994;32(3):201-209.

[35] Boersma L.J., Damen E.M., de Boer R.W., et al. Recovery of overall and local lung function loss 18 months after irradiation for malignant lymphoma. *J Clin Oncol.* 1996;14(5):1431-1441.

[36] Seppenwoolde Y., Muller S.H., Theuws J.C., et al. Radiation dose-effect relations and local recovery in perfusion for patients with non–small-cell lung cancer. *Int J Radiat Oncol.* 2000;47(3):681-690.

[37] Woel R.T., Munley M.T., Hollis D., et al. The time course of radiation therapy-induced reductions in regional perfusion: a prospective study with ¿5 years of follow-up. *Int J Radiat Oncol.* 2002;52(1):58-67.

[38] Zhang J., Ma J., Zhou S., et al. Radiation-induced reductions in regional lung perfusion: 0.1-12 year data from a prospective clinical study. *Int J Radiat Oncol.* 2010;76(2):425-432.

[39] Scheenstra A.E., Rossi M.M., Belderbos J.S., Damen E.M., Lebesque J.V., Sonke J.J.. Local dose – effect relations for lung perfusion post stereotactic body radiotherapy. *Radiother Oncol.* 2013;107(3):398-402.

[40] Farr K.P., Moller D.S., Khalil A.A., Kramer S., Morsing A., Grau C.. Loss of lung function after chemo-radiotherapy for NSCLC measured by perfusion SPECT/CT: Correlation with radiation dose and clinical morbidity. *Acta Oncol.* 2015;54(9):1350-1354.

[41] Emami B., Lyman J., Brown A., et al. Tolerance of normal tissue to therapeutic irradiation. *Int J Radiat Oncol.* 1991;21(1):109-122.

[42] Rodrigues G., Lock M., D'Souza D., Yu E., Van Dyk J.. Prediction of radiation pneumonitis by dose–volume histogram parameters in lung cancer—a systematic review. *Radiother Oncol.* 2004;71(2):127-138.

[43] Kim T.H., Cho K.H., Pyo H.R., et al. Dose-volumetric parameters for predicting severe radiation pneumonitis after three-dimensional conformal radiation therapy for lung cancer. *Radiology.* 2005;235(1):208-215.

[44] Marks L.B., Bentzen S.M., Deasy J.O., et al. Radiation Dose–Volume Effects in the Lung. *Int J Radiat Oncol.* 2010;76(3):S70-S76.

[45] Marks L.B., Yorke E.D., Jackson A., et al. Use of normal tissue complication probability models in the clinic. *Int J Radiat Oncol.* 2010;76(3):S10-S19.

[46] Farr K.P., Kallehauge J.F., Moller D.S., et al. Inclusion of functional information from perfusion SPECT improves predictive value of dose–volume parameters in lung toxicity outcome after radiotherapy for non-small cell lung cancer: A prospective study. *Radiother Oncol.* 2015;117(1):9-16.

[47] Kimura T., Doi Y., Nakashima T., et al. Combined ventilation and perfusion imaging correlates with the dosimetric parameters of radiation pneumonitis in radiation therapy planning for lung cancer. *Int J Radiat Oncol.* 2015;93(4):778-787.

[48] Anger H.O.. Scintillation Camera. *Rev Sci Instrum.* 1958;29(1):27-33.

[49] Kuhl D.E., Edwards R.Q.. Image separation radioisotope scanning. *Radiology.* 1963;80:653-662.

[50] Kuhl D.E., Hale J., Eaton W.L.. Transmission scanning: a useful adjunct to conventional emission scanning for accurately keying isotope deposition to radiographic anatomy. *Radiology.* 1966;87:278-284.

[51] Madsen M.. Recent Advances in SPECT Imaging. *J Nucl Med.* 2007;48:661 - 673.

[52] Healthineers Siemens. Symbia T Series SPECT/CT. Accessed November 19, 2020. https://www.siemens-healthineers.com/en-us/molecular-imaging/spect-and-spect-ct/symbia-t.

[53] Beijst C., Elschot M., Viergever M.A., de Jong H.W.A.M.. A Parallel-Cone Collimator for High-Energy SPECT. *J Nucl Med.* 2015;56(3):476 - 482.

[54] Cyclotron Based Production of Technetium-99m. tech. rep.International Atomic Energy Agency. 2017. https://www-pub.iaea.org/MTCD/Publications/PDF/P1743_web.pdf.

[55] Mettler Jr. F.A., Guiberteau M.J.. *Essentials of Nuclear Medicine and Molecular Imaging.* Elseiver.7th ed. 2019.

[56] Pretorius E.S., Solomon J.A.. *Radiology Secrets Plus.* Mosby.3rd ed. 2011.

[57] Bajc M., Markstad H., Jarenback L., Tufvesson E., Bjermer L., Jogi J.. Grading obstructive lung disease using tomographic pulmonary scintigraphy in patients with chronic obstructive pulmonary disease (COPD) and long-term smokers. *Ann Nucl Med.* 2015;29(1):91-99.

[58] Strickland N.H., Hughes J.M., Hart D.A., Myers M.J., Lavender J.P.. Cause of regional ventilation-perfusion mismatching in patients with idiopathic pulmonary fibrosis: a combined CT and scintigraphic study. *Am J Roentgenol.* 1993;161(4):719-725.

[59] Bajc M., Chen Y., Wang J., et al. Identifying the heterogeneity of COPD by V/P SPECT: a new tool for improving the diagnosis of parenchymal defects and grading the severity of small airways disease. *Int J Chronic Obstr.* 2017;12:1579-1587.

[60] Ireland R.H., Tahir B.A., Wild J.M., Lee C.E., Hatton M.Q.. Functional Image-guided Radiotherapy Planning for Normal Lung Avoidance. *J Clin Oncol.* 2016;28(11):695-707.

[61] Theuws J.C.M., Kwa S.L.S., Wagenaar A.C., et al. Dose–effect relations for early local pulmonary injury after irradiation for malignant lymphoma and breast cancer. *Radiother Oncol.* 1998;48(1):33-43.

[62] De Jaeger K., Seppenwoolde Y., Boersma L.J., et al. Pulmonary function following high-dose radiotherapy of non–small-cell lung cancer. *Int J Radiat Oncol.* 2003;55(5):1331-1340.

[63] Christian J.A., Partridge M., Nioutsikou E., et al. The incorporation of SPECT functional lung imaging into inverse radiotherapy planning for non-small cell lung cancer. *Radiother Oncol.* 2005;77(3):271-277.

[64] Maguire S.M., Zhou S., Marks L.B., Dewhirst M., Yin D.V.M., Das S.K.. A methodology for using SPECT to reduce intensity-modulated radiation therapy (IMRT) dose to functioning lung. *Int J Radiat Oncol.* 2006;66(5):1543-1552.

[65] Bucknell N.W., Hardcastle N., Bressel M., et al. Functional lung imaging in radiation therapy for lung cancer: A systematic review and meta-analysis. *Radiother Oncol.* 2018;129(2):196-208.

[66] Abratt R.P., Willcox P.A., Smith J.A.. Lung cancer in patients with borderline lung functions - zonal lung perfusion scans at presentation and lung function after high dose irradiation. *Radiother Oncol.* 1990;19(4):317-322.

[67] Marks L.B., Munley M.T., Bentel G.C., et al. Physical and biological predictors of changes in whole-lung function following thoracic irradiation. *Int J Radiat Oncol.* 1997;39(3):563-570.

[68] Lind P.A., Marks L.B., Hollis D., et al. Receiver operating characteristic curves to assess predictors of radiation-induced symptomatic lung injury. *Int J Radiat Oncol.* 2002;54(2):340-347.

[69] Yorke E.D., Jackson A., Rosenzweig K.E., et al. Dose-volume factors contributing to the incidence of radiation pneumonitis in non-small-cell lung cancer patients treated with three-dimensional conformal radiation therapy. *Int J Radiat Oncol.* 2002;54(2):329-339.

[70] Seppenwoolde Y., De Jaeger K., Boersma L.J., Belderbos J.S.A., Lebesque J.V.. Regional differences in lung radiosensitivity after radiotherapy for non–small-cell lung cancer. *Int J Radiat Oncol.* 2004;60(3):748-758.

[71] Gayed I.W., Chang J., Kim E.E., et al. Lung Perfusion Imaging Can Risk Stratify Lung Cancer Patients for the Development of Pulmonary Complications after Chemoradiation. *Int J Radiat Oncol.* 2004;60(3):748-758.

[72] Wang D., Sun J., Zhu J., Li X., Zhen Y., Sui S.. Functional dosimetric metrics for predicting radiation-induced lung injury in non-small cell lung cancer patients treated with chemoradiotherapy. *Radiother Oncol.* 2012;7(69).

[73] Hoover D.A., Reid R.H., Wong E., et al. SPECT-based functional lung imaging for the prediction of radiation pneumonitis: A clinical and dosimetric correlation. *J Med Imag Radiat On.* 2014;58:214-222.

[74] Owen D.R., Boonstra P.S., Viglianti B.L., et al. Modeling Patient-Specific Dose-Function Response for Enhanced Characterization of Personalized Functional Damage. *Int J Radiat Oncol.* 2018;102(4):1265-1275.

[75] Castillo R., Castillo E., Martinez J., Guerrero T.. Ventilation from four-dimensional computed tomography: density versus Jacobian methods.. 2010;55(16):4661-4685.

[76] Rietzel E., Pan T., Chen G.T.Y.. Four-dimensional computed tomography: image formation and clinical protocol. *Med Phys.* 2005;32(4):874-879.

[77] Guerrero T., Sanders K., Castillo E., et al. Dynamic ventilation imaging from four-dimensional computed tomography.. 2006;51(4):777-791.

[78] Vinogradskiy Y.Y., Castillo R., Castillo E., et al. Use of 4-Dimensional Computed Tomography-Based Ventilation Imaging to Correlate Lung Dose and Function With Clinical Outcomes. *Int J Radiat Oncol.* 2013;86(2):366-371.

[79] Vinogradskiy Y.Y., Koo P.J., Castillo R., et al. Comparison of 4-Dimensional Computed Tomography Ventilation With Nuclear Medicine Ventilation-Perfusion Imaging: A Clinical Validation Study. *Int J Radiat Oncol.* 2014;89(1):199-205.

[80] Hegi-Johnson F., Keall P., Barber J., Bui C., Kipritidis J.. Evaluating the accuracy of 4D-CT ventilation imaging: First comparison with Technegas SPECT ventilation. *Med Phys.* 2017;44(8):4045-4055.

[81] Kipritidis J., Tahir B.A., Cazoulat G., et al. The VAMPIRE challenge: A multi-institutional validation study of CT ventilation imaging. *Med Phys.* 2019;46(3):1198-1217.

[82] Vinogradskiy Y.Y., Rusthoven C.G., Schubert L., et al. Interim Analysis of a Two-Institution, Prospective Clinical Trial of 4DCT-Ventilation-based Functional Avoidance Radiation Therapy. *Int J Radiat Oncol.* 2018;102(4):1357-1365.

[83] Dehing-Oberije C., De Ruysscher D., van Baardwijk A., Yu S., Rao B., Lambin P.. The importance of patient characteristics for the prediction of radiation-induced lung toxicity. *Radiother Oncol.* 2009;91(3):421-426.

[84] Appelt A.L., Vogelius I.R., Farr K.P., Khalil A.A., Bentzen S.M.. Towards individualized dose constraints: Adjusting the QUANTEC radiation pneumonitis model for clinical risk factors. *Acta Oncol.* 2014;53(5):605-612.

[85] Kong F.M., Wang S.. Nondosimetric Risk Factors for Radiation-Induced Lung Toxicity. *Semin Radiat Oncol.* 2015;25(2):100-109.

[86] Gutte H., Mortensen J., Jensen C.V., et al. Detection of Pulmonary Embolism with Combined Ventilation-Perfusion SPECT and Low-Dose CT: Head-to-Head Comparison with Multidetector CT Angiography. *J Nucl Med.* 2009;50(12):1987-1992.

[87] Ozawa Y., Abe T., Omae M., et al. Impact of Preexisting Interstitial Lung Disease on Acute, Extensive Radiation Pneumonitis: Retrospective Analysis of Patients with Lung Cancer. *Plos One.* 2015;10(10):e0140437.

[88] Bahig H., Filion E., Vu T., et al. Severe radiation pneumonitis after lung stereotactic ablative radiation therapy in patients with interstitial lung disease. *Pract Radiat Oncol.* 2016;6(5):367-374.

[89] Han S.Y., Lee Y.J., Park J.S., et al. Prognosis of non-small-cell lung cancer in patients with idiopathic pulmonary fibrosis. *Sci Rep Nat.* 2019;9(12561).

[90] Kim H., Pyo H., Noh J.M., et al. Preliminary result of definitive radiotherapy in patients with non-small cell lung cancer who have underlying idiopathic pulmonary fibrosis: comparison between X-ray and proton therapy. *Radiother Oncol.* 2019;14(19).

[91] Yamashita H., Kobayashi-Shibata S., Terahara A., et al. Prescreening based on the presence of CT-scan abnormalities and biomarkers (KL-6 and SP-D) may reduce severe radiation pneumonitis after stereotactic radiotherapy. *Radiother Oncol.* 2010;5(32).

[92] Ueki N., Matsuo Y., Togashi Y., et al. Impact of pretreatment interstitial lung disease on radiation pneumonitis and survival after stereotactic body radiation therapy for lung cancer. *J Thorac Oncol.* 2015;10(1):116-125.

[93] Kocak Z., Evans E.S., Zhou S.M., et al. Challenges in defining radiation pneumonitis in patients with lung cancer. *Int J Radiat Oncol.* 2005;62(3):635-638.

[94] Yamaguchi S., Ohguri T., Ide S., et al. Stereotactic body radiotherapy for lung tumors in patients with subclinical interstitial lung disease: The potential risk of extensive radiation pneumonitis. *Lung Cancer.* 2013;82(2):260-265.

[95] Rancati T., Ceresoli G.L., Gagliardi G., Schipani S., Cattaneo G.M.. Factors predicting radiation pneumonitis in lung cancer patients: a retrospective study. *Radiother Oncol.* 2003;67(3):275-283.

[96] Jin H., Tucker S.L., Liu H.H., et al. Dose-volume thresholds and smoking status for the risk of treatment-related pneumonitis in inoperable non-small cell lung cancer treated with definitive radiotherapy. *Radiother Oncol.* 2009;91(3):427-432.

[97] Takeda A., Kunieda E., Ohashi T., et al. Severe COPD is correlated with mild radiation pneumonitis following stereotactic body radiotherapy. *Radiother Oncol.* 2012;141(4):858-866.

[98] Castillo R., Pham N., Ansari S., et al. Pre-radiotherapy FDG PET predicts radiation pneumonitis in lung cancer. *Radiother Oncol.* 2014;9(74).

[99] Han S.Y., Lee Y.J., Park J.S., et al. Evaluation of lung toxicity risk with computed tomography ventilation image for thoracic cancer patients. *Plos One.* 2018;13(10):e0204721.

[100] Bradley J.D., Hope A., El Naqa I., et al. Severe COPD is correlated with mild radiation pneumonitis following stereotactic body radiotherapy. *Int J Radiat Oncol.* 2007;69(4):985-992.

[101] Tsoutsou P.G., Koukourakis M.I.. Radiation Pneumonitis and Fibrosis: Mechanisms Underlying its Pathogenesis and Implications for Future Research. *Int J Radiat Oncol.* 2006;66(5):1281-1293.

[102] Siva S., MacManus M., Kron T., et al. A pattern of early radiation-induced inflammatory cytokine expression is associated with lung toxicity in patients with non-small cell lung cancer. *Plos One.* 2014;9(10).

[103] Rubin P., Johnston C.J., Williams J.P., McDonald S., Finkelstein J.N.. A perpetual cascade of cytokines postirradiation leads to pulmonary fibrosis. *Int J Radiat Oncol.* 1995;33(1):99-109.

[104] Kolb M., Margetts P.J., Anthony D.C., Pitossi F., Gauldie J.. Transient expression of IL-1β induces acute lung injury and chronic repair leading to pulmonary fibrosis. *J Clin Invest.* 2001;107(12):1529-1536.

[105] Zhang Y., Lee T.C., Guillemin B., Yu M.C., Rom W.N.. Enhanced IL-1β and tumor necrosis factor-alpha release and messenger RNA expression in macrophages from idiopathic pulmonary fibrosis or after asbestos exposure. *J Immunol.* 1993;150(9):4188-4196.

[106] Pan L.H., Ohtani H., Yamauchi K., Nagura H.. Co-expression of TNFα and IL-1β in human acute pulmonary fibrotic diseases: An immunohistochemical analysis. *Pathol Int.* 1996;46(2):91-99.

[107] Chen Y., Hyrien O., Williams J., Okunieff P., Smudzin T., Rubin P.. Interleukin (IL)-1α and IL-6: applications to the predictive diagnostic testing of radiation pneumonitis. *Int J Radiat Oncol.* 2005;62(1):260-266.

[108] Kainthola A., Haritwal T., Tiwari M., et al. Immunological Aspect of Radiation-Induced Pneumonitis, Current Treatment Strategies, and Future Prospects. *Front Immunol.* 2017;8(506).

[109] Rube C.E., Wilfert F., Uthe D., et al. Modulation of radiation-induced tumour necrosis factor alpha (TNF-alpha) expression in the lung tissue by pentoxifylline. *Radiother Oncol.* 2002;64(2):177-187.

[110] Leemans J.C., Vervoordeldonk M.J.B.M., Florquin S., van Kessel K.P., van der Poll T.. Differential Role of Interleukin-6 in Lung Inflammation Induced by Lipoteichoic Acid and Peptidoglycan from Staphylococcus aureus. *Am J Resp Cell Mol.* 2002;165(10):1445-1450.

[111] Scheller J., Chalaris A., Schmidt-Arras D., Rose-John S.. The pro- and anti-inflammatory properties of the cytokine interleukin-6. *BBA-Mol Cell Res.* 2011;1813(5):878-888.

[112] Moodley Y.P., Misso N.L.A., Scaffidi A.K., et al. Inverse effects of interleukin-6 on apoptosis of fibroblasts from pulmonary fibrosis and normal lungs. *Am J Resp Cell Mol.* 2003;29(4):490-498.

[113] Yu M., Zheng X., Witschi H., Pinkerton K.E.. The Role of Interleukin-6 in Pulmonary Inflammation and Injury Induced by Exposure to Environmental Air Pollutants. *Toxicol Sci.* 2002;68(2):488-497.

[114] Le T.T.T., Karmouty-Quintana H., Melicoff E., et al. Blockade of IL-6 Trans Signaling Attenuates Pulmonary Fibrosis. *J Immunol.* 2014;93(7):3755-3768.

[115] Chen Y., Rubin P., Williams J., Hernady E., Smudzin T., Okunieff P.. Circulating IL-6 as a Predictor of Radiation Pneumonitis. *Int J Radiat Oncol.* 2001;49(3):641-648.

[116] Yoshida M., Sakuma J., Hayashi S., et al. A histologically distinctive interstitial pneumonia induced overexpression of the interleukin 6, transforming growth factor beta 1, or platelet-derived growth factor B gene. *Proc Natl Acad Sci.* 1995;92(21):9570-9574.

[117] Bartram U., Speer C.P.. The Role of Transforming Growth Factor β in Lung Development and Disease. *Chest.* 2004;125(2):754-765.

[118] Abratt R.P., Morgan G.W.. Lung toxicity following chest irradiation in patients with lung cancer. *Lung Cancer.* 2002;35(2):103-109.

[119] De Jaeger K., Seppenwoolde Y., Kampinga H.H., Boersma L.J., Belderbos J.S., Lebesque J.V. Significance of plasma transforming growth factor-beta levels in radiotherapy for non-small-cell lung cancer. *Int J Radiat Oncol.* 2004;58(5):1378-1387.

[120] Zhao L., Wang L., Ji W., et al. Elevation of Plasma TGF-β1 During Radiation Therapy Predicts Radiation-Induced Lung Toxicity in Patients With Non-Small-Cell Lung Cancer: A Combined Analysis From Beijing and Michigan. *Int J Radiat Oncol.* 2009;74(5):1385-1390.

[121] Zhang X.J., Sun J.G., Sun J., et al. Prediction of radiation pneumonitis in lung cancer patients: A systematic review. *J Cancer Res Clin.* 2012;138(12):2103-2116.

[122] Anscher M.S.. Targeting the TGF-beta1 pathway to prevent normal tissue injury after cancer therapy. *Oncologist.* 2010;15(4):350-359.

[123] Carl C., Flindt A., Hartmann J., et al. Ionizing radiation induces a motile phenotype in human carcinoma cells in vitro through hyperactivation of the TGF-beta signaling pathway. *Cell Mol Life Sci.* 2016;73(2):427-443.

[124] Morgan G.W., Breit S.N.. Radiation and the lung: a reevaluation of the mechanisms mediating pulmonary injury. *Int J Radiat Oncol.* 1995;31(2):361-369.

[125] Zhang M., Qian J., Xing X., et al. Inhibition of the tumor necrosis factor-alpha pathway is radioprotective for the lung. *Clin Cancer Res.* 2008;14(6):1868-1876.

[126] Dubsky S., Fouras A.. Imaging regional lung function: A critical tool for developing inhaledantimicrobial therapies. *Adv Drug Deliver Rev.* 2015;85:100-109.

[127] Bajc M., Neilly B., Miniati M., Mortensen J., Jonson B.. Methodology for ventilation/perfusion SPECT. *Semin Nucl Med.* 2010;40(6):415-425.

[128] Schembri G.P., Roach P.J., Bailey D.L., Freeman L.. Artifacts and Anatomical Variants Affecting Ventilation and Perfusion Lung Imaging. *Semin Nucl Med.* 2015;45(5):373-391.

[129] Van Esch A., Tillikainen L., Pyykkonen J., et al. Testing of the analytical anisotropic algorithm for photon dose calculation. *Med Phys.* 2006;33(11):4130-4148.

[130] Li A.X., Alber M., Deasy J.O., et al. The use and QA of biologically related models for treatment planning: short report of the TG-166 of the therapy physics committee of the AAPM. *Med Phys.* 2012;39(3):1386-1409.

[131] Kong F.M., Ritter T., Quint D.J., et al. Consideration of dose limits for organs at risk of thoracic radiotherapy: atlas for lung, proximal bronchial tree, esophagus, spinal cord, ribs, and brachial plexus. *Int J Radiat Oncol.* 2011;81(5):1442-1457.

[132] Kreinbrink P., Blumenfeld P., Tolekidis G., Sen N., Sher D., Marwaha G.. Lung stereotactic body radiation therapy (SBRT) for early-stage non-small cell lung cancer in the very elderly ($\geq$80 years old): Extremely safe and effective. *J Geriatr Oncol.* 2017;8(5):351-355.

[133] Wang J.Z., Huang Z., Lo S.S., Yuh W.T.C., Mayr N.A.. A Generalized Linear-Quadratic Model for Radiosurgery, Stereotactic Body Radiation Therapy, and High–Dose Rate Brachytherapy. *Sci Transl Med.* 2010;2(39):39-48.

[134] Kong F.M., Moiseenko V., Zhao J., et al. Organs at Risk Considerations for Thoracic Stereotactic Body Radiation Therapy: What Is Safe for Lung Parenchyma? *Int J Radiat Oncol.* 2018.

[135] U.S Department of Human and Health Services, National Institutes of Health, National Cancer Institute . Common Terminology Criteria for Adverse Events (CTCAE). Vol 4. 2009.

[136] Davidian M., Giltinan D.M.. Nonlinear models for repeated measurement data: An overview and update. *J Agr Biol Envir St.* 2003;8(4):387-419.

[137] Pinheiro J., Bates D., DebRoy S., et al. nlme: Linear and Nonlinear Mixed Effects Models. 2020. `https://cran.r-project.org/web/packages/nlme/index.html`.

[138] Fan M., Marks L.B., Hollis D., et al. Can we predict radiation-induced changes in pulmonary function based on the sum of predicted regional dysfunction?. *J Clin Oncol.* 2001;19(2):543-550.

[139] Jin J.Y., Kong F.M., Chetty I.J., et al. Impact of Fraction Size on Lung Radiation Toxicity: Hypofractionation may be Beneficial in Dose Escalation of Radiotherapy for Lung Cancers. *Int J Radiat Oncol.* 2010;76(3):782-788.

[140] Rasmi R., Guruvayoorappan C.. Pulmonary injury associated with radiation therapy – Assessment,complications and therapeutic targets. *Biomed Pharmacother.* 2017;89:1092-1104.

[141] Jensen J.L.W.V.. Sur les fonctions convexes et les inégalités entre les valeurs moyennes. *Acta Math.* 1906;30:175-193.

[142] Chun S.G., Hu C., Choy H., et al. Impact of Intensity-Modulated Radiation Therapy Technique for Locally Advanced Non-Small-Cell Lung Cancer: A Secondary Analysis of the NRG Oncology RTOG 0617 Randomized Clinical Trial. *J Clin Oncol.* 2017;35(1):56-62.

[143] Kong F.M., Ten Haken R.K., Schipper M.J., et al. Effect of Midtreatment PET/CT-Adapted Radiation Therapy With Concurrent Chemotherapy in Patients With Locally Advanced Non-Small-Cell Lung Cancer: A Phase 2 Clinical Trial. *JAMA Oncol.* 2017;3(10):1358-1365.

[144] Bayouth J., Schuster J.. Improving Pulmonary Function Following Radiation Therapy. 2016; NCT02843568. `https://clinicaltrials.gov/ct2/show/nct02843568`.

[145] Zeng J., Patel S., Rengan R., Bowen S.. FLARE RT for Patients With Stage IIB-IIIB Non-small Cell Lung Cancer: Personalizing Radiation Therapy Using PET/CT and SPECT/CT Imaging. 2016; NCT02843568. https://clinicaltrials.gov/ct2/show/nct02843568.

[146] Jolly S.. Using Imaging and Molecular Markers to Predict Tumor Response and Lung Toxicity in Lung Cancer. 2008; NCT00603057. https://clinicaltrials.gov/ct2/show/nct00603057.

[147] Ramella S., Trodella L., Mineo T.C., et al. Adding ipsilateral V20 and V30 to conventional dosimetric constraints predicts radiation pneumonitis in stage IIIA-B NSCLC treated with combined-modality therapy. *Int J Radiat Oncol.* 2010;76(1):110-115.

[148] Yuan S.T., Frey K.A., Gross M.A., et al. Semiquantification and classification of local pulmonary function by V/Q single photon emission computed tomography in patients with non-small cell lung cancer: potential indication for radiotherapy planning. *J Thorac Oncol.* 2011;6(1):71-78.

[149] Gelblum D., Rimner A., Wu A.J., Colemann A.. Treatment Toxicity From Lung Radiation Therapy in Patients With Underlying Idiopathic Pulmonary Fibrosis. *Int J Radiat Oncol.* 2015;93(3):E442.

[150] Keffer S., Guy C.L., Weiss E.. Fatal Radiation Pneumonitis: Literature Review and Case Series. *Adv Radiat Oncol.* 2020;5(2):238-249.

[151] Makimoto T., Tsuchiya S., Hayakawa K., Saitoh R., Mori M.. Risk Factors for Severe Radiation Pneumonitis in Lung Cancer. *Jpn J Clin Oncol.* 1999;29(4):192-197.

[152] Phillips T.L.. *Radiation Fibrosis. In: Fishman AP, editor. Pulmonary Diseases and Disorders Vol 1.* New York: McGraw-Hill 1988.

[153] Monson J.M., Stark P., Reilly J.J., et al. Clinical radiation pneumonitis and radiographic changes after thoracic radiation therapy for lung carcinoma. *Cancer.* 1998;82(5):842-850.

[154] Kim H., Yoo H., Pyo H., et al. Impact Of Underlying Pulmonary Diseases On Treatment Outcomes In Early-Stage Non-Small Cell Lung Cancer Treated With Definitive Radiotherapy. *Int J Chronic Obstr.* 2019;14:2273-2281.

[155] Chaudhuri A.A., Binkley M.S., Rigdon J., et al. Pre-treatment non-target lung FDG-PET uptake predicts symptomatic radiation pneumonitis following Stereotactic Ablative Radiotherapy (SABR). *Radiother Oncol.* 2016;119(3):454-460.

[156] Tsoutsou P.G.. The interplay between radiation and the immune system in the field of post-radical pneumonitis and fibrosis and why it is important to understand it. *Front Oncol.* 2019;15(13):1781-1783.

[157] Mehta V.. Radiation Pneumonitis and Pulmonary Fibrosis in Non-Small-Cell Lung Cancer: Pulmonary Function, Prediction, and Prevention. *Int J Radiat Oncol.* 2005;63(1):5-24.

[158] Giuranno L., Ient J., De Ruysscher D., Vooijs M.A.. Radiation-Induced Lung Injury (RILI). *Expert Opin Pharmacother.* 2014;9(877).

[159] Schoenfeld J., Nishino M., Severgnini M., Manos M., Mak R.H., Hodi F.S.. Pneumonitis resulting from radiation and immune checkpoint blockade illustrates characteristic clinical, radiologic and circulating biomarker features. *J Immunother Cancer.* 2019;7(1):112-118.

[160] Tian S., Switchenko J.M., Buchwald J.W., et al. Lung Stereotactic Body Radiation Therapy and Concurrent Immunotherapy: A Multicenter Safety and Toxicity Analysis. *Int J Radiat Oncol.* 2020;108(1):304-313.

[161] Asmis T.R., Ding K., Seymour L., et al. Age and comorbidity as independent prognostic factors in the treatment of non small-cell lung cancer: a review of National Cancer Institute of Canada Clinical Trials Group trials. *J Clin Oncol.* 2008;26(1):54-59.

[162] Gould M.K., Munoz-Plaza C.E., Hahn E.E., Lee J.S., Parry C., Shen E.. Comorbidity profiles and their effect on treatment selection and survival among patients with lung cancer. *Ann Am Thor Soc.* 2017;14(10):1571-1580.

[163] Fox M.S., Ouriadov A., Thind K., et al. Detection of radiation induced lung injury in rats using dynamic hyperpolarized 129Xe magnetic resonance spectroscopy. *Med Phys.* 2014;41(7).

[164] van Elmpt W., Landry G., Das M., Verhaegen F.. Dual energy CT in radiotherapy: Current applications and future outlook. *Radiother Oncol.* 2016;119(1):137-144.

[165] Petit S.F., van Elmpt W.J.C., Oberije C.J.G., et al. [18F]fluorodeoxyglucose uptake patterns in lung before radiotherapy identify areas more susceptible to radiation-induced lung toxicity in non-small-cell lung cancer patients. *Int J Radiat Oncol.* 2011;81(3):698-705.

[166] Galban C.J., Han M.K., Boes J.L., et al. CT-based Biomarker Provides Unique Signature for Diagnosis of COPD Phenotypes and Disease Progression. *Nat Med.* 2012;18(11):1711-1715.

[167] Bhatt S.P., Soler X., Wang X., et al. Association between Functional Small Airway Disease and FEV1 Decline in Chronic Obstructive Pulmonary Disease. *Am J Respir Crit Care Med.* 2016;194(2):178-184.

[168] Vasilescu D.M., Martinez F.J., Marchetti N., et al. Noninvasive Imaging Biomarker Identifies Small Airway Damage in Severe Chronic Obstructive Pulmonary Disease. *Am J Respir Crit Care Med.* 2019;200(5):575-581.

[169] Galban C.J., Boes J.L., Bule M., et al. Parametric response mapping as an indicator of bronchiolitis obliterans syndrome after hematopoietic stem cell transplantation. *Biol Blood Marrow Tr.* 2014;20(10):1592-1598.

[170] Sharifi H., Lai Y.K., Guo H., et al. Machine Learning Algorithms to Differentiate Among Pulmonary Complications After Hematopoietic Cell Transplant. *Chest.* 2020;158(3):1090-1103.

[171] Belloli E.A., Degtiar I., Wang X., et al. Parametric response mapping as an imaging biomarker in lung transplant recipients. *Am J Respir Crit Care Med.* 2017;195(7):942-952.

[172] Hoff B.A., Pompe E., Galban S., et al. CT-Based Local Distribution Metric Improves Characterization of COPD. *Sci Rep Nat.* 2017;7(2999).

[173] Shamonin D.P., Bron E.E., Lelieveldt B.P.F., et al. Fast parallel image registration on CPU and GPU for diagnostic classification of Alzheimer's disease. *Front Neuroinform.* 2014;7(50).

[174] Klein S., Staring M., Murphy K., Viergever M.A., Pluim J.P.W.. Elastix: a toolbox for intensity-based medical image registration. *IEEE T Med Imaging.* 2010;29(1):196-205.

[175] Gevenois P.A., De Vuyst P., de Maertelaer V., et al. Comparison of computed density and microscopic morphometry in pulmonary emphysema. *Am J Respir Crit Care Med.* 1996;154(1):187-192.

[176] Coxson H.O., Rogers R.M., Whittall K.P., et al. A quantification of the lung surface area in emphysema using computed tomography. *Am J Respir Crit Care Med.* 1999;159(3):851-856.

[177] Mascalchi M., Camiciottoli G., Diciotti S.. Lung densitometry: why, how and when. *J Thorac Dis.* 2017;9(9):3319-3345.

[178] Leduc C., Antoni D., Charloux A., Falcoz P.E., Quoix E.. Comorbidities in the management of patients with lung cancer. *Eur Respir J.* 2017;49(3).

[179] Usui K., Tanai C., Tanaka Y., Noda H., Ishihara T.. The prevalence of pulmonary fibrosis combined with emphysema in patients with lung cancer. *Respirology.* 2011;16(2):326-331.

[180] Loganathan R.S., Stover D.E., Shi W., Venkatraman E.. Prevalence of COPD in women compared to men around the time of diagnosis of primary lung cancer. *Chest.* 2006;129(5):1305-1312.

[181] Sigel K., Wisnivesky J.P.. Comorbidity Profiles of Patients with Lung Cancer: A New Approach to Risk Stratification? *Ann Am Thor Soc.* 2017;14(10):1512-1513.

[182] Spyratos D., Papadaki E., Lampaki S., Kontakiotis T.. Chronic obstructive pulmonary disease in patients with lung cancer: Prevalence, impact and management challenges. *Lung Cancer.* 2017;8:101-107.

[183] Podolanczuk A.J., Oelsner E.C., Barr R.G., et al. High attenuation areas on chest computed tomography in community-dwelling adults: the MESA study. *Eur Respir J.* 2016;48(5):1442-1452.

[184] Defraene G., van Elmpt W., Crijns W., Slagmolen P., De Ruysscher D.. CT characteristics allow identification of patient-specific susceptibility for radiation-induced lung damage. *Radiother Oncol.* 2015;117(1):29-35.

[185] Defraene G., van Elmpt W., Crijns W., De Ruysscher D.. Regional variability in radiation-induced lung damage can be predicted by baseline CT numbers. *Radiother Oncol.* 2017;122(2):300-306.

[186] Lowe K.E., Regan E.A., Anzueto A., et al. COPDGene 2019: Redefining the Diagnosis of Chronic Obstructive Pulmonary Disease. *Int J Chronic Obstr.* 2019;6(5):384-399.

[187] Sieren J.P., Newell Jr J.D., Barr R.G., et al. SPIROMICS Protocol for Multicenter Quantitative Computed Tomography to Phenotype the Lungs. *Am J Respir Crit Care Med.* 2016;194(7):794-806.